First CLAS12 Double-Pion ($N\pi\pi$) Electroproduction Analysis

by

Krishna Chandra Neupane

Bachelor of Science
Tribhuvan University, 2011

Master's Degree in Physics
Tribhuvan University, 2014

Submitted in Partial Fulfillment of the Requirements

for the Degree of Doctor of Philosophy in

Physics

College of Arts and Sciences

University of South Carolina

2025

Accepted by:

Ralf Gothe, Major Professor

Fred Myhrer, Committee Member

Steffen Strauch, Committee Member

Viktor Mokeev, Committee Member

Ann Vail, Dean of the Graduate School

Dedication

This dissertation is dedicated to my parents, Tul Bahadur Neupane and Kamala Neupane. They grew up in a remote village in Nepal, where my mother never had the opportunity to go to school. She cannot read a book, but her life itself has been both a school and a book for me. Through her daily hard work, she taught me the true meaning of dedication, perseverance, and patience. My father's love for learning and passion for education, despite not having the chance to study beyond the 5^{th} grade, has been my biggest inspiration on this journey. Mama, Baba, this dissertation belongs to you as much as it does to me.

Acknowledgments

I express my gratitude to my advisor, Dr. Ralf Gothe, for his guidance, support, and motivation throughout my Ph.D. His mentorship has allowed me to learn, grow, and excel as a student. His kindness and generosity have been invaluable to me and I consider myself fortunate to have him as my advisor. He has supported throughout this journey, being very close and listening to every issue raised during the physics analysis and giving his ideas to solve them. This would not have been possible without his proper guidance.

I am grateful to my wife, Narayan Devi Manandhar, for her unconditional love and support throughout my Ph.D. Her hard work in raising our two children, Jason and Aayush, made my Ph.D possible. With her care and sacrifices, my experience has been filled with happiness and joy.

I would like to thank my respected dissertation committee members, Dr. Fred Myhrer, Dr. Steffen Strauch, and Dr. Viktor Mokeev, for their time and effort in reviewing my work. Their valuable feedback helped me refine my research and improve my writing. A special thanks to Dr. Viktor Mokeev for his comments and suggestions during the weekly 'First Experiment Hadron Structure Group Meeting' and other meetings and discussions, which have been very helpful and guiding for me.

I would like to thank Dr. Nick Tyler for his help with coding, software, and setting up environments on different remote clusters. His hipo_tools software for converting hipo files to ROOT format has been incredibly useful for me, my colleagues, and many other collaborators. From the very beginning, Nick has helped me develop my programming skills, and I truly appreciate his support throughout my Ph.D.

I acknowledge Dr. Iuliia Skorodumina for developing the TWOPEG event generator, making simulations easier and faster for my physics analysis. I am grateful to my colleagues Dr. Arjun Trivedi, Dr. Suraj Poudel, Dr. Ye Tian, Dr. Gary Hollis, Dr. Christopher McLauchlin, Dr. Nassim Beiranvand, David Edwins, Dr. Vincent Dowling, and Dr. Chatura Kuruppu for their support and collaboration. Special thanks to Alexis Osmond and Noah Smith for reviewing my dissertation and providing valuable feedback.

I want to thank people from the Jefferson Lab CLAS Collaboration, especially Dr. Daniel S. Carman and Dr. Chaden Djalali for their valuable input, comments, and suggestions on this work. Many thanks to Dr. Kyungseon Joo, Dr. Volker Burkert, Dr. Latifa Elouadrhiri, Dr. Philip Cole, and Dr. Bryan McKinnon for their feedback on my physics analysis. A special thanks to Dr. Raffaella De Vita, Dr. Timothy Hayward, Dr. Christopher Dilks, Dr. Maurizio Ungaro, Dr. Nathan Baltzel, Dr. Cole Smith, Dr. Stepan Stepanyan, and all software group people for their help in understanding various software, data management, and analysis processes. I also appreciate the support of Dr. Stefan Diehl, Dr. Valerii Klimenko, Dr. Pierre Chatagnon, Dr. Sangbaek Lee, Dr. Utsav Shrestha, and Dr. Richard Capobianco, for their assistance with my analysis and data corrections.

I sincerely thank the faculty and staff of the Department of Physics and Astronomy for their support. In particular, Dr. Matthias Schindler, Dr. Brett Altschul, Dr. Yordanka Ilieva, Dr. David Tedeschi, Dr. Vladimir Gudkov, and former faculty member Dr. Milind Purohit for their lectures and discussions, which have deepened my understanding of nuclear and particle physics. Also, a big thanks goes to Beth Powell, James Clawson, Nancy Kesar, and former staff member Sam Beals for their administrative support.

I express my sincere appreciation for the computing resources and support provided by the University of South Carolina Hyperion Cluster team, particularly Nathan

Elger, Milligan Myk, and others, for their invaluable assistance throughout this work.

I want to thank Jackie Richards, a true friend who is always ready to help, support, and listen. Her kindness and support will always be in my heart. Because of her, this place felt like home. I also want to thank my brother Bishnu Chandra Neupane, sister Indra Kala Neupane, and brother-in-law Rashmi Bahadur K.C. for their love, support, and encouragement during my Ph.D., even from the other half of the world.

I am grateful to the University of South Carolina, the Department of Physics and Astronomy, and the National Science Foundation for their funding and support.

Abstract

The N* program aims to explore strong interaction dynamics of the three-valence quark distance-dependent structure. The electroproduction and photoproduction studies provide insight into the nucleon resonance structure. One of the primary objectives of N* is to extract the electroexcitation amplitudes, which are crucial in determining the inner structure of various nucleon excitation states and their underlying degrees of freedom. Studying them on the nucleon length scale reveals also parts of the complex nature of the universe and its origin at their most fundamental level. The extraction of these amplitudes is mostly based on the single-pion, and particularly at higher invariant masses W, on the double-pion electroproduction channels, because nucleon resonance dominantly couple to them. CLAS has produced mostly all of the world data on charged double-pion electroproduction in the nucleon resonance region for photon virtualities Q^2 up to 5 GeV^2. The kinematic range can be extended with CLAS12, which can explore these amplitudes in the still almost unexplored range of $Q^2 > 5.0$ GeV^2. This will offer opportunities to understand the resonance structure at distances where the three-bound quark degree of freedom dominates and pave the way towards perturbative Quantum Chromodynamics (pQCD). This dissertation presents new double-pion electroproduction cross sections in the W range [1.4, 2.10] GeV and the Q^2 range [2.0, 8.0] GeV^2, using the Run Group A Fall-2018 dataset. This data was taken with the CLAS12 detector in Hall B at Thomas Jefferson National Laboratory (JLab) at an electron beam energy of 10.6 GeV. These cross sections are the basis for the extraction of resonance electroexcitation amplitudes using the phenomenological JLab - Moscow State University (JM) model.

Table of Contents

Dedication iii

Acknowledgments iv

Abstract vii

List of Tables xi

List of Figures xii

Chapter 1 Introduction 1

1.1 JM Model 6

Chapter 2 Experiment 9

2.1 CEBAF Large Acceptance Spectrometer 11

2.2 Data acquisition and reconstruction of events 24

Chapter 3 Event Selection 27

3.1 Particle identification 27

3.2 Energy loss corrections 46

3.3 Momentum corrections 49

3.4 Simulations and smearing 57

3.5 Double-pion event selection 64

3.6 Kinematic coverage 67

Chapter 4 Detector Inefficient Regions 69

4.1 Inefficient PCAL regions 69

4.2 Experimental over MC data ratio 70

Chapter 5 Cross Sections Calculation 74

5.1 Analysis variables 74

5.2 Cross section formulae 79

5.3 Beam currents and Faraday cup charge adjustments 82

Chapter 6 Acceptance Correction and Hole Filling 85

6.1 Acceptance correction factor from MC data 85

6.2 Background merging in MC data 87

6.3 Cross section scaling factor 88

6.4 Radiative effect corrections 90

6.5 Binning 92

6.6 Acceptance studies and error cuts 92

6.7 Hole filling 95

Chapter 7 Corrections 98

7.1 Particle detection efficiency corrections 98

7.2 Background subtraction 107

7.3 Bin centering corrections 111

Chapter 8 Statistical and Systematic Uncertainties 115

8.1 Statistical uncertainties 115

8.2 Systematic uncertainties 115

Chapter 9 Results and Conclusions 118

Bibliography 121

Appendix A Measured single-differential cross sections 127

List of Tables

Table 2.1 All data runs used in this analysis. 10

Table 7.1 Binning for the proton efficiency factors. 99

Table 7.2 Binning for the π^+ efficiency factors. 105

Table 8.1 List of estimated systematic uncertainties. 117

List of Figures

Figure 1.1 Schematic drawing of charged double-pion electroproduction off the proton. 5

Figure 1.2 The key mechanisms of the JM model for double-pion electroproduction: plot (a) is for full amplitude, (b) for $\pi^-\Delta^{++}$ and $\pi^-\Delta^{++}(1600)\,3/2^+$ sub-channels, (c) for $\pi^+\Delta^0$, $\pi^+N^0(1520)\,3/2^-$, and $\pi^+N^0(1680)\,5/2^+$ sub-channels, (d) for ρp sub-channel, and (e) direct double-pion production mechanisms. Figure is adapted from [1]. 7

Figure 1.3 Description of the nine single-differential $\pi^+\pi^-p$ electroproduction cross sections measured with CLAS [2][3] (black points) achieved within the JM23 model, at W[1.55, 1.58] GeV and Q^2[3.50, 4.20] GeV^2. First row corresponds to the three invariant masses: $M_{\pi^+p'}$ (left), $M_{\pi^+\pi^-}$ (middle), and $M_{\pi^-p'}$ (right). The second row corresponds to the three θ angles: θ_{π^-} (left), θ_{π^+} (middle), $\theta_{p'}$ (right). The third row corresponds to the three α angles: α_{π^-} (left), α_{π^+} (middle), $\alpha_{p'}$ (right). All the variables are in center of mass frame, more details on variables are at Sec. 5.1. The computed differential cross sections are shown by the black solid lines, while the contributions from the $\pi^-\Delta^{++}$ and $\pi^+\Delta^0$ channels are shown by the red dashed and blue dotted lines, respectively. The contributions from direct double-pion production are shown by the magenta long-dashed lines. Figure is adapted from [1]. 8

Figure 2.1 Schematic illustration of the CEBAF accelerator, which delivered electron beams with energies up to 10.6 GeV. Figure is adapted from [4]. 9

Figure 2.2 Electron yields normalized to the Faraday cup charge in sector 1 of Forward Detector system Figure is adapted from [5]. 11

Figure 2.3 CLAS12 detector system. Figure is adapted from [6]. 12

Figure 2.4 Simplified model illustration of CLAS12 solenoid and torus magnets (left), solenoid and torus magnetic fields are shown at full current (right), open boxes represent various CLAS12 detector elements. Figures are adapted from [7]. 14

Figure 2.5 Illustration of the of three regions comprised of six drift chambers each in CLAS12 forward tracking system. Figure is adapted from [8]. 15

Figure 2.6 Wire layout for one superlayer, track detected is represented by red line. Figure is adapted from [8]. 16

Figure 2.7 Lateral view of HTCC with its surrounding CLAS12 detector components (left), self-supporting mirror composed of 60 ellipsoidal mirrors (right). Figures are adapted from [9]. 17

Figure 2.8 CLAS12 FTOF system showing the panel-1b counters on the inside (dark blue color), panel 1-a are behind panel 1-b (not visible in the figure) and the panel-2 counters on the outside (orange color). Figure is adapted from [10]. 18

Figure 2.9 CLAS12 calorimeter system showing installation of PCAL in front of EC. PMTs are also shown at the edge of PCAL sector. Figures are adapted from [11]. 20

Figure 2.10 Alternating U, V, and W planes of the calorimeter along with the lead sheets. Figure is adapted from [11]. 21

Figure 2.11 Event display view in CLAS12 CD system. Starting from the inner three SVT regions surrounded by six BMT layers, then the CTOF, and finally the CND scintillation bars. Figure is adapted from [6]. 22

Figure 2.12 CLAS12 Central vertex tracker with the SVT, BMT, and FMT. The inner three regions of SVT are surrounded by the outer six layers of BMT. Six layers of FMT disks are shown downstream of all SVT and BMT layers. Figure is adapted from [12]. 23

Figure 2.13 Schematic view of a resistive MVT detector. Figure is adapted from [13]. 23

Figure 2.14 CLAS12 CTOF scintillation bars along with PMTs. Figure is adapted from [14]. 24

Figure 3.1 The z component of the vertex position cut for electrons for all six sectors of CLAS12 FD. Exp stands for experimental measurement and Sim for Monte-Carlo simulated data. 30

Figure 3.2 The z component of the vertex position showing empty target subtraction for all six sectors of CLAS12 FD. The red histograms represent events from the empty target runs, the blue histograms correspond to the full target, and the green histograms show the subtracted distributions (full minus empty). . . 30

Figure 3.3 Sampling fraction distribution with Gaussian fit for one particular momentum bin [5.5, 6.0] GeV, in sector 1, using experimental data (left) and simulated data (right). The data are represented by blue histograms, Gaussian fit by red curves. 31

Figure 3.4 Sampling fraction versus momentum for electrons for all six sectors using measured data. Red lines are the applied cuts. . . . 32

Figure 3.5 Sampling fraction versus momentum for electrons for all six sectors using MC simulated data. Red lines are the applied cuts. . 32

Figure 3.6 PCAL measured electron yield distribution versus y for the x slice from 100 to 120 cm in sector 1. The data are represented by blue histogram, fit by red curve, and green lines are used cuts. 34

Figure 3.7 Electron PCAL fiducial cut plots showing y vs. x distributions for all six sectors after applying the rotations defined in Eq.(3.3). The red lines and circle indicate the fitted fiducial cut boundaries. 34

Figure 3.8 Super-Gaussian fit to the DC R1 experimental yield distribution as a function of y, for the x slice from 40 to 45 cm, for electron candidates in sector 1. The blue histogram represents the data, the red curve shows the fit, and the green vertical lines indicate the applied selection cuts. 35

Figure 3.9 Measured DC R1 y versus x coordinates for electron candidates, with fiducial and inner circular cuts. Cuts are shown by red fitted lines and dashed circle. 36

Figure 3.10 Difference in the z component of the vertex position for the proton and electron of each event. Left plot is for CD detected proton candidates and right plot is for FD detected protons. . . . 38

Figure 3.11 Chi-square PID cuts for proton candidates. Left plot is for CD detected protons candidates and right plot is for FD detected protons. 39

Figure 3.12 Gaussian fit to Δt distribution calculated using mass of proton, shown for momentum bin [3.45, 3.70] GeV, experimental at left, and simulation at right. Red dashed lines are the 3.5σ cuts. . . . 40

Figure 3.13 Δt versus momentum distribution for positive particles detected by FTOF assuming the mass of a proton, experimental at left, and simulation at right. 40

Figure 3.14 Δt versus momentum distribution for positive particles detected by CTOF assuming the mass of a proton, experimental at left, and simulation at right. 41

Figure 3.15 Super-Gaussian fit to the DC R1 experimental yield distribution as a function of y, for the x slice from 55 to 60 cm, for proton candidates in sector 1. The blue histogram represents the data, the red curve shows the fit, and the green vertical lines indicate the applied selection cuts. 42

Figure 3.16 Measured DC R1 y versus x coordinates for proton candidates, with fiducial and inner circular cuts. Cuts are shown by red fitted lines and dashed circle. 42

Figure 3.17 Super-Gaussian fit to the DC R1 experimental yield distribution as a function of y, for the x slice from 45 to 50 cm, for π^+ candidates in sector 1. The blue histogram represents the data, the red curve shows the fit, and the green vertical lines indicate the applied selection cuts. 43

Figure 3.18 Measured DC R1 y versus x coordinates for π^+ candidates, with fiducial and inner circular cuts. Cuts are shown by red fitted lines and dashed circle. 44

Figure 3.19 Transverse momentum versus ϕ cuts for CD protons; left plot is for experimental data and right plot is for simulated data. . . . 45

Figure 3.20 Difference in momentum, θ, and ϕ angles for the π^+ detected in both CD and FD tracking, upper three histograms are for experimental data and lower three are for simulation data. 45

Figure 3.21 Typical ΔP distribution for FD protons in $P_{rec}[0.85, 0.95]$ GeV, and $\theta_{rec} < 27^\circ$ bin. 46

Figure 3.22 ΔP versus $P_{\rm rec}$ for FD protons $< 27^\circ$ (left) and FD protons $\geq 27^\circ$ (right). Red dots are the shift values, the red solid curve is the polynomial fit and the red dashed line is the constant extrapolation. 47

Figure 3.23 ΔP versus $P_{\rm rec}$ for CD, FD $\theta_{rec} < 27^\circ$ and FD $\theta_{rec} \geq 27^\circ$ protons using MC data. 48

Figure 3.24 ΔP versus $P_{\rm rec}$ for CD, FD $\theta_{rec} < 27^\circ$ and FD $\theta_{rec} \geq 27^\circ$ $\pi^+ s$ using MC data. 48

Figure 3.25 ΔP versus $P_{\rm rec}$ for CD, FD $\theta_{rec} < 27^\circ$ and FD $\theta_{rec} \geq 27^\circ$ $\pi^- s$ using simulation data. 49

Figure 3.26 Typical ΔP distributions for CD protons with momenta [1.3, 1.5] GeV, ϕ_{rec}[120°, 240°]. The left plot is before corrections, and the right after. 51

Figure 3.27 ΔP versus P_{rec} for CD protons using experimental data. The first row is before correction and the second row is after correction. 52

Figure 3.28 ΔP versus P_{rec} for FD protons before corrections. 52

Figure 3.29 ΔP versus P_{rec} for FD protons after corrections. 53

Figure 3.30 ΔP versus P_{rec} for CD π^+'s. The top row is before correction and the bottom row is after correction. 53

Figure 3.31 ΔP versus P_{rec} for FD π^+'s before corrections. 54

Figure 3.32 ΔP versus P_{rec} for FD π^+'s after corrections. 54

Figure 3.33 ΔP versus P_{rec} for CD $\pi^- s$. The top row is before correction and the bottom row is after correction. 55

Figure 3.34 ΔP versus P_{rec} for FD π^-s, before corrections. 55

Figure 3.35 ΔP versus P_{rec} for FD π^-s, after corrections. 56

Figure 3.36 MMSQ distributions for $\pi^- s$ in FD (left) and CD (right) π^-s. Red histograms (labeled 'bc') are before momentum corrections and blue histograms (labeled 'ac') after. 57

Figure 3.37 MMSQ distributions for $\pi^- s$ in the six FD sectors. Red histograms are before momentum corrections, and blue after. 57

Figure 3.38 MMSQ missing π^- distributions. Blue histograms are for measured data and red histograms are for simulated data, before smearing (left), after smearing (right). 60

Figure 3.39 Typical π^- MMSQ distributions from simulated data, before smearing (top row left) and after smearing (top row right), measured data (bottom row). In all plots, red dots represent the background data, red curves are the background, green the signal, and orange the total fits. The red vertical lines on either side of the peak maxima mark the locations of 1/5th of the peak height. 61

Figure 3.40 Ratio (MC/experimental) of the MMSQ σs distributions for FD protons. Green points represents the ratios for the missing π^+, and blue for the missing π^-, and red points their averages, which are fitted with polynomial function (red line). Before smearing (top row, left), after smearing without including AS (top row, right). The third plot is after the modification including AS (bottom row). 62

Figure 3.41 π^- MMSQ distributions for all FD proton momentum bins. Green histograms based on normalized experimental data and red on smeared MC data. 63

Figure 3.42 MMSQ missing π^- distributions for various CD proton momentum bins. Green histograms are for normalized experimental data and the red histograms are for smeared MC data. 63

Figure 3.43 MMSQ π^- distributions for W[1.70, 1.75] GeV and Q^2[2.4,3.0] GeV^2, measured at left, and simulation at right. 65

Figure 3.44 MMSQ π^- cuts for all Q^2 bins. W bins vary from 1.4 GeV to 2.1 GeV. 66

Figure 3.45 Q^2 versus W distribution using experimental data (left column) and simulation data (right column). Top row is normal scale and bottom row is log z scale. The red box represents the selected region for the analysis, and the grid lines represent the bin edges. 68

Figure 4.1 PCAL y versus x hit positions of electrons to show the inefficient region cuts for PCAL. Red straight lines represent the applied cuts. The left plot is before the application of these cuts and the right plot is after the application of all electron PID and additional fiducial cuts. These plots are based on the experimental data. 69

Figure 4.2 PCAL y vs x hit positions of electrons, the left plot is experimental data, the middle plot is MC data and the right plot is the ratio of an experiment to normalized simulation to show the inefficient regions. Black dashed circles, inner and outer, are applied to cut out the inefficient regions. 70

Figure 4.3 DCR1 (first row), DCR2 (second row), and DCR3 (third row) y versus x hit positions of electrons. In each row, the left plot is experimental, the middle MC, and the right the ratio of measured to normalized simulated data, showing the inefficient regions. Black dashed inner and outer circles are used to cut out inefficient regions. 71

Figure 4.4 DCR3 y versus x hit positions of protons, the left plot is experimental, the middle MC, and the right the ratio of measured to normalized simulated data, showing the inefficient regions. Black dashed inner and outer circles are used to cut out inefficient regions. 72

Figure 4.5 DCR3 y versus x hit positions of π^+, the left plot is experimental, the middle MC, and the right the ratio of measured to normalized simulated data, showing the inefficient regions. Black dashed inner and outer circles are used to cut out inefficient regions. 72

Figure 4.6 DCR3 y versus x hit positions of protons, the left plot is experimental, the middle MC, and the right the ratio of measured to normalized simulated data, after the application of inefficient region cuts. 72

Figure 4.7 DCR3 y versus x hit positions of π^+ the left plot is experimental, the middle MC, and the right the ratio of measured to normalized simulated data after the application of the inefficient region cuts. 73

Figure 5.1 Lab frame (LAB) with incoming electron, scattered electron, and virtual photon γ_v with their polar and azimuthal angles. The Z-axis is in the beam direction. 75

Figure 5.2 Polar (θ_{π^-}) and azimuthal (ϕ_{π^-}) angles of π^- in the center of mass frame of initial proton and virtual photon. Figure adapted from [15]. 77

Figure 5.3 Angle α_{π^-} between two planes: plane A defined by the three-momenta of π^- and initial proton and plane B is defined by the three-momenta of all three final hadrons. The definitions of auxiliary vectors β, γ, and δ are given in the text. Figure is adapted from [15]. 79

Figure 5.4 Nine single-differential experimental yields in a kinematic region, W[1.55, 1.60] GeV, Q^2[3.5, 4.2] GeV^2. First row corresponds to the three invariant masses $M_{\pi^+p'}$ (left), $M_{\pi^-p'}$ (middle), and $M_{\pi^+\pi^-}$ (right). The second row shows to the three Θ angles Θ_{π^-} (left), Θ_{π^+} (middle), $\Theta_{p'}$ (right). The third row shows to the three α angles α_{π^-} (left), α_{π^+} (middle), $\alpha_{p'}$ (right). . 82

Figure 5.5 Comparison of electron reconstruction efficiencies in the FD as a function of the beam current with fits. Used runs: 5418 (5 nA), 5335 (40 nA), 5197 (45 nA), 5342 (50 nA), 5407 (55 nA). Red dots and fit is for artificial intelligence assisted denoised tracking and black are for conventional tracking. Figure is adapted from [16]. 83

Figure 5.6 Normalized yields for all RGA Fall 2018 inbending runs. Different colors represent different sectors of each run. Figure is adapted from [5]. 84

Figure 6.1 Acceptance correction factors for various Q^2 bins in the W[1.4, 2.15] GeV region. 86

Figure 6.2 Acceptance correction factors in Q^2 versus W dependence. 87

Figure 6.3 Experimental (blue squares) and simulated (green triangles) inclusive electron ($ep \rightarrow e'X$) relative yields versus various beam current. Relative yields stands for the ratio of the yields with beam current I nA background to 5 nA background merging condition. 88

Figure 6.4 Ratio CLAS over TWOPEG integrated cross sections for various Q^2 bins. Red points with error bars are the ratio and the red line is the fit function F_{new}. 89

Figure 6.5 CLAS (blue), TWOPEG (red), and TWOPEG adjusted (green), integrated cross sections for various Q^2 bins. 90

Figure 6.6 Radiative correction factors for various Q^2 bins in the W[1.4, 2.1] GeV range. 91

Figure 6.7 Relative acceptance error $\delta A/A$ (left) and relative acceptance error $\delta A/A$ versus acceptance A (right) for W[1.80, 1.85] GeV, Q^2[2.0, 2.4] GeV^2. 94

Figure 6.8 Relative acceptance error $\delta A/A$ (left) and relative acceptance error $\delta A/A$ versus acceptance A (right) for W[1.80, 1.85] GeV, Q^2[6.0, 7.0] GeV^2. 94

Figure 6.9 Fraction of holes (empty 5D bins) to all 5D bins in Q^2 versus W dependence using MC data. 97

Figure 7.1 MMSQ distributions for the exclusive $ep \to e'p'\pi^+\pi^-$ reaction from experimental data. In the first plot, the blue curve represents a fit using a combination of a skewed Gaussian and a third-order polynomial function, while in the remaining three plots, it represents a Gaussian fit. The red vertical lines indicate the applied cuts for each MMSQ distribution. 100

Figure 7.2 Proton MMSQ in the P[1.1, 1.4] GeV, $\theta < 37°$, and $\phi[120°, 180°]$ bin for the proton efficiency factor calculation. The left plot is for measured data and the right plot is for reconstructed MC data. 101

Figure 7.3 Proton efficiency correction factors versus momentum. 102

Figure 7.4 (Left) Proton's missing and measured θ distributions, in the measured $\theta[19°, 22°]$ bin. (Right) Ratio of mid-values of measured and missing proton's θ angles along with a second-order polynomial fit. For $\theta > 42°$, a constant fit function is used. 103

Figure 7.5 For protons in the $\theta < 37°$ bin: (Left) Proton's missing and measured ϕ distributions, in the measured $\phi[90°, 100°]$ bin. (Right) Ratio of mid-values of measured and missing proton's ϕ angles along with a 2nd order polynomial fit. 103

Figure 7.6 For protons in the $\theta < 37^\circ$ bin: (Left) Proton's missing and measured momentum distributions, for measured momentum P[1.1 − 1.4] GeV, $\phi[0^\circ, 60^\circ]$ bin. (Right) Ratio of mid-values of measured and missing proton momenta for six ϕ bins along with 2nd order polynomial fits. 104

Figure 7.7 Missing mass square distributions of missing π^+ in the momentum P[0.75, 0.9] GeV, $\theta < 37^\circ$ and ϕ $[240^\circ, 300^\circ]$ bin that are used for π^+ efficiency factor calculations. Left plot is for measured data and the right plot is for MC data. 105

Figure 7.8 π^+ efficiency correction factors versus momentum. Top panel for FD π^+ and bottom for CD. 106

Figure 7.9 MMSQ distributions for missing π^- topology (blue curve) along with selected background using MMSQ technique (red curve), using experimental data (left), using MC simulation data (right). The pink curve in left plot represents the three-pion distribution. 107

Figure 7.10 Missing mass square distributions used for background selection in MC dataset using exclusive $ep \to e'p'\pi^+\pi^-$ topology. The blue curve represents the Gaussian MMSQ peak fits, and the red lines are the applied cuts for each missing mass topology. . . . 109

Figure 7.11 Background subtraction for experimental data in the W[1.7, 1.75] GeV and Q^2[2.4, 3.0] GeV^2 bin. 110

Figure 7.12 Background subtraction for simulation data for W[1.7, 1.75] GeV and Q^2[2.4, 3.0] GeV^2 bin. 110

Figure 7.13 Effect of bin-centering corrections for nine single-differential cross sections on W[1.80, 1.85] GeV, Q^2[4.2, 5.0] GeV^2. The filled markers represent after bin-centering corrections and empty markers before. Error bars include both statistical and hole filling errors. 113

Figure 7.14 Effect of bin-centering corrections for integrated cross sections in $Q^2[3.5, 4.2]$ GeV^2. The blue points with error bars represent the bin centering corrected cross sections and the red points represent uncorrected. 114

Figure 9.1 Measured integrated cross-section for all W ranges in $Q^2(\mathrm{GeV}^2)$ bins of (a) $[2.0, 2.4]$, (b)$[2.4, 3.0]$, (c)$[3.0, 3.5]$, and (d)$[3.5, 4.2]$. The red dots with error bars are for the hole-filled cross sections, blue after bin centering corrections, cyan before hole filling and green previous CLAS results [3]. The filled gray histograms are for the total systematic error. 119

Figure 9.2 Measured integrated cross-section for all W ranges in $Q^2(\mathrm{GeV}^2)$ of (a) $[4.2, 5.0]$, (b)$[5.0, 6.0]$, (c)$[6.0, 7.0]$, and (d)$[7.0, 8.0]$. The red dots with error bars are for the hole-filled cross sections, blue after bin centering corrections, cyan before hole filling and green (where available) previous CLAS results [3]. The filled gray histograms are for the total systematic error. 120

Figure A.1 Measured nine single-differential cross sections for $W(\mathrm{GeV})-Q^2(\mathrm{GeV}^2)$ bins: (a)$[1.40, 1.45]-[2.0, 2.4]$, (b)$[1.45, 1.50]-[2.0, 2.4]$, (c)$[1.50, 1.55]-[2.0, 2.4]$, and (d)$[1.55, 1.60] - [2.0, 2.4]$. 127

Figure A.2 Measured nine single-differential cross sections for $W(\mathrm{GeV})-Q^2(\mathrm{GeV}^2)$ bins: (a)$[1.60, 1.65]-[2.0, 2.4]$, (b)$[1.65, 1.70]-[2.0, 2.4]$, (c)$[1.70, 1.75]-[2.0, 2.4]$, and (d)$[1.75, 1.80] - [2.0, 2.4]$. 128

Figure A.3 Measured nine single-differential cross sections for $W(\mathrm{GeV})-Q^2(\mathrm{GeV}^2)$ bins: (a)$[1.80, 1.85]-[2.0, 2.4]$, (b)$[1.85, 1.90]-[2.0, 2.4]$, (c)$[1.90, 1.95]-[2.0, 2.4]$, and (d)$[1.95, 2.00] - [2.0, 2.4]$. 129

Figure A.4 Measured nine single-differential cross sections for $W(\mathrm{GeV})-Q^2(\mathrm{GeV}^2)$ bins: (a)$[2.00, 2.05] - [2.0, 2.4]$, and (b)$[2.05, 2.10] - [2.0, 2.4]$. . . 130

Figure A.5 Measured nine single-differential cross sections for $W(\mathrm{GeV})-Q^2(\mathrm{GeV}^2)$ bins: (a)$[1.40, 1.45]-[2.0, 2.4]$, (b)$[1.45, 1.50]-[2.0, 2.4]$, (c)$[1.50, 1.55]-[2.4, 3.0]$, and (d)$[1.55, 1.60] - [2.4, 3.0]$. 131

Figure A.6 Measured nine single-differential cross sections for $W(\mathrm{GeV})-Q^2(\mathrm{GeV}^2)$ bins: (a)$[1.60, 1.65]-[2.0, 2.4]$, (b)$[1.65, 1.70]-[2.0, 2.4]$, (c)$[1.70, 1.75]-[2.4, 3.0]$, and (d)$[1.75, 1.80] - [2.4, 3.0]$. 132

Figure A.7 Measured nine single-differential cross sections for $W(\mathrm{GeV})-Q^2(\mathrm{GeV}^2)$ bins: (a)$[1.80, 1.85]-[2.0, 2.4]$, (b)$[1.85, 1.90]-[2.0, 2.4]$, (c)$[1.90, 1.95]-[2.4, 3.0]$, and (d)$[1.95, 2.00] - [2.4, 3.0]$. 133

Figure A.8 Measured nine single-differential cross sections for $W(\mathrm{GeV})-Q^2(\mathrm{GeV}^2)$ bins: (a)$[2.00, 2.05] - [2.4, 3.0]$, and (b)$[2.05, 2.10] - [2.4, 3.0]$. . . 134

Figure A.9 Measured nine single-differential cross sections for $W(\mathrm{GeV})-Q^2(\mathrm{GeV}^2)$ bins: (a)$[1.40, 1.45]-[3.0, 3.5]$, (b)$[1.45, 1.50]-[3.0, 3.5]$, (c)$[1.50, 1.55]-[3.0, 3.5]$, and (d)$[1.55, 1.60] - [3.0, 3.5]$. 135

Figure A.10 Measured nine single-differential cross sections for $W(\mathrm{GeV})-Q^2(\mathrm{GeV}^2)$ bins: (a)$[1.60, 1.65]-[3.0, 3.5]$, (b)$[1.65, 1.70]-[3.0, 3.5]$, (c)$[1.70, 1.75]-[3.0, 3.5]$, and (d)$[1.75, 1.80] - [3.0, 3.5]$. 136

Figure A.11 Measured nine single-differential cross sections for $W(\mathrm{GeV})-Q^2(\mathrm{GeV}^2)$ bins: (a)$[1.80, 1.85]-[3.0, 3.5]$, (b)$[1.85, 1.90]-[3.0, 3.5]$, (c)$[1.90, 1.95]-[3.0, 3.5]$, and (d)$[1.95, 2.00] - [3.0, 3.5]$. 137

Figure A.12 Measured nine single-differential cross sections for $W(\mathrm{GeV})-Q^2(\mathrm{GeV}^2)$ bins: (a)$[2.00, 2.05] - [3.0, 3.5]$, and (b)$[2.05, 2.10] - [3.0, 3.5]$. . . 138

Figure A.13 Measured nine single-differential cross sections for $W(\mathrm{GeV})-Q^2(\mathrm{GeV}^2)$ bins: (a)$[1.40, 1.45]-[3.5, 4.2]$, (b)$[1.45, 1.50]-[3.5, 4.2]$, (c)$[1.50, 1.55]-[3.5, 4.2]$, and (d)$[1.55, 1.60] - [3.5, 4.2]$. 139

Figure A.14 Measured nine single-differential cross sections for $W(\mathrm{GeV})-Q^2(\mathrm{GeV}^2)$ bins: (a)$[1.60, 1.65]-[3.5, 4.2]$, (b)$[1.65, 1.70]-[3.5, 4.2]$, (c)$[1.70, 1.75]-[3.5, 4.2]$, and (d)$[1.75, 1.80] - [3.5, 4.2]$. 140

Figure A.15 Measured nine single-differential cross sections for $W(\mathrm{GeV})-Q^2(\mathrm{GeV}^2)$ bins: (a)$[1.80, 1.85]-[3.5, 4.2]$, (b)$[1.85, 1.90]-[3.5, 4.2]$, (c)$[1.90, 1.95]-[3.5, 4.2]$, and (d)$[1.95, 2.00] - [3.5, 4.2]$. 141

Figure A.16 Measured nine single-differential cross sections for $W(\mathrm{GeV})-Q^2(\mathrm{GeV}^2)$ bins: (a)$[2.00, 2.05] - [3.5, 4.2]$, and (b)$[2.05, 2.10] - [3.5, 4.2]$. . . 142

Figure A.17 Measured nine single-differential cross sections for $W(\mathrm{GeV})-Q^2(\mathrm{GeV}^2)$ bins: (a)$[1.40, 1.45]-[4.2, 5.0]$, (b)$[1.45, 1.50]-[4.2, 5.0]$, (c)$[1.50, 1.55]-[4.2, 5.0]$, and (d)$[1.55, 1.60] - [4.2, 5.0]$. 143

Figure A.18 Measured nine single-differential cross sections for $W(\mathrm{GeV})-Q^2(\mathrm{GeV}^2)$ bins: (a)$[1.60, 1.65]-[4.2, 5.0]$, (b)$[1.65, 1.70]-[4.2, 5.0]$, (c)$[1.70, 1.75]-[4.2, 5.0]$, and (d)$[1.75, 1.80] - [4.2, 5.0]$. 144

Figure A.19 Measured nine single-differential cross sections for $W(\mathrm{GeV})-Q^2(\mathrm{GeV}^2)$ bins: (a)$[1.80, 1.85]-[4.2, 5.0]$, (b)$[1.85, 1.90]-[4.2, 5.0]$, (c)$[1.90, 1.95]-[4.2, 5.0]$, and (d)$[1.95, 2.00] - [4.2, 5.0]$. 145

Figure A.20 Measured nine single-differential cross sections for $W(\mathrm{GeV})-Q^2(\mathrm{GeV}^2)$ bins: (a)$[2.00, 2.05] - [4.2, 5.0]$, and (b)$[2.05, 2.10] - [4.2, 5.0]$. . . 146

Figure A.21 Measured nine single-differential cross sections for $W(\mathrm{GeV})-Q^2(\mathrm{GeV}^2)$ bins: (a)$[1.40, 1.45]-[5.0, 6.0]$, (b)$[1.45, 1.50]-[5.0, 6.0]$, (c)$[1.50, 1.55]-[5.0, 6.0]$, and (d)$[1.55, 1.60]-[5.0, 6.0]$. 147

Figure A.22 Measured nine single-differential cross sections for $W(\mathrm{GeV})-Q^2(\mathrm{GeV}^2)$ bins: (a)$[1.60, 1.65]-[5.0, 6.0]$, (b)$[1.65, 1.70]-[5.0, 6.0]$, (c)$[1.70, 1.75]-[5.0, 6.0]$, and (d)$[1.75, 1.80]-[5.0, 6.0]$. 148

Figure A.23 Measured nine single-differential cross sections for $W(\mathrm{GeV})-Q^2(\mathrm{GeV}^2)$ bins: (a)$[1.80, 1.85]-[5.0, 6.0]$, (b)$[1.85, 1.90]-[5.0, 6.0]$, (c)$[1.90, 1.95]-[5.0, 6.0]$, and (d)$[1.95, 2.00]-[5.0, 6.0]$. 149

Figure A.24 Measured nine single-differential cross sections for $W(\mathrm{GeV})-Q^2(\mathrm{GeV}^2)$ bins: (a)$[2.00, 2.05]-[5.0, 6.0]$, and (b)$[2.05, 2.10]-[5.0, 6.0]$. . . 150

Figure A.25 Measured nine single-differential cross sections for $W(\mathrm{GeV})-Q^2(\mathrm{GeV}^2)$ bins: (a)$[1.40, 1.45]-[6.0, 7.0]$, (b)$[1.45, 1.50]-[6.0, 7.0]$, (c)$[1.50, 1.55]-[6.0, 7.0]$, and (d)$[1.55, 1.60]-[6.0, 7.0]$. 151

Figure A.26 Measured nine single-differential cross sections for $W(\mathrm{GeV})-Q^2(\mathrm{GeV}^2)$ bins: (a)$[1.60, 1.65]-[6.0, 7.0]$, (b)$[1.65, 1.70]-[6.0, 7.0]$, (c)$[1.70, 1.75]-[6.0, 7.0]$, and (d)$[1.75, 1.80]-[6.0, 7.0]$. 152

Figure A.27 Measured nine single-differential cross sections for $W(\mathrm{GeV})-Q^2(\mathrm{GeV}^2)$ bins: (a)$[1.80, 1.85]-[6.0, 7.0]$, (b)$[1.85, 1.90]-[6.0, 7.0]$, (c)$[1.90, 1.95]-[6.0, 7.0]$, and (d)$[1.95, 2.00]-[6.0, 7.0]$. 153

Figure A.28 Measured nine single-differential cross sections for $W(\mathrm{GeV})-Q^2(\mathrm{GeV}^2)$ bins: (a)$[2.00, 2.05]-[6.0, 7.0]$, and (b)$[2.05, 2.10]-[6.0, 7.0]$. . . 154

Figure A.29 Measured nine single-differential cross sections for $W(\mathrm{GeV})-Q^2(\mathrm{GeV}^2)$ bins: (a)$[1.40, 1.45]-[7.0, 8.0]$, (b)$[1.45, 1.50]-[7.0, 8.0]$, (c)$[1.50, 1.55]-[7.0, 8.0]$, and (d)$[1.55, 1.60]-[7.0, 8.0]$. 155

Figure A.30 Measured nine single-differential cross sections for $W(\mathrm{GeV})-Q^2(\mathrm{GeV}^2)$ bins: (a)$[1.60, 1.65]-[7.0, 8.0]$, (b)$[1.65, 1.70]-[7.0, 8.0]$, (c)$[1.70, 1.75]-[7.0, 8.0]$, and (d)$[1.75, 1.80]-[7.0, 8.0]$. 156

Figure A.31 Measured nine single-differential cross sections for $W(\mathrm{GeV})-Q^2(\mathrm{GeV}^2)$ bins: (a)$[1.80, 1.85]-[7.0, 8.0]$, (b)$[1.85, 1.90]-[7.0, 8.0]$, (c)$[1.90, 1.95]-[7.0, 8.0]$, and (d)$[1.95, 2.00]-[7.0, 8.0]$. 157

Figure A.32 Measured nine single-differential cross sections for $W(\mathrm{GeV})-Q^2(\mathrm{GeV}^2)$ bins: (a)$[2.00, 2.05]-[7.0, 8.0]$, and (b)$[2.05, 2.10]-[7.0, 8.0]$. . . 158

Chapter 1

Introduction

Physics explores the fundamental principles of the universe, from tiny elementary particles that form matter to the largest cosmic structures, such as galaxies. These principles are explored through various experiments that test, refine, and prove their validity. Experimental exploration helps to confirm well-established laws, identify their boundaries, and sometimes reveal deeper insights and discover new laws. To understand the laws governing the nature of matter at the fundamental level, physicists have studied the fundamental forces responsible for the interactions of all existing matter in nature. There are four fundamental forces: gravitational, electromagnetic, strong, and weak. The gravitational interaction is responsible for the attraction between masses. It plays a key role on cosmic scales, from planets to galaxies. This force has a negligible contribution to the short-range scale at which strong and weak forces typically operate. The electromagnetic interaction acts on particles with net electric charge, such as electrons, protons, and ions, and also on neutral particles with a magnetic moment, such as neutrons. This force covers electric and magnetic phenomena and is well explained and understood by the theory of Quantum Electrodynamics (QED). The weak interaction is responsible for processes such as radioactive decay or quark-flavor change and operates on a short-range scale because of the large mass of the exchanged boson. The electroweak theory unifies the electromagnetic and weak forces, unification occurs at high energy scales, on the order of hundreds of GeV, revealing them as manifestations of a single fundamental interaction. The strong interaction is the strongest of the four forces in the fempto-meter range. Several the-

oretical models, known as Grand Unified Theories (GUTs), predict that at extremely high energy scales, on the order of 10^{15} to 10^{16} GeV, strong, weak and electromagnetic interactions merge into a single fundamental force. However, this unification has not been tested or proven to be true, as such energy scales are far beyond the reach of current experimental capabilities.

The purpose of this analysis is related to understanding the strong interaction. This interaction acts between quarks and gluons by coupling to the strong charge (color), protons, neutrons, pions, kaons, and other hadrons emerge. A strong nuclear force also holds the protons and neutrons within the atomic nucleus together and cancels out the electromagnetic repulsive force between positively charged protons, allowing for stable nuclei to form. Quantum Chromodynamics (QCD) has been developed to explain a theory of strong interaction, but it explains strong interactions only at very small length scales or high energies, where current quarks and gluons become asymptotically free. However, it cannot explain the strong interaction at larger length scales (≈ 1 fm). At this scale, the degrees of freedom shift from asymptotically free valence quarks to more and more dressed valence quarks, and even strong meson baryon contributions [17][18]. Also, the strong interaction's coupling constant (α_s) becomes large, and the perturbative approach of QCD (pQCD) is no longer applicable. This regime, typically at scales $\approx 10^{-15}$ m, is known as the non-perturbative or strong QCD (sQCD) regime. To understand the nature of strong interactions in this non-perturbative domain, new theories and principles, which emerge from the fundamental framework of QCD, are needed. In the sQCD regime current quarks become dressed by gluons and sea quarks, and confined colorless bound systems, called hadrons, emerge [17]. The mass of the constituent quarks undergoes a significant increase during this dressing process, driven by the Dynamical Chiral Symmetry Breaking (DCSB) process [18][19].

In the electroproduction scattering experiments, the probing electron exchanges

a virtual photon with the target. The four-momentum transfer squared (Q^2) known as photon virtuality represents the four-momentum carried by the virtual photon γ_v during this exchange. This momentum transfer can be calculated using the four-momenta of the initial electron and final scattered electrons,

$$Q^2 = -q_\mu q^\mu, \tag{1.1}$$

with

$$q^\mu = e^\mu - e'^\mu, \tag{1.2}$$

where e^μ and e'^μ are the four-momenta of the initial and scattered electron, respectively. The negative sign in (1.1) arises because the virtual photon exchanged in electron scattering is not massless and always space-like, i.e. the virtual photon carries more spatial momentum than energy. This leads to a negative value for the four-vector product $q_\mu q^\mu$ as the space-time interval in the Minkowski metric given by, $ds^2 = dt^2 - (dx^2 + dy^2 + dz^2)$ results in a negative value.

The distinction between the perturbative and non-perturbative regimes of strong interaction can be exposed by experimentally choosing appropriate values for these photon virtualities Q^2. Probing the perturbative region requires a high $Q^2 \to \infty$, while the non-perturbative region, where the strong coupling constant α_s approaches one, requires a low $Q^2 \to 0$. The variation of Q^2 from low to high provides a unique opportunity to probe QCD and the different parts of the hadronic structure by mapping out the behavior of the strong interaction across different length scales. At higher Q^2, it allows the investigation of fundamental asymptotically free current quarks and gluons, while at lower Q^2, it offers insight into the structure and properties of composite particles such as mesons and baryons or the hadronic bound system in general.

The excited nucleons (N*s) play an important role in defining the transition from the strong to the pQCD. Nucleon excitations are complex many-body systems composed of three valence quarks exhibiting a wide variety of quantum number-dependent

structures, which provide a platform to comprehensively study the scale-dependent properties of the strong interaction. The study of N* states and their decay products has been ongoing for a while now. This program brings theorists and experimentalists from around the world together to extract various observables using experimental data and to develop models and theories to explain the hadron structure using those extracted observables. The combined goal is to understand the structure and properties of hadrons from the high Q^2 to the low Q^2 regions, and particularly the transition region between them [18]. Various analyses of inclusive and exclusive photoproduction and electroproduction cross sections based on the data produced by the experiment performed in Hall B at Jefferson Lab using a CLAS have been carried out [3][2][20][15][21]. During CLAS experiments with up to 5.75 GeV electron beam energy the typical maximum Q^2 was about 5 GeV^2. After the upgrade to CLAS12 in 2017/2018, with the use of a 10.6 GeV polarized electron beam, the achievable Q^2 limit increased up to about 10 GeV^2. This dissertation contributes to the experimental aspect of the N* program, focusing on intermediate Q^2 values ranging from 2.0 GeV^2 to 8 GeV^2, including the less explored range of Q^2 greater than 5.0 GeV^2 which was not achievable using the CLAS data.

The experiment was carried out in Hall B of the Jefferson Laboratory, where a 10.6 GeV polarized electron beam was directed to a liquid hydrogen (LH_2) target. The electron-proton interactions include various processes such as elastic scattering, resonance excitation (producing N* states), and meson production. The N* state produced then decays to various final states. Those final states are then analyzed to understand the nature of the interaction and structure of the nucleon, which provides insights into the underlying strong interaction. The invariant mass distribution of the reaction represented by W and given by (1.3), shows a series of resonance peak regions, representing one or more of those excited nucleon states. W is the $\sqrt{s}$,

$$W = \sqrt{(p_\mu + q_\mu)\,(p^\mu + q^\mu)} = \sqrt{(p'_\mu + \pi^+_\mu + \pi^-_\mu)\,(p'^\mu + \pi^{+\mu} + \pi^{-\mu})}, \qquad (1.3)$$

and s is the Mandelstam variable that represents the total energy in the center of mass system (CMS) squared.

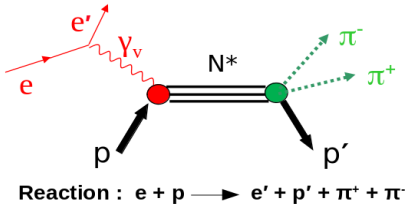

Figure 1.1 Schematic drawing of charged double-pion electroproduction off the proton.

Experimentally, many final states like πN, $\pi^-\pi^+p'$, and KY can be observed simultaneously. Different N* states have different branching fractions than those of the final states. This analysis focuses on the final state $\pi^-\pi^+p'$, which is called the charged double-pion electroproduction channel (see Figure 1.1): $ep \rightarrow$N*$\rightarrow e'\pi^-\pi^+p'$. The virtual photon($\gamma_v$) is exchanged between the incoming electron and the target proton, which then may form the excited nucleon state (N*). The kinematic variable W, which is the invariant mass of the virtual photon and the initial nucleon system, plays a crucial role in characterizing their interaction. The cross section of the reaction, which is the primary objective of this analysis, depends on the W. The existing results show that the πN final state is more prominent in the low W region and the $\pi^-\pi^+p'$ final state is more significant in the high $W > 1.6$ GeV region. Consistent results from the different decay channels are very important to verify the correct extraction of the resonance amplitudes. The goal of this dissertation is to extract the differential cross section of $\pi^-\pi^+p'$ final state. The cross section extracted in this reaction channel will serve as an input to reaction models (such as the JM Model) [22][23] [24], which will extract transition helicity amplitudes.

1.1 JM Model

The JM model analyzes nine experimentally measured single-differential cross sections from charged double-pion electroproduction to extract transition helicity amplitudes, also called resonance electrocouplings (γ_vNN*) or transition form factors, between the ground and excited state nucleon in various Q^2 ranges in the resonance region. Additionally, the model calculates the hadronic decay widths of various resonant states [23]. It accounts for all essential reaction mechanisms contributing to the measured $\pi^+\pi^- p'$ cross sections and distinguishes the resonant and nonresonant contributions to extract the γNN* electrocouplings. Figure 1.2 sketches the mechanisms included in the recent JM model, where double-pion reaction amplitudes are constructed as a sum of several intermediate-state contributions, including $\pi^-\Delta^{++}$, $\pi^-\Delta^{++}(1600)$, $\pi^+\Delta^0$, $\pi^+N^0(1520)$, $\pi^+N^0(1680)$, and ρp channels. These involve the production of unstable hadronic states that subsequently decay in to the final double-pion production particles $\pi^+\pi^- p'$. The model also accounts for direct double-pion production processes, in which the $\pi^+\pi^- p'$ final state is generated without the formation of intermediate resonances. Resonant amplitudes in the model are described using a unitarized Breit-Wigner approach and non-resonant contributions are modeled through current-conserving Reggeized Born terms [1] [22][23]. The recent JM23 reaction model [1] has been used to extract the electrocouplings of nucleon resonances such as $N(1440)\,1/2^+$, $N(1520)\,3/2^-$, and $\Delta(1600)\,3/2^+$ within a photon virtuality range of Q^2 from 2.0 to 5.0 GeV^2. This extraction is achieved by fitting the data of the $\pi^+\pi^- p$ electroproduction differential cross sections from CLAS experiments [2][3]. The model fits various meson-baryon channels, such as $\pi^-\Delta^{++}$, $\pi^+\Delta^0$, ρp, $\pi^+N^0(1520)$, and $\pi^+N^0(1680)$, along with direct double-pion production mechanisms to the measured data, see Fig. 1.3. The figure gives an example of the nine single-differential cross sections, both measured and modeled, along with contributions from various reaction sub-channels at W bin [1.55, 1.58] GeV and Q^2 bin [3.50, 4.20] GeV^2. In this kinematic range, the

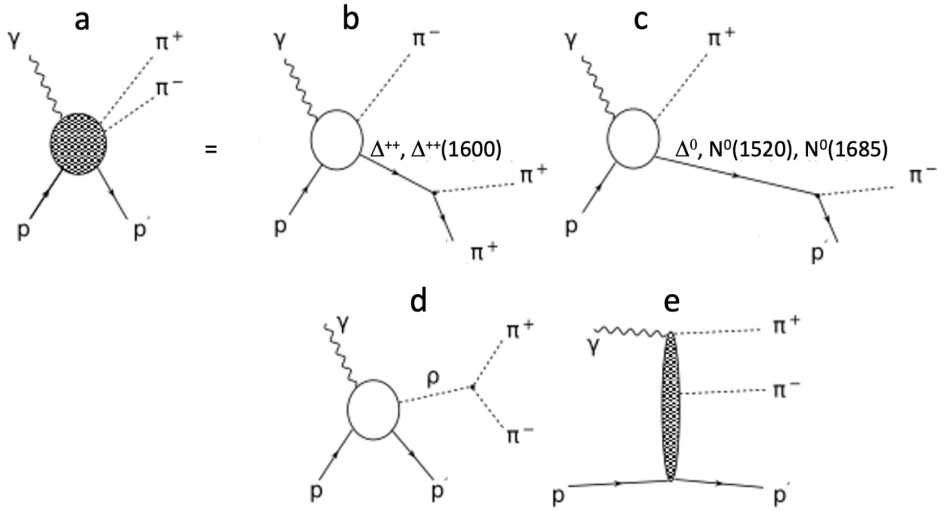

Figure 1.2 The key mechanisms of the JM model for double-pion electroproduction: plot (a) is for full amplitude, (b) for $\pi^-\Delta^{++}$ and $\pi^-\Delta^{++}(1600)\,3/2^+$ sub-channels, (c) for $\pi^+\Delta^0$, $\pi^+N^0(1520)\,3/2^-$, and $\pi^+N^0(1680)\,5/2^+$ sub-channels, (d) for ρp sub-channel, and (e) direct double-pion production mechanisms. Figure is adapted from [1].

sub-channels $\pi^-\Delta^{++}$ and $\pi^+\Delta^0$ are the dominant contributors to the overall cross section.

The extracted electrocouplings serve as valuable information for understanding the N* resonances. It enables the exploration of the non-perturbative strong interaction mechanisms responsible for the emergence of the N* structure and mass in dependence on their quantum numbers [24]. The resonant and non-resonant parts of the electroproduction amplitudes are extracted by minimizing the model dependence during the fit procedure and the extracted resonance parameters are cross-checked with independent analyses from various single-meson electroproduction channels [25]. The electrocouplings obtained from this model align well with the results of those analyses, despite their different non-resonant background components. This consistency confirms the reliability of the electrocoupling γ_vNN* extraction and also opens the opportunity to perform combined analyzes to map out the evolution of resonance electrocouplings in various Q^2 ranges.

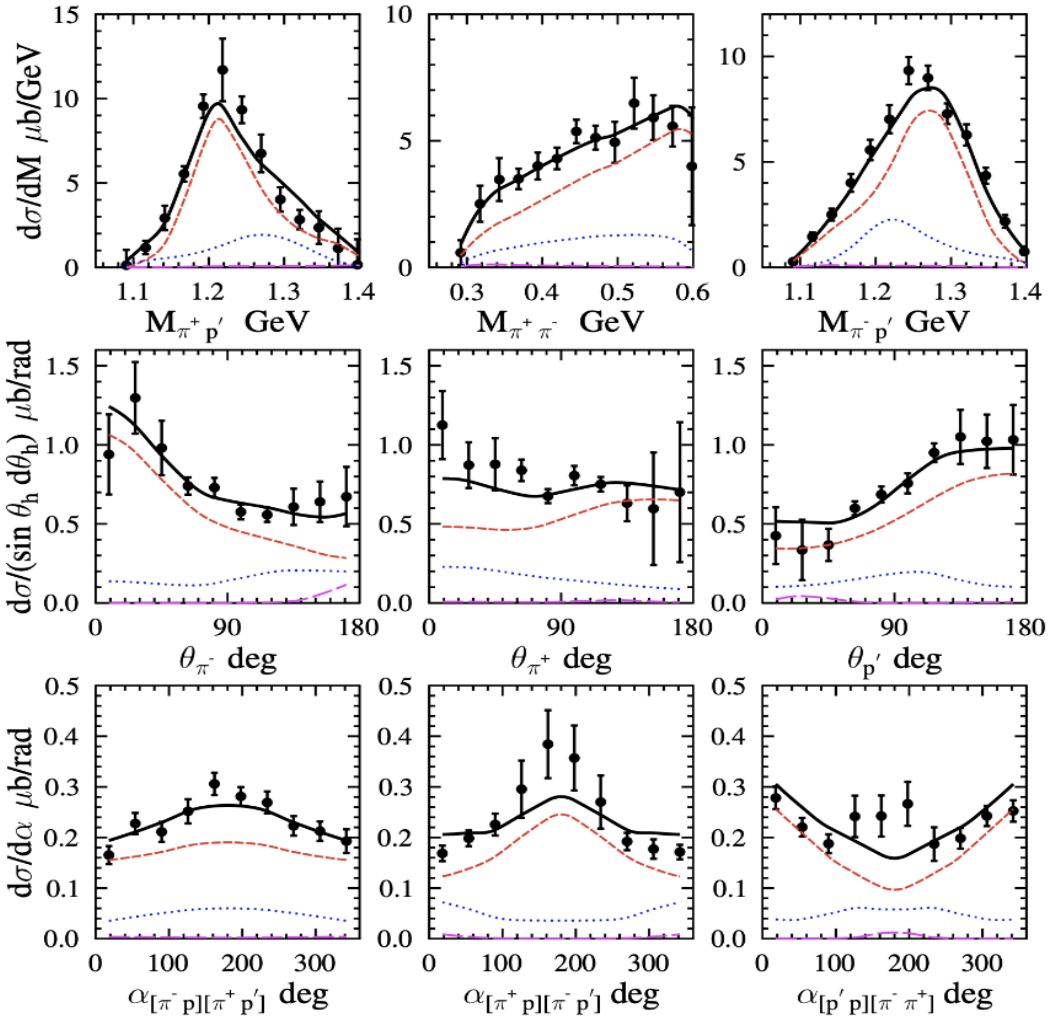

Figure 1.3 Description of the nine single-differential $\pi^+\pi^- p$ electroproduction cross sections measured with CLAS [2][3] (black points) achieved within the JM23 model, at W[1.55, 1.58] GeV and Q^2[3.50, 4.20] GeV^2. First row corresponds to the three invariant masses: $M_{\pi^+ p'}$ (left), $M_{\pi^+\pi^-}$ (middle), and $M_{\pi^- p'}$ (right). The second row corresponds to the three θ angles: θ_{π^-} (left), θ_{π^+} (middle), $\theta_{p'}$ (right). The third row corresponds to the three α angles: α_{π^-} (left), α_{π^+} (middle), $\alpha_{p'}$ (right). All the variables are in center of mass frame, more details on variables are at Sec. 5.1. The computed differential cross sections are shown by the black solid lines, while the contributions from the $\pi^-\Delta^{++}$ and $\pi^+\Delta^0$ channels are shown by the red dashed and blue dotted lines, respectively. The contributions from direct double-pion production are shown by the magenta long-dashed lines. Figure is adapted from [1].

Chapter 2

Experiment

This chapter will provide a detailed description of the experimental setup for the data used in this analysis. Data were obtained from an experiment conducted during the Run Group A (RGA) period in Fall 2018 in JLab's Hall B. The experiment utilized a continuous wave of a longitudinally polarized electron beam of energy 10.6 GeV delivered from the Continuous Electron Beam Accelerator Facility (CEBAF). CEBAF consists of two anti-parallel linear accelerators (linacs) designed to accelerate the electron beam bunches produced by the injector. Five passes are connected by beam transport arcs at both ends.

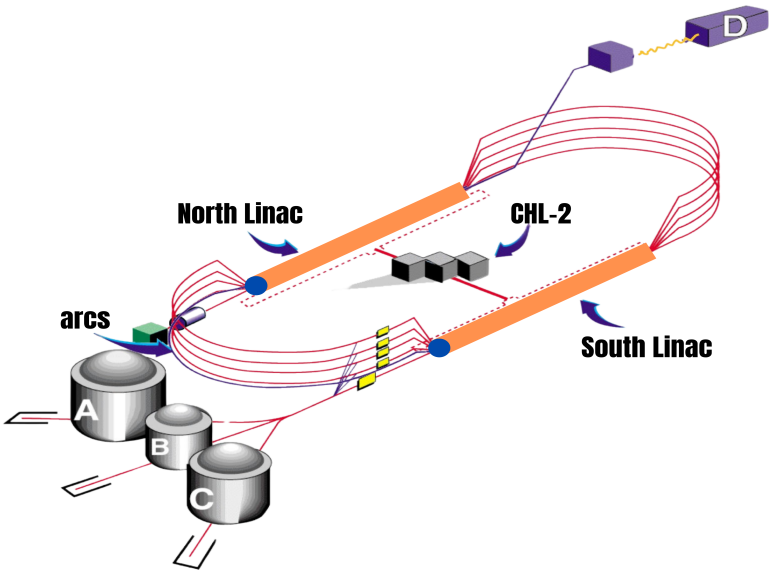

Figure 2.1 Schematic illustration of the CEBAF accelerator, which delivered electron beams with energies up to 10.6 GeV. Figure is adapted from [4].

The CEBAF Large Acceptance Spectrometer for 12 GeV (CLAS12) is housed in Hall B to detect different particles in the final states that originate from the inter-

action of the continuous electron beam with the unpolarized liquid hydrogen (LH_2) target. The LH_2 is kept inside the target cell, which is a 50 mm long Kapton cone with a diameter of 23.66 mm upstream and 15.08 mm downstream [26]. Before completion of the upgrade to CLAS12 in 2017/2018, the CEBAF Large Angle Spectrometer (CLAS) detector had collected data using an electron beam with energies up to 6 GeV. Hall B now receives an electron beam from the accelerator with energies up to 10.6 GeV, allowing the coverage of Q^2 to be extended to 10 GeV^2 [4].

The RGA Fall 2018 data set consists of two detector configurations: inbending and outbending. This analysis focuses only on the inbending dataset, collected under an inbending torus field configuration, where negatively charged particles bend toward the beamline and positively charged particles bend away from the beamline. Among the available data, 126 golden runs and 3 empty target runs are chosen for this analysis, based on the quality assurance of the runs. Table 2.1 shows the list of the runs utilized.

Table 2.1 All data runs used in this analysis.

Runs Used
5032 5036 5038 5039 5040 5041 5043 5045 5052 5053 5116 5117 5119 5120 5124
5125 5126 5127 5139 5153 5158 5162 5163 5164 5181 5191 5193 5195 5196 5197
5198 5199 5200 5201 5202 5203 5204 5205 5206 5208 5211 5212 5215 5216 5219
5220 5221 5222 5223 5230 5231 5232 5233 5234 5235 5237 5238 5248 5249 5252
5253 5257 5258 5259 5261 5262 5300 5301 5302 5303 5304 5305 5306 5307 5310
5311 5315 5317 5318 5319 5320 5323 5324 5335 5339 5340 5342 5343 5344 5345
5346 5347 5349 5351 5354 5355 5356 5357 5358 5359 5360 5361 5362 5366 5367
5368 5369 5372 5373 5374 5375 5376 5377 5378 5379 5380 5381 5383 5386 5390
5391 5392 5393 5398 5401 5403 5404 5406 5407

Data used in this analysis were collected mainly (about 80%) with a beam current of 45 nA. The remaining data were taken at currents between 50 nA and 55 nA. The quality check of the data used in this analysis was performed using the CLAS12 Quality Assurance Database (QADB) [5] for all full target runs. QADB evaluates the quality of each Data Summary Tape (DST) file in a given run and determines whether

it contains defects characterized by individual bits. For this study, the Golden criteria from QADB were chosen. Defect bits indicate different data quality issues. There are various defect bits such as 'TotalOutlier', 'MarginalOutlier', 'SectorLoss', 'LowLivetime', 'Misc' and so on. The 'TotalOutlier' bit is based on the electron yield normalized to the accumulated Faraday cup charge (N/F). Ideally, this ratio remains constant, but various experimental conditions can cause deviations. Files with abnormal N/F values are flagged by the 'TotalOutlier' bit and rejected by the 'Golden' criteria defined for this analysis. Figure 2.2 illustrates the N/F ratio for electrons in run number 5038. The plot shows that file 190 has an N/F ratio outside the cut lines defined by the interquartile range, indicating that it should be excluded. More details on this procedure can be found in Chapter 6 of the common RGA analysis note [26]. The QADB software is also used to calculate the total accumulated Faraday cup charge for each run.

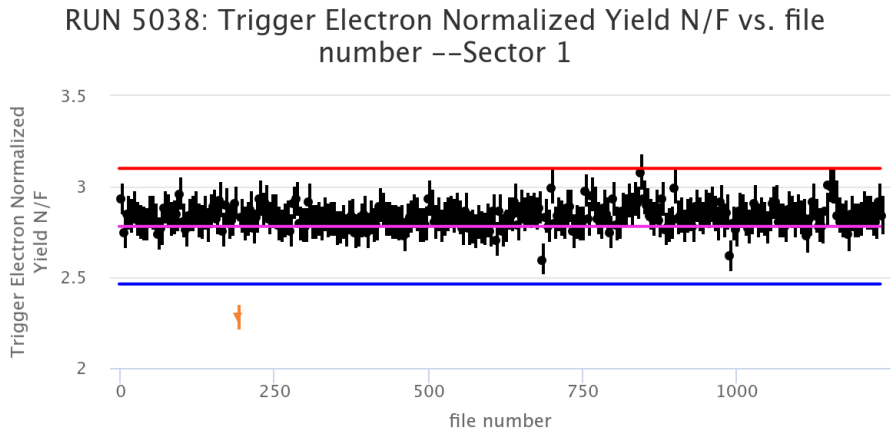

Figure 2.2 Electron yields normalized to the Faraday cup charge in sector 1 of Forward Detector system Figure is adapted from [5].

2.1 CEBAF Large Acceptance Spectrometer

CLAS12 receives the continuous wave electron beam that is bundled by the 499 MHz cavity frequency of the CEBAF linear accelerator. To enable effective detection of

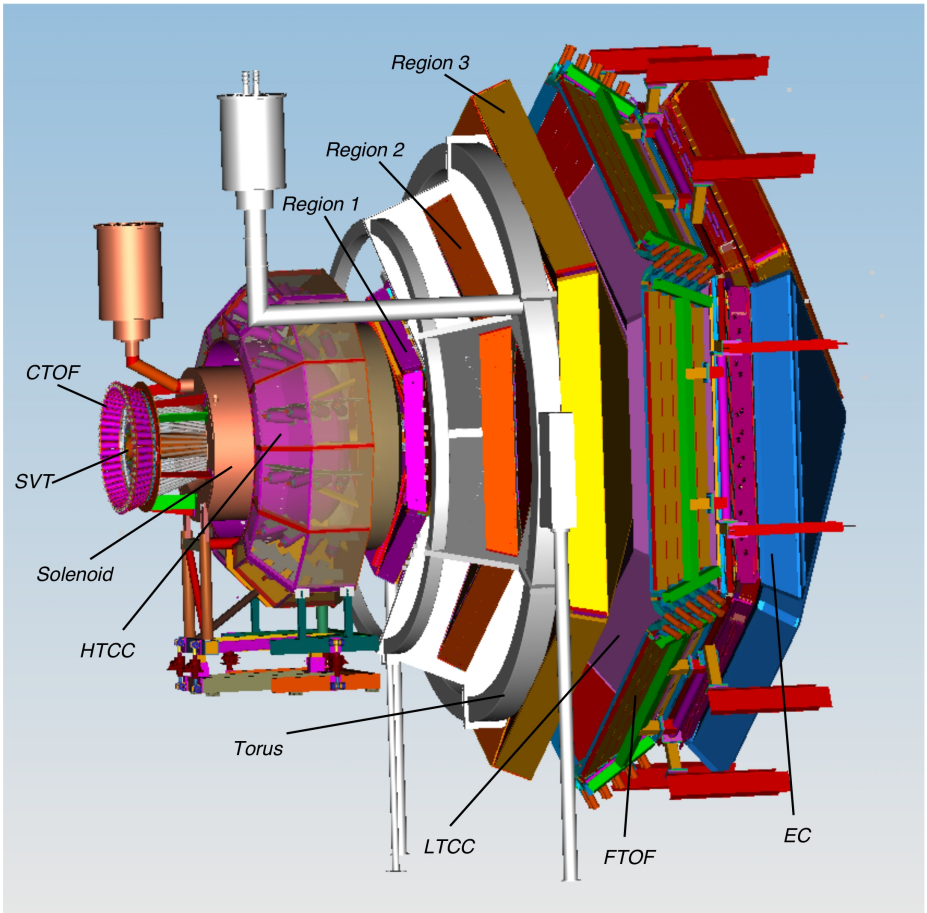

Figure 2.3 CLAS12 detector system. Figure is adapted from [6].

neutral and particularly charged particles with large solid angle acceptance, CLAS12 was designed (Fig. 2.3) [6]. Given the extremely low cross sections for exclusive final states in this kinematic region, the luminosity has been increased to 10^{35} cm^{-2}s^{-1} [4], representing a ten-fold increase over that of the CLAS. To accommodate more forward-boosted particles after the 12 GeV upgrade of CEBAF, the CLAS12 detector has been partitioned into various subsystems. The forward detector system located downstream of the target, which covers a polar angle range (θ) from 5° to 35° and nearly all azimuthal angles (ϕ), and the central detector system located around the target, which covers θ angles from 35° to 125° and also nearly all ϕ angles. Furthermore, the forward tracker detector system, located downstream of the target, covers θ angles from 2° to 5° and again nearly all ϕ angles.

2.1.1 Torus and Solenoid Fields

As the charged particle passes through the toroidal magnetic field of CLAS12 [7], its path bends, and the charge and momentum of the particle can be determined using the curvature of its trajectory. CLAS12 is designed to measure reactions resulting from electron-proton or electron-nucleus scattering in a large kinematic phase space.

The solenoid magnet is positioned around the target and generates a magnetic field of up to 5.0 T. It consists of five NbTi coils connected in series and a current of up to 2416 A is used to operate [7]. Four of the five coils are the inner main coils located inside the fifth shielding coil. The fifth coil provides an effective shielding of the solenoid magnetic field to minimize the impact on the photomultiplier tubes, which are located just outside the solenoid. The CLAS12 solenoid serves as the main component of the central tracking system, which is partially embedded within its magnetic field. In the central region, most of the particles have lower momenta. The solenoidal magnetic field bends these low-momenta particles within the central detector system that tracks them. It also shields the forward detector from Moller electrons, enabling CLAS12 to operate at high data rates. Moller electrons are generated when beam electrons interact with target LH_2 target electrons. Most of these electrons follow spiral trajectories along the magnetic field of the solenoid. They are subsequently captured by a passive Moller cone shield located downstream of the target.

The CLAS12 torus magnet features six superconducting NbTi coils connected in series. It encircles the beamline located downstream of the solenoid magnet and operates at a current up to 3770 A [7]. This magnet produces a magnetic field of up to 3.6 T in the azimuthal direction (i.e. perpendicular to the beam direction). The forward detector system is segmented into six identical sectors to accommodate the six toroid coils. As the coils are connected in series, the magnetic field is the same in all six sectors. The toroid frame also provides mechanical support for three regions of drift chambers within the forward detector system. The charged particles passing

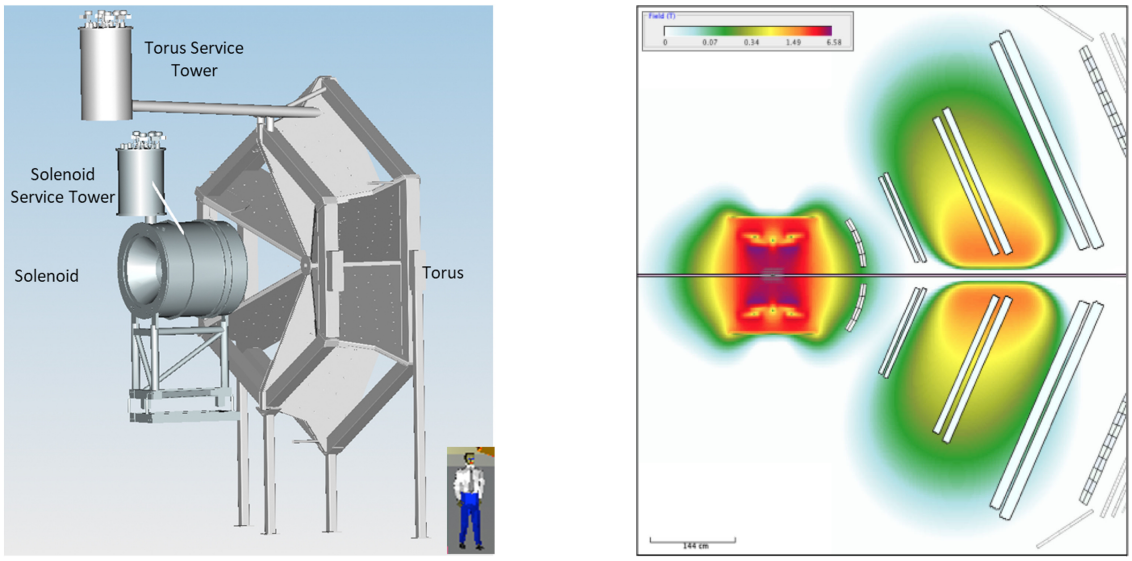

Figure 2.4 Simplified model illustration of CLAS12 solenoid and torus magnets (left), solenoid and torus magnetic fields are shown at full current (right), open boxes represent various CLAS12 detector elements. Figures are adapted from [7].

through this toroidal magnetic field bend toward or away from the beamline. In the inbending configuration, the negative charge particle bends toward the beamline and the positive charge particle bends away from the beamline. The curvature of the trajectory of the particle is used to determine the charge and momentum of the particle in the forward region.

2.1.2 Forward Detector (FD) System

As the energy of the incoming beam increases to 10.6 GeV, more particles are boosted into the forward angle region, and they tend to have higher momentum compared to those moving sideways or backwards.

The FD system is specifically designed to detect charged particles in the polar angle range from 5° to 35°, but can also detect neutral particles. It comprises several detectors located downstream of the target cell, including the Forward Micromegas Tracker (FMT), High Threshold Cherenkov Counters (HTCC), Drift Chambers (DC), Low Threshold Cherenkov Counters (LTCC), the Ring Imaging Cherenkov detector (RICH), Forward Time-of-Flight Counters (FTOF), and Electromagnetic Calorime-

ters (EC).

Drift Chambers (DC): The CLAS12 Drift Chambers [8] are advanced wire chambers designed to measure the path of charged particles that emerge from the target. The curvature of the path of the particle, influenced by the magnetic field generated by the torus coils, is used to calculate its momentum and determine its charge. These chambers are distributed across three distinct regions: before the torus coils (R1), within them (R2), and just after them (R3), consisting of a total of 18 individual wire chambers as shown in Fig. 2.5.

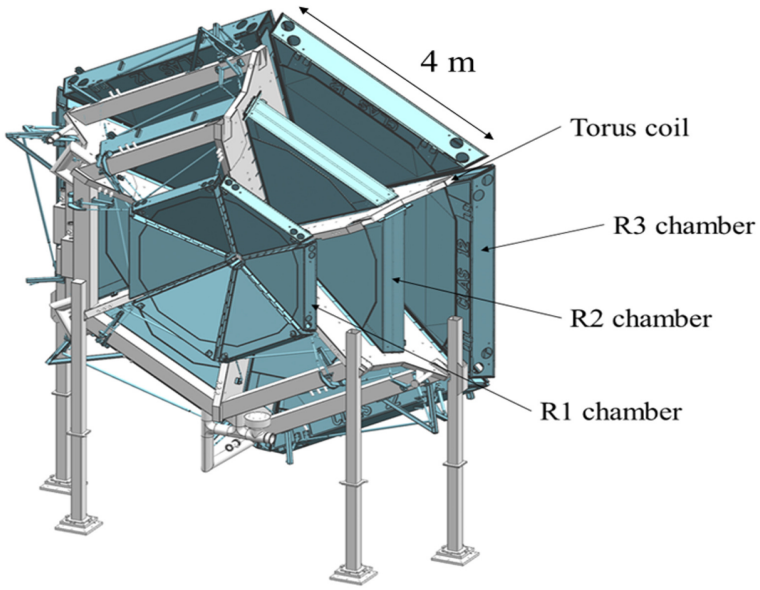

Figure 2.5 Illustration of the of three regions comprised of six drift chambers each in CLAS12 forward tracking system. Figure is adapted from [8].

Each chamber contains two superlayers, each superlayer consisting of six layers of hexagonal drift cells formed by a combination of sense and field wires. The wires are in a gas mixture of 90% argon and 10% CO_2. The structure of a single superlayer is shown in Fig. 2.6.

When a charged particle passes through the drift chamber, it ionizes the gas mixture, which produces free electrons. The field wire's electric field accelerates those free electrons and the secondary ionization electrons toward the sense wires,

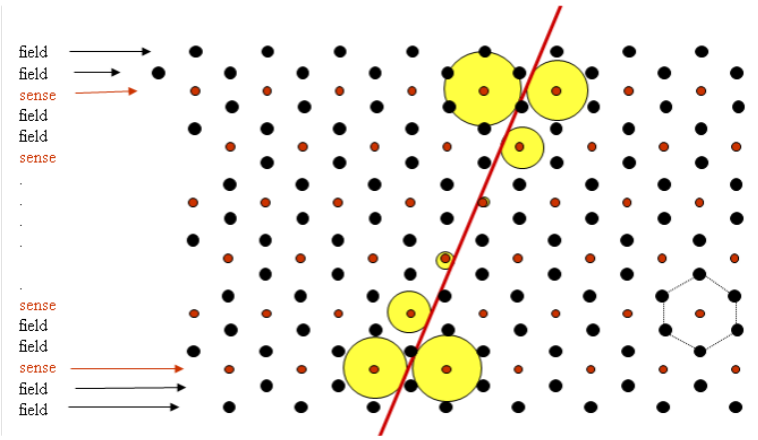

Figure 2.6 Wire layout for one superlayer, track detected is represented by red line. Figure is adapted from [8].

where they are collected. The time taken by the electrons to drift to the sense wires (known as the drift time) is recorded. This drift time is directly proportional to the distance the primary electrons traveled, which enhances the reconstruction resolution of the particle's trajectory. Adjacent superlayers have their wires arranged with $\pm 6°$ stereo angles to enhance the resolution of momentum measurements further.

Cherenkov Counters (CC): The CLAS12 FD system has two distinct Cherenkov Counters; the High Threshold Cherenkov Counter (HTCC) [9] and the Low Threshold Cherenkov Counter (LTCC) [27]. Because negative pions also have relatively low mass, they are difficult to distinguish from electrons. HTCC, which is positioned just before the first region of the drift chambers, is used for the separation of electrons (also positrons), particularly from charged pions with momenta below 4.9 GeV, but also from kaons and protons. HTCC has a pion rejection efficiency above 99% up to the threshold of 4.9 GeV [9]. It is filled with CO_2 gas at 1 atm and 25° C, possessing a refractive index slightly exceeding 1.0. Electrons traveling through this gaseous medium have velocities exceeding the velocities of light, which results in the generation of Cherenkov light, also called Cherenkov radiation. This radiation is reflected by the mirrors and detected by photomultiplier tubes (PMTs). This

phenomenon enables the effective separation of electrons from pions. HTCC features a self-supporting mirror composed of 60 ellipsoidal mirror facets with twelve identical half-sectors as shown in Fig. 2.7 (right). Each half-sector has four ellipsoidal mirrors that focus the Cherenkov light on 48 photomultiplier tubes. The outermost mirrors in each half-sector are trimmed into two mirrors in such a way that they still focus the Cherenkov light into the same photomultiplier tube.

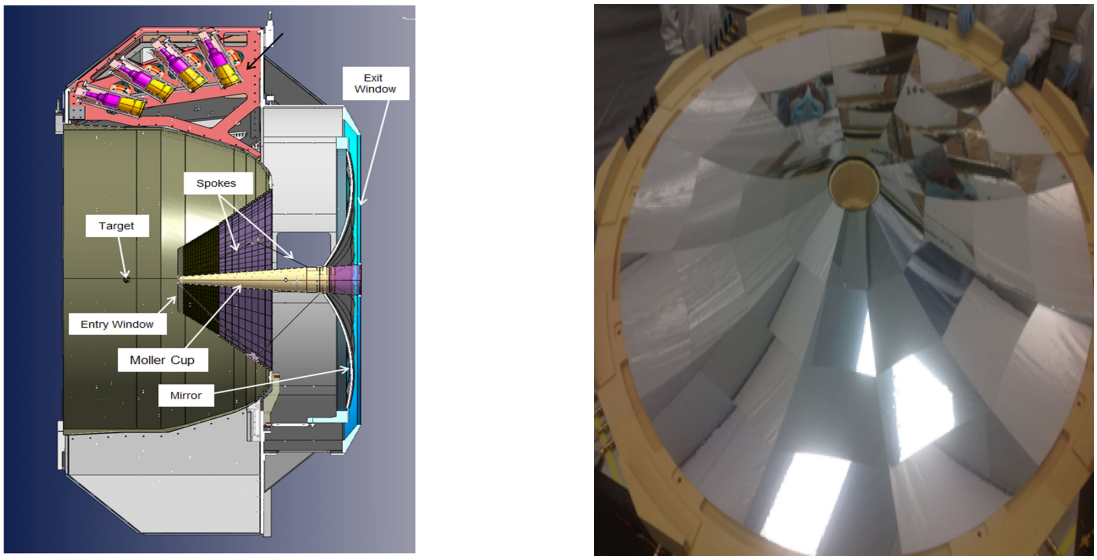

Figure 2.7 Lateral view of HTCC with its surrounding CLAS12 detector components (left), self-supporting mirror composed of 60 ellipsoidal mirrors (right). Figures are adapted from [9].

LTCC is positioned just after the third region of the Drift Chamber and is designed to distinguish pions from kaons. During the Fall 2018 run period, LTCC was installed and operational only in sector 3 and sector 5. Sector 3 utilized C4F10 gas, while sector 5 used N_2 gas. Each sector of LTCC features 108 lightweight mirrors. In the CLAS era, LTCC served as a primary detector to distinguish electrons from pions. However, with the HTCC performing this role in CLAS12, the LTCC now focuses on differentiating pions and kaons in the momentum range of 3.5 to 9 GeV [27]. Operating on the same principle as HTCC, LTCC relies on the fact that pions, being lighter, emit Cherenkov radiation, whereas kaons do not. This dual Cherenkov

counter system enhances the particle identification capabilities of the CLAS12 FD system.

Forward Time of Flight Counters (FTOF): The CLAS12 Forward Time of Flight Counter [10] system, positioned between the LTCC and the EC, serves the purpose of measuring the time it takes for a particle to travel the distance from the interaction point in the target to the FTOF. Each sector of CLAS12 FD consists of three panels of plastic scintillation bars, panel-1a, panel-1b, and panel-2, with a photomultiplier tube (PMT) at both ends of each bar. The scintillators of panels 1a and 1b cover an angular region of $\theta = 5^\circ$ to 35° and $\phi = -180^\circ$ to $+180^\circ$, while panel 2 encompasses an angular region of $\theta = 35^\circ$ to 45° and $\phi = -180^\circ$ to $+180^\circ$.

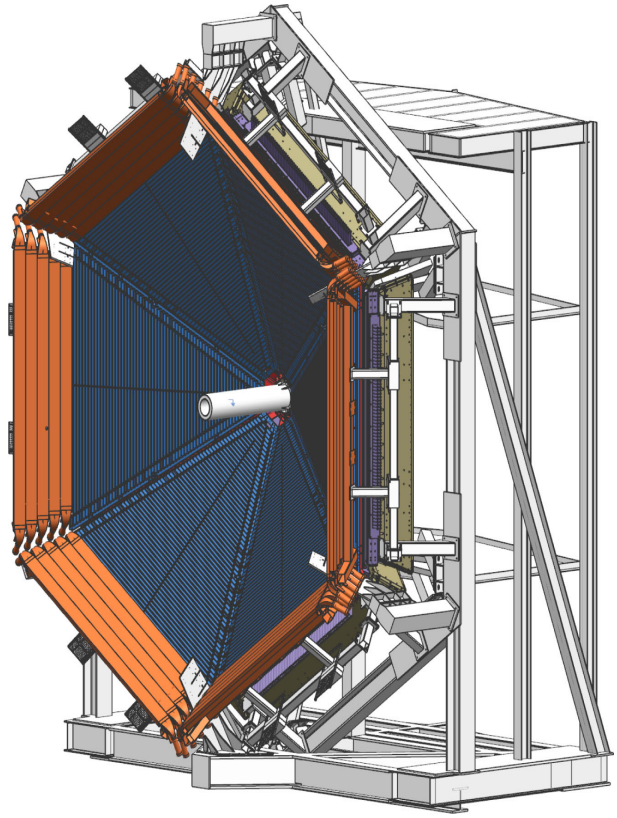

Figure 2.8 CLAS12 FTOF system showing the panel-1b counters on the inside (dark blue color), panel 1-a are behind panel 1-b (not visible in the figure) and the panel-2 counters on the outside (orange color). Figure is adapted from [10].

When particles hit the scintillation bar (SC), they generate light signals of varying

intensities depending on their energy deposit, which are then channeled to PMTs for amplification, yielding measurable signals. By comparing the measured time of flight with the calculated time based on the particle's track and momentum, hadrons can be identified by the time difference (Δt), assuming the desired particle mass (m). Δt is defined by

$$\Delta t = \frac{l_{SC}}{\beta c} - t_{SC} + t^e_{vx}, \tag{2.1}$$

with the velocity of the hadron $\beta = pc/E = pc/\sqrt{m^2 + p^2}$. Here, p is momentum, and m is mass of the hadron. The term t^e_{vx} accounts for the reference time at the interaction vertex and is defined as $t^e_{vx} = t^e_{SC} - \frac{l^e_{SC}}{c}$, with l^e_{SC} the path length from the vertex to the SC and, t^e_{SC} time measured in SC for the electron. Similarly, l_{SC} and t_{SC}, denote the path length and the time measured at SC for the hadron. The constant c is the speed of light. For more details, see Ch. 3, Sec. 3.1.2.

Electromagnetic Calorimeters (EC): The CLAS12 electromagnetic calorimeters [11] located downstream of the FTOF counters are used to identify electrons, photons, and neutrons. Each sector CLAS12 of the FD system consists of two distinct modules of calorimeters, namely the pre-shower calorimeter (PCAL) and the electromagnetic calorimeters (ECAL). ECAL is the refurbished CLAS era ECAL calorimeter, and it consists of the inner calorimeter (ECIN) and outer calorimeter (ECOUT). With the 12 GeV energy upgrade leading to an increase in the momentum of forward-moving particles, the PCAL is added in front of the ECAL, see Fig. 2.9, to ensure complete absorption of electromagnetic showers.

PCAL and ECIN have 15 layers of triangular scintillators sandwiched with triangular lead sheets, while ECOUT has 24 layers of triangular scintillators sandwiched with triangular lead sheets [11]. The scintillators are 1 cm thick bars, and the lead sheets are 2.2 mm thick. Together, the CLAS12 calorimeter system has a radiation

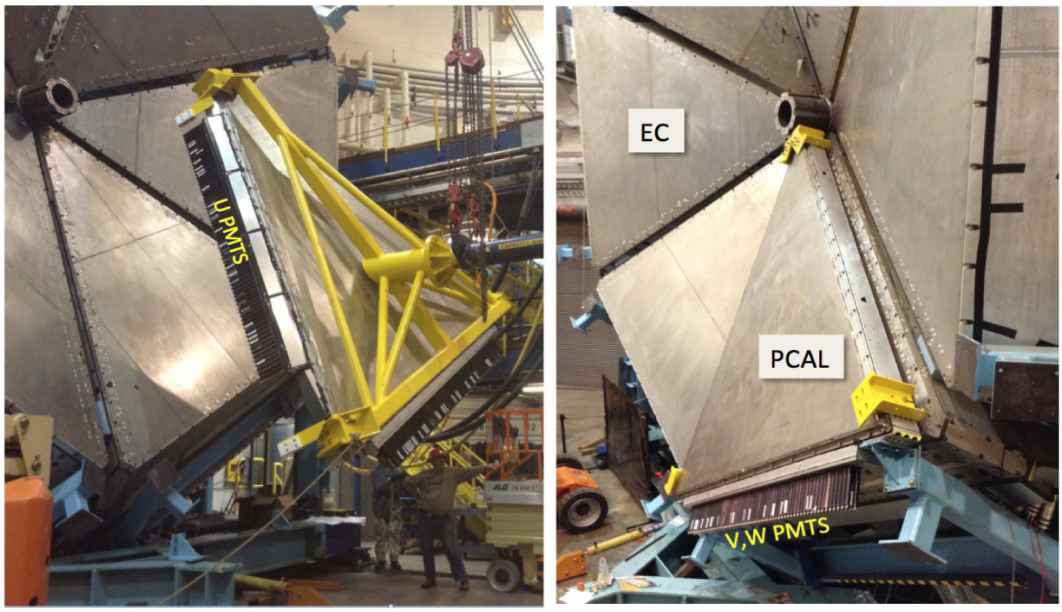

Figure 2.9 CLAS12 calorimeter system showing installation of PCAL in front of EC. PMTs are also shown at the edge of PCAL sector. Figures are adapted from [11].

length thickness of about 20.5 with alternating scintillator and lead sheet layers. The scintillator layers consist of three readout planes, labeled U, V, and W, as shown in Fig. 2.10. Plane U has 84 strips and V, and W have 77 strips. The strip orientation in each layer aligns with one side of the triangular shape. The light collected from the scintillation strips in each layer is summed optically and read out via PMTs.

When electrons emerging from the interaction region enter the EC, they lose all their energy by producing electromagnetic showers. These showers occur via Bremsstrahlung radiation and subsequent pair production. Because of this, the energy deposition is highly localized and occurs within a relatively small volume of the EC.

In contrast, hadrons such as protons, pions, and kaons lose energy primarily through ionization, gradually dissipating their energy over a much larger distance. Unlike electrons, hadrons do not produce electromagnetic showers in the EC. This distinct energy-deposition pattern allows for the effective separation of electrons from hadrons. A hardware-level cut is also applied to the PCAL prevent ionizing hadrons

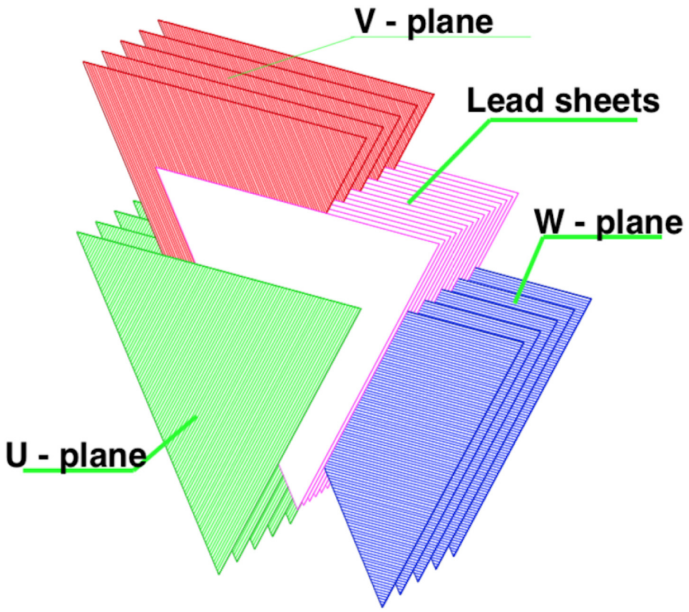

Figure 2.10 Alternating U, V, and W planes of the calorimeter along with the lead sheets. Figure is adapted from [11].

from triggering the data acquisition system.

2.1.3 Central Detector System

The CLAS12 Central Detector system (CD) positioned mostly within the magnetic field of the solenoid surrounding the target covers a polar angle range extending from 35° to 125° and nearly all azimuthal angles. It consists of the Central Vertex Tracker (CVT), the Central Time-of-Flight (CTOF), and the Central Neutron Detector (CND). CVT composed of Silicon Vertex Trackers (SVTs) and Barrel Micromegas Trackers (BMTs). An event display view in CD can be seen in Fig. 2.11.

Central Vertex Tracker: The Central Vertex Tracker (CVT) in CLAS12 is located near the target within the solenoid coil to track and identify lower-momentum recoiling hadrons, such as pions, kaons, and protons, originating from the interaction point. It consists of three inner regions (two layers in each region) of Silicon Vertex Trackers [12] surrounded by six layers of Barrel Micromegas Trackers and Forward Micromegas Trackers (FMTs) [13] as shown in Fig. 2.12.

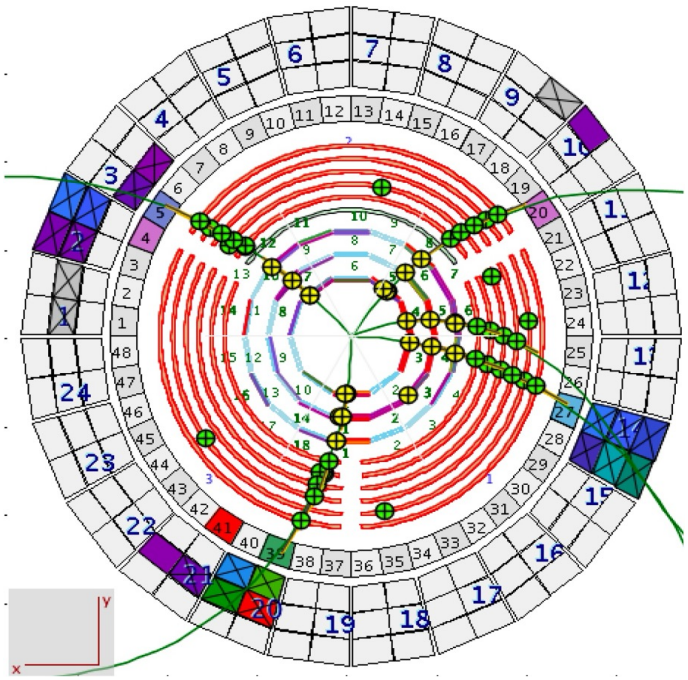

Figure 2.11 Event display view in CLAS12 CD system. Starting from the inner three SVT regions surrounded by six BMT layers, then the CTOF, and finally the CND scintillation bars. Figure is adapted from [6].

The SVT uses silicon strip technology to track the particle trajectories. As a charged particle traverses a silicon layer, it induces electron ionization, generating a measurable current through the electronic readout, which allows for a precise determination of the particle track.

BMTs are micro-pattern gaseous detectors. In a narrow conversion gap with an electric field of typically a few kV/cm, free electrons produced by gas (90% argon + 10% isobutane) ionization drift towards the micro-mesh and enter the amplification gap, see Fig. 2.13. Here, the electric field intensifies to several hundreds of kV/cm, propelling electrons from the conversion gap to ionize the gas, leading to the creation of an electron shower. Then the signal produced is collected by the readout strips.

The CVT tracking system enables the calculation of the four-momenta for the tracked particles in the CD region. By matching up with the hits in the CTOF with tracks from the CVT, particle identification in the CD is accomplished. FMT is used

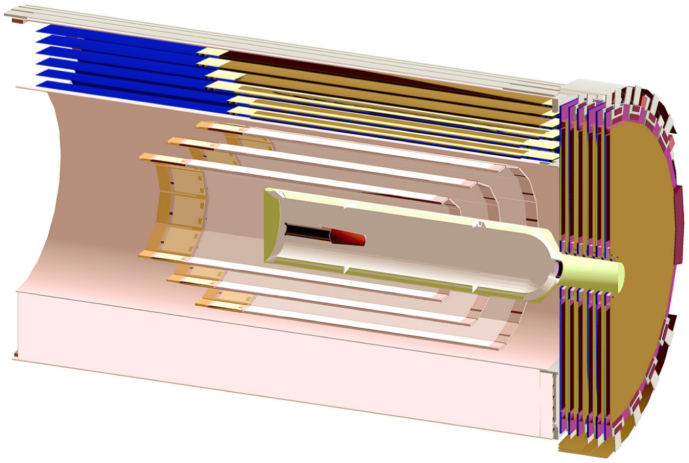

Figure 2.12 CLAS12 Central vertex tracker with the SVT, BMT, and FMT. The inner three regions of SVT are surrounded by the outer six layers of BMT. Six layers of FMT disks are shown downstream of all SVT and BMT layers. Figure is adapted from [12].

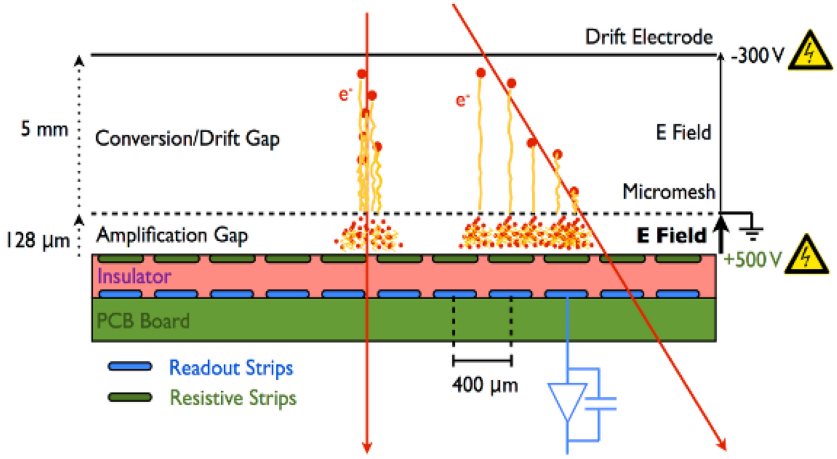

Figure 2.13 Schematic view of a resistive MVT detector. Figure is adapted from [13].

for forward angles ranging from 5° to 35°. However, it was not used for the RGA Fall 2018 dataset.

Central Time of Flight: The CLAS12 Central Time of Flight (CTOF) [14] is located between the CVT and the CND. CTOF operates as a scintillator barrel. It is designed to measure the flight time in the central region (i.e., in the (θ) range from about 35° to about 125°). CTOF consists of 48 scintillation counters equipped with light guides and PMTs positioned at both ends. These scintillation counters detect

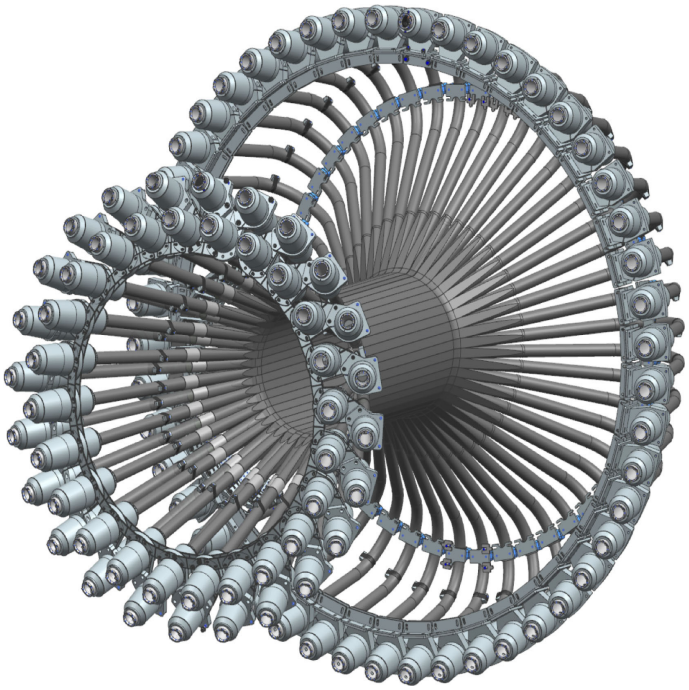

Figure 2.14 CLAS12 CTOF scintillation bars along with PMTs. Figure is adapted from [14].

the arrival time of particles passing through the central region. The operational principle of CTOF is the same as that of FTOF. CND that surrounds the CTOF also works with the same principle as FTOF and CTOF, but is used to detect neutrons as its name suggests. CND is not used in this analysis.

2.2 Data acquisition and reconstruction of events

CLAS12 operates at high luminosity of the order of 10^{35} $cm^{-2}s^{-1}$. The CLAS12 trigger system is designed to select specific events in which an electron interacts with the target through the reaction of interest. The RGA Fall 2018 inbending dataset used the electron trigger with the following criteria [28],

- **DC roads:** Predefined drift chamber (DC) roads were used to identify valid tracks. These roads represent matching particle tracks within the same sector of DC, HTCC, and PCAL.

- **HTCC photon threshold:** A minimum of two photoelectrons detected in the HTCC was required. This ensured the identification of electrons while rejecting most background particles.

- **Combined energy cut:** The total energy deposited in PCAL and EC (ECIN and ECOUT) was required to exceed 300 MeV. This criterion effectively filtered out low-energy ionizing particles, preventing them from triggering the Data Acquisition (DAQ) system. This helped suppress noise and improve the quality of the collected data.

- **PCAL energy cut:** A minimum energy deposition of 60 MeV in the PCAL to ensure that the signal originates from a valid electromagnetic interaction. This energy threshold is set up in hardware to ensure that the pions and other minimum ionizing particles do not trigger PCAL.

- **EC Energy Cut:** A minimum energy deposition of 10 MeV in EC was required. As in PCAL, this is also to ensure that pions and other minimum-ionizing particles do not trigger the ECAL.

The events triggered by the trigger system are then recorded by the DAQ system [29]. These data are stored in EVIO (Event Input/Output) file format on data tapes. These files are then used for the calibration and reconstruction of the data. The CLAS12 Offline Analysis Tools (COATJAVA) process the raw detector signals and produce reconstructed tracks. The reconstruction process is carried out using the CLAS12 reconstruction framework called CLARA (CLAS12 Analysis and Reconstruction Architecture) [30]. COATJAVA produces high performance output (HIPO) format files. These HIPO files store detector-related information for each event as structured data banks called DST (Data Summary Table) banks. The DST bank has stored REC::Event, REC::Particle, REC::Calorimeter, REC::Scintillator, REC::Cherenkov, REC::Track, REC::Traj (track trajectory) and so on for different detector systems.

Various variables from those banks are used for this physics analysis. Specific data for physics analyses are processed along with DSTs during data reconstruction, called cooking, which produces specialized datasets called trains. In this analysis, the train named 'resIncl' is used. This train has inclusive reaction data in the resonance region with $W < 3.0$ GeV cut.

The final processed or cooked data are stored in the location of the ifarm tape directory: /mss/clas12/rg-a/production/recon/fall2018/torus-1/pass2/main/train/.

For this analysis, the data in HIPO bank format is converted to ROOT file format using the hipo_tools software [31].

Chapter 3

Event Selection

The physics analysis involves several critical stages such as identification of particles, event selection, data simulation, cross sections calculations, various corrections, error analysis, and more. All of these processes will be discussed in more detail in the following chapters. This chapter will focus on particle identification, data simulation, and event selection processes.

3.1 Particle identification

The CLAS12 event reconstruction software COATJAVA [30] processes and organizes reconstructed responses from different detector subsystems and associates them with particles through identification schemes. It uses specific particle identification criteria to link detector responses across multiple CLAS12 subsystems to charged and neutral particles. For charged particles in FD, electrons and positrons are identified based on criteria such as a minimum of two photoelectrons in the HTCC, a minimum energy deposition of 60 MeV in the PCAL, and five-sigma cuts on momentum-dependent sampling fractions. If charged particles are not identified as electrons or positrons, they proceed to hadron identification. Hadron identification is based on the difference between the hadron vertex time and the event start time, using associated time of flight hits from the FTOF and CTOF systems.

In this analysis, the first task is to filter out bad events by ensuring that the number of reconstructed particles in an event is less than 20, and any event with more than 20 particles is discarded, this is basic sanity check, and its impact is minimal

to nothing. After filtering out bad events, a series of refinement cuts are applied to identify final-state electron and hadron candidates for the double-pion reaction, $ep \to e'p'\pi^+\pi^-$. These refinement procedures are discussed in detail in the following sections.

3.1.1 Electron Identification

In the inbending configuration of the torus magnetic field, electrons, negatively charged particles traveling at nearly the speed of light, are bent toward the beamline. These electrons are used to reconstruct the vertex and identify other particles. To ensure the quality of the detected electrons, various selection criteria are applied, including general and detector-specific cuts. Electrons are mostly scattered in the forward direction, and thus only electrons detected by FD are used. As mentioned before, see Sec. 2.2, the electron is used as the trigger particle in this experiment and must meet the required matching criteria for DC, HTCC, and EC. In this analysis, the events are selected for further analysis if the electron is the first particle registered in that event. Electrons are by far the lightest particles out of the four particles in the double-pion ($ep \to e'p'\pi^+\pi^-$) reaction channel, and thus must reach the detector the fastest. The second cut is the event builder PID cut. Electrons are given the PID number '11' in DST banks by event builder software. Thus, particles with PID other than '11' are not considered electrons in this analysis.

Charge cut: In the inbending configuration of the toroidal magnetic field, the tracks that bend toward the beam are assigned a charge of -1. Therefore, to select FD electrons, a charge cut on -1 is applied.

Status cut: The status value represents the presence of the particle in different detector systems and is calculated as the sum of several components. It includes 2000 times a factor for the FD, 4000 times a factor for the CD, with each factor

being 1 if the respective subsystem measured the particle and 0 otherwise. For this analysis, only electrons detected in the forward detector are used. Thus, the status value is as given as,

$$Status = 2000 \times 1 + 100 \times N_{SC} + 10 \times N_{CAL} + N_{CHE}, \tag{3.1}$$

where, $N_{SC},\ N_{CAL},\ N_{CHE}$ are the numbers of responses from the scintillator, calorimeter, and Cherenkov detectors of the FD subsystems, respectively [32]. As an electron is used as the trigger particle, the negative sign is assigned in front of the status value. Thus, the cut, $2000 < abs(Status) < 4000$, is used to select electron candidates, abs represents the absolute value.

Minimum momentum cut: In this analysis, particles with momentum below 1.5 GeV are excluded from electron candidate selection. The momentum distribution indicates that low-momentum electrons are rare in the forward detector. Since negative pions contribute significantly to contamination in the low-momentum region, this cut is applied to reduce their presence.

Vertex position cut: For electrons detected in the six individual sectors of the forward detector, cuts at -10 cm and $+5$ cm are applied to the z position of the vertex (vz). These cuts are illustrated in Fig. 3.1.

Figure 3.2 presents the distribution of vz for both full and empty targets. The empty target histograms are normalized using the ratio of total accumulated charge measured by the Faraday cup during the full and empty target runs. The empty target histogram has three distinct peaks. The first two on the left arise from contributions from the target cell entering and exiting windows. The rightmost peak is from the film of the target window. The distribution of vz is not completely zero in the center of the target cell, indicating the presence of the remaining cold hydrogen gas inside the

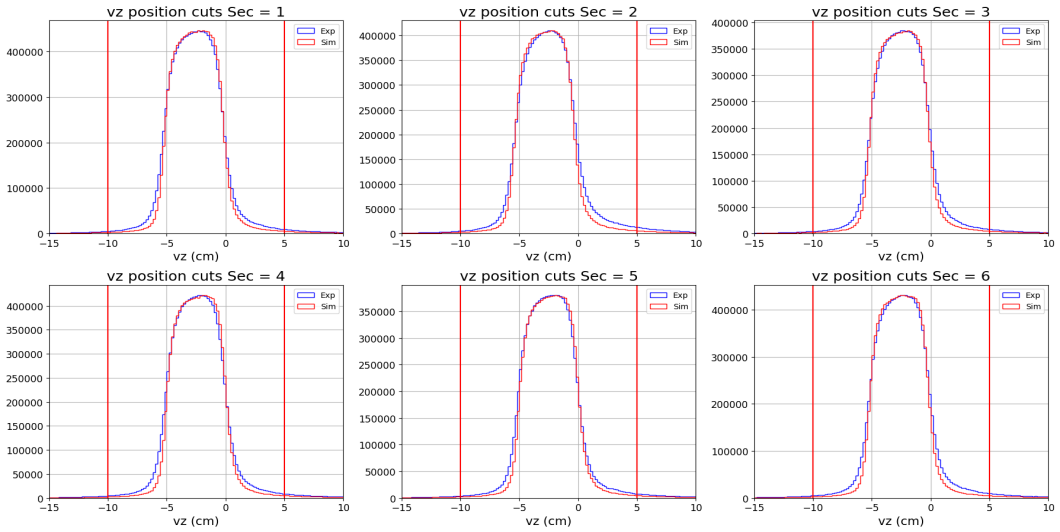

Figure 3.1 The z component of the vertex position cut for electrons for all six sectors of CLAS12 FD. Exp stands for experimental measurement and Sim for Monte-Carlo simulated data.

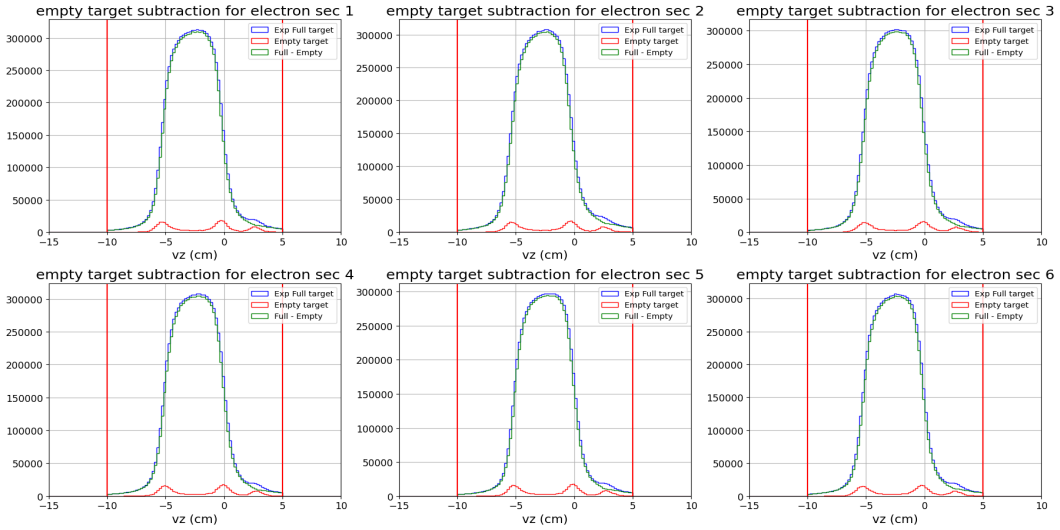

Figure 3.2 The z component of the vertex position showing empty target subtraction for all six sectors of CLAS12 FD. The red histograms represent events from the empty target runs, the blue histograms correspond to the full target, and the green histograms show the subtracted distributions (full minus empty).

cell. This contribution needs to be corrected for, and the correction is applied using the density of the cold hydrogen gas during the luminosity determination process.

Sampling fraction cuts: Sampling Fraction (SF) is the energy fraction sampled by electromagnetic calorimeters. Because there are alternating active (scintillator)

and passive (lead sheet) layers in the calorimeters, electrons deposit only fractions of the total energy in the active region of the calorimeters. That fraction is called a sampling fraction and is roughly a constant value. In the case of CLAS12 calorimeters, its value is about 0.25 for electrons. The formula for the sampling fraction is,

$$SF = \frac{E_{tot}}{p}, \tag{3.2}$$

where E_{tot} is the total energy deposited in the EC system and p the momentum of the electron.

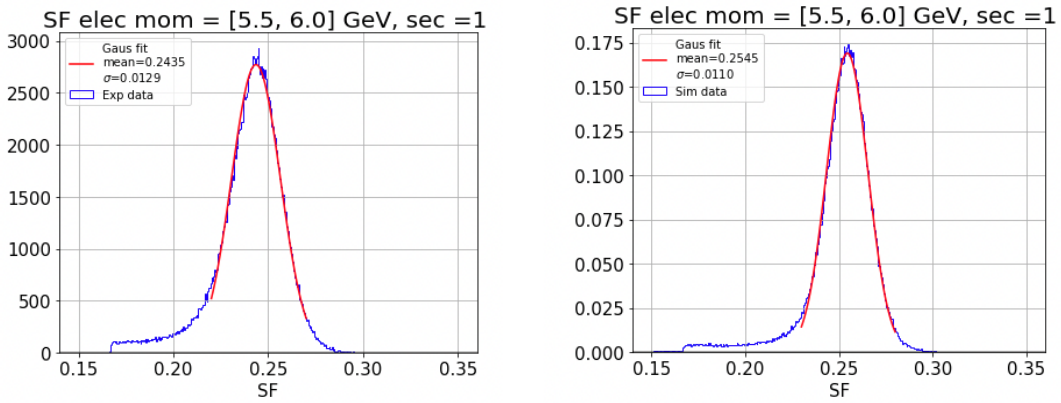

Figure 3.3 Sampling fraction distribution with Gaussian fit for one particular momentum bin [5.5, 6.0] GeV, in sector 1, using experimental data (left) and simulated data (right). The data are represented by blue histograms, Gaussian fit by red curves.

The sampling fraction cuts are developed separately for the six sectors of the FD. First, the data are divided into several electron momentum bins. For each momentum bin, the sampling fraction distribution is plotted and fitted using a Gaussian distribution function, see Fig. 3.3. The cuts are then defined using the mean $\pm\, 3.5\,\sigma$, where σ represents the standard deviation from the Gaussian fit. Next, a second-order polynomial is fitted for both the upper cut (mean + $3.5\,\sigma$) and the lower cut (mean - $3.5\,\sigma$). Electrons falling within these upper and lower cuts are retained, while those outside the range are excluded from further analysis. A similar procedure is applied to the simulation data.

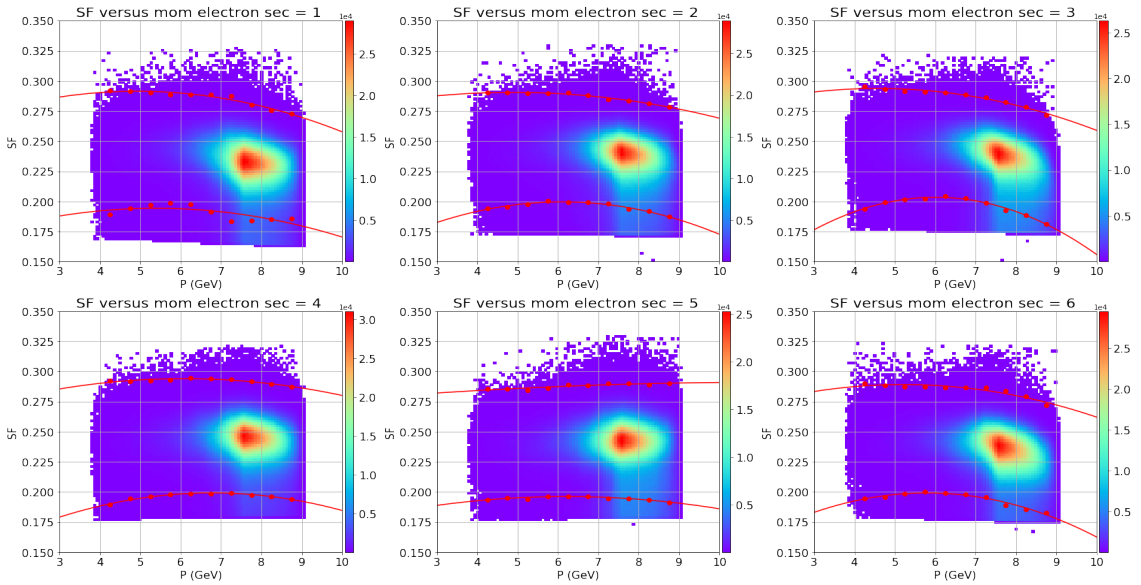

Figure 3.4 Sampling fraction versus momentum for electrons for all six sectors using measured data. Red lines are the applied cuts.

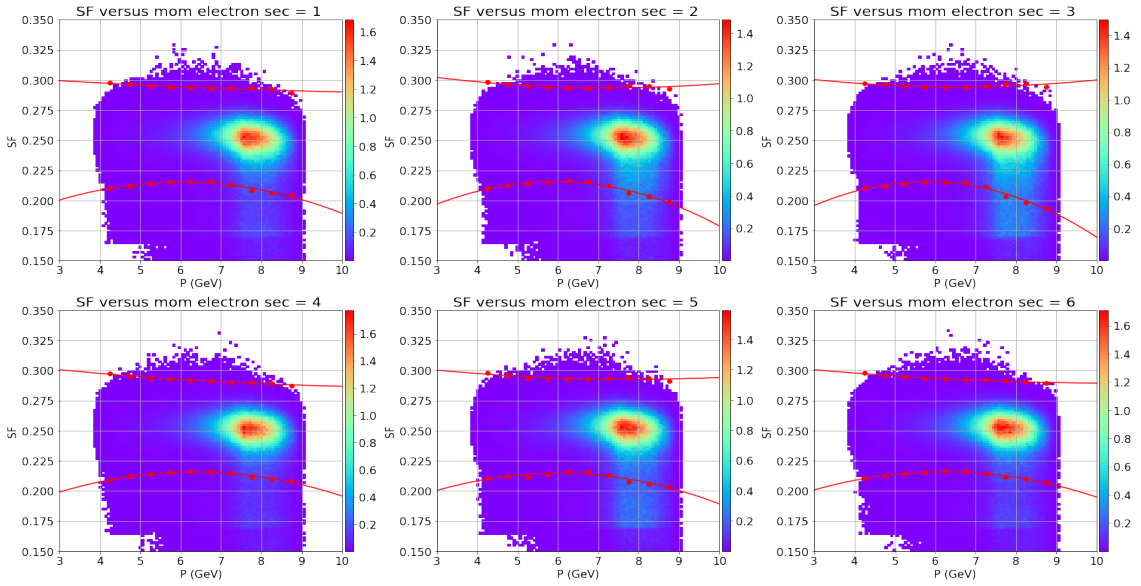

Figure 3.5 Sampling fraction versus momentum for electrons for all six sectors using MC simulated data. Red lines are the applied cuts.

Figures 3.4 and 3.5 show the SF versus momentum distributions for the six FD sectors along with the SF cuts (red lines) to the experimental and simulation data, respectively.

PCAL fiducial cuts: The CLAS12 detector includes physical gaps, such as the forward-angle hole resulting from beamline components and sector gaps. Additionally, factors such as coil re-scattering and magnetic field distortions can affect particles near the detector's edges. When an electromagnetic shower created by an electron occurs near these edges, energy leakage can lead to incomplete energy reconstruction and a potential misidentification of electrons.

To mitigate these effects, two distinct cuts are implemented. The first set of cuts is based on the scintillator bars in the V and W planes of the PCAL, rejecting data below 11.5 cm and above 400 cm to eliminate edge-related distortions. The second cut involves the PCAL y versus x distributions of electron candidates, developed independently for each sector in the PCAL plane. For selected events, basic electron cuts such as charge, status, and PID at zero cuts are applied. The PCAL x and y coordinates of the electrons passing all the cuts mentioned above are then rotated using (3.3).

$$\begin{aligned} x' &= x \cdot \cos\Big(\frac{\pi}{180} \cdot (-60 \cdot sec)\Big) - y \cdot \sin\Big(\frac{\pi}{180} \cdot (-60 \cdot sec)\Big), \\ y' &= x \cdot \sin\Big(\frac{\pi}{180} \cdot (-60 \cdot sec)\Big) + y \cdot \cos\Big(\frac{\pi}{180} \cdot (-60 \cdot sec)\Big), \end{aligned} \tag{3.3}$$

where *sec* represents for EC sector. Now the data is binned into various x' bins, and the typical y' distributions are plotted, as shown in Fig. 3.6.

The cut points on both sides are determined by selecting 20% of the maximum value of the super-Gaussian 3.4 curve fit on either side of the peak. The super-Gaussian function is given by,

$$f(x) = A \cdot \exp\left(-\left(\frac{x-\mu}{\sigma}\right)^n\right), \tag{3.4}$$

where A is the amplitude, μ is the mean, σ is the standard deviation, and n is an exponent power chosen to be even.

The green lines in Fig. 3.6 represent these cut boundaries. After determining the y' cut points on both sides of the x' bins, straight lines (first-order polynomials) are

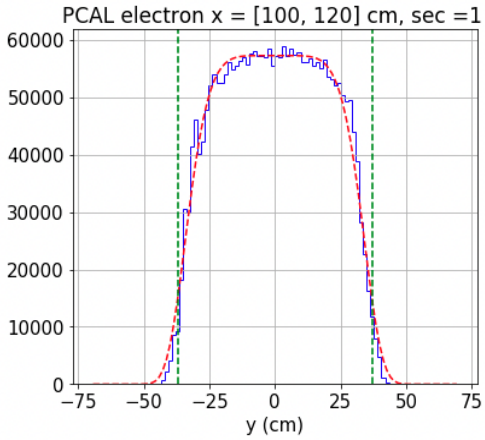

Figure 3.6 PCAL measured electron yield distribution versus y for the x slice from 100 to 120 cm in sector 1. The data are represented by blue histogram, fit by red curve, and green lines are used cuts.

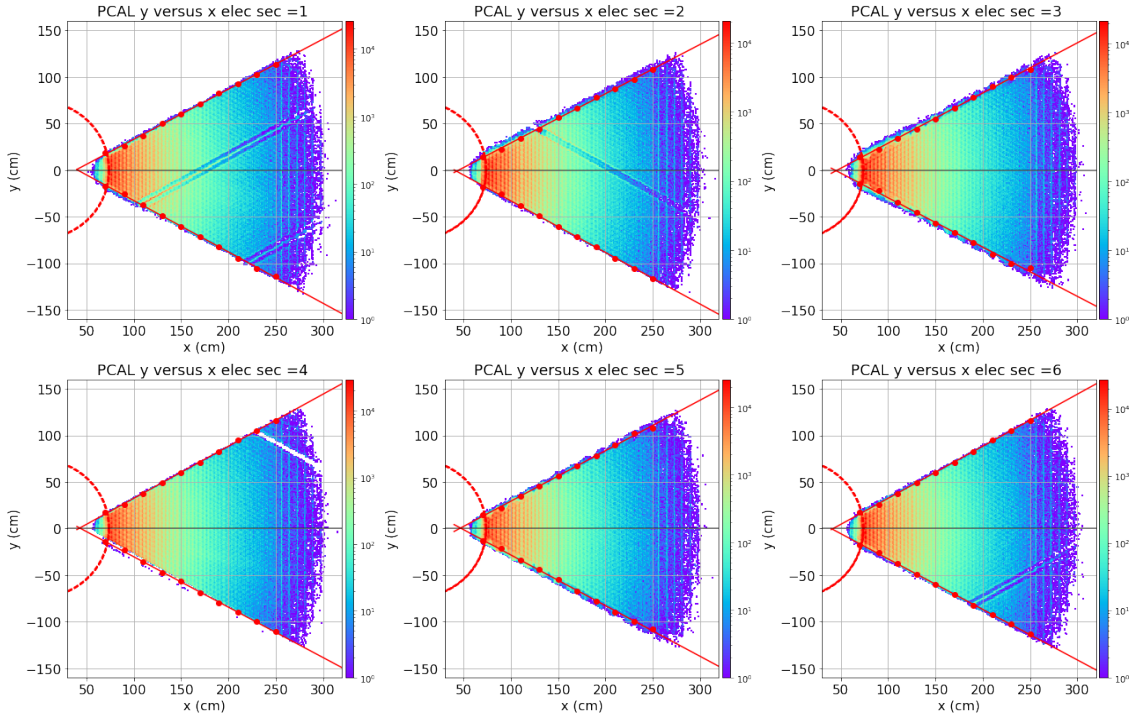

Figure 3.7 Electron PCAL fiducial cut plots showing y vs. x distributions for all six sectors after applying the rotations defined in Eq.(3.3). The red lines and circle indicate the fitted fiducial cut boundaries.

fitted through the cut points on the upper and lower sides. In addition, inner circular cuts are also applied to avoid the inefficient edge region near the forward hole, as shown in Fig. 3.7. This is an inner circular cut at the radius ($\sqrt{x^2 + y^2}$) is where

97% of the data are lying outside the circle. The data within these straight lines and outside of the inner-circular cut are selected for further analysis. The same cuts are applied for the experimental and simulated data.

DC fiducial cuts: CLAS12 DC has similar inefficient areas near the edges of each of the 18 chambers. To select data not affected by these edge-related issues, DC fiducial cuts are developed for the 18 chambers in the three different DC regions, R1, R2, R3. The cuts develop in a similar way to the PCAL y versus x fiducial cuts. Firstly, the x and y coordinates in each region are rotated using 3.3 with sec being the DC sector. The data is then grouped into various x' bins, and the corresponding y' distributions are plotted and fitted using the super-Gaussian function (3.4), as shown in Fig.3.8.

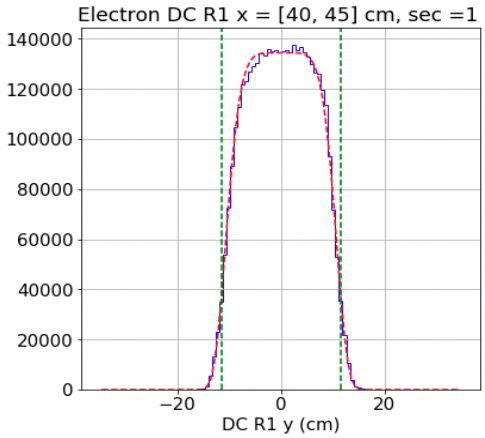

Figure 3.8 Super-Gaussian fit to the DC R1 experimental yield distribution as a function of y, for the x slice from 40 to 45 cm, for electron candidates in sector 1. The blue histogram represents the data, the red curve shows the fit, and the green vertical lines indicate the applied selection cuts.

The cut points on both sides are determined by selecting 20% of the maximum value of the fit of the super-Gaussian curve on either side of the peak. The green lines in Fig. 3.8 represent these cut boundaries. After determining the cut points on both sides for all bins, straight lines (first-order polynomials) are fitted through the cut points on the upper and lower sides, as shown in Fig. 3.9. Inner circular cuts as

described previously for PCAL are also applied for all 18 drift chambers in all three regions and are shown in Fig.3.9 along with the straight line cuts.

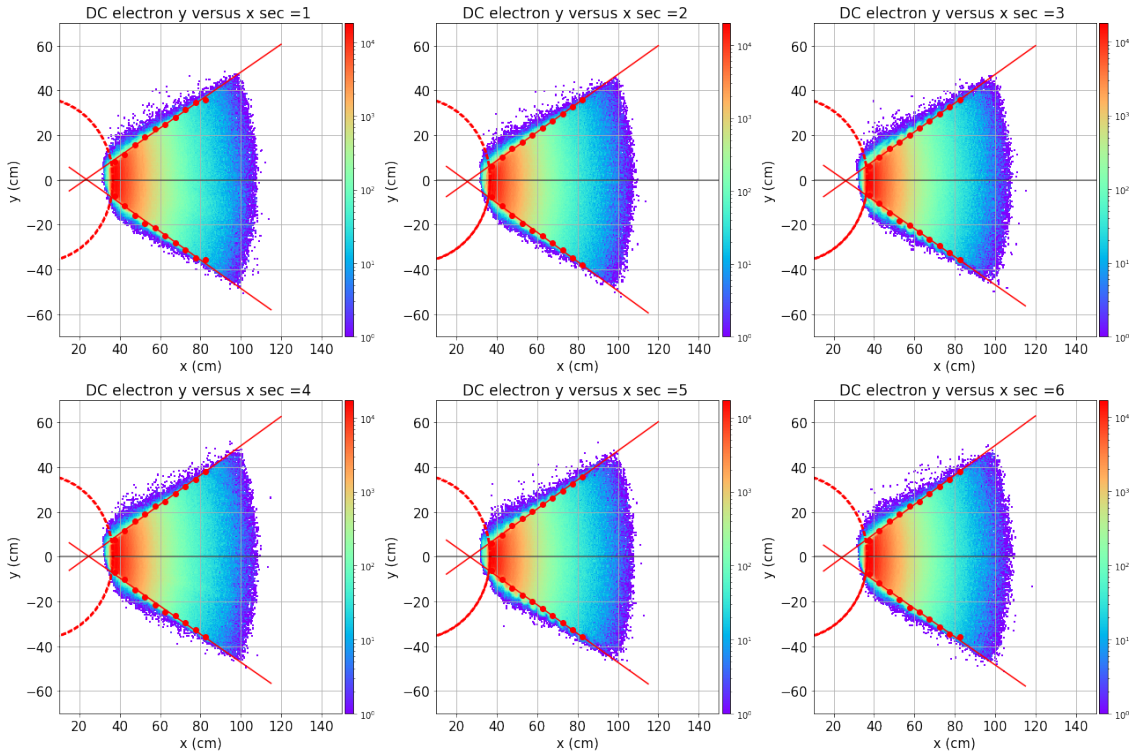

Figure 3.9 Measured DC R1 y versus x coordinates for electron candidates, with fiducial and inner circular cuts. Cuts are shown by red fitted lines and dashed circle.

Data within these straight lines and outside the inner circle are retained for further analysis. The process of obtaining cuts in all three DC regions is the same, and the same DC fiducial cuts are applied to both the experimental and the simulated data.

3.1.2 Hadron Identification

In the double-pion electroproduction channel of analysis, there are three hadrons in the final state. In the missing π^- topology (used in this analysis), only protons and $\pi^+ s$ are directly measured and the $\pi^- s$ four momenta are reconstructed using the known four momenta of all other participating particles. Thus, hadron cuts are applied only to the measured protons and $\pi^+ s$. The hadrons detected by both the forward and the central detector systems are used in this analysis. General basic

cuts are applied for both FD and CD hadrons, while more specific cuts are applied separately.

Charge cut: Protons and π^+s are positively charged particles. In the inbending configuration of the torus magnet, the positive tracks that bend away from the beam are assigned a charge of +1. Therefore, to select protons and $\pi^+ s$, a charge cut of +1 is applied.

Status cut: The status value represents the presence of the particle in different detector systems and is calculated as the sum of several components. It includes 2000 times a factor for the FD, 4000 times a factor for the CD, with each factor being 1 if the respective subsystem measured the particle and 0 otherwise. As this analysis uses both FD and CD hadrons, the status value for FD particles is given by 3.5 and for CD particles it is as given as

$$Status = 4000 \times +100 \times N_{SC} + 10 \times N_{CND}, \tag{3.5}$$

where, N_{SC}, N_{CND}, are the numbers of responses from the CTOF scintillator, and CND scintillator of the CD subsystems, respectively [32]. Thus, the cut, $2000 < abs(Status) < 6000$, is used to select the FD and CD hadrons, *abs* representing the absolute value.

Minimum momentum cut: The particles with momentum less than 0.2 GeV in CD and 0.5 GeV for π^+ and 0.4 GeV for protons in FD are rejected from the hadron candidate in this analysis. At very low momenta, hadrons are more susceptible to misidentification, multiple scattering, and energy loss, which can degrade the momentum and trajectory resolution.

Vertex position cut: The difference in the z component of the vertex position between the hadron candidates and the electron vertex must be within the range of

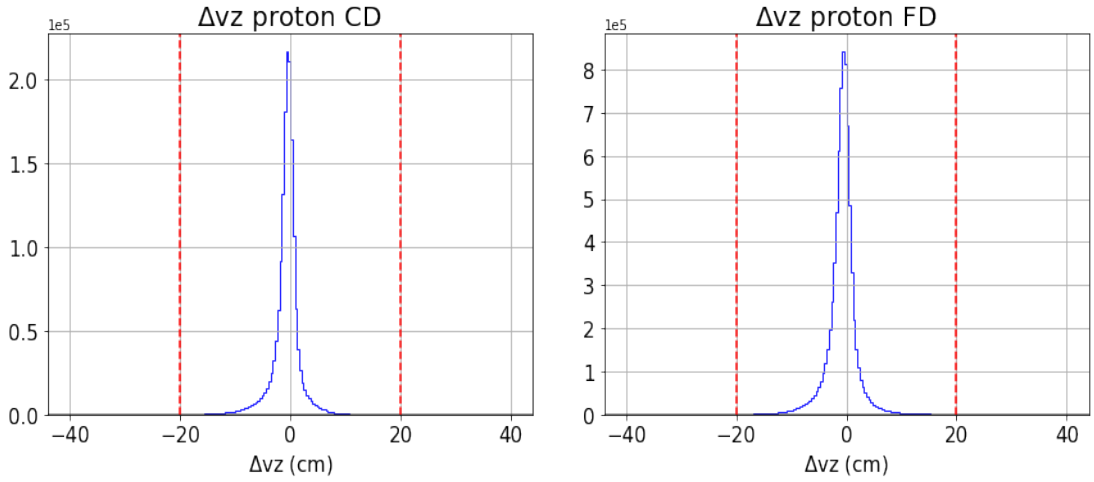

Figure 3.10 Difference in the z component of the vertex position for the proton and electron of each event. Left plot is for CD detected proton candidates and right plot is for FD detected protons.

-20 cm to 20 cm. This cut is applied to both forward detector and central detector hadron candidates, as illustrated in Fig. 3.10 for protons. The π^+ distributions are similar to those of the proton Δvz. The same cuts are applied for both the experimental and simulated data.

Chi-Square PID cuts: The chi-square PID is the estimate of the quality of particle identification and is determined on the basis of the vertex time difference and the time resolution of the FTOF and CTOF paddles, which varies between different scintillator bars. The number of deviations $N\sigma$ quantifies how well the measured timing matches the expected values for different hadrons [32]. This number N is the value assigned as the chi-square PID during particle reconstruction by COATJAVA. In this analysis, chi-square PID cuts are applied to all hadron candidates. For FD candidates, the absolute value of the chi-square PID must be less than 5.0, while for CD candidates, it must be less than 7.0 as shown in Fig. 3.11 for protons. The π^+ distributions are similar to those of the proton. The same chi-square PID cuts are applied to both the experimental and simulated data.

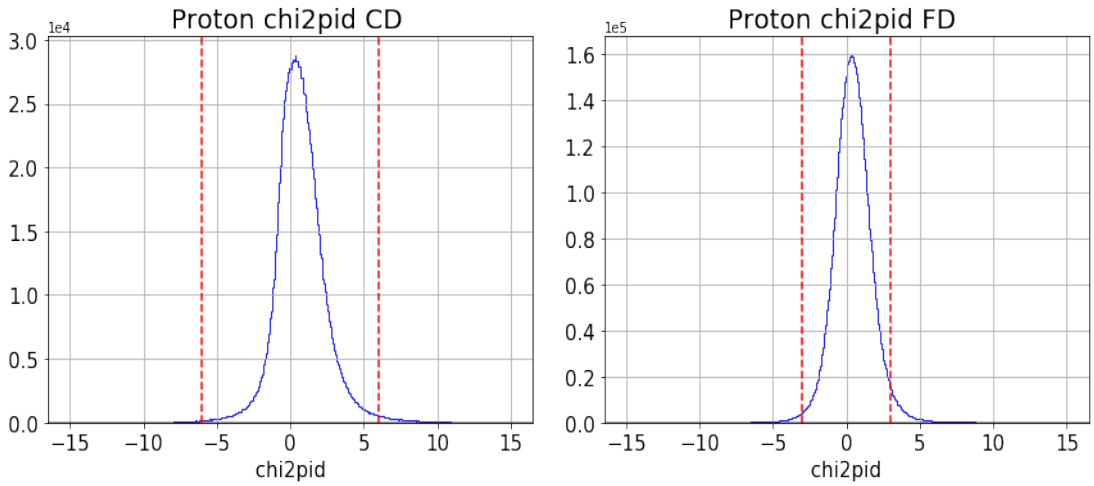

Figure 3.11 Chi-square PID cuts for proton candidates. Left plot is for CD detected protons candidates and right plot is for FD detected protons.

Δt cuts: The Δt cuts are based on the difference between the flight time measured by the FTOF or CTOF and the time calculated using the path length and momentum measured by DC or CVT, along with the assumed mass of the hadron. If the particle is detected by FD, FTOF and DC are used, and if the particle is detected by a CD system, CTOF and CVT are used instead. The formula for Δt is given by (2.1). As this analysis uses an electron as the first particle and is detected in FD, the vertex time t^e_{vx} depends only on the path length and time of the electron measured at FTOF. Hadrons start at the same time, and at the same interaction point, travel slower than electron. The electron travels with a velocity equal to the speed of light c, but the hadrons are massive compared to the electron, and they travel with a velocity βc. If the assumed mass of the hadron in 2.1 is correct, the value of Δt will be close to zero, and the distributions of Δt peaks at zero. If the assumed mass is not the correct mass of the particle, the Δt distributions have offset based on the mass and momentum of the particle. Due to detector resolution and other factors, the Δt distributions differ significantly between candidates for FD and CD. The FD distributions show clear separation between protons, $\pi^+ s$ and $K^+ s$, see Fig. 3.13, while the CD distributions show more overlap for higher-momentum hadrons, see Fig. 3.14 , making it harder

to distinguish them. To develop the Δt cuts, hadrons in an event have a so-called good electron that has passed all electron selections.

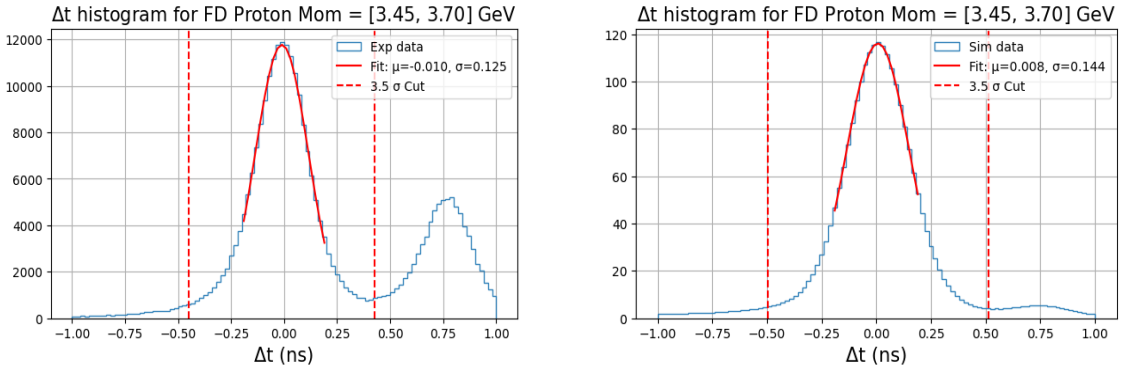

Figure 3.12 Gaussian fit to Δt distribution calculated using mass of proton, shown for momentum bin [3.45, 3.70] GeV, experimental at left, and simulation at right. Red dashed lines are the 3.5σ cuts.

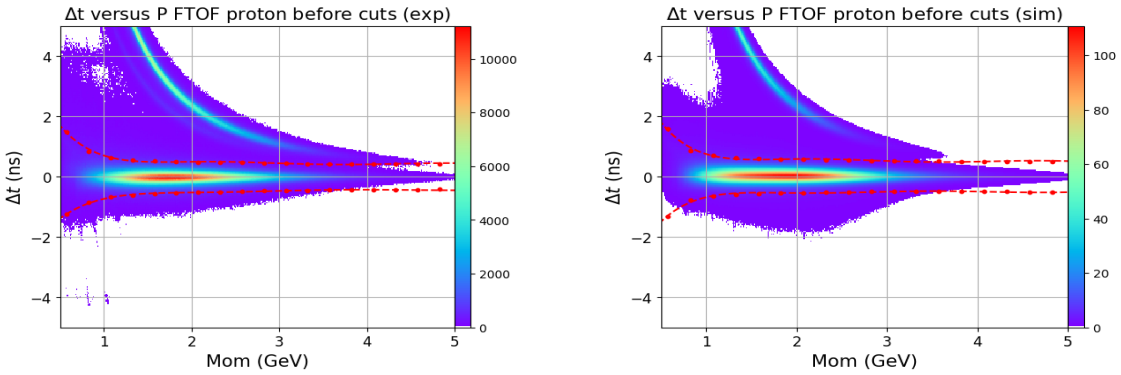

Figure 3.13 Δt versus momentum distribution for positive particles detected by FTOF assuming the mass of a proton, experimental at left, and simulation at right.

The procedure for applying Δt cuts is as follows.

1. The Δt distribution for the hadron candidates is divided into various momentum bins.

2. For each momentum bin, the Δt distribution is fitted with a Gaussian curve to determine the mean and σ values. Figure 3.12 shows the Gaussian fit with the dashed red lines at positions mean $\pm$ 3.5σ. The second peak predominant in experimental data at 0.75 GeV is due to the pion band, see Fig. 3.13.

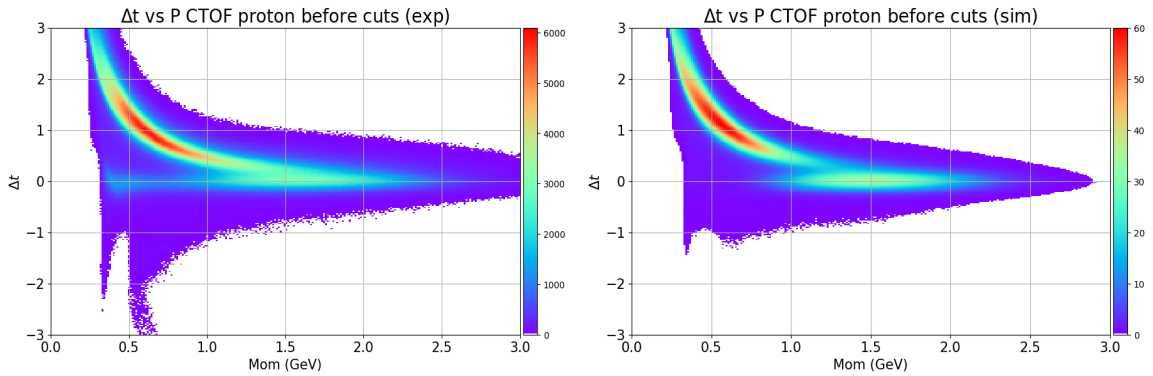

Figure 3.14 Δt versus momentum distribution for positive particles detected by CTOF assuming the mass of a proton, experimental at left, and simulation at right.

3. Suitable polynomial functions are fitted using the values mean $\pm 3.5\sigma$ from each momentum bin, as illustrated in Fig. 3.13.

4. Particles within these polynomial boundaries are selected for further analysis.

5. The same methodology is applied separately for the hadron candidates in FD and CD.

6. This procedure is performed for both experimental and simulated data.

Figure 3.13 shows the Δt versus momentum distribution for all positive forward tracks assuming a proton mass. In addition, Figure 3.14 shows the corresponding plots for the CD tracks assuming the proton mass.

Hadron DC fiducial cuts: The CLAS12 DC system exhibits tracking inefficiencies and distortions near the geometric edges of the detector. These edge regions often suffer from reduced hit resolution, incomplete track reconstruction, and nonuniform acceptance. To mitigate these edge-related effects, DC fiducial cuts are implemented for all hadrons. These cuts are developed following the same methodology as the DC fiducial cuts for electrons.

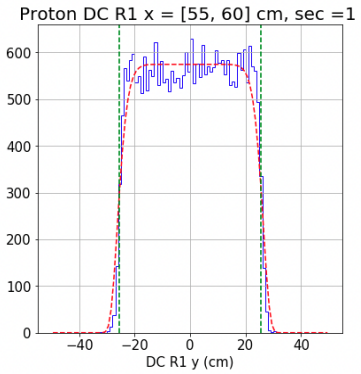

Figure 3.15 Super-Gaussian fit to the DC R1 experimental yield distribution as a function of y, for the x slice from 55 to 60 cm, for proton candidates in sector 1. The blue histogram represents the data, the red curve shows the fit, and the green vertical lines indicate the applied selection cuts.

First, each region's x and y coordinates are rotated using (3.3). Next, the data are divided into multiple rotated x-bins, and the corresponding rotated y distributions are fitted using the super-Gaussian function (3.4), as illustrated in Fig. 3.15.

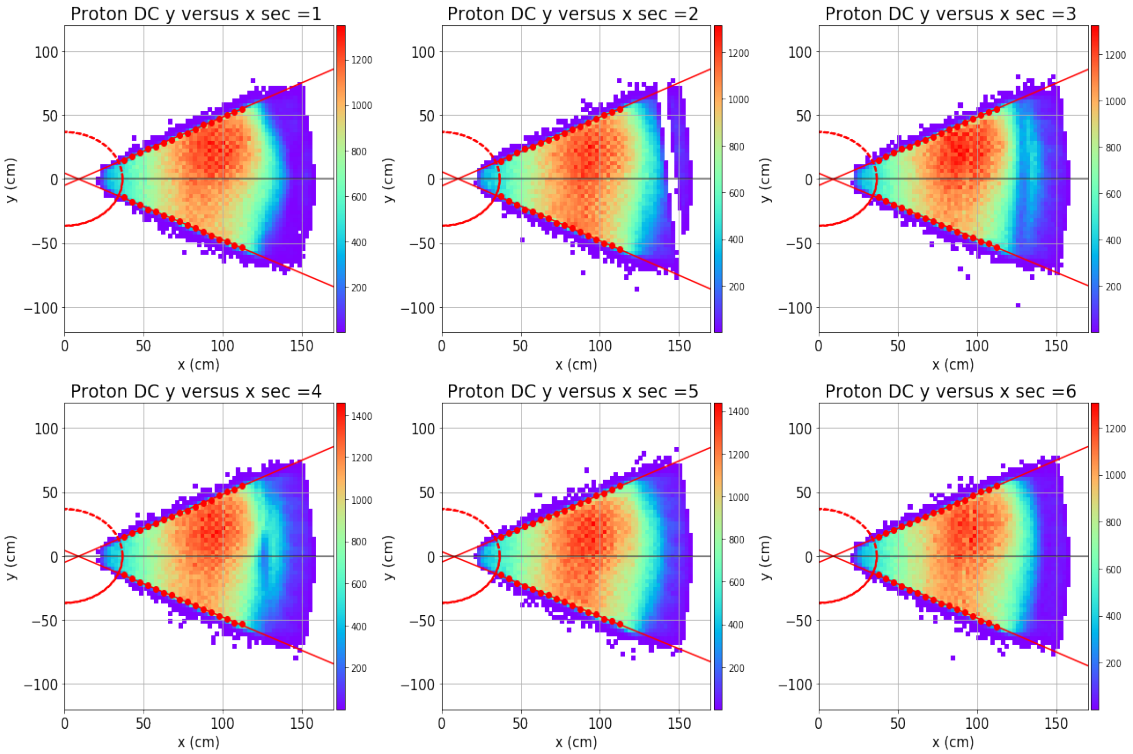

Figure 3.16 Measured DC R1 y versus x coordinates for proton candidates, with fiducial and inner circular cuts. Cuts are shown by red fitted lines and dashed circle.

The cut boundaries on both sides are established by identifying the points where the value of the super-Gaussian curve fit drops to 40% of its maximum on either side of the peak. These boundaries are illustrated by the green lines in Fig. 3.15. Once the y cut points are determined for all x bins, first-order polynomials are fitted to the cut points on the upper and lower sides, as shown in Fig. 3.16. In addition to these cuts, inner circular cuts are determined as for electron fiducial cuts and applied for all 18 drift chambers of all three regions. Only data that fall within these fitted straight lines and outside the inner circle are retained for subsequent analysis.

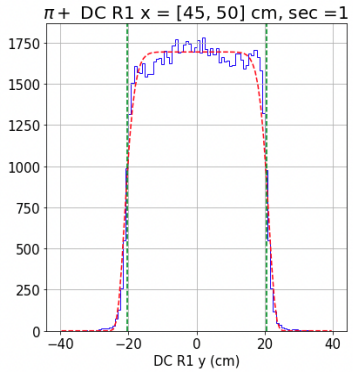

Figure 3.17 Super-Gaussian fit to the DC R1 experimental yield distribution as a function of y, for the x slice from 45 to 50 cm, for π^+ candidates in sector 1. The blue histogram represents the data, the red curve shows the fit, and the green vertical lines indicate the applied selection cuts.

The fiducial cuts for the π^+ tracks are developed using the same procedure as that applied to protons. Figure 3.17 represents the super-Gaussian fit for a particular DC R1 x bin, and Figure 3.18 represents the final applied DC fiducial cuts for π^+.

The procedure for determining fiducial cuts is identical across all three DC regions (R1, R2, and R3), and the same set of cuts is applied to both the experimental and simulation datasets. This ensures uniformity in acceptance corrections and reduces systematic discrepancies between data and simulation.

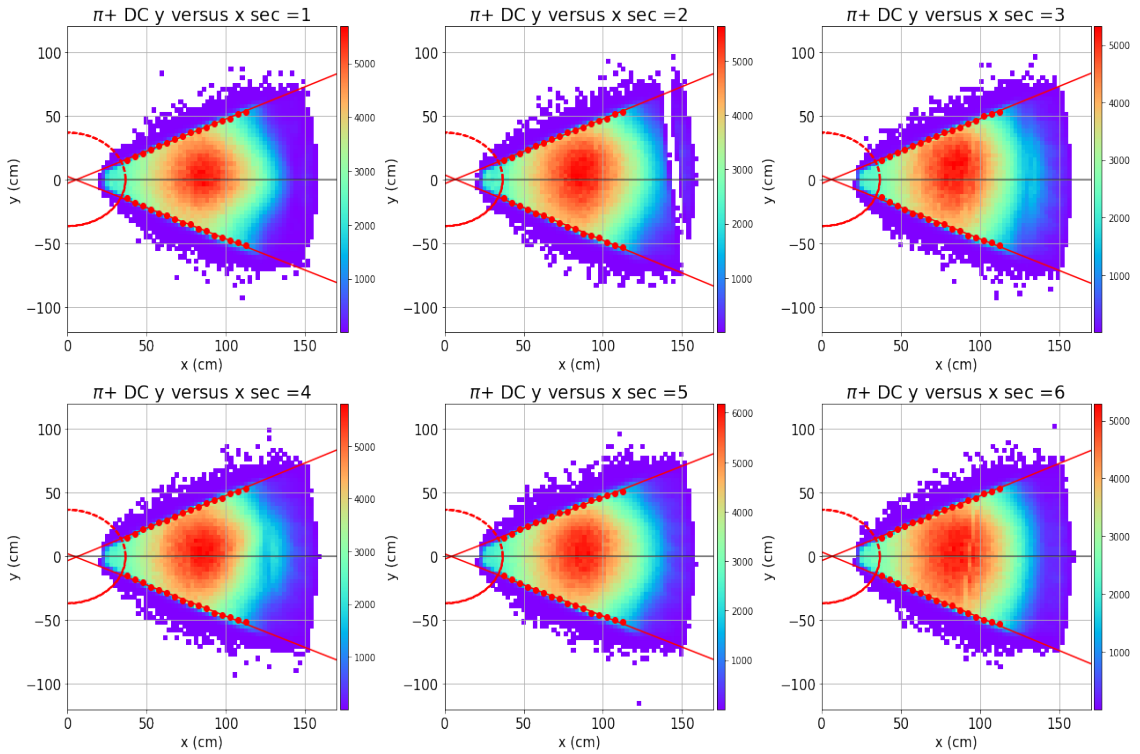

Figure 3.18 Measured DC R1 y versus x coordinates for π^+ candidates, with fiducial and inner circular cuts. Cuts are shown by red fitted lines and dashed circle.

3.1.3 Momentum versus ϕ Cuts for CD Hadrons

The CD system exhibits inefficiencies near the edges of the BMT regions. To mitigate these edge-related inefficiencies, cuts based on the transverse momentum ($p_T = \sqrt{p_x^2 + p_y^2}$) and the azimuthal angle (ϕ) of the hadrons are applied. These cuts exclude hadron tracks that lie in specific ϕ regions near the BMT edges, where tracking performance is unreliable. Figure 3.19 shows these fiducial cuts for a proton candidate in CD. The figure shows the three BMT regions and the applied cuts for the experimental data (on the left) and the simulated data (on the right).

This fiducial cut is uniformly applied to both protons and π^+ tracks in the CD, and the same cuts are used for both experimental and simulated data.

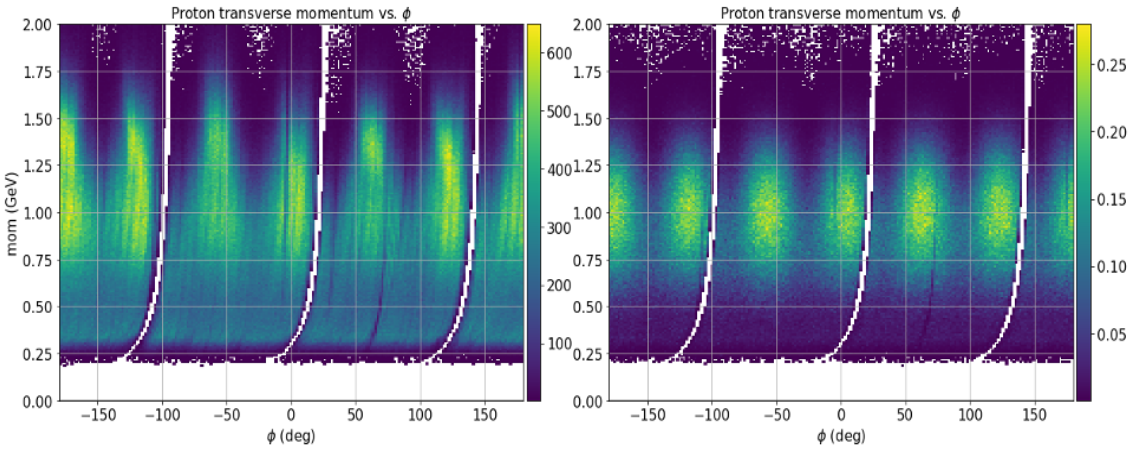

Figure 3.19 Transverse momentum versus ϕ cuts for CD protons; left plot is for experimental data and right plot is for simulated data.

3.1.4 Removal of CD-FD tracks

Hadrons can be measured in both FD and CD, as CLAS12 has some overlapping region for the two detector systems. Those particles are registered as separate tracks on the DST banks during cooking. Figure 3.20 shows the distributions for the difference in momentum (left), θ (middle), and ϕ (right) of π^+ tracks detected in the FD and the CD. Tracks within the red dashed lines in all three distributions are excluded

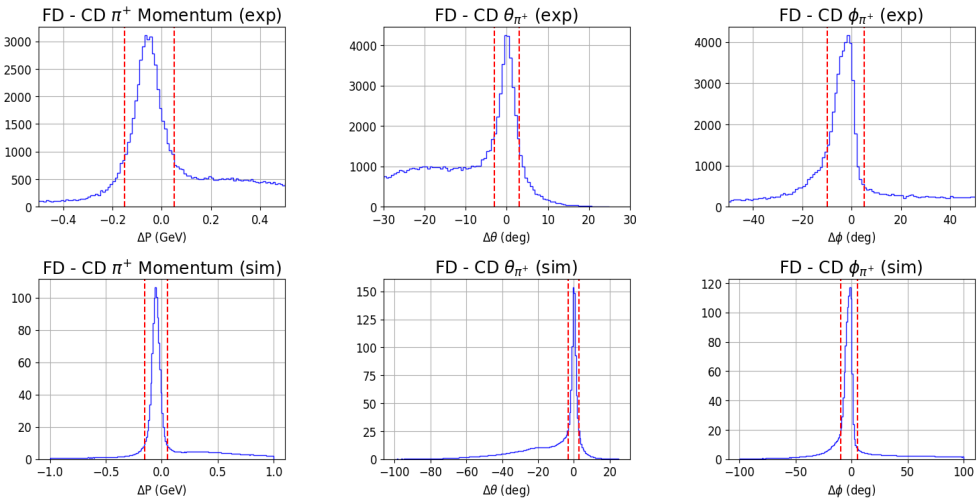

Figure 3.20 Difference in momentum, θ, and ϕ angles for the π^+ detected in both CD and FD tracking, upper three histograms are for experimental data and lower three are for simulation data.

from further analysis. If a track falls within only one or two of the distributions, it is still retained for subsequent analysis. This procedure is applied to both the proton and π^+ tracks. The removal of these tracks, which include both proton and π^+ candidates, leads to a reduction of approximately 1.1% of double-pion events for experimental data and 1.4% for simulated data.

3.2 Energy loss corrections

As the particles traverse through the target and the CLAS12 detector system, they interact with the materials present there, causing energy loss. Any deviations or anomalies in the magnetic field map or misalignment in the detector systems can introduce irregularities in the reconstruction of a particle's momentum. Since protons are the heaviest particles in this $p\pi^+\pi^-$ final state channel, they undergo the greatest energy loss. The energy loss of protons in both FD and CD cases is corrected.

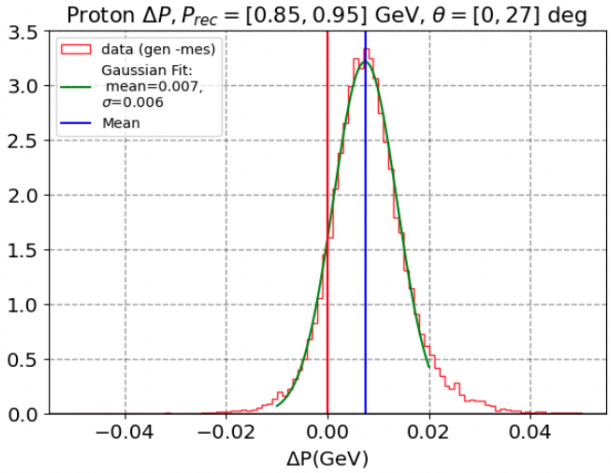

Figure 3.21 Typical ΔP distribution for FD protons in $P_{rec}[0.85, 0.95]$ GeV, and $\theta_{rec} < 27°$ bin.

The correction factors are determined based on the difference between the generated and reconstructed momenta, ΔP, of the particle within specific kinematic bins defined by the reconstructed momentum, P_{rec}, and the polar angle, θ_{rec}. For optimal results, protons from the exclusive $ep \to e'p'\pi^+\pi^-$ topology are taken for this

calculation. The FD protons are divided into two θ bins: $\theta_{rec} < 27^{\circ}$ and $\theta_{rec} \geq 27^{\circ}$, and further subdivided into smaller momentum bins. The ΔP distributions within each momentum bin are fitted by the Gaussian distribution function, as shown in Fig. 3.21. The mean values from the Gaussian fit provide the ΔP momentum shifts.

To derive the correction function, these shifts are fitted with a fourth-order polynomial, see red curves in Fig. 3.22. Since the polynomial diverges at higher momenta, a constant correction is applied beyond the momentum > 2.4 GeV, see dashed lines in Fig. 3.22.

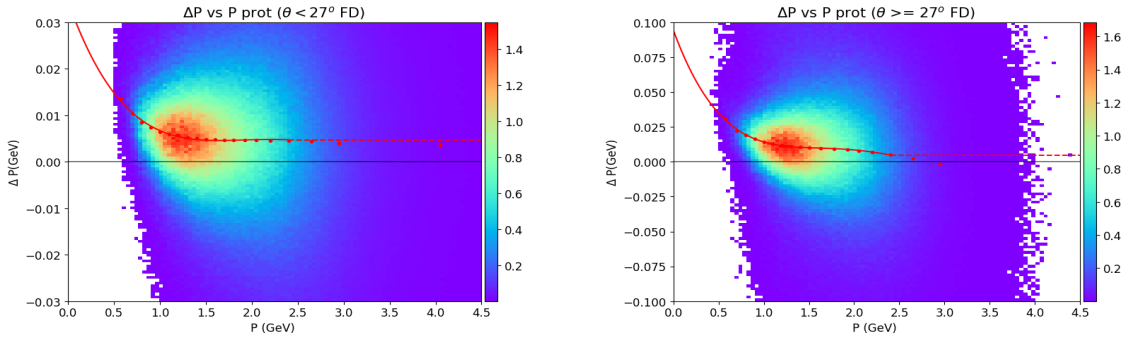

Figure 3.22 ΔP versus $P_{\rm rec}$ for FD protons $< 27^{\circ}$ (left) and FD protons $\geq 27^{\circ}$ (right). Red dots are the shift values, the red solid curve is the polynomial fit and the red dashed line is the constant extrapolation.

Figure 3.23 displays the ΔP versus P_{rec} distributions for the CD protons, as well as for FD protons with angles $\theta_{rec} < 27^{\circ}$ and $\theta_{rec} \geq 27^{\circ}$. The top panels show the distributions before applying energy loss corrections, while the bottom panels show the results after. In the FD region, there is a significant difference between the distributions for $\theta < 27^{\circ}$ and $\theta \geq 27^{\circ}$, attributed to additional material, such as HTCC and CTOF light guides, in the higher-angle range. The relative ΔP momentum difference is typically less than 2% for $\theta_{rec} < 27^{\circ}$ but up to 6% for $\theta_{rec} \geq 27^{\circ}$. Energy loss corrections are already applied during the pass2 reconstruction process for CD protons. Thus, no further corrections are needed nor applied. The correction developed for the momentum of the FD hadrons is applied as $P_{corr} = P_{rec} + \Delta P$, where P_{corr} represents the energy loss corrected momentum.

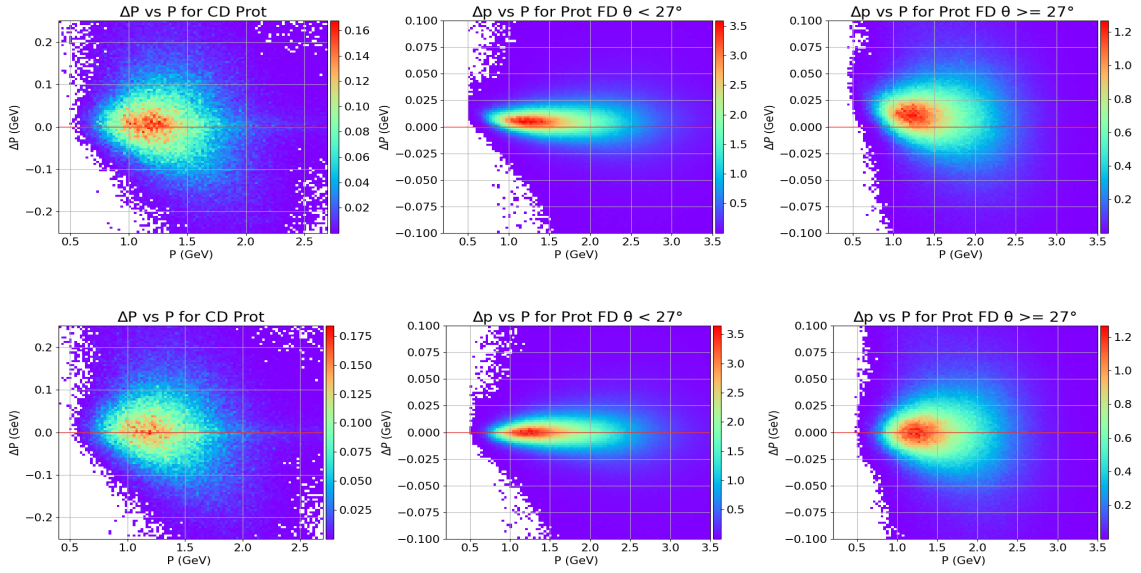

Figure 3.23 ΔP versus P_{rec} for CD, FD $\theta_{rec} < 27^{\circ}$ and FD $\theta_{rec} \geq 27^{\circ}$ protons using MC data.

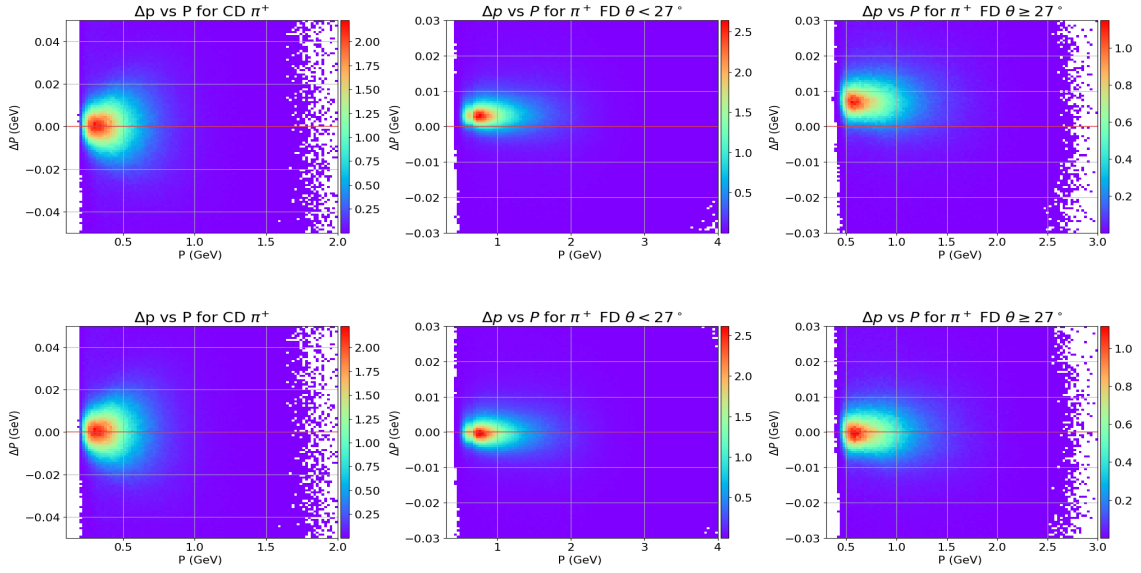

Figure 3.24 ΔP versus P_{rec} for CD, FD $\theta_{rec} < 27^{\circ}$ and FD $\theta_{rec} \geq 27^{\circ}$ $\pi^{+}s$ using MC data.

The pions experience relatively minor energy loss in comparison to the proton. Corrections for the energy losses of CD $\pi^{+}s$ and CD $\pi^{-}s$ were included during pass2 cooking as for CD protons. Figure 3.24 shows the ΔP versus P_{rec} for CD as well as FD $\theta_{rec} < 27^{\circ}$ and $\theta_{rec} \geq 27^{\circ}$ of $\pi^{+}s$. The top panels show the ΔP distributions before applying the energy loss corrections, and the bottom panels show the results

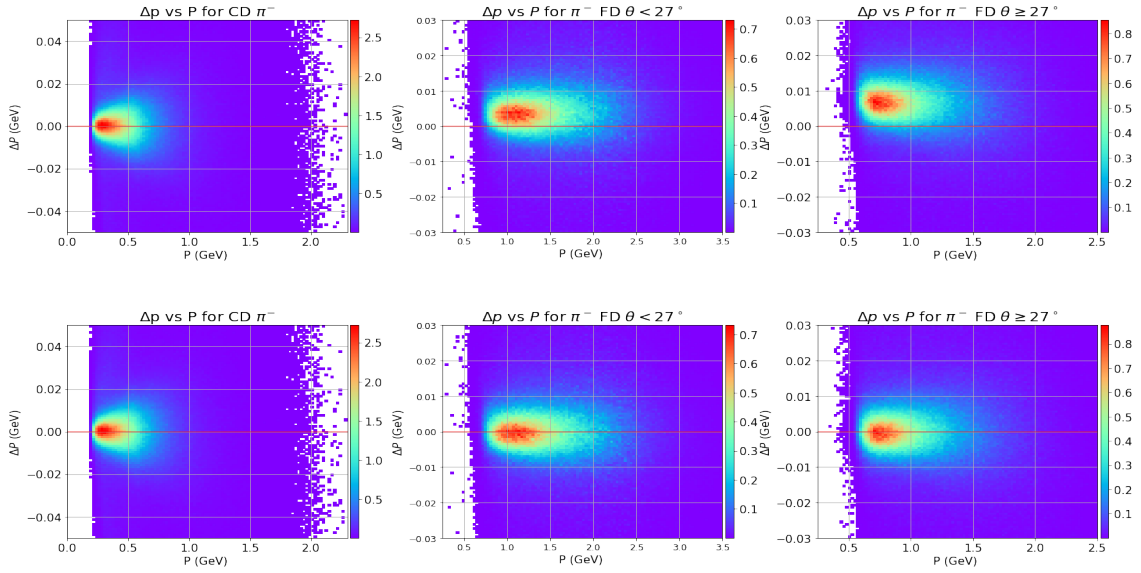

Figure 3.25 ΔP versus P_{rec} for CD, FD $\theta_{rec} < 27^{\circ}$ and FD $\theta_{rec} \geq 27^{\circ}$ $\pi^{-}s$ using simulation data.

afterward. These ΔP corrections are significantly smaller for FD $\pi^{+}s$ at both $\theta_{rec} < 27^{\circ}$ and $\theta_{rec} \geq 27^{\circ}$ than for protons.

Figure 3.25 shows the ΔP versus P_{rec} distributions for the CD as well as FD $\theta_{rec} < 27^{\circ}$ and $\theta_{rec} \geq 27^{\circ}$ $\pi^{-}s$. The top plot is before the energy loss corrections and the bottom plot is after the corrections. ΔP corrections for FD $\pi^{-}s$ with $\theta_{rec} < 27^{\circ}$ and $\theta_{rec} \geq 27^{\circ}$, are similar to those of FD $\pi^{+}s$. Electron energy loss is not considered to be significant in the kinematic range used in this analysis.

3.3 Momentum corrections

After these energy-loss corrections, further momentum corrections are needed. This analysis has used the standard momentum corrections developed and provided by the momentum correction task force formed by the CLAS collaboration. For RGA pass2 data, these corrections are still in the development phase, only the corrections for FD electron and $\pi^{+}s$ are fully developed, which are included in this analysis. These corrections are based on the difference between the measured momentum of a particle and its calculated momentum using the four vectors of the remaining particles

in the reaction. First, electron momentum corrections are implemented using the $ep \rightarrow e'\pi^+(N)$ channel. Corrections are developed for electrons in the momentum range 1.95 GeV $< P_e <$ 9.8 GeV and for $\pi^+ s$ in the momentum range 0.3 GeV $< P_{\pi^+} <$ 8.3 GeV. A detailed procedure and discussion on these corrections can be found in [33].

After these task force momentum corrections are applied, additional momentum corrections derived from the experimental data are applied for each final-state hadron. The data in the exclusive topology are used to develop these corrections. The data are cleaned for background by selecting only the data within $\pm 3.5\sigma$ around the mean of the Gaussian fit of the proton missing mass square (MMSQ) peak, π^+ MMSQ peak, and π^- MMSQ peak and within 1/10th of the maximum value peak for the exclusive MMSQ peak. These corrections are based on the difference between the detected momentum of a particle and the momentum calculated using the four vectors of the remaining three particles in the reaction. For example, in the case of protons, this difference is given by (3.6).

$$\Delta P = P_{\rm rec} - P_{\rm calc}, \quad P^{\mu}_{calc} = p'^{\mu} = \gamma^{\mu} + p^{\mu} - \pi^{+\mu} - \pi^{-\mu}, \quad P_{calc} = \sqrt{P_x^2 + P_y^2 + P_z^2} \quad (3.6)$$

The detailed procedure for this correction is described next. First, particles detected in the FD and CD are separated. The data is then binned into suitable momentum and ϕ_{rec} bins. Three ϕ_{rec} bins corresponding to three distinct ϕ_{rec} angle regions (based on three BMT sectors) are used for the CD particles. In the case of FD particles, the data are separated into six different sectors based on the DC sectors. The momentum bins in each case are dynamically adjusted on the basis of the statistics. The quantity ΔP, the difference between the measured and calculated momenta of the reconstructed particle, is calculated for each bin. The ΔP distributions are then fitted with a Gaussian function in the peak region and the mean value of the peak is determined. The mean value gives the momentum shift ΔP. Figure 3.26 shows the distribution of ΔP for CD protons in the momentum [1.3, 1.5] GeV and

$\phi_{rec}[120°,\ 240°]$ bin, the left plot is for before correction and the right plot is for after correction being applied.

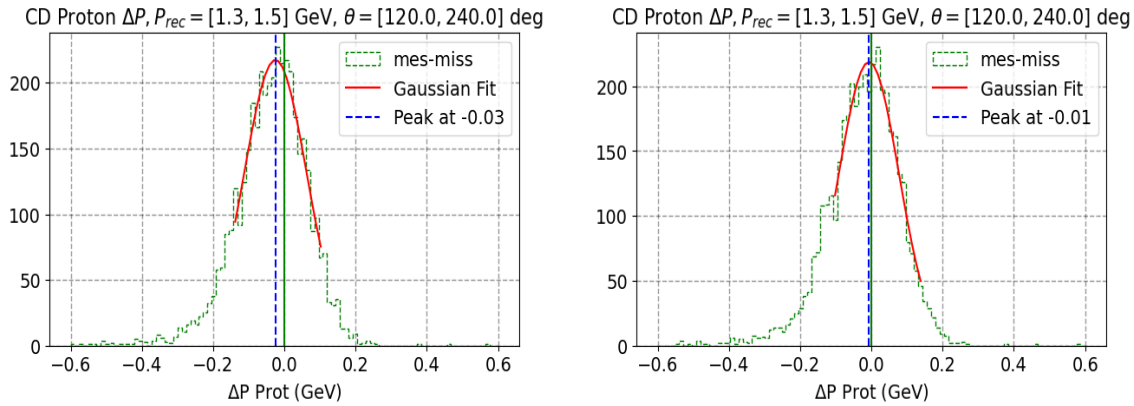

Figure 3.26 Typical ΔP distributions for CD protons with momenta [1.3, 1.5] GeV, $\phi_{rec}[120°,\ 240°]$. The left plot is before corrections, and the right after.

The ΔPs are then fitted with a polynomial function. The values provided by the polynomial fits are scaled by a multiplicative factor. This scaling factor is important because the calculated momentum is based on the four-momentum of the other three particles in this channel. This means that the correction factor depends not only on the particle's momentum but also on the other three particle's momenta as well. This factor is estimated and optimized based on an educated guess, refined with more than 100 trials. For protons, the factor is 1.0, and for pions, the factor is 0.9. Finally, the adjusted values are subtracted from the initial measured momenta to obtain the corrected momenta $P_{corr} = P_{rec} - \alpha_m \cdot \Delta P$, where α_m is the multiplicative factor.

Figure 3.27, shows the distributions of ΔP versus P_{rec} for the protons in the CD. The upper row represents the data before the corrections and the lower row shows the results after the corrections. Each column corresponds to a distinct ϕ_{rec} angle bin. The red dots with error bars are the mean values of the Gaussian fit in each momentum bin. The red line is a second-order polynomial fit (only shown in the top panel), which is scaled by the multiplicative factor and applied for the correction.

Figure 3.28 shows the ΔP versus P_{rec} for protons in FD. In this case, the shift in

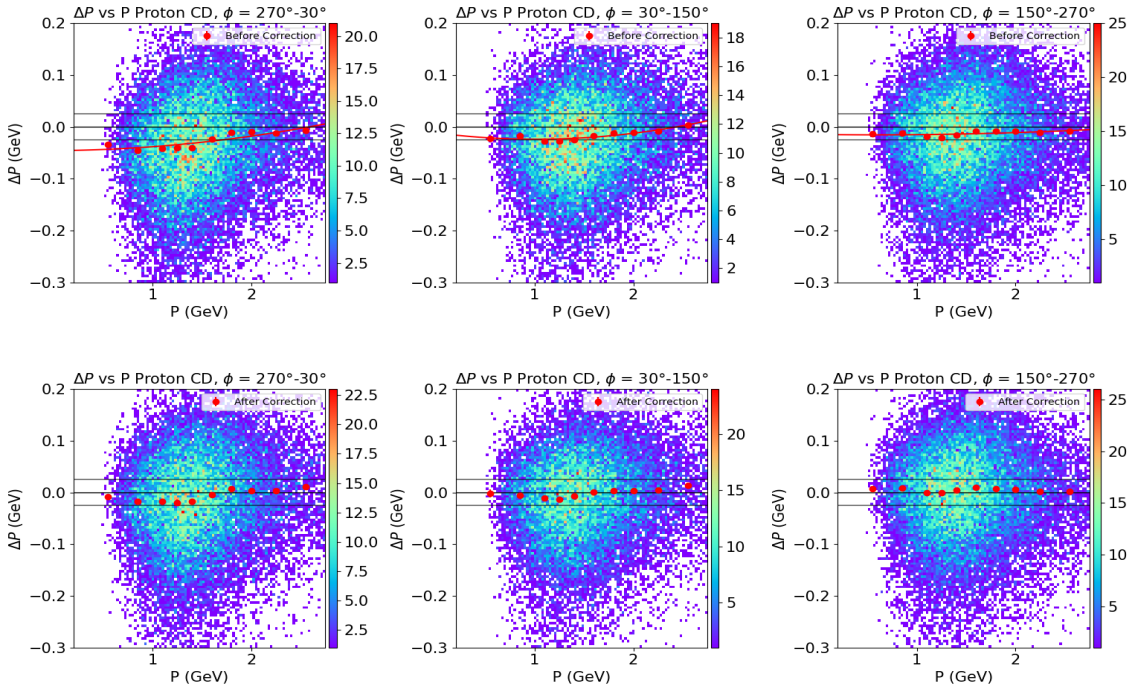

Figure 3.27 ΔP versus P_{rec} for CD protons using experimental data. The first row is before correction and the second row is after correction.

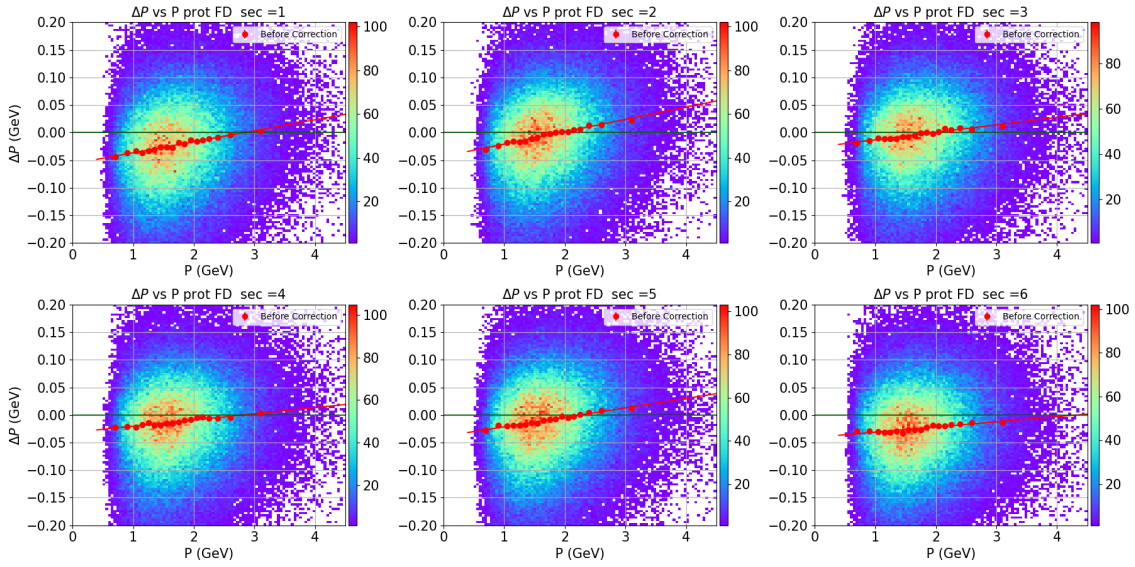

Figure 3.28 ΔP versus P_{rec} for FD protons before corrections.

momentum is mostly negative and can reach up to 50 MeV. The shift ΔP reduced after the correction, see Fig. 3.29.

Figure 3.30 shows the ΔP versus P_{rec} for $\pi^+ s$ in CD. The top row represents the before corrections, while the bottom row shows the after-corrections shifts. Each

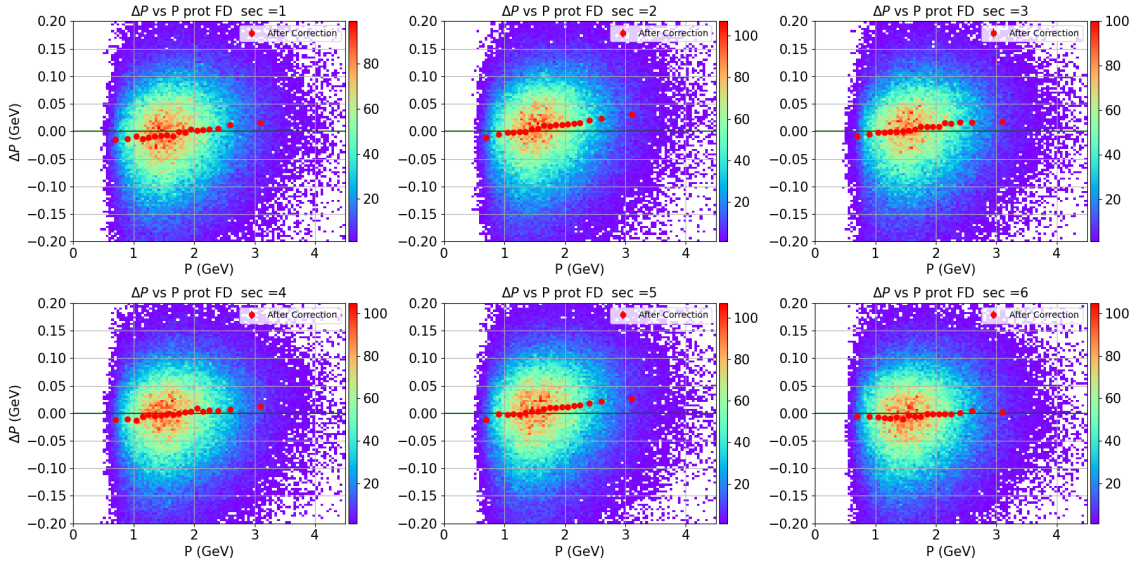

Figure 3.29 ΔP versus P_{rec} for FD protons after corrections.

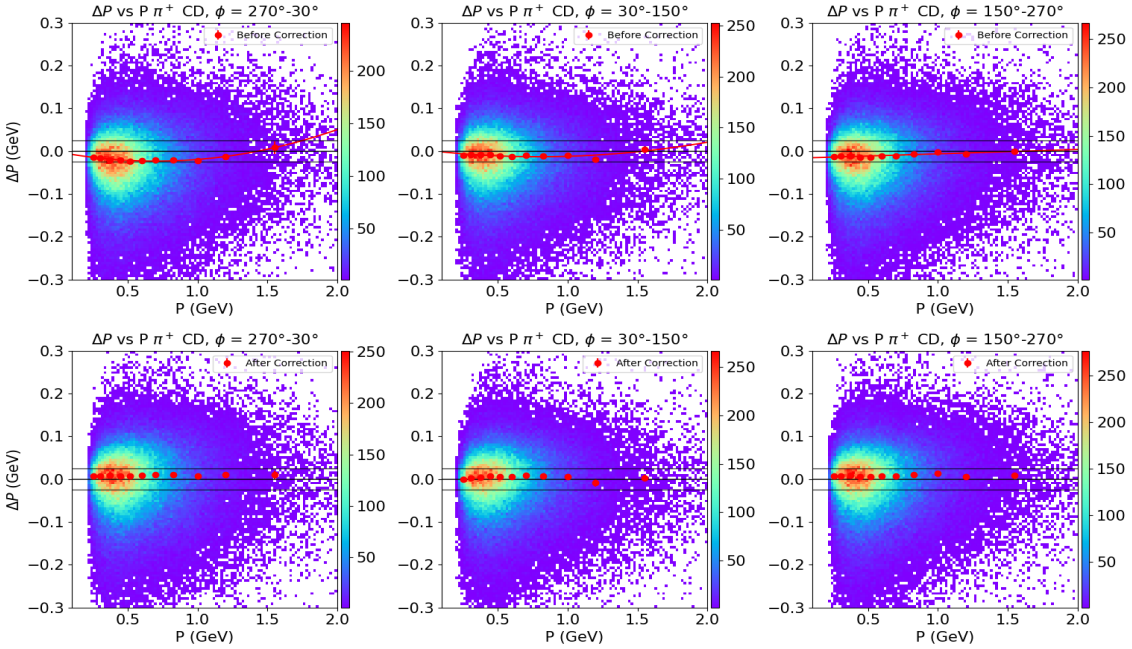

Figure 3.30 ΔP versus P_{rec} for CD π^+'s. The top row is before correction and the bottom row is after correction.

column corresponds to a different ϕ_{rec} bin. The shift in the momentum, (ΔP), is again significantly reduced after the correction has been applied.

Figure 3.31 shows the ΔP versus P_{rec} for π^+s in FD. In this case, the shift in momentum is smaller and can reach up to 25 MeV. The shift becomes even smaller

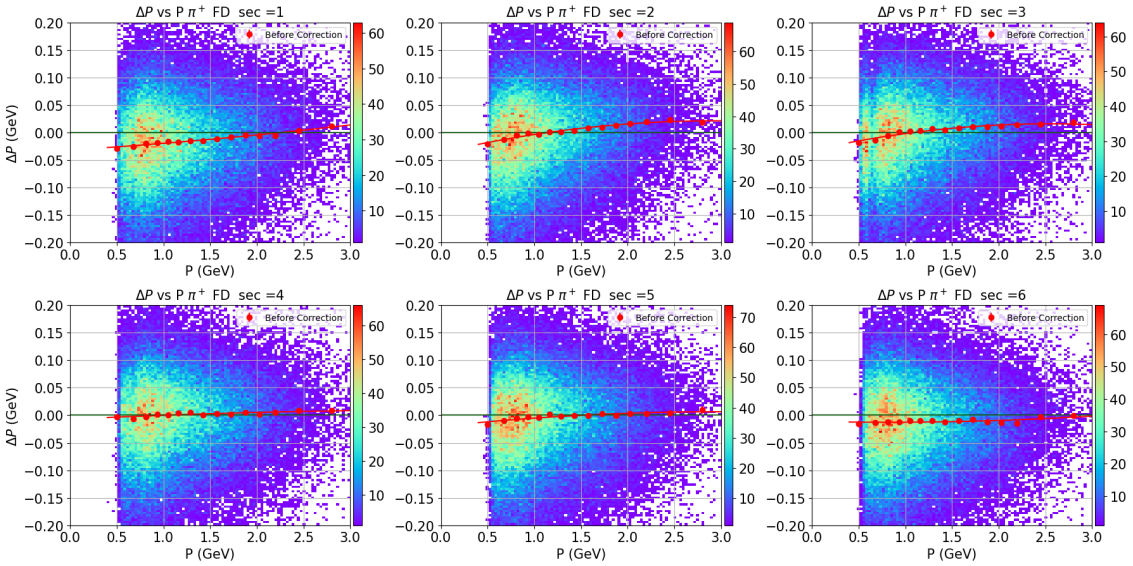

Figure 3.31 ΔP versus P_{rec} for FD π^+'s before corrections.

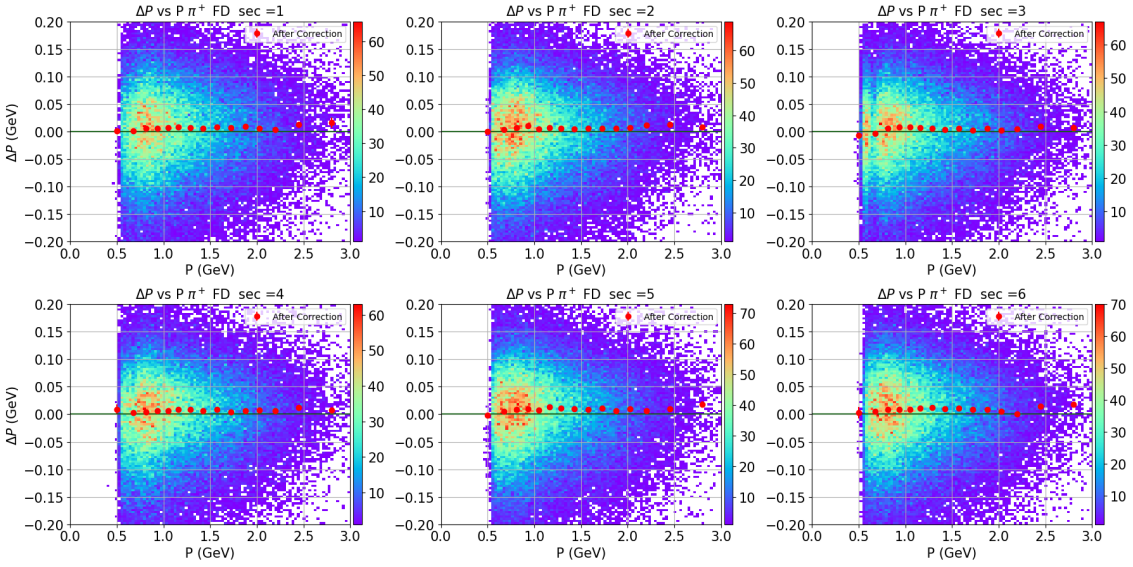

Figure 3.32 ΔP versus P_{rec} for FD π^+'s after corrections.

after correction, as can be seen in Fig. 3.32.

As the values of ΔP depend on the momenta of all three hadrons, it is essential to apply the necessary corrections also to the negative pions. Figure 3.33 presents the distribution of ΔP as a function of the measured momentum, P_{rec}, for $\pi^- s$ detected in the CD. The top panel of the figure displays the data before applying momentum corrections. It can be observed that most of the $\pi^- s$ particles in the CD have small

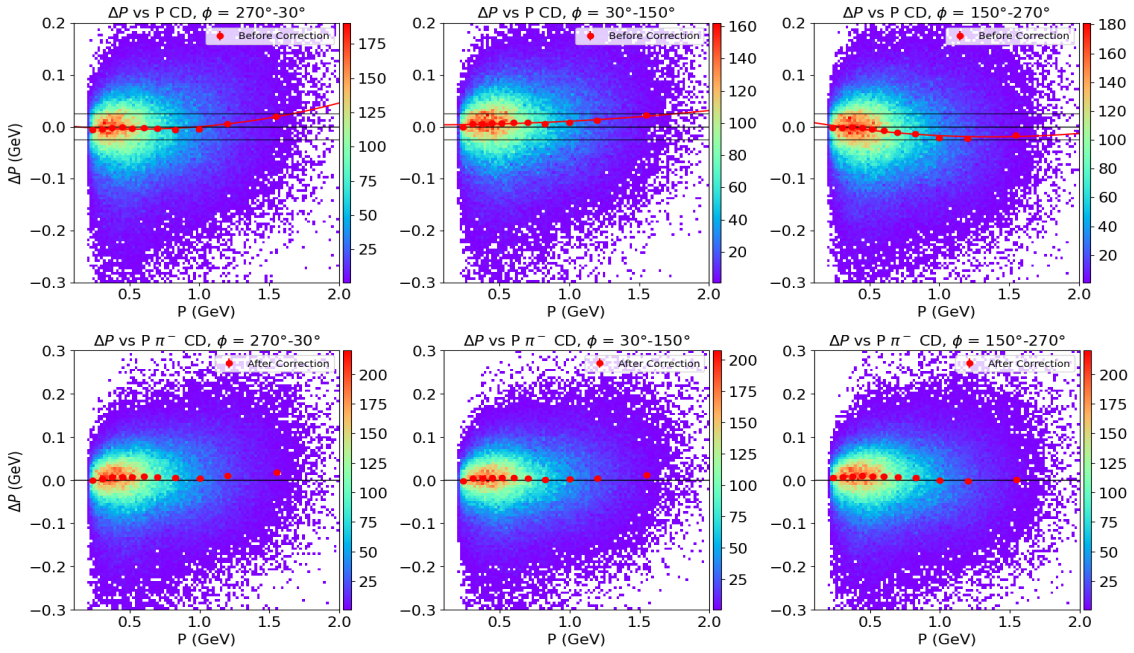

Figure 3.33 ΔP versus P_{rec} for CD $\pi^{-}s$. The top row is before correction and the bottom row is after correction.

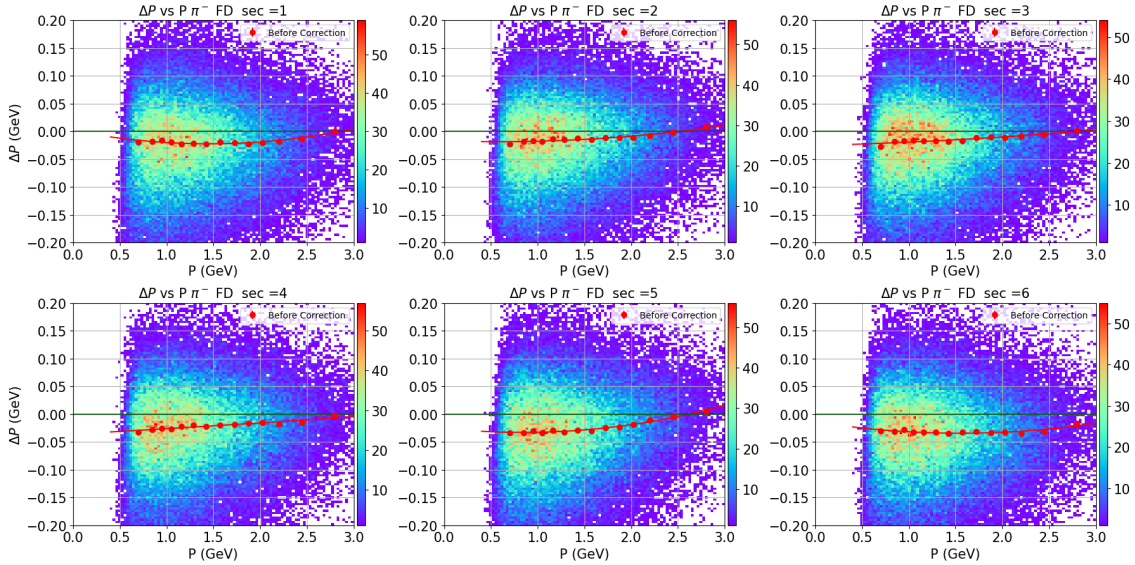

Figure 3.34 ΔP versus P_{rec} for FD π^{-}s, before corrections.

shifts, typically up to 10 MeV. However, for higher momenta, some larger deviations are present, likely due to the limited number of events in that region. The bottom row of Fig. 3.33 shows the distribution after the corrections have been applied. Here, it is evident that the momentum shifts have been reduced, demonstrating the effectiveness

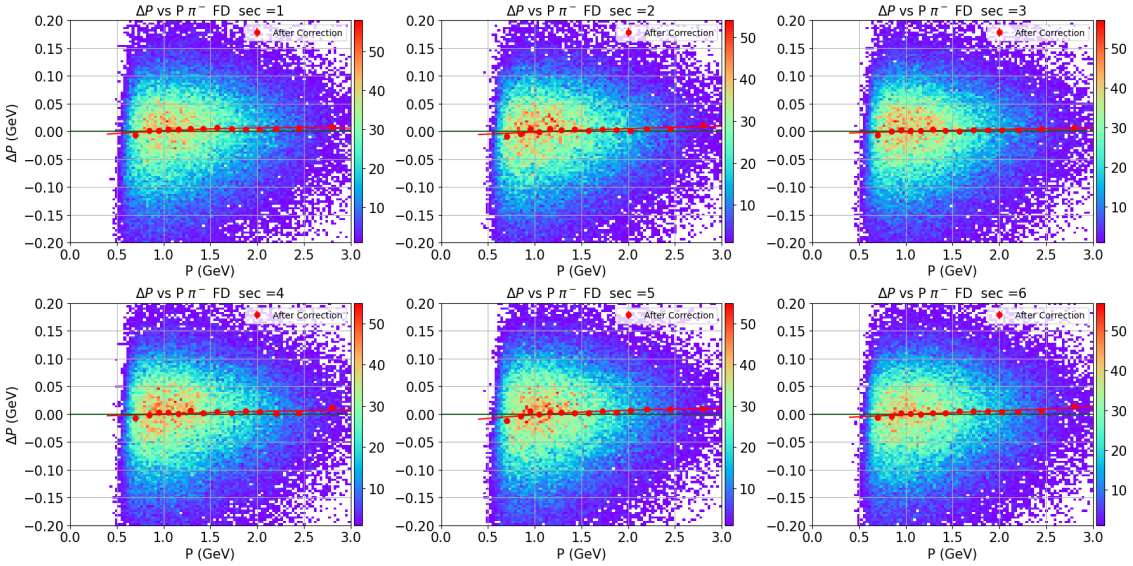

Figure 3.35 ΔP versus P_{rec} for FD π^-s, after corrections.

of the applied corrections.

Similarly, Figure 3.34 shows the ΔP versus P_{rec} distribution for $\pi^- s$ particles detected in the FD. In contrast to the CD case, the momentum shifts in the FD are more pronounced, reaching up to 40 MeV in specific cases such as sector 5. After applying the corrections, the shifts are almost reduced to zero with some exceptions, as shown in Fig. 3.35.

The MMSQ distribution for π^- is checked after applying the momentum corrections for all three final state hadrons using the same exclusive dataset used for the correction development. Figure 3.36 shows π^- MMSQ distributions before and after momentum corrections for all FD and CD hadrons. The figure indicates that MMSQ distributions peaked at the expected square mass of the π^- position, and the momentum corrections do not impact them significantly in both the FD and CD cases. Figure 3.37 shows π^- MMSQ distributions, before and after the correction for the six FD sectors.

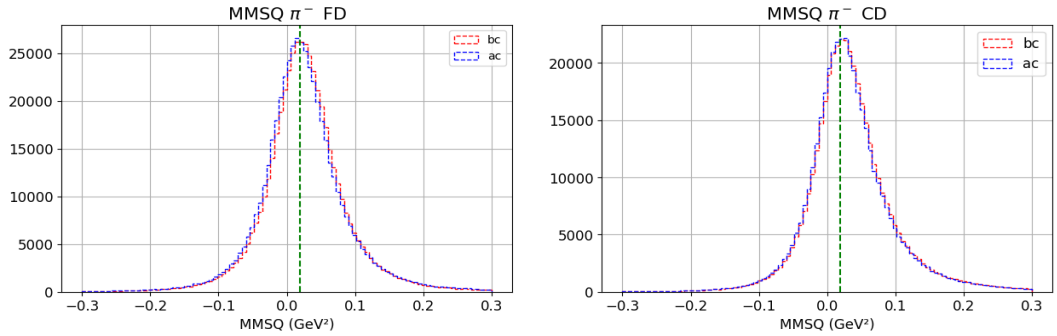

Figure 3.36 MMSQ distributions for π^-s in FD (left) and CD (right) π^-s. Red histograms (labeled 'bc') are before momentum corrections and blue histograms (labeled 'ac') after.

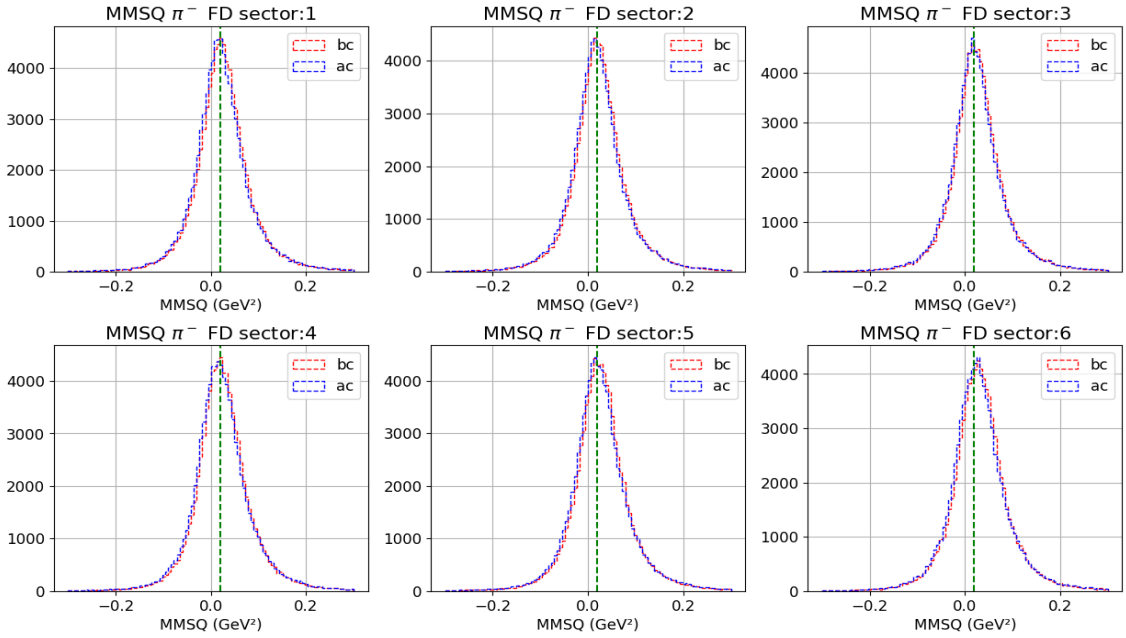

Figure 3.37 MMSQ distributions for π^-s in the six FD sectors. Red histograms are before momentum corrections, and blue after.

3.4 Simulations and smearing

In this analysis, the TWOPEG event generator is used to simulate exclusive charged double-pion electroproduction off the proton under the same conditions and selection criteria as in the experiment. The simulation is carried out through the JLab open science grid portal [34], using the Geant4-based Monte Carlo package (GEMC), which models the CLAS12 detector response, geometric acceptance, and tracking efficiency

in a given experimental configuration [35]. TWOPEG employs a weighted event generation approach to throw events uniformly in the selected kinematic range. The range used for simulation in this analysis is the W range [1.35, 2.15] GeV and the Q^2 range [1.5, 9.0] GeV^2. The cross sections value are assigned as weights to each generated event. These cross sections are derived from the phenomenological JM model, which is fitted to the measured cross sections from the CLAS detector [36]. In kinematic regions where experimental cross sections are unavailable, the weights are estimated through interpolation and extrapolation of the known structure functions [36]. TWOPEG is designed for a wide kinematic range and is suitable for the CLAS12 energy range as well. Events can be generated including radiative effects on the basis of the Mo-Tsai approach.

Ideally, the resolution of the MMSQ peaks of the simulated data should match that of the experimental data. However, simulated data often have better MMSQ peak resolution because CLAS12 simulations have not yet fully replicate the detector imperfections, noise, and other uncertainties present in real experimental conditions, see Fig. 3.38 (left). To ensure optimized yield extractions, efficiency studies, background analyses, and precise cross section extractions, it is necessary to smear the MMSQ distributions to match the resolutions.

The smearing functions, developed by CLAS collaboration [37], are available for the in-bending and out-bending datasets of RGA Fall 2018 to match the MMSQ resolutions of the experimental with the MC data. These functions, given in (3.7), apply to all charged particles. This method smears the momentum p, θ, and ϕ of the reconstructed charged particles, including electrons, protons, and pions.

Since these functions were originally developed for different kinematic ranges and application of these functions makes the resolution of the MC MMSQ distributions about 1.6 times the experimental resolutions, see Fig. 3.40 (top right). For that reason, modifications are needed to use them in this analysis. Modification is carried

out by including the final multiplicative terms AS in (3.7), ensuring that the smearing functions are appropriately adjusted to the kinematic phase space of this analysis.

$$\begin{aligned}
\phi_{\text{new}} &= \phi + \phi_R \cdot \text{gRandom} \rightarrow \text{Gaus}(0,\, 1) \cdot AS, \\
\theta_{\text{new}} &= \theta + \theta_R \cdot \text{gRandom} \rightarrow \text{Gaus}(0,\, 1) \cdot AS, \\
p_{\text{new}} &= p + p_R \cdot \text{gRandom} \rightarrow \text{Gaus}(0,\, 1) \cdot p \cdot AS.
\end{aligned} \tag{3.7}$$

Here, gRandom $\rightarrow$ Gaus(0, 1) represents a random value drawn from a normal distribution with mean 0 and standard deviation 1. The factors ϕ_R, θ_R, and p_R are given by

$$\begin{aligned}
p_{S1} &= 0.018429 - 0.011008 \cdot \theta + 0.0022766 \cdot \theta^2 - 0.00014015 \cdot \theta^3 + 3.07424 \cdot 10^{-6} \cdot \theta^4, \\
p_R &= 0.02 \cdot \sqrt{(p_{S1} \cdot p)^2 + (0.02 \cdot \theta)^2}, \\
\theta_R &= 2.5 \cdot \sqrt{(0.004 \cdot \theta + 0.1)^2 \cdot \frac{p^2 + 0.13957^2}{p^2}}, \\
\phi_{S1} &= 0.85 - 0.015 \cdot \theta, \\
\phi_{S2} &= 0.17 - 0.003 \cdot \theta, \textit{ and} \\
\phi_R &= 3.5 \cdot \sqrt{\left(\phi_{S1} \cdot \frac{\sqrt{p^2 + 0.13957^2}}{p^2}\right)^2 + \phi_{S2}^2}.
\end{aligned} \tag{3.8}$$

Here, p and θ are the reconstructed momentum and the polar angle of the corresponding particle.

The factor AS varies for electrons, protons, and π^+s. For electrons, the factor is chosen to be a constant value of 0.4, based on educated guess after few initial trials, while for protons and π^+s, the factor is momentum dependent and developed separately for FD and CD, because CD particles have lower MMSQ resolutions compared to FD particles. These smearing factors are derived using exclusive $ep \rightarrow e'p'\pi^+\pi^-$ topology data. The procedure begins by applying the smearing factors defined in (3.7) (excluding AS) to the reconstructed electrons, protons, and π^+s particles. Details on how these factors are determined for protons are described in next paragraph.

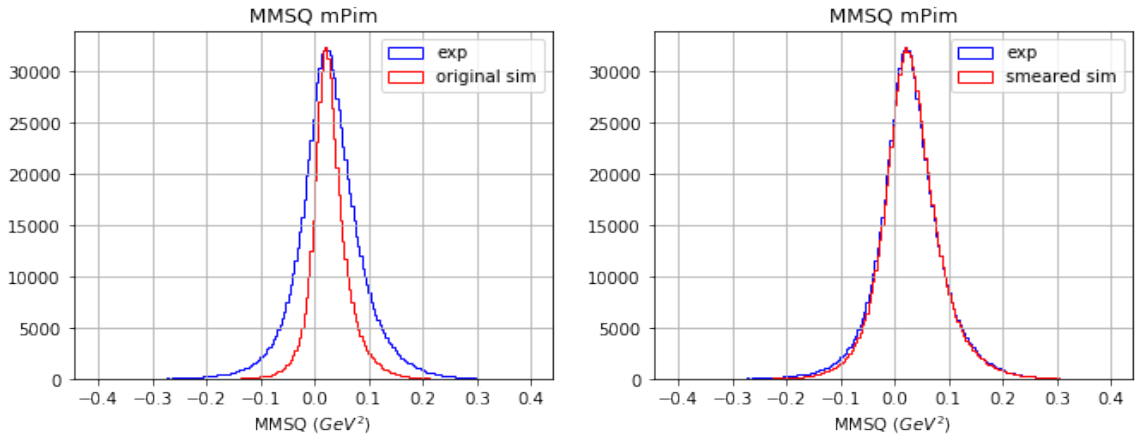

Figure 3.38 MMSQ missing π^- distributions. Blue histograms are for measured data and red histograms are for simulated data, before smearing (left), after smearing (right).

To determine the *AS* factors for the proton momentum, θ and ϕ, the MMSQ distributions of missing π^+ and missing π^- are analyzed separately for FD and CD protons. Data are binned into various momentum ranges depending on the available statistics. As the smearing of protons affects both the missing π^+ and the π^- MMSQ distributions, they are both considered to develop *AS*.

The MMSQ distributions are carefully fitted using the Python lmfit package. In exclusive topology, there are four MMSQ distributions (missing proton, missing π^+, missing π^-, and missing zero). Background shapes are determined based on cuts applied to MMSQ distributions (all three except self) and missing-energy distributions. To model both the background and the signal, the built-in models in the lmfit library are used. The RectangleModel is used for the background, and the peak is fitted using the Skewed-Voigt model. The Voigt model is a convolution of the Cauchy-Lorentz and Gaussian distributions, which form the basis of the Skewed-Voigt model, where the skewness is incorporated via an error function. Details on the error function can be found in [38], while further information on the RectangleModel and other models can be found in the lmfit documentation [39].

In Fig. 3.39, the top left plot represents the MMSQ distribution before smearing,

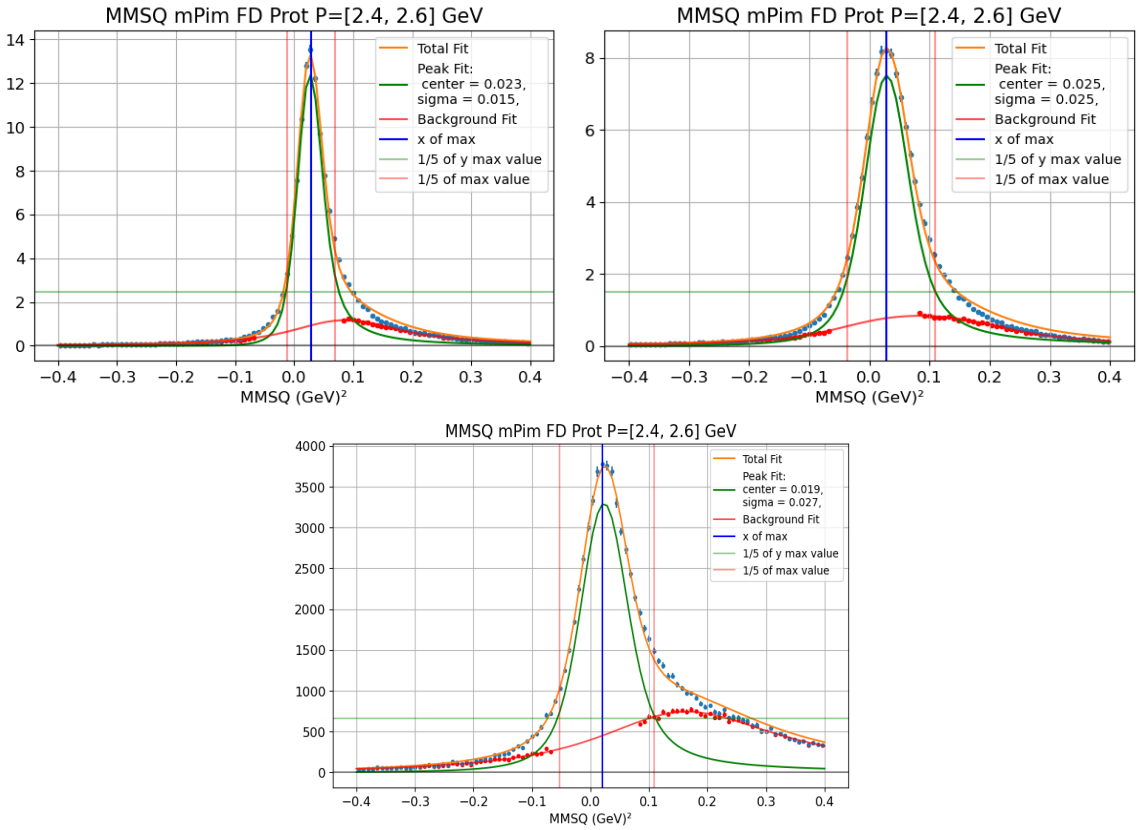

Figure 3.39 Typical π^- MMSQ distributions from simulated data, before smearing (top row left) and after smearing (top row right), measured data (bottom row). In all plots, red dots represent the background data, red curves are the background, green the signal, and orange the total fits. The red vertical lines on either side of the peak maxima mark the locations of 1/5th of the peak height.

while the top right plot shows the distribution after smearing the MC data for a particular momentum bin [2.4, 2.6] GeV of FD protons. The bottom row shows the MMSQ distribution from the experimental data for the same momentum range.

Once the resolutions of the experimental and MC data are determined for each momentum bin, the ratios of their resolutions are calculated. The average of the resolution ratios for missing π^+ and missing π^- distributions is then computed and fitted with a third-order polynomial function, as illustrated in Fig. 3.40.

The corresponding fit function provides the momentum dependence of AS. This procedure is carried out separately for the FD and CD protons, and is repeated to obtain the AS for FD and CD π^+s using the missing proton and missing π^- MMSQ

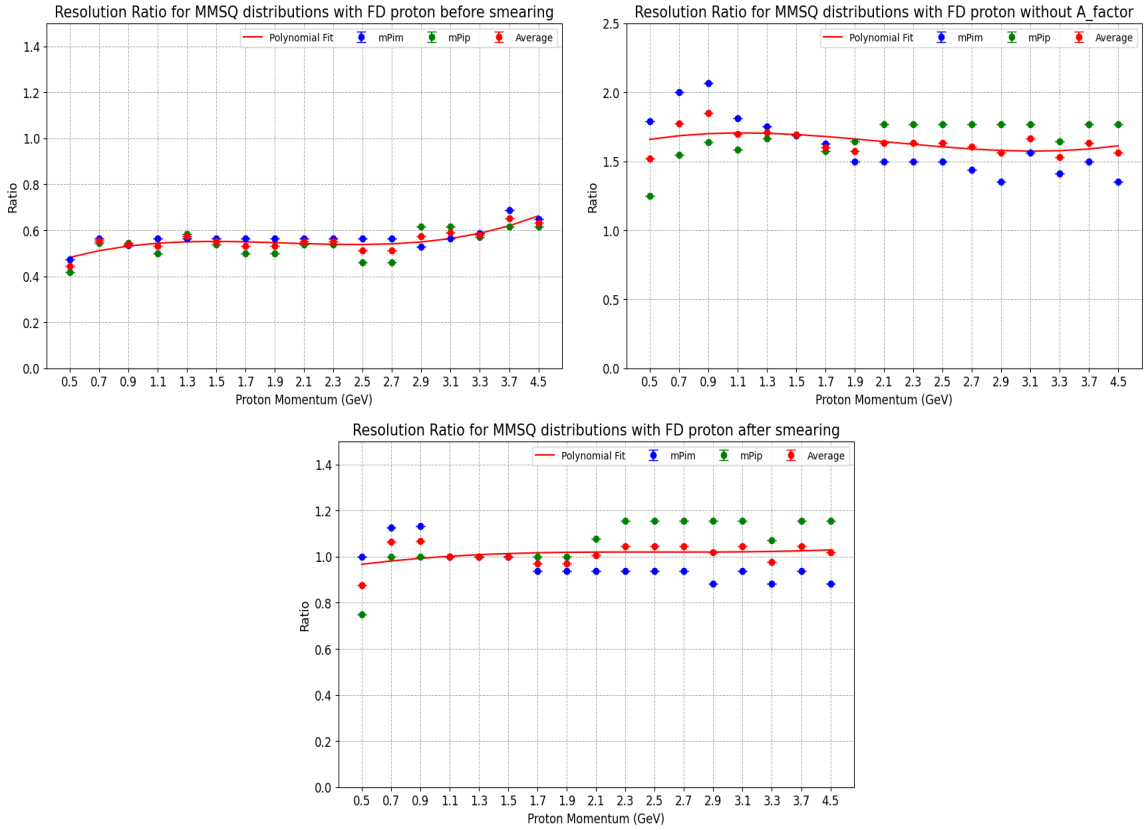

Figure 3.40 Ratio (MC/experimental) of the MMSQ σs distributions for FD protons. Green points represents the ratios for the missing π^+, and blue for the missing π^-, and red points their averages, which are fitted with polynomial function (red line). Before smearing (top row, left), after smearing without including AS (top row, right). The third plot is after the modification including AS (bottom row).

distributions.

Figure 3.40 also shows that the measured resolutions for the missing π^+ and missing π^- MMSQ distributions are approximately two times lower and therefore worse than those of the MC data. With the original smearing functions [37], the MC resolutions become too low. The corresponding σs are about 1.6 times those of the measured data. However, after applying AS, the resolutions match well.

Figure 3.41 shows the simulated π^- MMSQ distributions for all FD proton momentum bins after applying the final smearing factors, and how well the implemented smearing method matches the measured resolution. The lowest and highest momentum bins show some discrepancies because of statistical fluctuations.

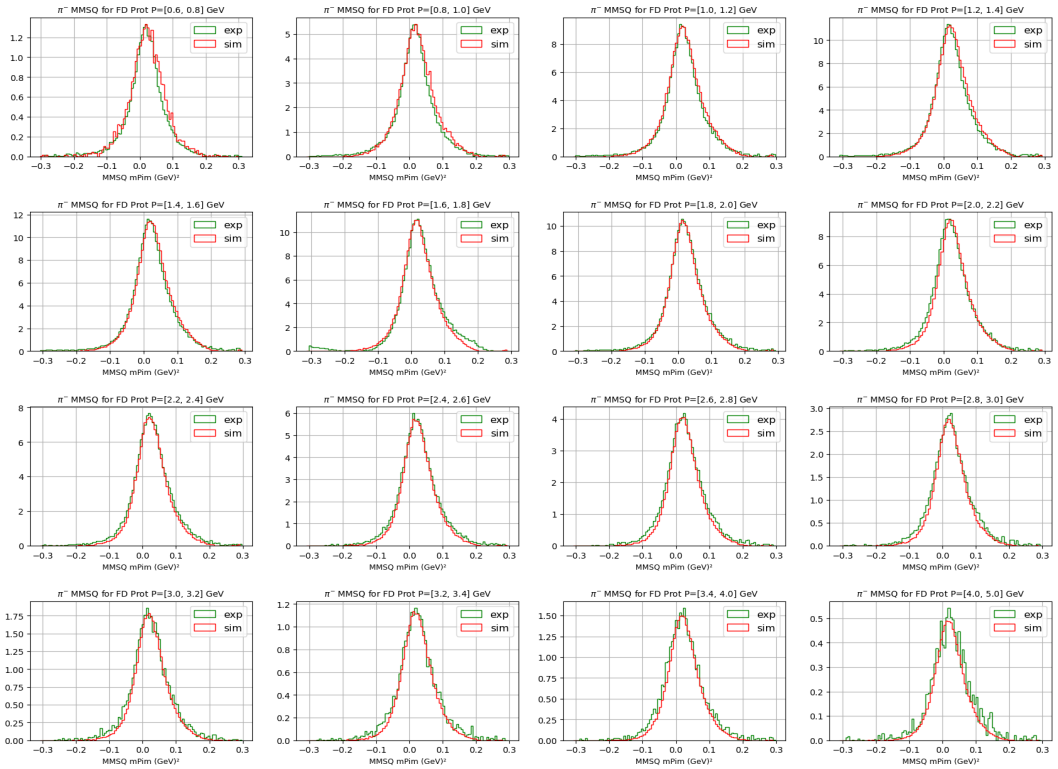

Figure 3.41 π^- MMSQ distributions for all FD proton momentum bins. Green histograms based on normalized experimental data and red on smeared MC data.

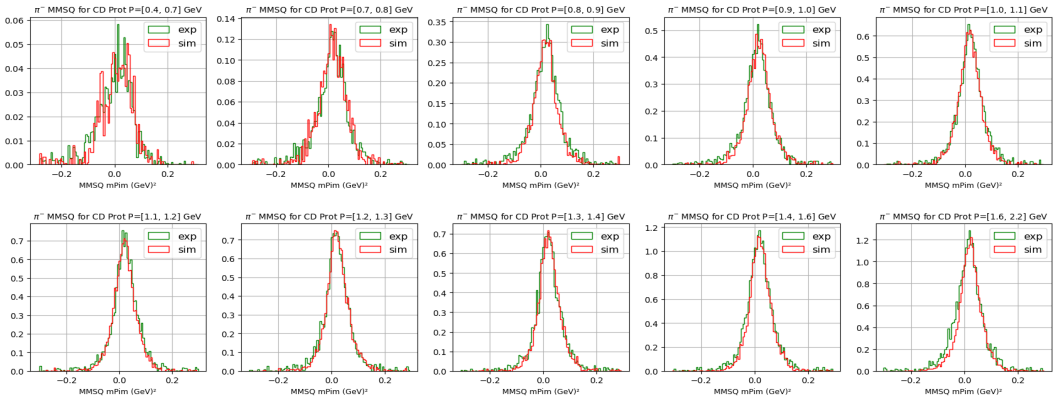

Figure 3.42 MMSQ missing π^- distributions for various CD proton momentum bins. Green histograms are for normalized experimental data and the red histograms are for smeared MC data.

Similarly, Figure 3.42 shows the π^- MMSQ distributions for all CD proton momentum bins after applying final smearing. There is a much smaller amount of protons detected by the CD system, and thus larger statistical fluctuations are seen in the MMSQ distributions. However, their resolutions are in good agreement. Similarly, a

good agreement has been seen for the FD/CD π^+ cases.

3.5 Double-pion event selection

Once the good electrons and hadrons have been identified, the momenta are corrected, and the resolutions are matched both in measurement and simulation, the next step is to choose events associated with the double-pion reaction channel. This is done using the missing-mass square technique. There are four topologies in this reaction channel to select the double-pion events.

1) $e\,(p, p'\pi^+\pi^-)\,e'$ (exclusive topology):

   - all final state particles are detected,
   - event must have an electron, proton, π^+, and π^-.

2) $e\,(p, p'\pi^+)\,e'\pi^-$ (missing π^- topology):

   - four-momentum $\pi^{-\mu}$ reconstructed using the four-momenta of the other particles,
   - event must have electron, proton, and π^+.

3) $e\,(p, p'\pi^-)\,e'\pi^+$ (missing π^+ topology):

   - four-momentum $\pi^{+\mu}$ reconstructed using the four-momenta of the other particles,
   - event must have an electron, proton, and π^-.

4) $e\,(p, \pi^+\pi^-)\,e'p'$ (missing proton topology):

   - four-momentum p'^{μ} reconstructed using the four-momenta of the other particles,
   - event must have an electron, π^+, and π^-.

This analysis uses only missing π^- topology to select the double-pion events using the cuts on the π^- MMSQ distribution. Using energy and momentum conservation, the MMSQ values are calculated as the magnitude square of the missing $\pi^{-\mu}$ four-momentum, which is equal to $\gamma^\mu + p^\mu - p'^\mu - \pi^{+\mu}$ with $\gamma^\mu = e^\mu - e'^\mu$.

The use of the missing π^- topology is advantageous, as it has higher statistics than the other topologies, because in the inbending CLAS12 detector setup, $\pi^- s$ are harder to detect as negatively charged particles bend toward the beamline due to the magnetic field. Consequently, a significant number of these particles pass through the forward hole (a region with no detector coverage near the beamline). This analysis does not exclude detected $\pi^- s$. If the MMSQ distribution of events with detected $\pi^- s$ falls within the defined MMSQ cuts, they are still selected for analysis.

The MMSQ cuts are W-Q^2 dependent. For each W-Q^2 bin, MMSQ distributions are fitted by a combined function of a Gaussian (for signal) and polynomial model of order 1 (for background). Figure 3.43 shows the combined fits for the MMSQ distributions for the W bin [1.70, 1.75] GeV and Q^2 [2.4, 3.0] GeV^2. The plot on the left is for the experimental data, and the plot on the right is for the MC data.

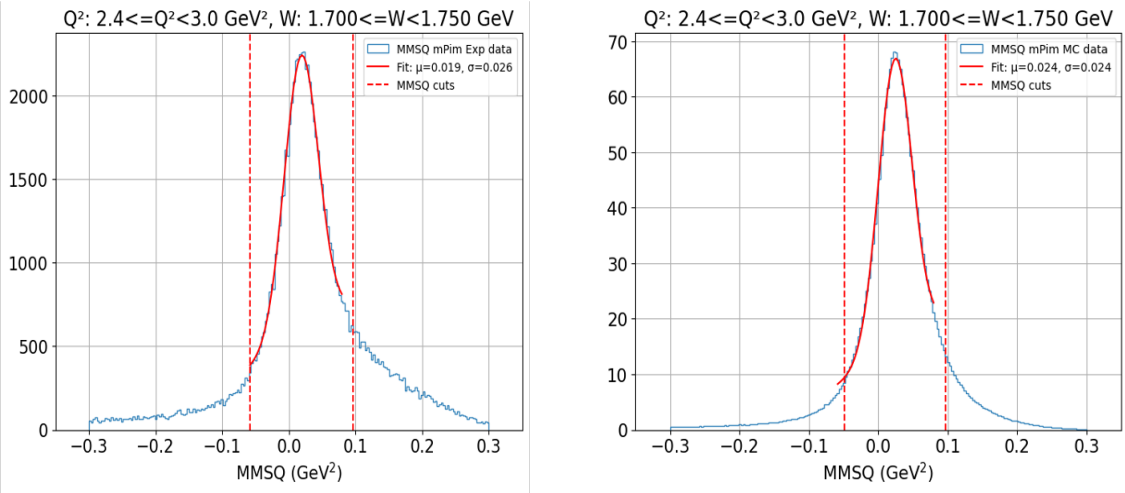

Figure 3.43 MMSQ π^- distributions for W[1.70, 1.75] GeV and Q^2[2.4,3.0] GeV^2, measured at left, and simulation at right.

The fitting procedure is crucial here because the cuts are directly based on the

fits and the selected double-pion events are based on the cuts. Any inconsistency can lead to wrong yields of double-pion events. In Figure 3.43, the data distributions are represented by the blue curve, with red curves overlaying them to represent the total fits. The red curve is the sum of two components, the signal and the background. The cuts, shown as vertical red dashed lines, are at mean $\pm 3\sigma$ of the Gaussian signal fit. After obtaining the MMSQ cut values for each W-Q^2 bin, a second-order polynomial function is fitted for each Q^2 bin as a function of W. The upper and lower MMSQ cuts are fitted separately. Figure 3.44 shows all MMSQ cuts applied for all Q^2 bins.

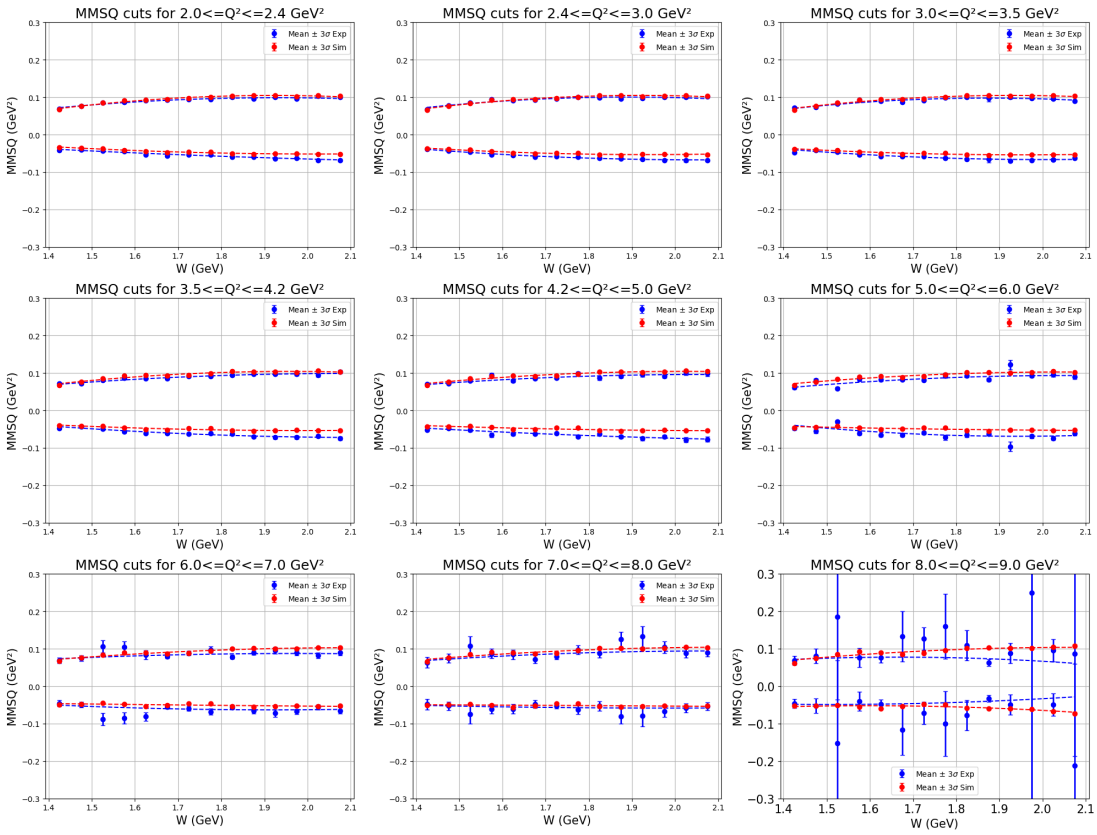

Figure 3.44 MMSQ π^- cuts for all Q^2 bins. W bins vary from 1.4 GeV to 2.1 GeV.

The blue points represent the experimental MMSQ cut values, whereas the blue dashed lines represent the polynomial fit to these points. The red points represent the simulated MMSQ cut values and the red dashed lines show the corresponding polynomial fit. The plots demonstrate that the resolutions of the MMSQ distributions

are similar, with the simulation being smeared to match the experimental resolution. The last Q^2 bin shows huge error bars in the experimental data points, this is due to the insufficient statistics, see Fig. 3.45. For that reason, the Q^2 coverage is limited to 8 GeV^2 in this analysis, excluding the last Q^2 bin [8.0, 9.0] GeV^2.

3.6 Kinematic coverage

The CLAS12 experiment provides wide kinematic coverage in both W and Q^2 for exclusive double-pion electroproduction, allowing access to the full resonance range in W for Q^2 up to 8 GeV^2. The evolution of the resonance contribution with Q^2 in this channel has been studied up to 5.0 GeV^2 using data from the CLAS detector. Thus, the Q^2 range beyond 5 GeV^2 represents a new and unexplored region. The bin sizes W and Q^2 for this analysis have been chosen on the basis of the resolution of the CLAS12 detector and to allow for a direct comparison to previously measured CLAS cross sections. A W bin width of 50 MeV is selected, covering the range from 1.4 GeV to 2.10 GeV, which corresponds to the region where cross sections previously analyzed based on CLAS data are available. The Q^2 bins in the overlapping region with the CLAS analyzes are matched with the work of Dr. Arjun Trivedi [3], to ensure consistency with previous studies. For higher Q^2 values, a bin size of 1.0 GeV^2 is chosen up to 8.0 GeV^2. The experimental data decreases steeply with increasing Q^2, making it difficult to achieve the required statistics with small Q^2 bins. Figure 3.45 shows the chosen W-Q^2 coverage for this analysis.

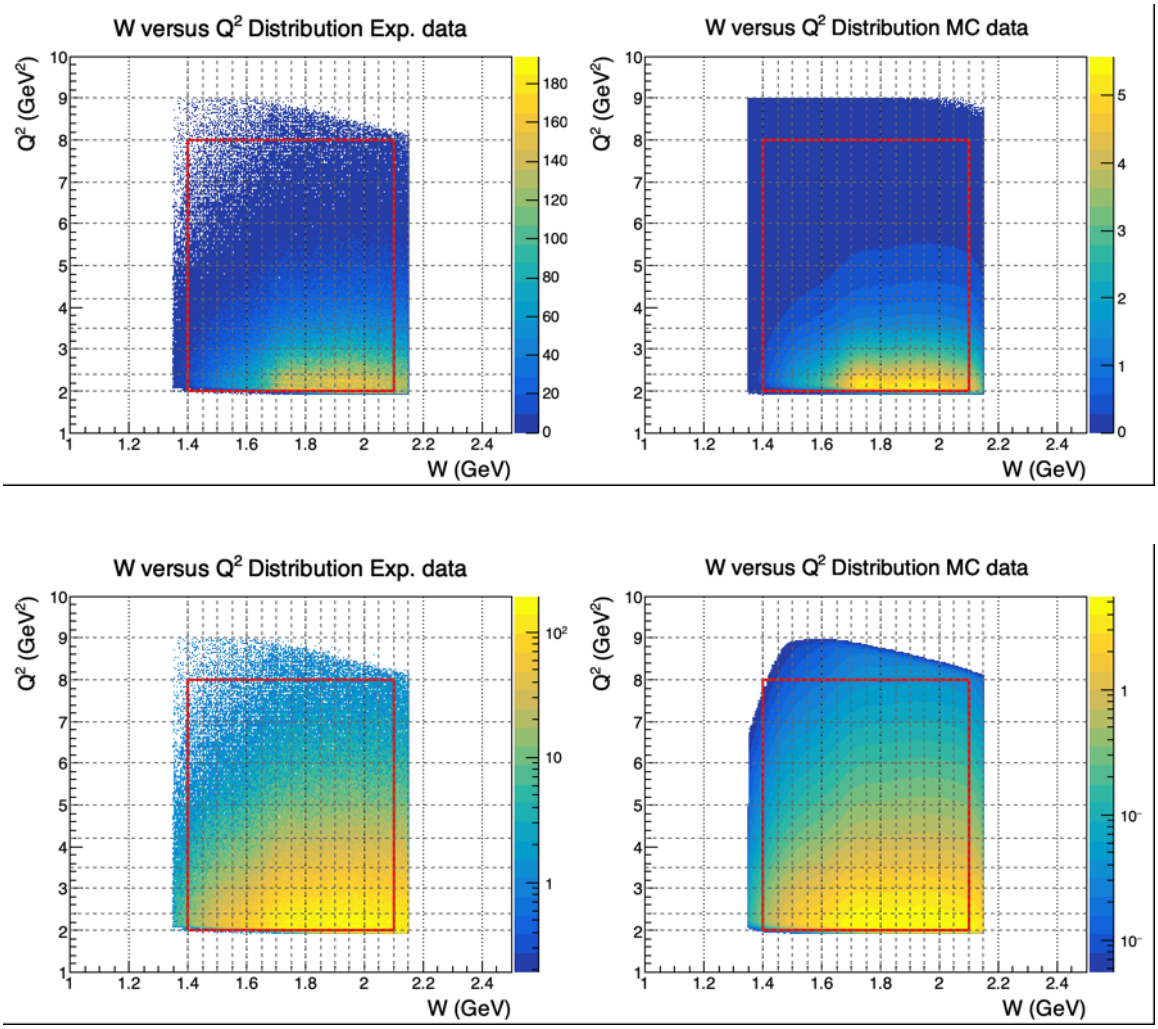

Figure 3.45 Q^2 versus W distribution using experimental data (left column) and simulation data (right column). Top row is normal scale and bottom row is log z scale. The red box represents the selected region for the analysis, and the grid lines represent the bin edges.

Chapter 4

Detector Inefficient Regions

4.1 Inefficient PCAL regions

Some regions of the PCAL detector are partially or completely inefficient, as seen on the left plot of Fig. 4.1. Since these inefficient areas are not fully included in the simulations, it is necessary to apply cuts to exclude these regions in both experimental and simulated data. This ensures that the acceptance is matched in both data sets. For this analysis, the straight-line cuts originally developed in the inclusive analysis

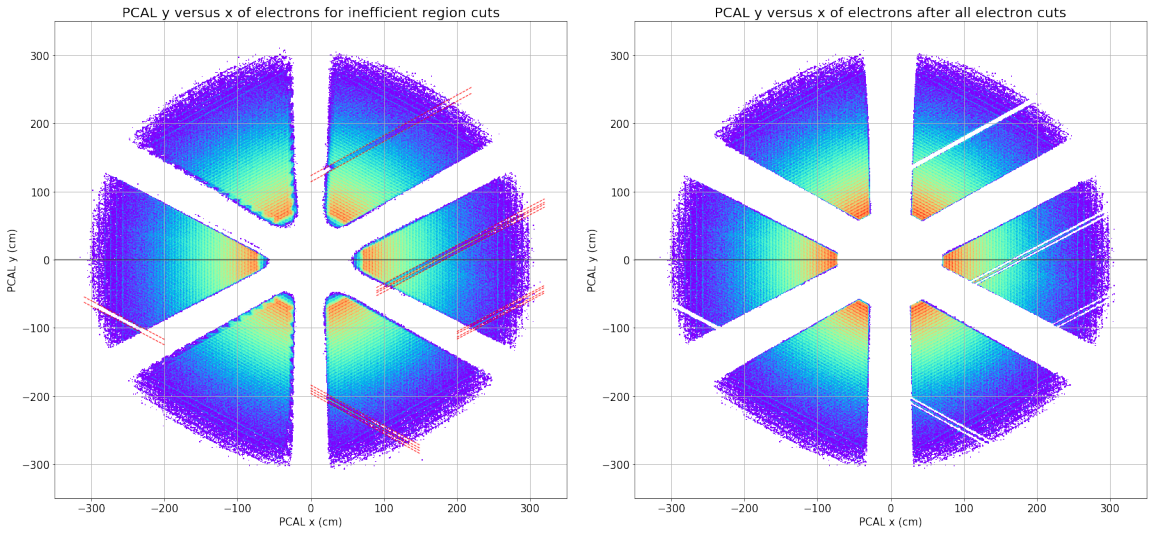

Figure 4.1 PCAL y versus x hit positions of electrons to show the inefficient region cuts for PCAL. Red straight lines represent the applied cuts. The left plot is before the application of these cuts and the right plot is after the application of all electron PID and additional fiducial cuts. These plots are based on the experimental data.

[40] are optimized and applied. These cuts are developed based on the hardware status table of the ECAL calibration constants database (CCDB) [41]. Figure 4.1

(right) shows the electron occupancy of PCAL after applying these inefficiency cuts along with all other electron PID cuts for the measured data.

4.2 Experimental over MC data ratio

Inefficient regions in the detector system can be identified by analyzing the occupancy ratio of the measured to normalized simulated data. This ratio has been investigated for electrons in PCAL as well as for electrons, protons, and $\pi^+ s$ in all three DC regions. Figure 4.2 illustrates the measured and simulated PCAL occupancy, along

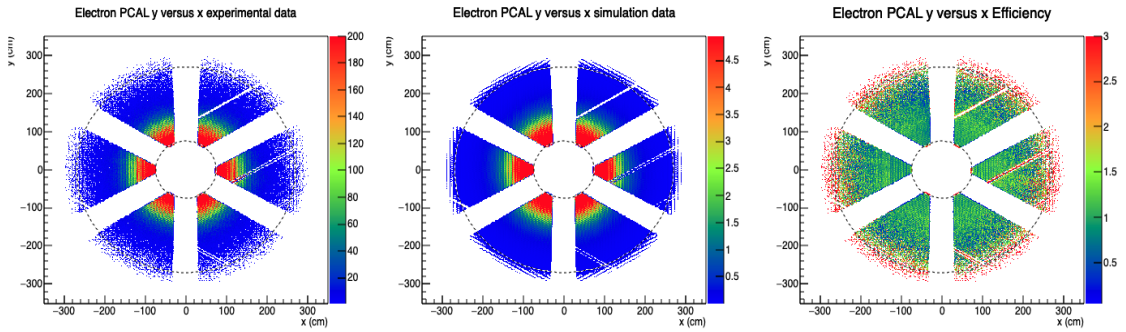

Figure 4.2 PCAL y vs x hit positions of electrons, the left plot is experimental data, the middle plot is MC data and the right plot is the ratio of an experiment to normalized simulation to show the inefficient regions. Black dashed circles, inner and outer, are applied to cut out the inefficient regions.

with the normalized ratio, for electrons in the six PCAL sectors. The ratio is mostly consistent with high experimental occupancy near the inner and outer radial edge regions of the PCAL compared to the normalized simulations. This could be due to the low statistics in that region. However, these inefficient regions are excluded by radial cuts, indicated by black dashed circles. Similarly, the three DC regions also exhibit a consistent ratio along with a high experimental occupancy at the inner and outer edges. To mitigate this, radial cuts are applied in all three regions, see Fig. 4.3, the three rows correspond to the three regions of DC.

For the proton and π^+, the occupancy plots of all three DC regions show various inefficient areas 4.4 and 4.5, especially near the outer edge of the drift chambers. The

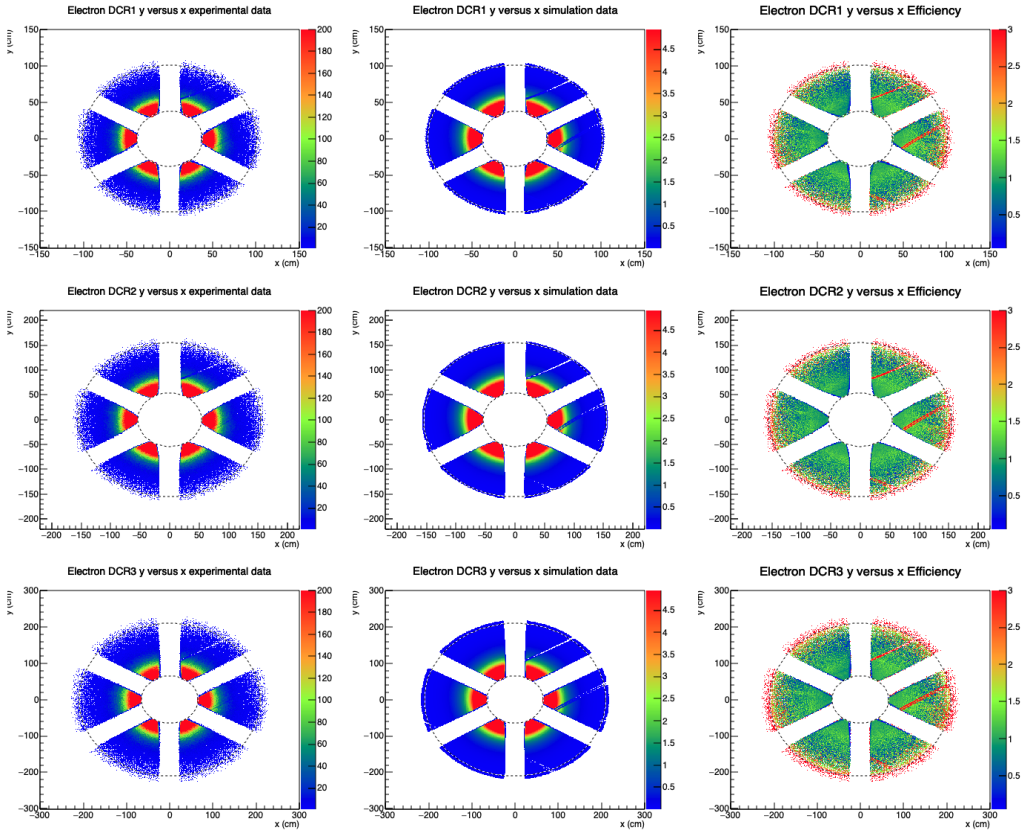

Figure 4.3 DCR1 (first row), DCR2 (second row), and DCR3 (third row) y versus x hit positions of electrons. In each row, the left plot is experimental, the middle MC, and the right the ratio of measured to normalized simulated data, showing the inefficient regions. Black dashed inner and outer circles are used to cut out inefficient regions.

inner and outer circular cuts are applied. In addition, straight-line cuts near edges are applied in DC region three as shown in Figs. 4.6 and 4.7.

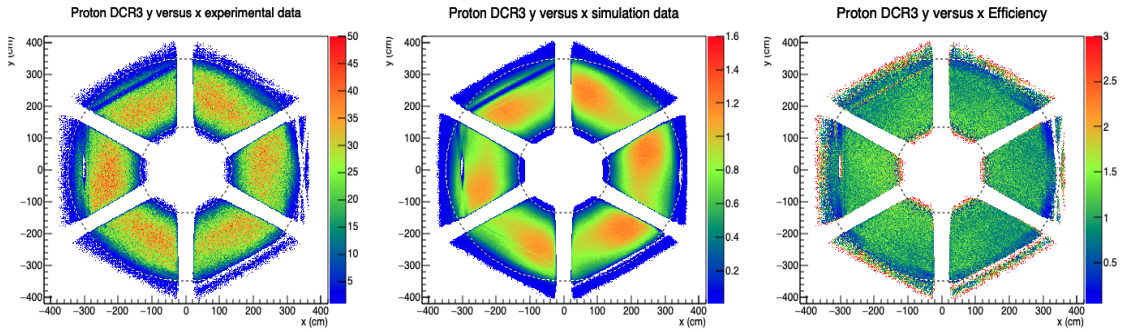

Figure 4.4 DCR3 y versus x hit positions of protons, the left plot is experimental, the middle MC, and the right the ratio of measured to normalized simulated data, showing the inefficient regions. Black dashed inner and outer circles are used to cut out inefficient regions.

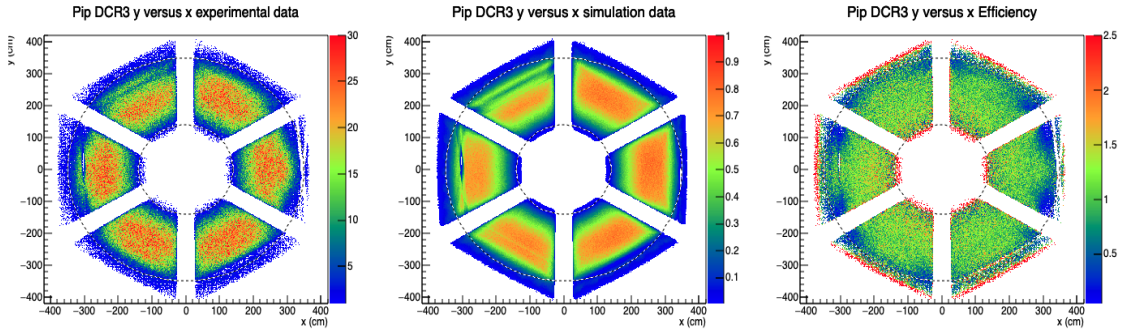

Figure 4.5 DCR3 y versus x hit positions of π^+, the left plot is experimental, the middle MC, and the right the ratio of measured to normalized simulated data, showing the inefficient regions. Black dashed inner and outer circles are used to cut out inefficient regions.

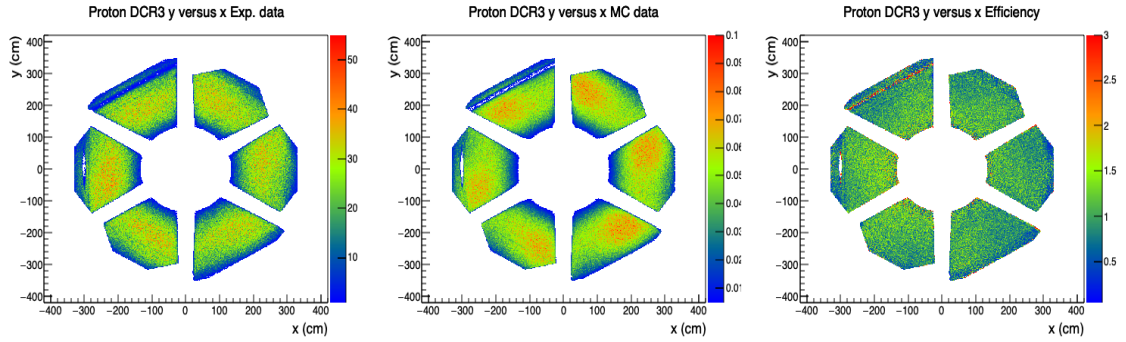

Figure 4.6 DCR3 y versus x hit positions of protons, the left plot is experimental, the middle MC, and the right the ratio of measured to normalized simulated data, after the application of inefficient region cuts.

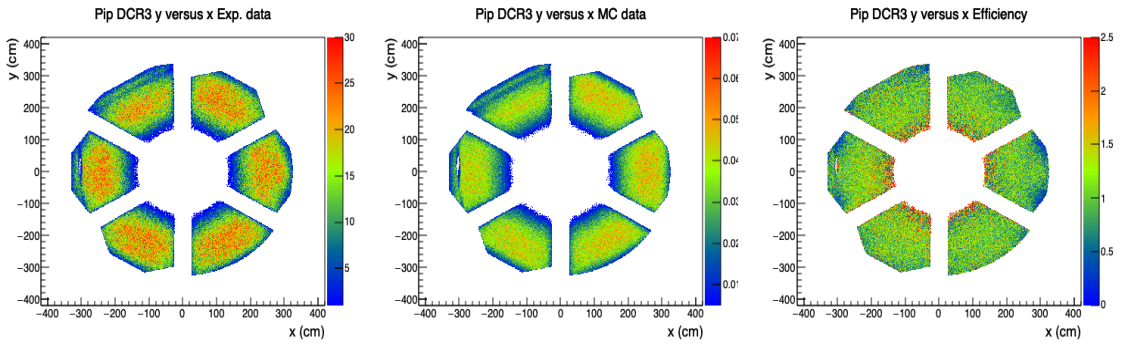

Figure 4.7 DCR3 y versus x hit positions of π^+ the left plot is experimental, the middle MC, and the right the ratio of measured to normalized simulated data after the application of the inefficient region cuts.

Chapter 5

Cross Sections Calculation

5.1 Analysis variables

For the selected double-pion events that pass through the corresponding missing-mass-squared cuts, the next step involves transforming the four-momenta of all particles into the center-of-mass frame system (CMS) of the virtual photon and the initial proton system. In this center-of-mass frame system, the virtual photon and initial proton are moving towards each other with a net momentum of all initial- and final-state particles being zero, making it easier to interpret the analysis using energy and momentum conservation. In the single-photon exchange approximation, the cross sections measured in the CMS system of a virtual photon and an initial proton factorize into a leptonic and a hadronic part [21]. As this analysis used the ROOT data analysis framework, the ROOT functions are used for all needed transformations. The step-by-step transformation process of all four-momenta into the CMS system is described next.

1. The unit vector along the direction of the virtual photon is formed, $uz = gamma$.Vect().Unit().

2. The initial x-axis, perpendicular to the incoming and outgoing electron momenta, is formed, ux =($beam$->Vect().Cross(e'.Vect())).Unit().

3. Now, ux is rotated by $3\pi/2$ around uz to make the intermediate x axis lie in the electron scattering plane, ux.Rotate($3 \times \pi/2$, uz).

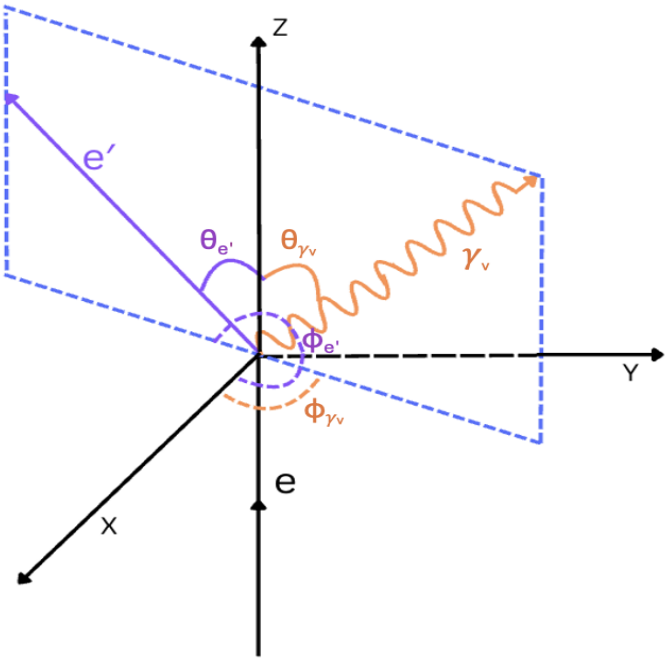

Figure 5.1 Lab frame (LAB) with incoming electron, scattered electron, and virtual photon γ_v with their polar and azimuthal angles. The Z-axis is in the beam direction.

4. The rotation using the 'TRotation' object in ROOT is then defined by,

   rot.SetZAxis(uz, ux).Invert(),

   sets the z-axis to the virtual photon direction.

5. The rotation is applied to the four-vectors of all particles (i.e. γ^{μ}, p'^{μ}, $\pi^{+\mu}$, and $\pi^{-\mu}$).

6. Finally, the boost into the CMS is performed by, particle.Boost(0, 0, -β). where β is defined as,

$$\beta = \frac{\sqrt{E_{\gamma}^2 + Q^2}}{E_{\gamma} + M_P}. \tag{5.1}$$

In the context of the $ep \rightarrow e'p'\pi^+\pi^-$ reaction, along with invariant mass W and four-momentum transfer Q^2, there are five additional independent variables [1] [42]. As it is a final-state system of three bodies (proton, π^+, and π^-), the four momenta of these particles, each having four components, contribute a total of $3\times4 = 12$ variables.

All three final particles are on their mass shell because they are real and exist freely. Thus, the energy can be determined by $E_i^2 = P_i^2 + m_i^2$, based on the magnitude of their three-momenta and rest masses. This holds for all three final particles, which reduces the number of unknowns by three. Additionally, energy and momentum conservation is simplified in CMS. As the initial net momentum of the virtual photon and the initial proton is zero, the net total momentum of all final particles must be equal to zero. This implies that,

$$\begin{aligned} P_x(\mathrm{p}) + P_x(\pi^+) + P_x(\pi^-) &= 0 \\ P_y(\mathrm{p}) + P_y(\pi^+) + P_y(\pi^-) &= 0 \\ P_z(\mathrm{p}) + P_z(\pi^+) + P_z(\pi^-) &= 0 \\ E(\mathrm{p}) + E(\pi^+) + E(\pi^-) &= W \end{aligned} \tag{5.2}$$

This reduces the number of independent variables by 4, which leaves only 5 independent variables. Thus, along with W and Q^2, the cross sections become seven-differentials. Those cross sections can be obtained in three sets of independent hadronic variables [15] depending on various choices for the first (h_1), second (h_2), and third (h_3) final hadrons. In general, invariant masses of the first pair of hadrons, $M_{h_1h_2}$, second pair of the hadrons, $M_{h_2h_3}$, and the angles of the first hadron are included in each set of hadronic variables, as described below.

1) Invariant mass of the $p'\pi^+$ pair $M_{p'\pi^+}$, invariant mass of the $\pi^+\pi^-$ pair $M_{\pi^+\pi^-}$, spherical angles of the proton $\theta_{p'}$ and $\varphi_{p'}$, and angle between the plane defined by the momenta of all final hadrons and the plane defined by the initial and final protons, $\alpha_{p'}$.

2) Invariant mass of the $\pi^-\pi^+$ pair $M_{\pi^-\pi^+}$, invariant mass of the π^+p' pair $M_{\pi^+p'}$, π^- spherical angles θ_{π^-}, and φ_{π^-}, and angle between the plane defined by the momenta of all final hadrons and the plane defined by the initial proton and π^-, α_{π^-}.

3) Invariant mass of the $\pi^+\pi^-$ pair $M_{\pi^+\pi^-}$, invariant mass of the $\pi^- p'$ pair $M_{\pi^- p'}$, π^+ spherical angles θ_{π^+} and φ_{π^+}, and angle between the plane defined by the momenta of all final hadrons and the plane defined by initial proton and π^+, α_{π^+}.

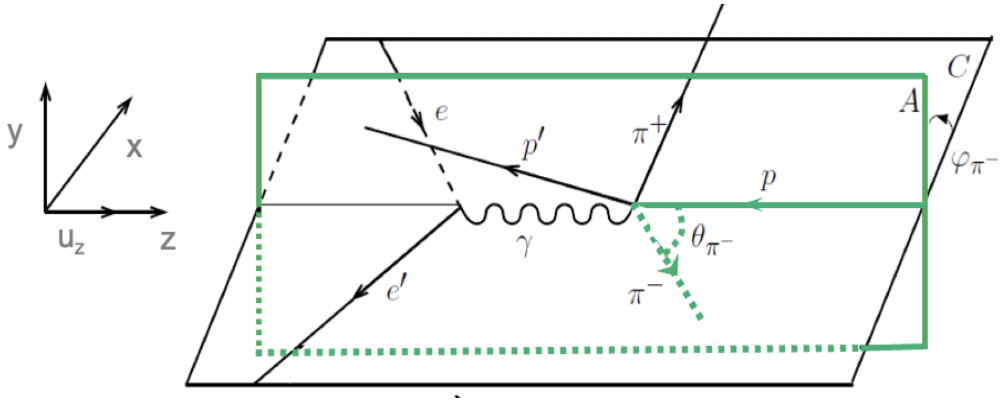

Figure 5.2 Polar (θ_{π^-}) and azimuthal (ϕ_{π^-}) angles of π^- in the center of mass frame of initial proton and virtual photon. Figure adapted from [15].

For the second set of variables, see also Figs. 5.2, 5.3, which will be discussed in more detail.

Invariant masses: The invariant masses and are calculated from the four-momenta of the final particles in the CMS as follows,

$$M_{\pi^-\pi^+} = \sqrt{(P^{\mu}_{\pi^-} + P^{\mu}_{\pi^+})^2}, \tag{5.3}$$

$$M_{\pi^+ p'} = \sqrt{(P^{\mu}_{\pi^+} + P^{\mu}_{p'})^2}. \tag{5.4}$$

In ROOT, the TLorentzVector class provides a method called $Mag()$ or $M()$ to compute mass of quantity for any four-vector.

Angle θ_{π^-}: The polar angle θ_{π^-} is the angle between the three-momentum of the virtual photon and the final π^-, see Fig. 5.2,

$$\theta_{\pi^-} = \arccos\left(\frac{\vec{P}_{\pi^-} \cdot \vec{P}\gamma}{|P\pi^-||P\gamma|}\right). \tag{5.5}$$

ROOT has a method called $Theta()$ to compute θ, which is defined as

$$\theta_{\pi^-} = \text{ATan2}\left(\frac{\sqrt{p_{x\pi^-}^2 + p_{y\pi^-}^2}}{p_{z\pi^-}}\right), \tag{5.6}$$

where, $p_{x\pi^-}$, $p_{y\pi^-}$, $p_{z\pi^-}$ are the three components of the π^- momentum vector.

Angle ϕ_{π^-}: The azimuthal angle ϕ_{π^-} is the angle between the electron scattering plane and π^-, see Fig. 5.2, it is defined as,

$$\phi_{\pi^-} = \begin{cases} \arctan\left(\frac{P_{y\pi^-}}{P_{x\pi^-}}\right) & \text{if } P_{x\pi^-} > 0 \text{ and } P_{y\pi^-} > 0 \\ \arctan\left(\frac{P_{y\pi^-}}{P_{x\pi^-}}\right) + 2\pi & \text{if } P_{x\pi^-} > 0 \text{ and } P_{y\pi^-} < 0 \\ \arctan\left(\frac{P_{y\pi^-}}{P_{x\pi^-}}\right) + \pi & \text{if } P_{x\pi^-} < 0 \text{ and } P_{y\pi^-} \neq 0 \\ \frac{\pi}{2} & \text{if } P_{x\pi^-} = 0 \text{ and } P_{y\pi^-} > 0 \\ \frac{3\pi}{2} & \text{if } P_{x\pi^-} = 0 \text{ and } P_{y\pi^-} < 0 \end{cases} \tag{5.7}$$

The ϕ angles are computed using the $Phi()$ method of ROOT, which is defined in the TVector3 class.

Angle α_{π^-}: The angle α_{π^-} is the angle between plane A defined by the three-momenta of π^- and the initial proton and plane B is defined by the three-momenta of all three final hadrons as seen in Fig. 5.3. All three final hadrons are coplanar in CMS, as their total three-momentum has to be equal to zero. $\vec{\beta}$ is the auxiliary unit vector perpendicular to the π^- momentum vector in plane B. $\vec{\gamma}$ is the auxiliary unit vector perpendicular to the π^- momentum vector in plane A. $\vec{\delta}$ is defined by the cross-product, $[\vec{\gamma} \times \vec{\beta}]$. Thus, $\vec{\delta}$ is colinear or anticolinear with the π^- three-momentum vector, see also [15]. If they are colinear then angle α_{π^-} is given by

$$\alpha_{\pi^-} = \cos^{-1}(\vec{\gamma} \cdot \vec{\beta}), \tag{5.8}$$

if not then angle α_{π^-} is given by

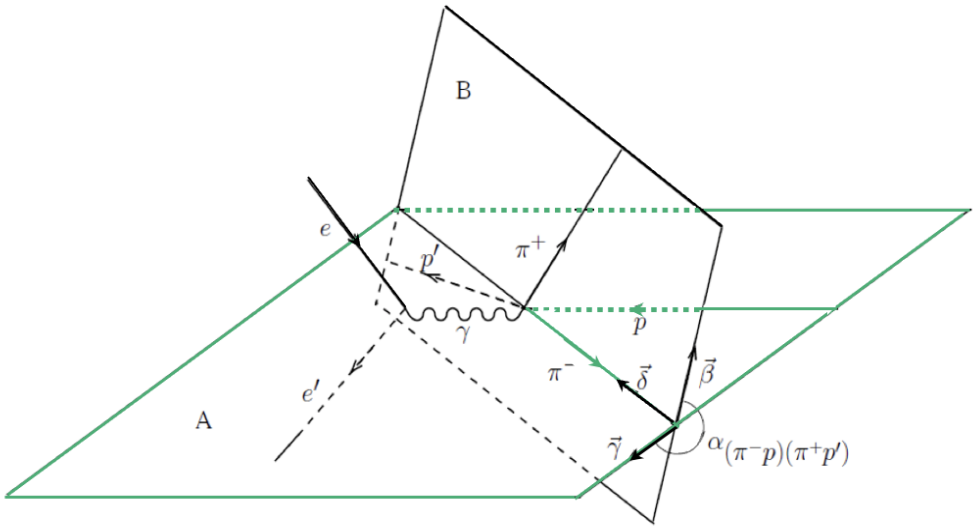

Figure 5.3 Angle α_{π^-} between two planes: plane A defined by the three-momenta of π^- and initial proton and plane B is defined by the three-momenta of all three final hadrons. The definitions of auxiliary vectors β, γ, and δ are given in the text. Figure is adapted from [15].

$$\alpha_{\pi^-} = 2\pi - \cos^{-1}(\vec{\gamma} \cdot \vec{\beta}). \tag{5.9}$$

5.2 Cross section formulae

The expression for the seven-differential electron scattering cross-section specific to the charged double-pion electroproduction reaction channel is given by

$$\frac{d^7\sigma}{dW dQ^2 dM_{h_1h_2} dM_{h_2h_3} d\Omega_{h_1} d\alpha_{h_1}} = \frac{1}{A.E_C.R} \frac{\left(\frac{\Delta N_{\text{full}}}{Q_{\text{full}}} - \frac{\Delta N_{\text{empty}}}{Q_{\text{empty}}}\right)}{\Delta W \Delta Q^2 \Delta^5 \tau L}, \tag{5.10}$$

.

where ΔN_{full} and ΔN_{empty} are the number of good double-pion events selected inside the seven-dimensional bin $\Delta W \Delta Q^2 \Delta^5 \tau$ with the target filled with liquid hydrogen and empty, respectively. Similarly, Q_{full} and Q_{empty} are the total charges collected in the Faraday Cup in full and empty target runs, respectively. For this analysis, those charges are 0.0291 C for all golden full runs and 0.0024 C for empty target runs. A is the acceptance correction factor obtained from the simulations, E_C is the

particle detection efficiency correction factor, and R is the radiative effect correction factor. ΔW, ΔQ^2, and $\Delta^5\tau$, are the bin sizes of the analysis variables out of which ΔW and ΔQ^2 are given by electron scattering kinematics and $\Delta^5\tau$ is the hadronic five-dimensional phase space cell given by

$$\Delta^5\tau = \Delta M_{h_1h_2}\Delta M_{h_2h_3}\Delta(\cos(\theta_{h_1}))\Delta\phi_{h_1}\Delta\alpha_{h_1}. \tag{5.11}$$

L is the luminosity calculated using experimental setup parameters,

$$L = \frac{l\rho N_A}{q_e M_H}, \tag{5.12}$$

where q_{e} is the elementary charge ($1.602 \cdot 10^{-19}$ C), ρ the density of liquid hydrogen (0.0708 g/cm^3), M_H the molar mass of hydrogen (1.0079 g/mole) and N_A ($6.022 \cdot 10^{22}$ mol^{-1}) the Avogadro constant. As mentioned earlier in the discussion of the empty target subtraction procedure, there is cold hydrogen gas present in the target cell during empty target runs. The density of the gas is reported as $\rho_{\mathrm{residual}} = 0.0010$ g/cm^3. Therefore, the correspondingly adjusted $\rho_{adj} = \rho - \rho_{\mathrm{residual}} = 0.0697$ g/cm^3 is used for the final calculations.

In single-photon exchange approximation, the 5-D hadronic cross-section is related to the 7-D electron scattering cross-section by

$$\frac{d^5\sigma}{dM_{h_1h_2}dM_{h_2h_3}d\Omega_{h_1}d\alpha_{h_1}} = \frac{1}{\Gamma_\upsilon}\frac{d^7\sigma}{dWdQ^2dM_{h_1h_2}dM_{h_2h_3}d\Omega_{h_1}d\alpha_{h_1}}, \tag{5.13}$$

where virtual photon flux,

$$\Gamma_v = \frac{\alpha}{4\pi}\frac{1}{E_{beam}^2 M_p^2}\frac{W(W^2 - M_p^2)}{(1-\varepsilon)Q^2}, \tag{5.14}$$

with α is the fine structure constant (1/137), M_{p} is the proton mass, and ε is the polarization of the virtual photon, which itself given by

$$\varepsilon = \left(1 + 2\left(1 + \frac{\omega^2}{Q^2}\right)\tan^2\left(\frac{\theta_{e'}}{2}\right)\right)^{-1}, \tag{5.15}$$

where $\theta_{e'}$ is the angle of scattering electron in the lab frame and ω is the difference between the energy of the initial beam and the final scattered electron.

In the context of this double-pion electroproduction channel, it becomes especially crucial to have enough measured and simulated data. Even for W-Q^2 bins with exceptionally high statistics, achieving a five-dimensional (5-D) hadronic cross section with reasonable accuracy is extremely challenging [43]. As a result, single-differential cross sections are extracted within a specific W-Q^2 bin. This is accomplished by integrating the five-differential cross section over four hadronic variables. Equation (5.16) gives an example of a single-differential cross section, here for the invariant mass of the first pair of hadron,

$$\frac{d\sigma}{dM_{h_1h_2}} = \int \frac{d^5\sigma}{d^5\tau} dM_{h_2h_3} d\Omega_{h_1} d\alpha_{h_1} \tag{5.16}$$

Similarly, other single-differential cross sections can be extracted by integrating the remaining four hadronic variables. From the three sets of hadronic variables, the nine individual single-differential cross sections are extracted. These nine single-differential cross sections are used by the JM model [24] to extract the reaction amplitudes. The nine single-differential yields extracted from the experimental data are shown in Fig. 5.4. Here, the peaks in the invariant-mass distributions help to identify intermediate resonances. For example, the invariant mass $M_{p\pi^+}$ distribution shows a characteristic peak corresponding to the Δ^{++} resonance, which dominates these intermediate resonance contributions in the shown energy range. The contributions of s- and t-channel reaction amplitudes on the other side have very distinct θ dependencies. Finally, the α angle distributions are sensitive to polarization-dependent observables, particularly in the decay Δ^{++} to $p\pi^+$. Generally, the α angle distributions have to be left-right symmetric with respect to 180°. After all normalizations and corrections, these yields will turn into the nine single-differential cross sections, which are essential for extracting resonance electrocouplings and reaction mechanisms

in double-pion electroproduction.

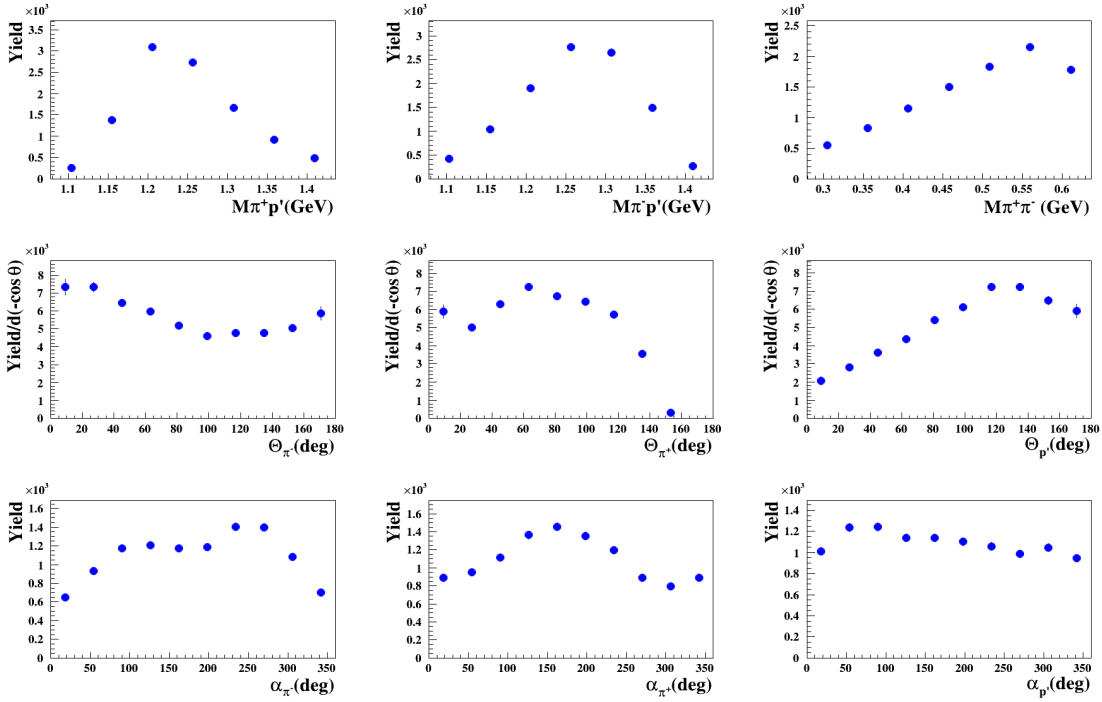

Figure 5.4 Nine single-differential experimental yields in a kinematic region, W[1.55, 1.60] GeV, Q^2[3.5, 4.2] GeV^2. First row corresponds to the three invariant masses $M_{\pi^+p'}$ (left), $M_{\pi^-p'}$ (middle), and $M_{\pi^+\pi^-}$ (right). The second row shows to the three Θ angles Θ_{π^-} (left), Θ_{π^+} (middle), $\Theta_{p'}$ (right). The third row shows to the three α angles α_{π^-} (left), α_{π^+} (middle), $\alpha_{p'}$ (right).

5.3 Beam currents and Faraday cup charge adjustments

Most of the data used in this analysis were collected with a beam current of 45 nA. The remaining data were taken at currents between 50 nA and 55 nA. However, simulations until now have only been performed using only 45 nA background merging files. Simulations with other background merging files are in progress, but are not included in the results of this analysis. A study of the CLAS12 software group found that the electron detection efficiency in the FD decreases by approximately 0.155% per nA [16], see Fig. 5.5. Because the simulations in this analysis are taken using denoised tracking, the red fit line is used to account for the decrease in electron

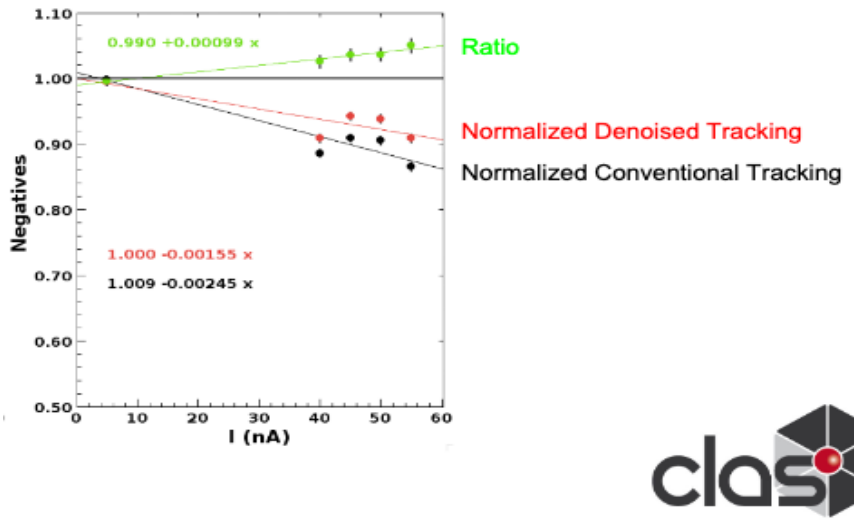

Figure 5.5 Comparison of electron reconstruction efficiencies in the FD as a function of the beam current with fits. Used runs: 5418 (5 nA), 5335 (40 nA), 5197 (45 nA), 5342 (50 nA), 5407 (55 nA). Red dots and fit is for artificial intelligence assisted denoised tracking and black are for conventional tracking. Figure is adapted from [16].

detection efficiency and the corresponding corrections are applied during FC charge calculations. The FC accumulated charge from the QADB software is multiplied by

$$F = 1 - 0.00155 \times (I - 45 \text{ nA}), \tag{5.17}$$

where I being the beam current of each individual run. After simulations are conducted with all types of background merging file in the same proportion as in the experimental data, this correction factor 5.17 will be removed. For the date set used in this analysis, a drop in the ratio of trigger electrons to Faraday cup charge (N/F) was observed for runs 5249 to 5340 and is shown in Fig. 5.6 taken from QADB software page [5]. This is due to an incorrect attenuation factor stored in the CCDB database, where 10.6130 was used instead of 9.8088. This is corrected by multiplying the FC charge accumulated for those runs by the factor (9.8088/10.6130). With these adjustments, the total Faraday cup charge for all full target runs is 0.0291 C.

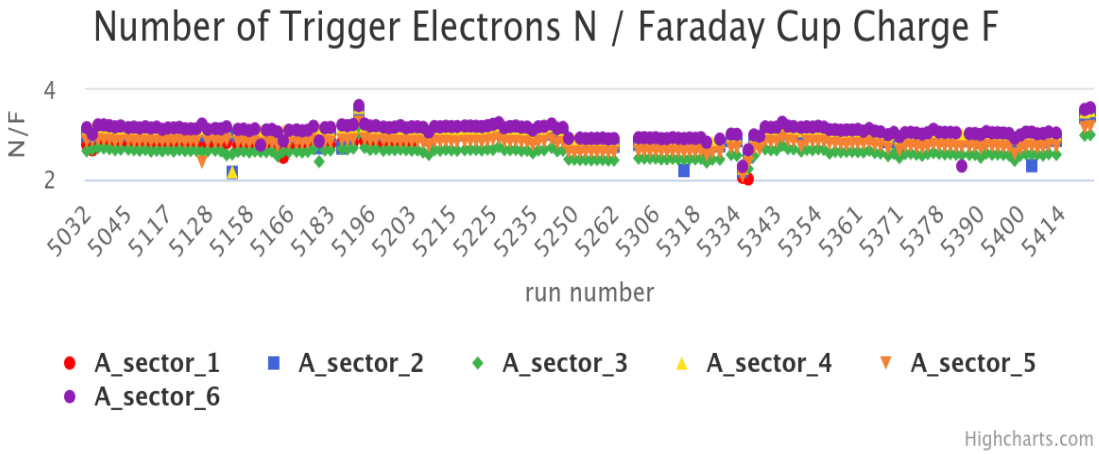

Figure 5.6 Normalized yields for all RGA Fall 2018 inbending runs. Different colors represent different sectors of each run. Figure is adapted from [5].

Chapter 6

Acceptance Correction and Hole Filling

6.1 Acceptance correction factor from MC data

Large-scale experiments such as this often encounter challenges due to various inefficiencies in the detector system. Detecting and reconstructing positive, negative, and neutral particles requires different techniques, each with specific criteria. Given the high luminosity of CLAS12, detecting, recording, and reconstructing all particles in the double-pion channel is a complex process, and not all double-pion reactions that occur during the experiment are recorded by the data acquisition system. Furthermore, the recorded data undergoes refinement through particle identification cuts. Only particles survived after fiducial cuts and other cuts in particle identification were selected. To determine the true double-pion cross sections, it is essential to account for events that were not measured by CLAS12 or excluded by the refinement cuts. This is achieved using a correction factor known as the acceptance correction factor (A), which is incorporated into the cross section formula (5.10). The acceptance factor is calculated through Monte Carlo simulations by comparing events generated by an event generator with those successfully reconstructed by the CLAS12 detector. Simulations are performed using a specific software package called Geant4 Monte Carlo (GEMC), which determines the acceptance of the CLAS12 detector, with knowledge of the detector response, geometric coverage, and tracking efficiency [35]. The acceptance correction ensures that the final results are adjusted for events lost due to inefficiencies in the experimental detector [3].

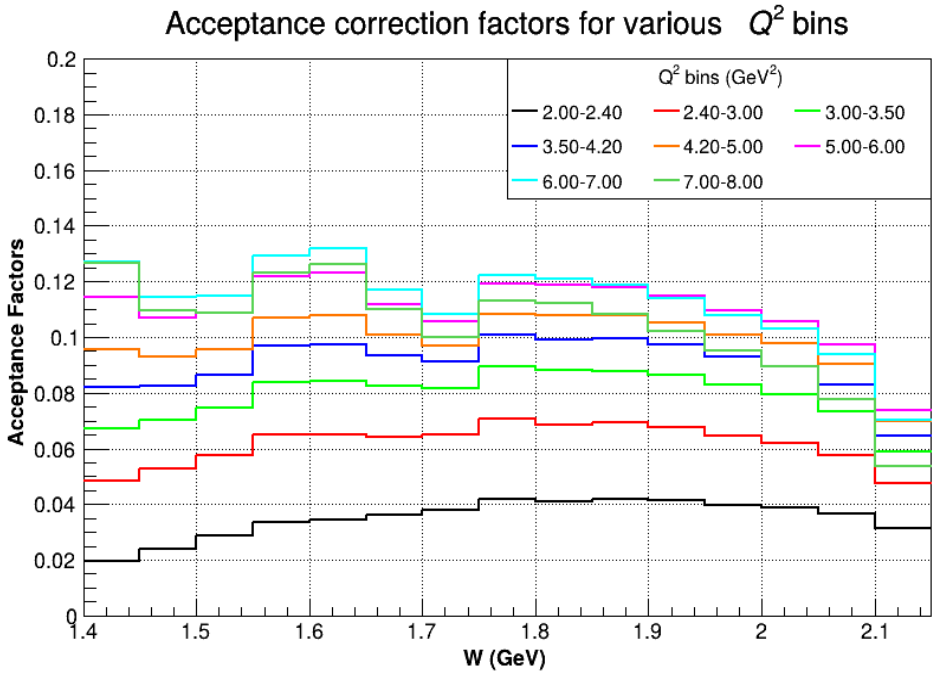

Figure 6.1 Acceptance correction factors for various Q^2 bins in the W[1.4, 2.15] GeV region.

The acceptance factor is defined by (6.1) as follows:

$$A(\Delta W, \Delta Q^2, \Delta^5\tau) = \frac{N_{\text{rec}}}{N_{\text{gen}}}. \tag{6.1}$$

Here, N_{gen} cross section weighted number of double-pion events generated within a given seven-dimensional kinematic bin, while N_{rec} corresponds to the weighted number of double-pion events successfully reconstructed in the same bin, weights are cross sections obtained by TWOPEG at each kinematic phase space point. In an ideal scenario with a perfect detector that captures all double-pion events and flawless reconstruction software, N_{rec} would be equal to N_{gen}, resulting in an acceptance factor A of 1. Acceptance correction also accounts for an effect known as bin migration. Due to measurement uncertainties in the experiment, an event that truly belongs in one bin may be recorded in a neighboring bin. Since the acceptance correction is applied bin by bin, events migrating from one bin to another result in a lower acceptance factor for the affected bin, effectively correcting for bin migration.

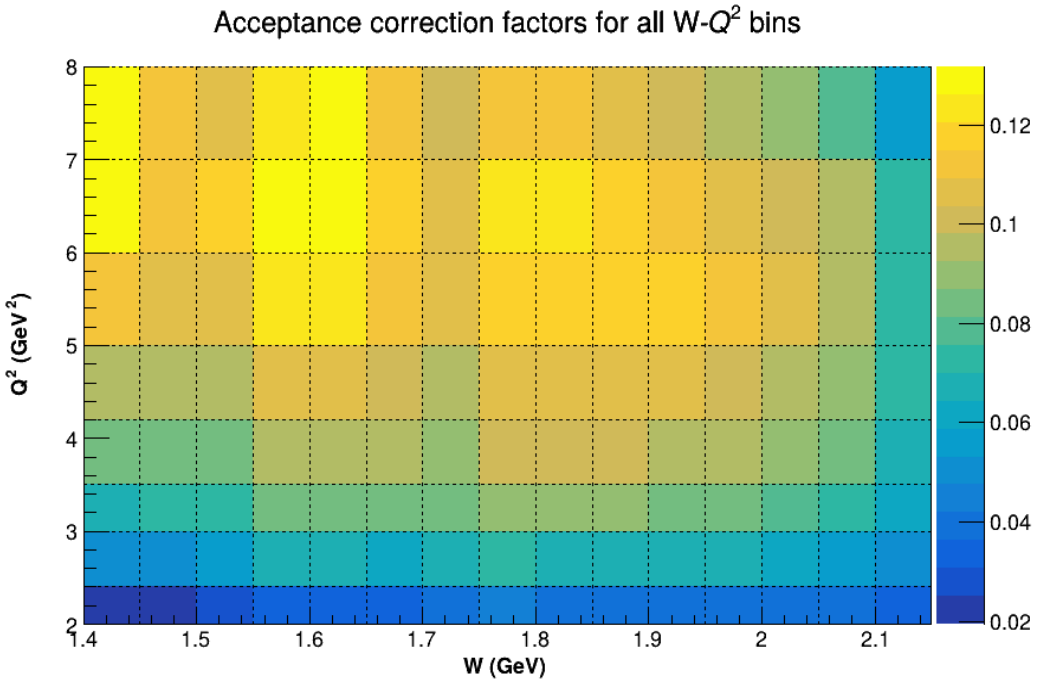

Figure 6.2 Acceptance correction factors in Q^2 versus W dependence.

6.2 Background merging in MC data

The Monte Carlo simulation generates only double-pion events, while nature produces all reactions that occur in the experiment simultaneously. Thus, the simulated and measured data have different background conditions. This discrepancy leads to the differences in the particle reconstruction efficiency in the two datasets. For CLAS12 forward detector systems, this issue has been studied by a CLAS12 task force group [44], which developed background merging files for MC simulations to better match the background in both datasets. These current dependent background files were created from the CLAS12 data collected with a random trigger during the experiment. Figure 6.3, taken from [44] Ch. IV, shows relative yields (ratio of the yields with beam current I nA to 5 nA background merging conditions) of inclusive electrons with various beam currents based on the luminosity scan runs from experimental inclusive electron data (blue squares) and the inclusive electron simulation (green triangles). In [44] it is concluded that there is an overall 3% mismatch between the simulated

reconstruction and the measured yield. Thus, a systematic error of 3% is included in the final result of this analysis. As this only takes care for electron reconstruction efficiency, the hadrons reconstruction efficiency is performed and is presented in Sec. 7.1.

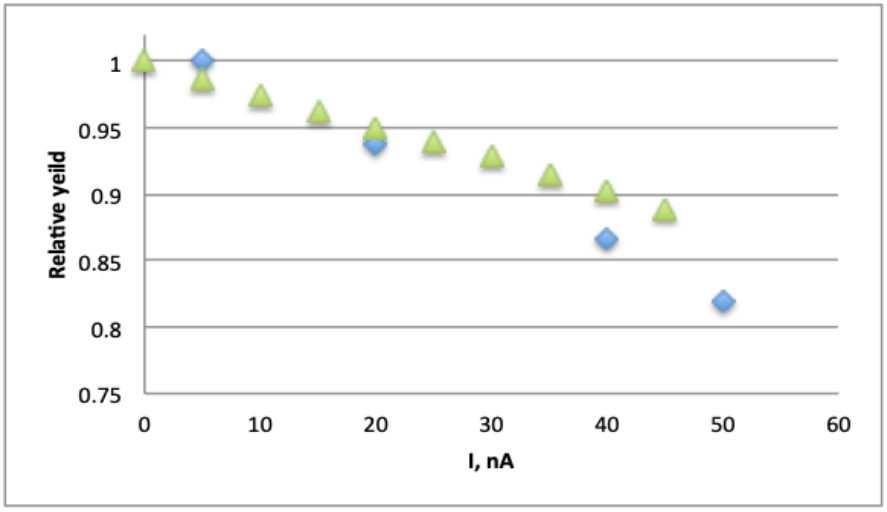

Figure 6.3 Experimental (blue squares) and simulated (green triangles) inclusive electron ($ep \rightarrow e'X$) relative yields versus various beam current. Relative yields stands for the ratio of the yields with beam current I nA background to 5 nA background merging condition.

6.3 Cross section scaling factor

TWOPEG assigns weights to each generated event based on the inter- and extrapolation of available cross section data. At the time TWOPEG was developed, cross sections measured by Dr. Trivedi [1] using CLAS 'E16' data over a wider W-Q^2 range were not yet available. Now that these data are accessible, the Q^2 dependence of the TWOPEG cross sections can be adjusted according to the new measured cross sections. As described in [36] CH.4 (4.4) and (4.5), the original extrapolation to higher Q^2 was obtained by

$$\frac{d^5\sigma}{d^5\tau} = \frac{d^5\sigma}{d^5\tau}\left(0.65\ \mathrm{GeV}^2\right)\frac{F_{\mathrm{approx}}(Q^2)}{F_{\mathrm{approx}}(0.65\ \mathrm{GeV}^2)}, \tag{6.2}$$

where $d^5\sigma/d^5\tau$ is the 5-differential hadronic cross sections and

$$F_{\text{approx}} = \frac{1}{\left(1 + \frac{Q^2}{0.7\ \text{GeV}^2}\right)^2}, \tag{6.3}$$

the Q^2 dependent scaling function.

The ratios of CLAS to TWOPEG cross sections are fitted by

$$F_{\text{new}} = \frac{(F_{\text{approx}}(Q^2))^a}{\left(F_{\text{approx}}(0.65\ \text{GeV}^2)\right)^b}, \tag{6.4}$$

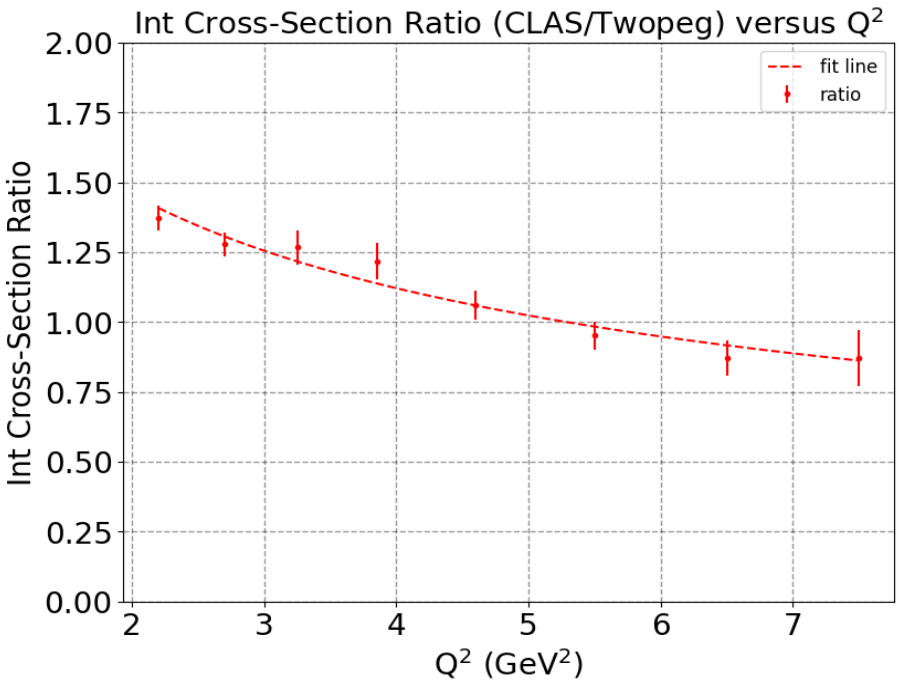

Figure 6.4 Ratio CLAS over TWOPEG integrated cross sections for various Q^2 bins. Red points with error bars are the ratio and the red line is the fit function F_{new}.

where a and b are the parameters determined by the fit shown in Fig. 6.4, Since the CLAS cross sections cover Q^2 values up to 5.0 GeV^2, while this CLAS12 analysis extends up to 8.0 GeV^2, the cross sections newly measured from this analysis are used. However, they are in good agreement with the extrapolation of the CLAS results from the first five Q^2 bins.

Figure 6.5 compares the original TWOPEG, CLAS, and adjusted TWOPEG cross sections for the first six Q^2 bins. This adjustment is particularly important for hole

filling, bin-centering corrections, and radiative effect corrections, all of which are modified using this new scaling function. Figure 6.5 also shows that the scaled cross sections are closer to the measured values; however, discrepancies remain in some bins. To address this, a next iteration bin-by-bin scaling of nine single-differential cross sections is applied across all W-Q^2 bins. This step is especially crucial for bins with larger hole fractions, as these are filled using TWOPEG-generated cross sections.

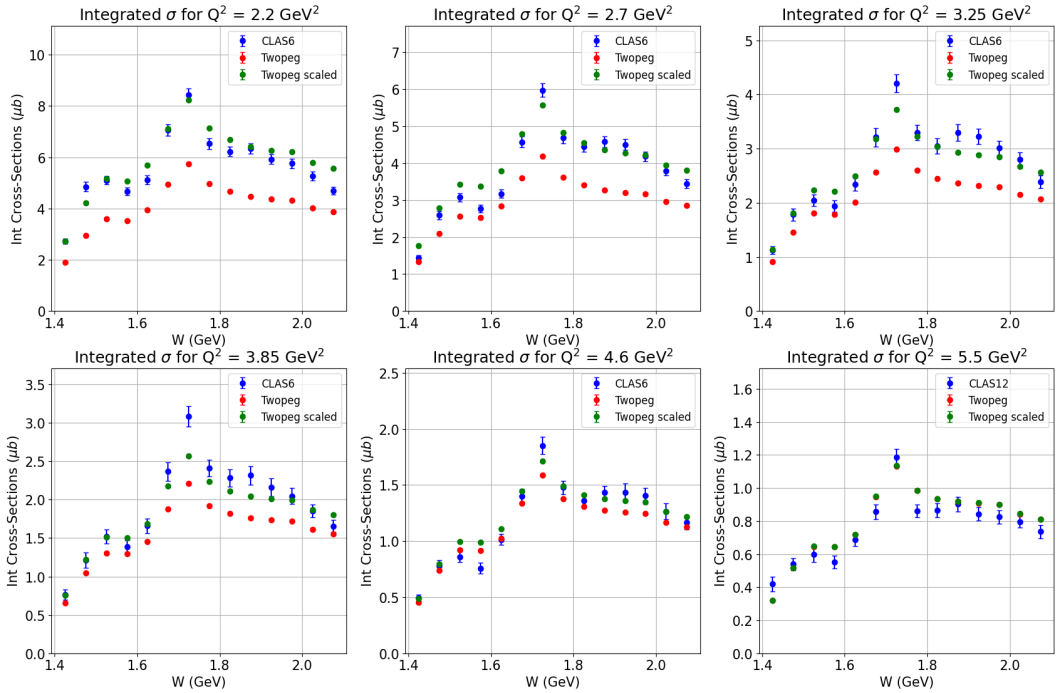

Figure 6.5 CLAS (blue), TWOPEG (red), and TWOPEG adjusted (green), integrated cross sections for various Q^2 bins.

6.4 Radiative effect corrections

Incoming, interacting, and scattered electrons can emit photons, reducing their energy. This energy loss influences the measured cross sections. Correction factors are applied to the cross sections to account for these radiative effects. The well-established Mo and Tsai method [45], although established for inclusive electron scattering, is commonly used successfully for radiative corrections of double-pion electroproduc-

tion, provides a framework for this adjustment. Using this method, the TWOPEG event generator is utilized to produce events that incorporate radiative effects.

TWOPEG generates events with and without radiative effects for a specified kinematic region to calculate the correction factors. The radiative effect correction factor $1/R$ is calculated by (6.5).

$$\frac{1}{R} = \frac{\Delta^7\sigma_{nr}(\Delta Q^2, \Delta W, \Delta\tau^5)}{\Delta^7\sigma_{wr}(\Delta Q^2, \Delta W, \Delta\tau^5)}. \tag{6.5}$$

Here, $\Delta^7\sigma_{nr}$ and $\Delta^7\sigma_{wr}$ are seven-differential cross sections without and with radiative effects, respectively. Equation 6.5 can be simplified to depend only on W and Q^2, as the radiative correction factor depends primarily on the electronic vertex. As TWOPEG weights the generated events accordingly, and the correction factor can be expressed by

$$\frac{1}{R} = \frac{\Delta^2 Wt_{nr}(\Delta Q^2, \Delta W)}{\Delta^2 Wt_{wr}(\Delta Q^2, \Delta W)}, \tag{6.6}$$

where Wt_{nr} and Wt_{wr} represent the sum of weights in the respective bins for events

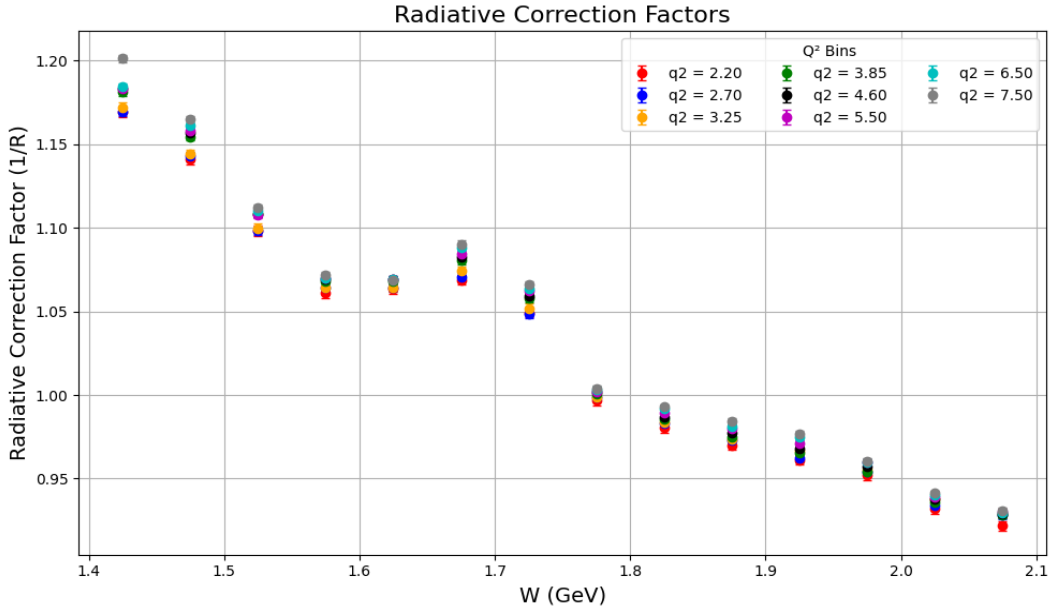

Figure 6.6 Radiative correction factors for various Q^2 bins in the W[1.4, 2.1] GeV range.

without and with radiative effects. Figure 6.6 shows these correction factors $1/R$ in

different Q^2 bins for the W[1.4,2.1] GeV range since 1/R serves as the multiplicative factor in the cross section formula described in (5.10).

6.5 Binning

The CLAS12 detector almost covers the angular coverage 4π and offers a wide range of W and Q^2 that in this analysis accesses the three resonance regions and four-momentum transfers up to 8 GeV^2. The limitations posed by available statistics and detector resolution significantly influence the binning strategy for the kinematic variables W and Q^2, restricting the possibility of having arbitrarily small W-Q^2 bins. In contrast, excessively large bins in W-Q^2 can impede the precise extraction of N* parameters. Currently, a pragmatic approach is adopted with a W-bin width of 50 MeV that is adapted to the W resolution. The Q^2-bin width ranges from 0.5 GeV^2 to 1.0 GeV^2. This decision is based on the available experimental and simulation data and the overlap with previous results [1][3]. For hadronic variables, this analysis employs seven bins for invariant mass distributions within their respective ranges, ten bins for theta (θ) angle distributions spanning 0° to 180°, six bins for phi (ϕ) angle distributions spanning -180° to 180°, and ten bins for alpha (α) angle distributions ranging from 0° to 360°.

6.6 Acceptance studies and error cuts

Acceptance is defined in the simulations as the ratio of reconstructed double-pion events (after all cuts have been applied) to the generated double-pion events. Each W-Q^2 bin contains a total of 29,400 five-dimensional bins, requiring extensive Monte Carlo simulation to populate them adequately (typically more than 10^8 events per W-Q^2 bin). TWOPEG generates flat events across the entire W-Q^2 range and assigns weights based on the cross section at each kinematic point. This optimized process overall requires significantly less Monte Carlo simulation time, but slightly

more to adequately populate bins with smaller sizes Q^2 bin, as the same number of five differential bins is formed for each W-Q^2 bins. Thus, the lower Q^2 bins tend to have larger hole fractions, leading to significant systematic uncertainties, since the systematic error for the bins filled using TWOPEG cross sections is conservatively estimated to be 50% of the missing cross section. For that reason, it is crucial to properly fill all five-dimensional bins for proper cross section extractions.

However, due to the complexity of the CLAS12 simulation process and limited computational resources, the generated event statistics remain insufficient, especially for lower Q^2 bins. Since the CLAS12 Monte Carlo simulation with pass2 cooking software became available on Jlab's OSG portal with all the geometry and CCDB constants implemented in 2024, more than 25 TB of Monte Carlo simulation data have been produced. However, this data set is still insufficient to adequately populate all five-dimensional bins. Additional simulations are ongoing on the JLab OSG portal, but due to limited resources, it will take more time to finish the simulations.

In ROOT, a THnSparse histogram is a sparse N-dimensional histogram designed to store multi-dimensional data efficiently. The method $Sumw2()$ is used to calculate and track bin errors by storing the sum of squared weights for each bin, that is, $\sqrt{\sum w^2}$, where w represents the weights, which are the cross section values assigned by TWOPEG. As the acceptance histogram is the ratio of a reconstructed histogram to a generated histogram, the bin errors in the acceptance histogram (δA) are propagated according to the standard error propagation for division,

$$\delta A = A\sqrt{\left(\frac{\delta A_{\text{rec}}}{N_{\text{rec}}}\right)^2 + \left(\frac{\delta A_{\text{gen}}}{N_{\text{gen}}}\right)^2}, \tag{6.7}$$

where N_{gen} and N_{gen} are the bin contents and δA_{rec} and δA_{gen} are the bin errors of the reconstructed and generated histograms, respectively. The value $\delta A/A$ is the relative acceptance error and it can be larger or even exceed 1 when the bin content of acceptance histogram is small while the error remains significant. In such cases, the

statistical fluctuations in the bin content become large relative to its value, leading large relative acceptance errors. To reduce the effect of this in the final cross section measurement cuts are applied on $\delta A/A$. Figures 6.7 and 6.8 illustrate the relative acceptance error cuts applied for the W[1.80,1.85] GeV, Q^2[2.0,2.4] GeV^2, and W[1.80, 1.85] GeV, Q^2[6.0,7.0] GeV^2 bins, respectively.

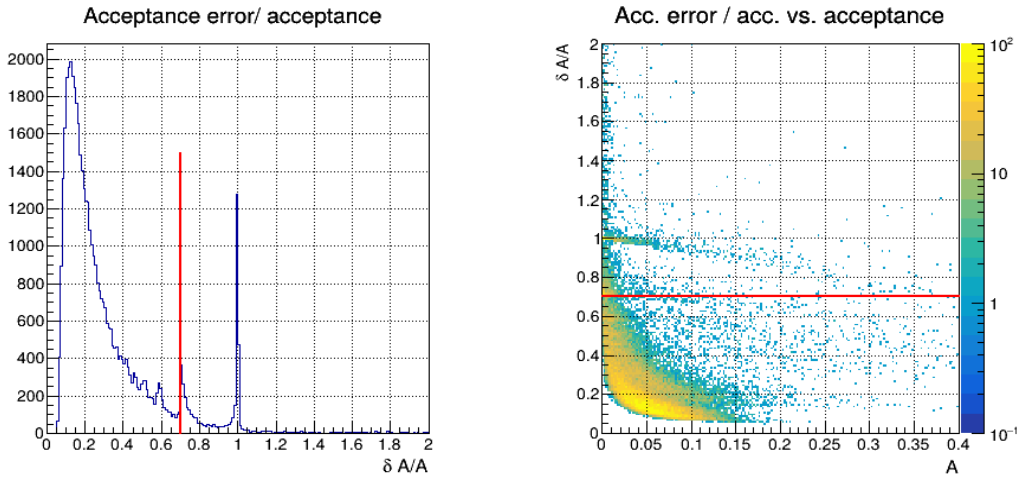

Figure 6.7 Relative acceptance error $\delta A/A$ (left) and relative acceptance error $\delta A/A$ versus acceptance A (right) for W[1.80, 1.85] GeV, Q^2[2.0, 2.4] GeV^2.

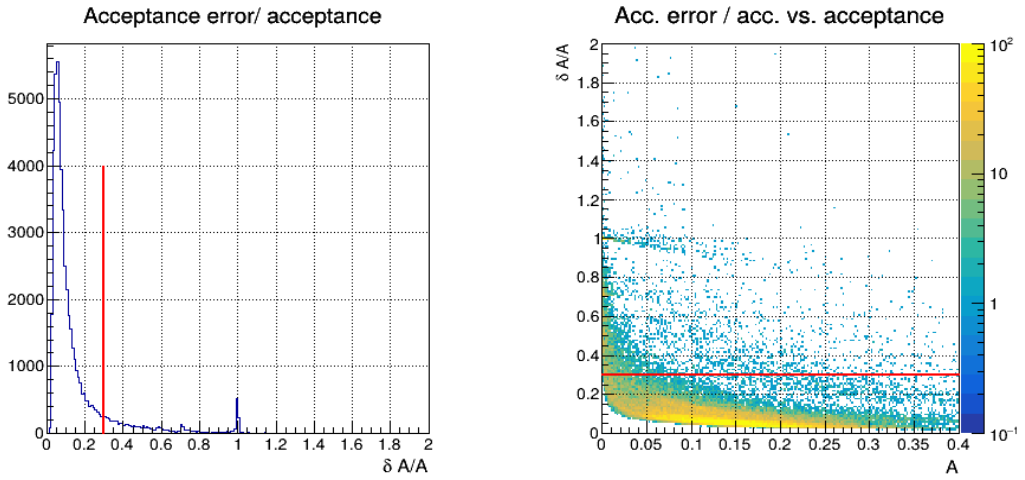

Figure 6.8 Relative acceptance error $\delta A/A$ (left) and relative acceptance error $\delta A/A$ versus acceptance A (right) for W[1.80, 1.85] GeV, Q^2[6.0, 7.0] GeV^2.

Figure 6.7 also shows that the lower Q^2 bin will be more affected if the same

relative acceptance error cuts are applied. After an initial investigation of the final results and systematics, the threshold cuts at 0.7 (red line in Fig. 6.7) are used for the first three lower Q^2 bins, and the cuts at 0.3 (see Fig. 6.8) are used for the next five Q^2 bins. Once sufficient simulation data are achieved, the cut will be placed at 0.3 as suggested in Chapter 4 of [15]. Any bins with an acceptance error to acceptance ratio greater than those thresholds are considered unreliable and excluded from the cross section measurement. These bins are treated as holes and filled using TWOPEG cross sections, as described in the next section.

6.7 Hole filling

Certain five-differential bins do not contain reconstructed double-pion events, leading to a zero acceptance factor. All bins with zero acceptance factor are called holes. As discussed in the previous section, the acceptance error cut, eliminating inefficient bins, creates more holes. To obtain more accurate cross sections, these effects have to be mitigated, as an integration is performed on four out of five hadronic variables to extract the cross sections. The experimental and MC simulated yields from the filled bins are used to estimate the anticipated measured yields in the holes, which are called hole yields. Corrections on the extracted cross sections are done using those hole yields. The ratio of the sum of the acceptance-corrected yields across all five-dimensional bins in the experimental data to the sum of acceptance-corrected yields in the simulation data determines the scaling factor (ScF).

The hole-filling process is done using five-dimensional (5D) THnSparse histograms for MC generated (5D-TH), MC reconstructed (5D-SR) and measured (5D-ER) double-pion data survived after the event selection process. The holes are filled separately for all three sets of variables used for the extraction of differential cross sections. The complete process of hole filling is described in 6.8 and in the following paragraph.

1. $\text{5D-AC} = \dfrac{\text{5D-SR}}{\text{5D-TH}}$,

2. $\text{5D-AcorrMC} = \dfrac{\text{5D-SR}}{\text{5D-AC}}$,

3. $\text{5D-HS} = \text{5D-TH} - \text{5D-AcorrMC}$,

4. $\text{5D-AcorrExp} = \dfrac{\text{5D-ER}}{\text{5D-AC}}$,

5. $ScF = \dfrac{\sum_{i=1}^{N} \text{5D-AcorrExp}_i}{\sum_{i=1}^{N} \text{5D-AcorrMC}_i}$,

6. $\text{5D-Exp} = \text{5D-ER} + (ScF \times \text{5D-HS} \times AF)$, (6.8)

where, i runs from the first bin to the last filled bin (N) in 5D-ACorrMC.

First, the 5D acceptance (5D-AC) histogram is determined by taking the ratio of the reconstructed MC to the generated MC. The acceptance-corrected MC histogram (5D-AcorrMC) is then obtained by dividing the reconstructed Monte Carlo (5D-SR) by the acceptance (5D-AC). The hole yields in the simulation 5D-HS is then estimated by subtracting the acceptance corrected MC (5D-AcorrMC) from the generated MC (5D-TH), which shows the discrepancies due to the empty reconstructed bins in the simulation. Next, for the experimental data, an acceptance-corrected experimental histogram (5D-AcorrExp) is generated by dividing the reconstructed experimental data (5D-ER) by the acceptance (5D-AC). This is used to get the scaling factor ScF as given in item number 5 in 6.8. This factor is an estimate of the proportionality factor between hole yields in simulation and measurement. Finally, the scaled hole yield ($ScF \times$ 5D-HS) is adjusted by factor AF, which is the adjustment of the cross section due to the mismatch between the TWOPEG and the cross sections measured from CLAS data, described in Sect. 6.3. The final hole-filled 5D experimental histograms are then obtained by adding experimental yields (5D-ER) and the adjusted scaled hole yields.

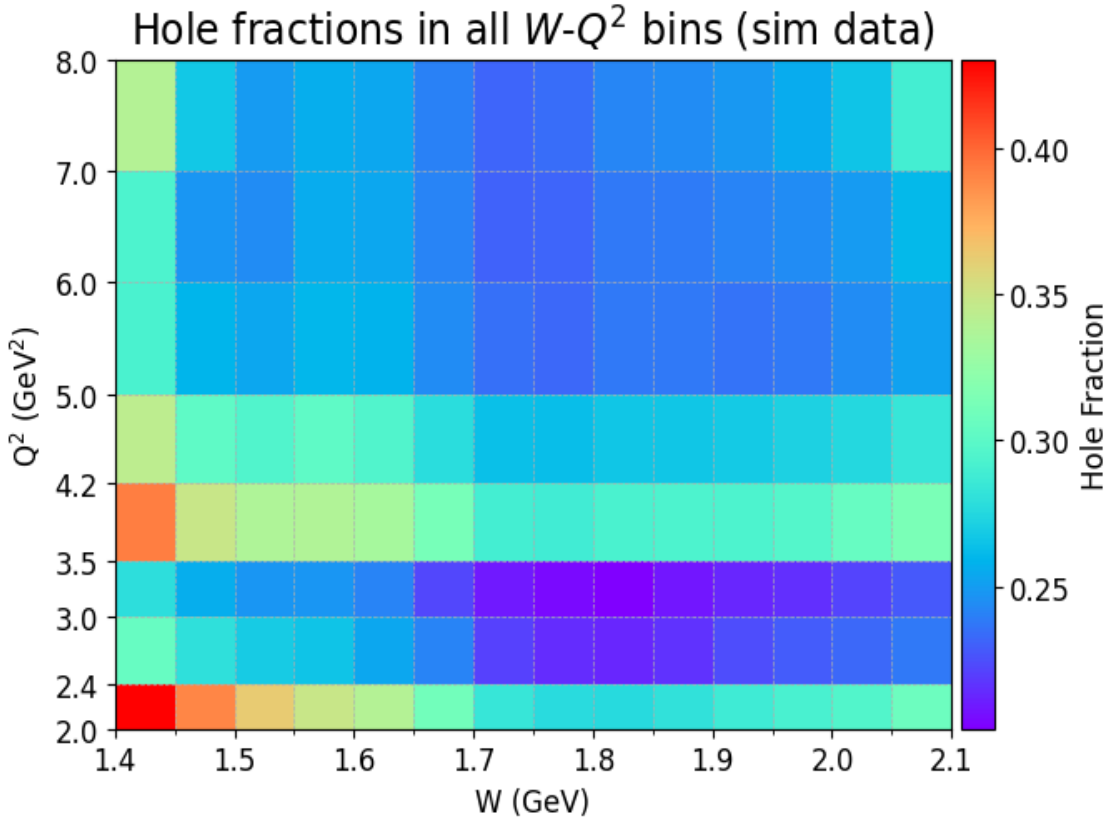

Figure 6.9 Fraction of holes (empty 5D bins) to all 5D bins in Q^2 versus W dependence using MC data.

Figure 6.9 displays the fraction of empty 5D bins for each W-Q^2 bin after applying acceptance error cuts (at 0.7 for the first three Q^2 bins and 0.3 for the last five bins). The hole fraction is higher near the double-pion production threshold in the low-W region. Figure 6.9 also shows that the lower Q^2 region, where most experimental data are concentrated, has lower statistics and, therefore, more holes. This is mainly due to the insufficient amount of Monte Carlo simulation data and the finer Q^2 binning in that range. To determine the true holes, the statistics in each $W - Q^2$ bin need to be sufficient. Otherwise, some 5D bins may be empty due to low statistics.

Chapter 7

Corrections

7.1 Particle detection efficiency corrections

Ideally, the particle detection efficiency of the experiment should be the same as the reconstruction efficiency of that particle in the Monte Carlo simulation. However, in this experiment, a full replication of all the experimental conditions in the simulations has not yet been achieved. This leaves unmatched experimental and simulated particle reconstruction efficiencies. To address this issue, a method has been developed to check whether the efficiency of the final hadron in the experiment is different from that of the simulation. If there are differences, then the efficiency correction factors are applied accordingly. The formula for the correction factor is given as

$$E_C = \frac{E_{Cexp}}{E_{Csim}}, \tag{7.1}$$

where, E_{Csim} is the simulated particle detection efficiency, i.e. the ratio of the reconstructed particles to the missing particles in simulation. Similarly, E_{Cexp} is the experimental particle detection efficiency, which is the ratio of the measured particles to the missing particles in the experiment for each kinematic bin.

This section will provide a comprehensive explanation of the particle detection efficiency correction procedure. The three-dimensional momentum P, polar angle θ, and azimuthal angle ϕ bins in the detector lab frame of reference are used to compute these efficiency correction factors. The proton and π^+ binnings are shown in the Tabs. 7.1 and 7.2, respectively. As this analysis uses missing π^- topology to calculate the cross sections, the efficiency factors of π^- are not needed.

First, the background shapes are determined by applying appropriate cuts on missing mass square peaks for the missing proton (i.e. $ep \rightarrow e'\pi^+\pi^-$), missing π^+ (i.e. $ep \rightarrow e'p'\pi^-$), missing π^- (i.e. $ep \rightarrow e'p'\pi^+\pi^-$) and exclusive (i.e. $ep \rightarrow e'p'\pi^+\pi^-$) processes. The background data are the data that lie outside of three MMSQ cuts excluding the one in which the efficiency factor is to be calculated. This means that for the efficiency of protons, the proton MMSQ cuts are excluded, and the other three MMSQ cuts are used to determine the background data. This is possible only in the exclusive topology. An appropriate scaling factor for the background data in the exclusive topology is applied to find the background data in the missing topology. This background data is subtracted from the original MMSQ distribution. The integral of the background-subtracted data, inside the mean $\pm 2\ \sigma$ from the Gaussian fit around the MMSQ peak, is obtained to determine the number of particles. This integral is calculated for both the exclusive (where the particle is measured) and missing particle topology, and the ratio of exclusive to missing integrals is determined. This ratio gives the fraction of the particles measured by the experiment, i.e. the experimental particle efficiency in that bin. Similarly, this ratio is calculated from the simulation data to obtain the particle reconstruction efficiency of the MC data. Finally, using the two ratios obtained from the experimental and MC data, the efficiency correction factor is calculated as outlined in (7.1) for each kinematic bin.

7.1.1 Efficiency correction factor for protons

Table 7.1 Binning for the proton efficiency factors.

θ (degree)	Momentum (GeV)	ϕ (degree)
0-37	0.4, 0.8, 1.1, 1.4, 1.7, 2.0, 2.5, 3.0, 4.0	0, 60, 120, 180, 240, 300, 360
37-50	0.5, 0.8, 1.0, 1.2, 1.4, 1.6, 1.8, 2.2	0, 120, 240, 360

To obtain the efficiency correction factors for the protons, the data are first divided into two bins of polar angle (θ), $\theta < 37^\circ$ and $\theta \geq 37^\circ$. For the first θ bin, it is expected

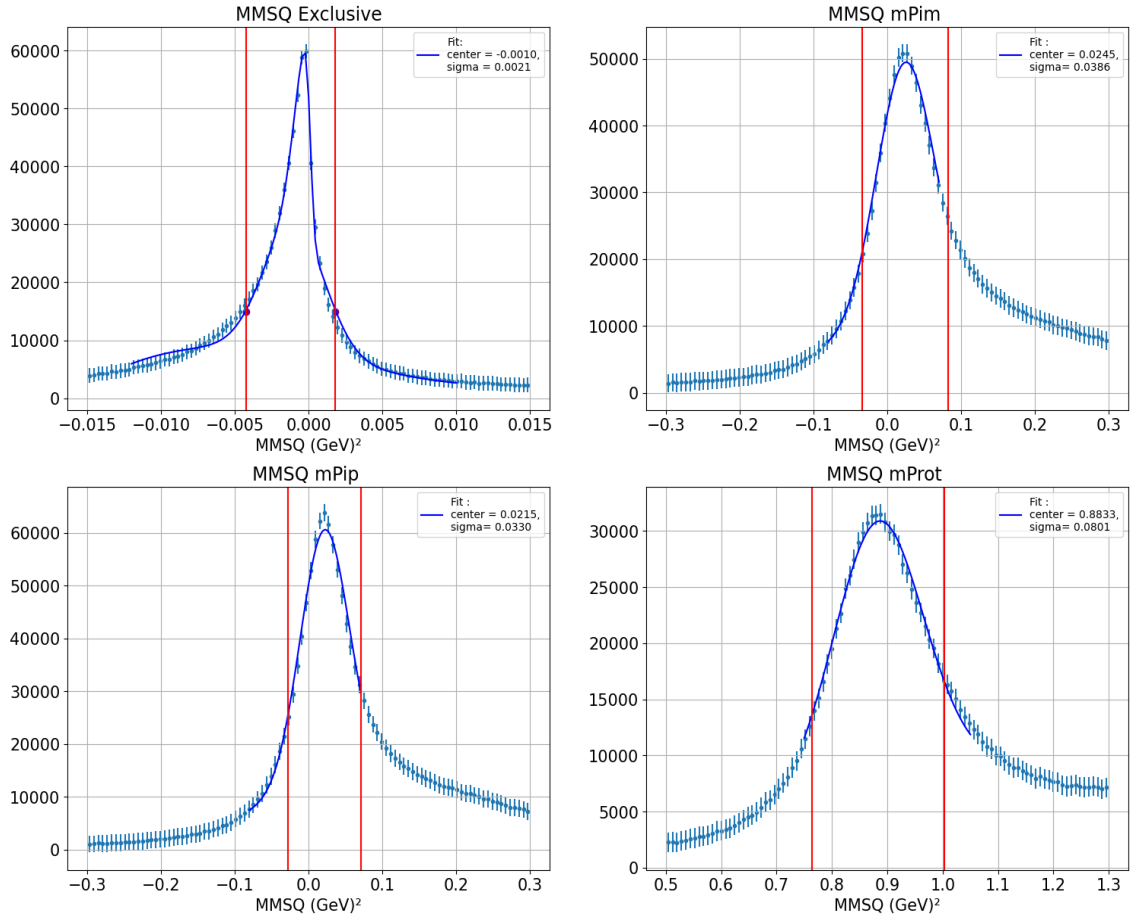

Figure 7.1 MMSQ distributions for the exclusive $ep \to e'p'\pi^+\pi^-$ reaction from experimental data. In the first plot, the blue curve represents a fit using a combination of a skewed Gaussian and a third-order polynomial function, while in the remaining three plots, it represents a Gaussian fit. The red vertical lines indicate the applied cuts for each MMSQ distribution.

to detect protons using the forward detector system, where six ϕ bins are defined, see Tab. 7.1. These ϕ bins differ slightly from the six FD sectors, as they are based on missing protons rather than measured ones. For the second θ bin, the central detector system is expected to measure protons, where three ϕ bins are defined. Momentum bins are determined on the basis of the available statistics.

The red lines in Fig. 7.1 indicate the cuts used for background selection. Data outside the cuts for missing π^+, missing π^- and exclusive (i.e. $ep \to e'p'\pi^+\pi^-$) MMSQ distributions are selected as background data for the proton efficiency correction. For

the MMSQ distribution corresponding to the exclusive peak at zero (top left graph in Fig. 7.1), the fit is performed using a combination of Gaussian, Skewed-Gaussian, and third-order polynomial functions. The cuts are placed at one-fourth of the maximum value of the fit. For the other MMSQ distributions, the peak regions are fitted with Gaussian distribution functions. Suitable cuts, based on the sigma values on either side of the peak center, are applied to obtain the background for the exclusive data, which is scaled appropriately to get the background for the missing proton data. The same procedure is applied to simulation data.

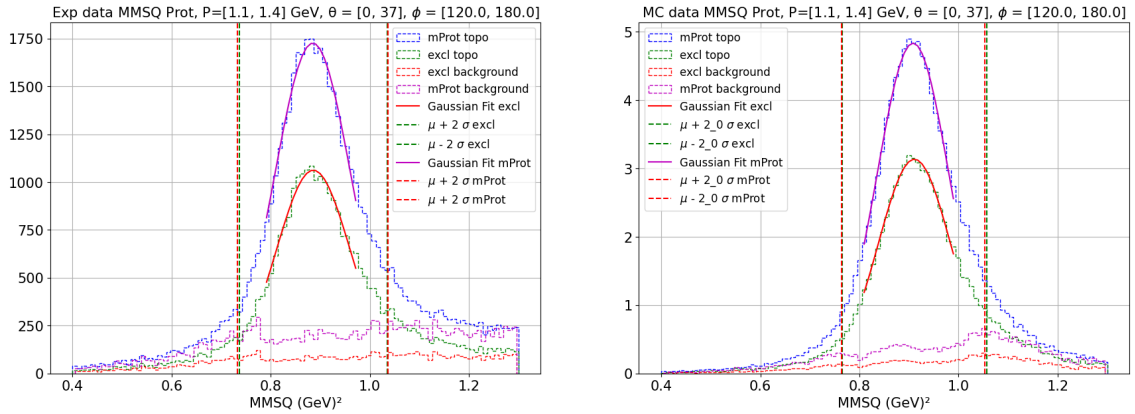

Figure 7.2 Proton MMSQ in the P$[1.1, 1.4]$ GeV, $\theta < 37°$, and $\phi[120°, 180°]$ bin for the proton efficiency factor calculation. The left plot is for measured data and the right plot is for reconstructed MC data.

Figure 7.2 shows typical MMSQ distributions for the missing proton and exclusive topologies within a typical three-dimensional bin. The plot on the left represents the experimental data, while the plot on the right corresponds to the MC data. The distributions are fitted with a Gaussian function in the peak region to extract the mean and σ values. Next, the integral of the background-subtracted distribution is calculated for both the exclusive and missing proton topologies. The ratio of these integrals gives the experimental proton efficiency in that particular three-dimensional bin. The same procedure is then applied to the MC data to determine the proton efficiency in the simulation. Finally, the efficiency correction factors are obtained by taking the ratio of the efficiencies, i.e. experiment over simulation. Figure 7.3 presents

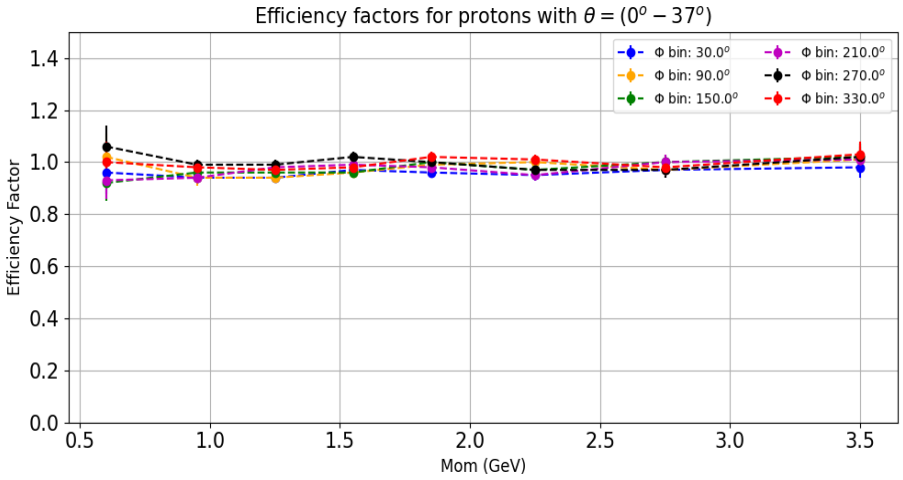

(a) Proton efficiency correction factors for the $\theta < 37°$

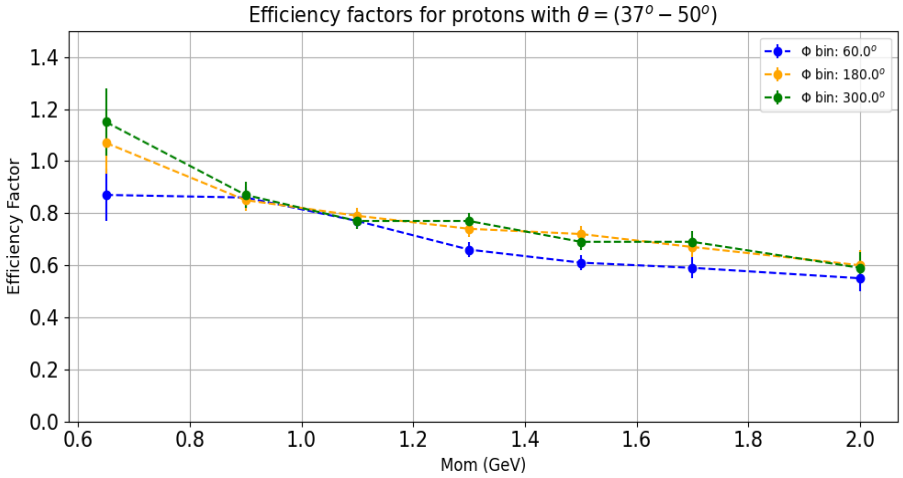

(b) Proton efficiency correction factors for the $\theta > 37°$

Figure 7.3 Proton efficiency correction factors versus momentum.

these correction factors; Figure 7.3(a) shows that the correction factors are close to one, indicating that the proton detection efficiency is similar in both experimental and MC data in this region. However, Figure 7.3(b) shows that the correction factors deviate from one in all three ϕ bins, suggesting that the proton detection efficiency is higher in the simulation compared to the experimental data.

The application of correction factors is not straightforward. Since these efficiency factors are derived based on the momentum, θ, and ϕ of the missing proton, and the missing topology lacks direct measurements of these variables, a mapping between the

missing and measured momentum, θ, and ϕ of the protons must be established. To achieve this, protons from the exclusive topology, where both measured and missing variables are available, are used. Furthermore, possible background contamination on these protons is reduced by selecting the data within $\pm 3.5\sigma$ around the mean of the Gaussian fit around the proton, π^+, and π^- MMSQ peaks and within 1/10th of the maximum value peak for the exclusive MMSQ peak.

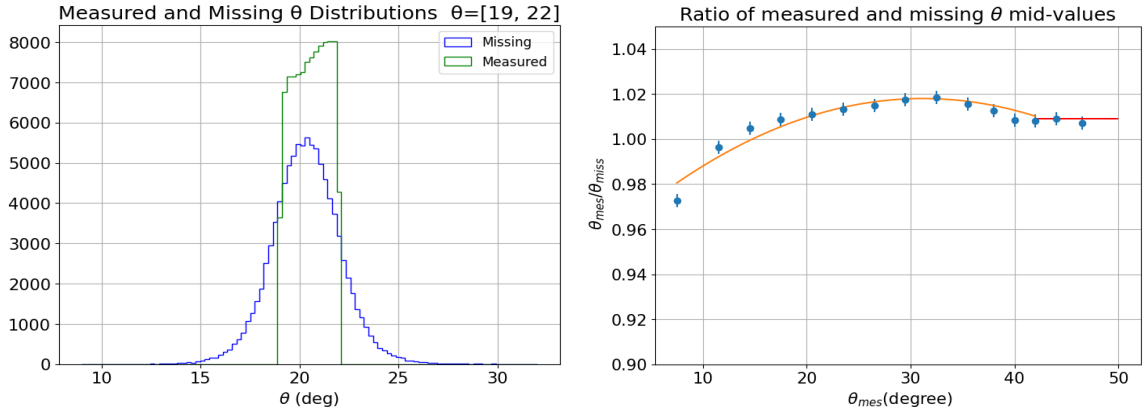

Figure 7.4 (Left) Proton's missing and measured θ distributions, in the measured $\theta[19°, 22°]$ bin. (Right) Ratio of mid-values of measured and missing proton's θ angles along with a second-order polynomial fit. For $\theta > 42°$, a constant fit function is used.

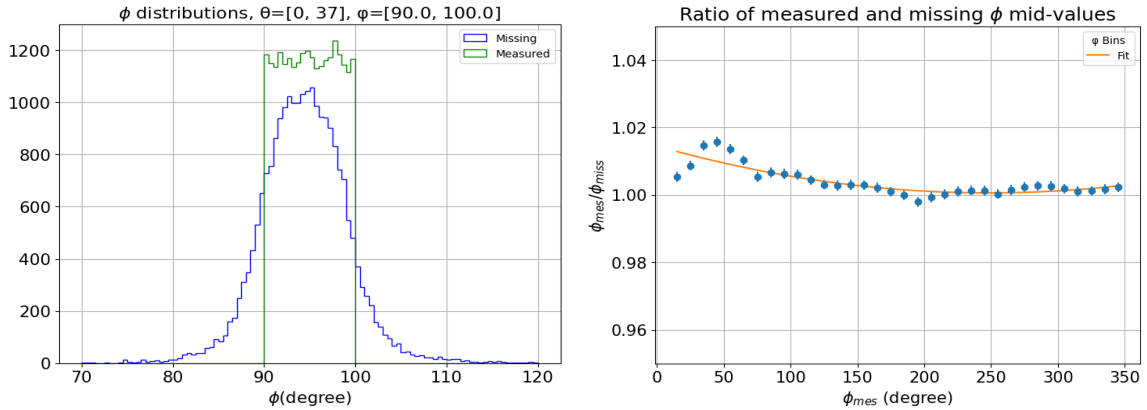

Figure 7.5 For protons in the $\theta < 37°$ bin: (Left) Proton's missing and measured ϕ distributions, in the measured $\phi[90°, 100°]$ bin. (Right) Ratio of mid-values of measured and missing proton's ϕ angles along with a 2nd order polynomial fit.

In the clean proton sample, the mapping is done by finding the mid-values of the measured and missing variables. Following the binning pattern used for efficiency

calculation (given in Tab. 7.1), the θ mapping is performed first. For this, the data are divided into finer θ bins. The mid-values of the missing and measured protons θ angles are obtained. Then their ratios are fitted using a second-order polynomial and a constant function, as shown in Fig. 7.4. The fitted parameters are then used to map the missing and measured proton θ values.

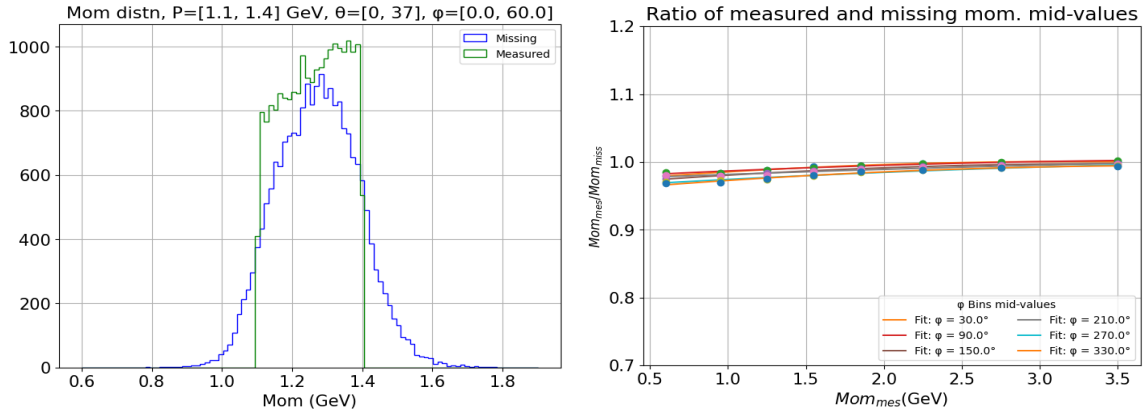

Figure 7.6 For protons in the $\theta < 37°$ bin: (Left) Proton's missing and measured momentum distributions, for measured momentum P$[1.1 - 1.4]$ GeV, $\phi[0°, 60°]$ bin. (Right) Ratio of mid-values of measured and missing proton momenta for six ϕ bins along with 2nd order polynomial fits.

For ϕ mapping, protons are first separated into two θ bins. Each dataset is then further divided into smaller ϕ bins. The mid-values of missing and measured protons ϕ angles are obtained. Then their ratios are fitted with suitable polynomial functions to obtain the mapping parameters. For $\theta < 37°$ bin, Figure 7.5 shows one particular ϕ distribution (left) and the ratios and fit for all ϕ bins (right).

Similarly, for momentum mapping, the ratio of the mid-values of measured and missing momentum distributions are fitted separately for each θ and ϕ bins, see Fig. 7.6. A second-order polynomial fit is used to determine the parameters for the momentum mapping.

Table 7.2 Binning for the π^+ efficiency factors.

θ (degree)	Momentum (GeV)	ϕ (degree)
0-37	0.4, 0.6, 0.75, 0.9, 1.1, 1.3, 1.5, 1.7, 2.3, 3.50	0, 60, 120, 180, 240, 300, 360
37-120	0.2 , 0.3, 0.4 , 0.5, 0.6, 0.7, 0.8, 0.9 1.0, 1.1, 1.7	0, 120, 240, 360

7.1.2 Efficiency correction factor for π^+

In calculating the efficiency correction factors for π^+, the method used for protons is adopted. The selected π^+s are separated into two distinct polar angle (θ) bins, as given in Tab. 7.2. The first θ bin corresponds to particles expected to be detected by the FD, subdivided into six ϕ bins. The CD is expected to detect the particles in the second θ bin, where three ϕ bins are used. Momentum bins are based on available statistics. To isolate background events for the π^+ efficiency correction, criteria based on the missing mass square of protons, the missing mass square of π^-, and the missing mass square at zero (i.e. $ep \rightarrow e'p'\pi^+\pi^-$) are chosen.

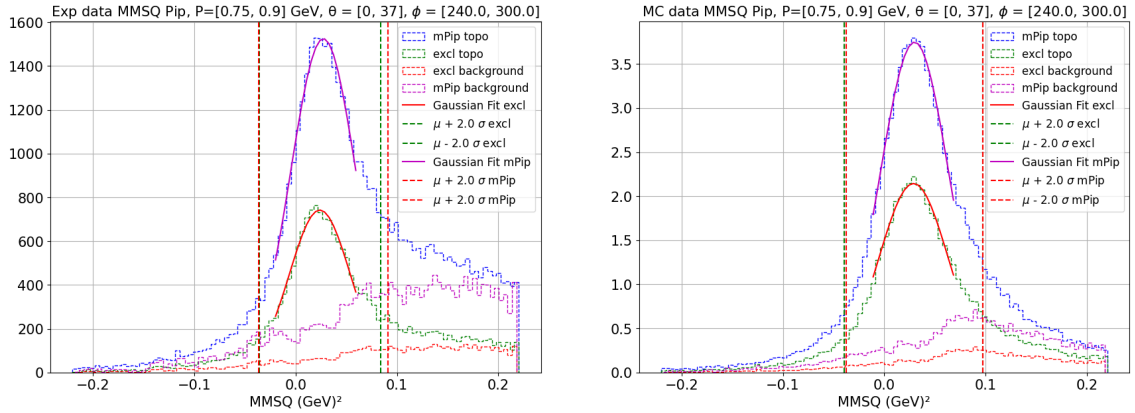

Figure 7.7 Missing mass square distributions of missing π^+ in the momentum P$[0.75, 0.9]$ GeV, $\theta < 37°$ and ϕ $[240°, 300°]$ bin that are used for π^+ efficiency factor calculations. Left plot is for measured data and the right plot is for MC data.

The Figure 7.2 illustrates the π^+ MMSQ distributions for the missing π^+ and exclusive topology for a typical 3-dimensional bin, the left side is for experimental data, and the right side is for MC data.

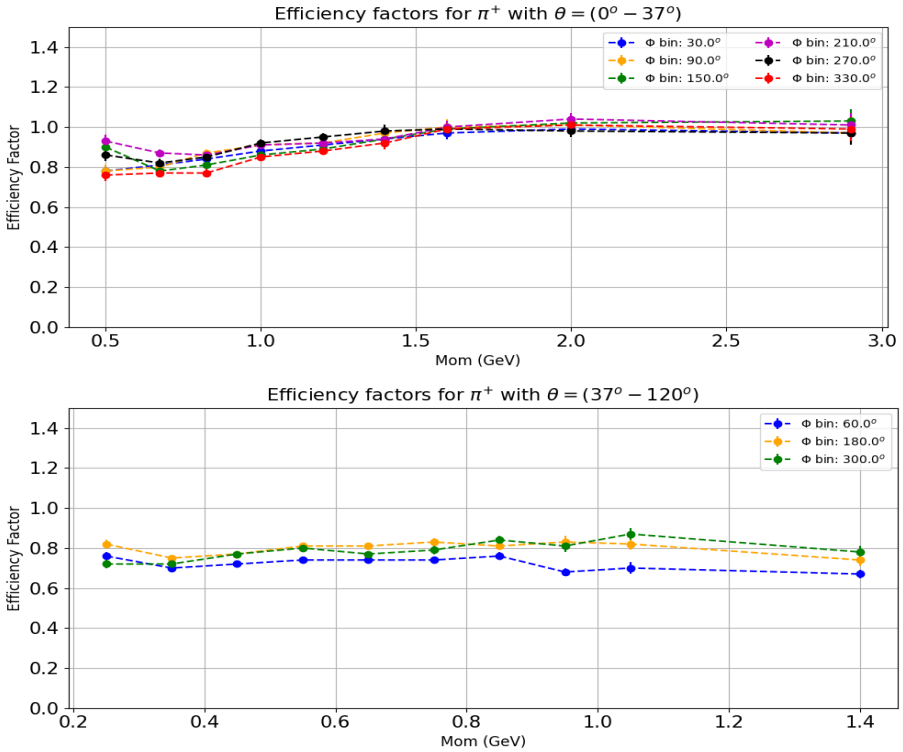

Figure 7.8 π^+ efficiency correction factors versus momentum. Top panel for FD π^+ and bottom for CD.

Figure 7.8 (top) illustrates the π^+ efficiency correction factors for $\theta < 37°$ bin across various ϕ and momentum bins. As the π^+s are mostly expected to be in the FD, it is expected that the efficiency correction factors would be small. However, the plot shows that the low momentum π^+s reconstruction is more efficient in MC than in the experiment, thus correction factors are needed and applied. Also, Figure 7.8 (bottom) shows that the efficiency correction factors are around 0.8 in all three ϕ bins in this θ region, suggesting that the π^+ reconstruction efficiency is higher for the MC data than for the experimental data. Thus, correction factors are applied. The kinematic mapping procedure described for the protons above is adopted to establish the mapping between the missing and measured π^+ variables.

7.2 Background subtraction

The double-pion electroproduction data, even after applying all particle identification and selection cuts, still contain background events. In nature and thus in this experiment, multiple reaction channels occur simultaneously, making it difficult to completely separate background events from double-pion events. The data used in this analysis were taken with a beam energy of 10.6 GeV, which is much higher than the beam energy of the data in the CLAS era. With higher beam energy, the double-pion events selected suffer from significant background. The main background source in this channel comes from the three-pion channel ($ep \rightarrow e'p'\pi^+\pi^-\pi^0$).

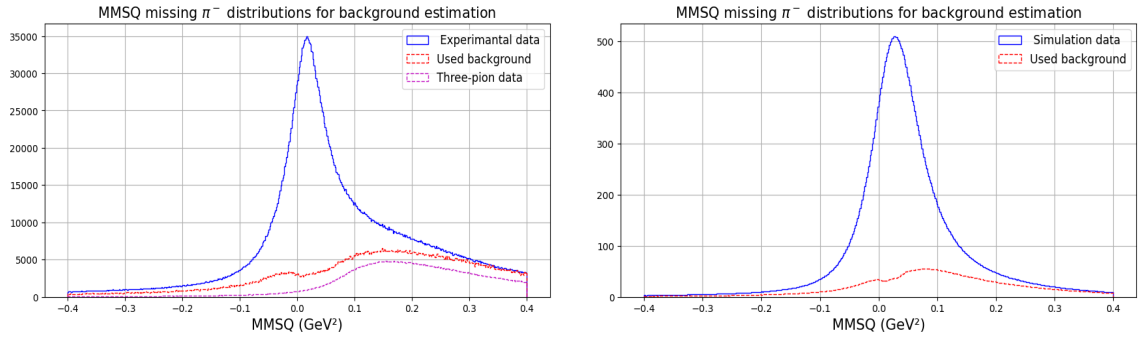

Figure 7.9 MMSQ distributions for missing π^- topology (blue curve) along with selected background using MMSQ technique (red curve), using experimental data (left), using MC simulation data (right). The pink curve in left plot represents the three-pion distribution.

The characteristics of this background are studied and illustrated in Fig. 7.9, where the pink dashed lines represent the contribution of the three-pion channel. Figure 7.9 shows that the right tail of the experimental data is well described by the three-pion channel, indicating that at least a majority of the background events in this region originate from this channel. However, the left tail of the distribution cannot be explained by the three-pion background. Although the source of the left tail is not fully understood, these events cannot all be considered true double-pion events as they contain an incorrect four-momentum vector, which produces MMSQ values that are largely deviated from the true MMSQ π^- peak. To handle this

background contamination in both tails, the missing mass squared technique is used once again. The true background shape is obtained from the exclusive $ep \to e'p'\pi^+\pi^-$ topology using the MMSQ distribution of the proton, π^+ and exclusive at zero. The background data are outside of the cuts (red lines in Fig. 7.1) at (-0.004 GeV^2 and 0.002 GeV^2) of exclusive and (-0.028 GeV^2 and 0.071 GeV^2) of π^+ and (0.763 GeV^2 and 1.003 GeV^2) of proton MMSQ peaks.

As particle identification in the MC data is done using methods equivalent to those for the experimental data, there are two sources of background in the MC data. Although TWOPEG generates only double-pion channel events, the external backgrounds are merged to match the efficiency in the MC data and the experimental data. In addition, the Δt versus momentum method used to identify hadrons leads to a potential misidentification of particles, particularly for protons and $\pi^+ s$. The Δt versus momentum bands for them are close and overlap, especially for central particles, which could lead to particle misidentification. Thus, a similar procedure is applied to select the background in the simulated data as in the measured data. To select the background in the MC data the cuts are at (-0.004 GeV^2 and 0.002 GeV^2) exclusive and (-0.024 GeV^2 and 0.079 GeV^2) of π^+ and (0.79 GeV^2 and 1.025 GeV^2) of proton MMSQ peaks based on the fits on simulation MMSQ peaks shown in Fig. 7.10. This approach helps isolate the true double-pion events by systematically removing contributions from all other reaction sources.

Since the background varies in the accessed kinematic phase space, individually adapted background subtractions are required for each kinematic W-Q^2 bins, from which cross sections are extracted. In essence, the portion of the yield contributed by the background needs to be subtracted in each W-Q^2 bin to obtain the proper yield of this reaction channel.

For typical W-Q^2 (W [1.7, 1.75] GeV and Q^2 [2.4, 3.0] GeV^2) bin, the true background shape from exclusive topology is represented by the pink dashed histograms

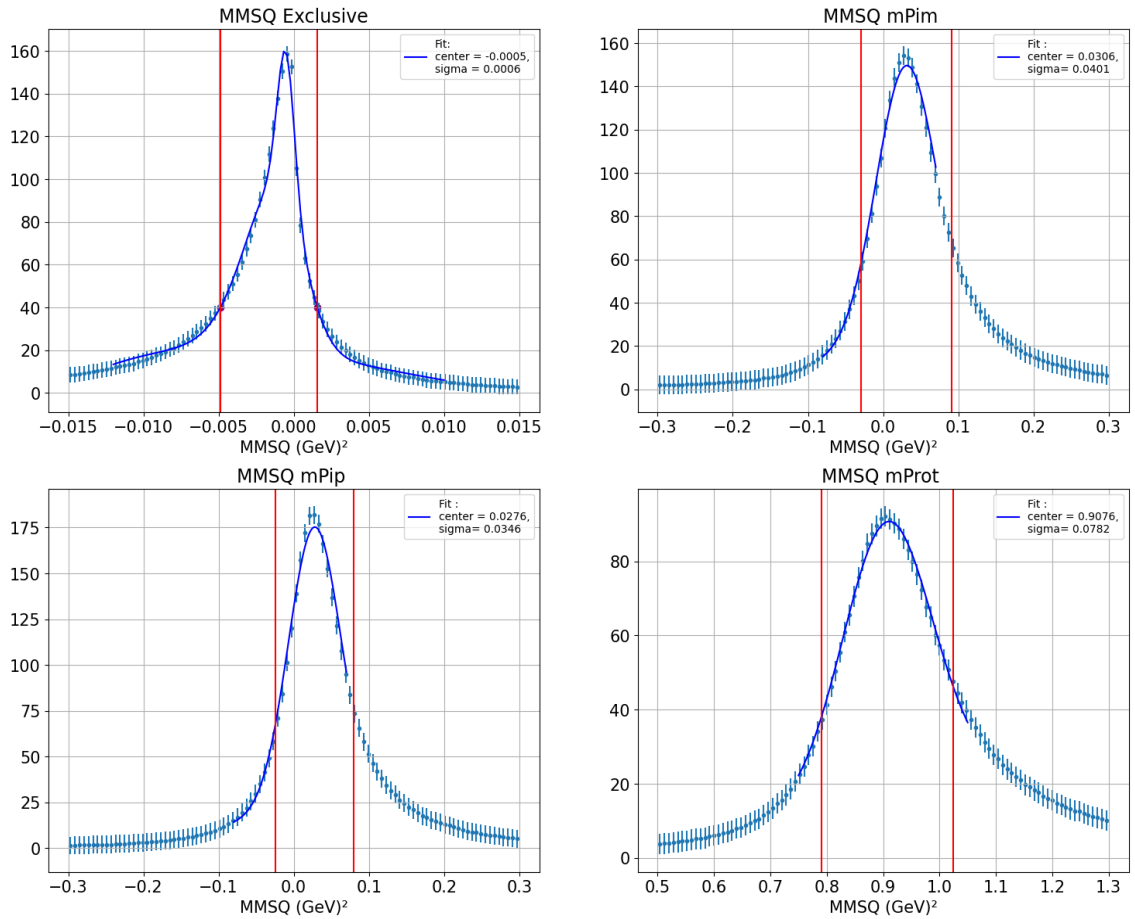

Figure 7.10 Missing mass square distributions used for background selection in MC dataset using exclusive $ep \rightarrow e'p'\pi^+\pi^-$ topology. The blue curve represents the Gaussian MMSQ peak fits, and the red lines are the applied cuts for each missing mass topology.

in Figs. 7.11 and 7.12. Then, this true background shape is scaled for the missing π^- topology. The scaling factor is determined using the integral of the background data (pink histogram in Fig. 7.11) and the MMSQ distribution of π^- (blue histogram in Fig. 7.11) in the left and right tails. The integrals of the MMSQ tails for both the background data and the missing π^- data are matched within each W-Q^2 bin. The final background after scaling is shown as red dashed histograms in Figs. 7.11 and 7.12. Both experimental and simulated results confirm that the tail of the MMSQ distribution for missing π^- is well matched to the scaled background.

After obtaining the background shape and corresponding scale factors for each

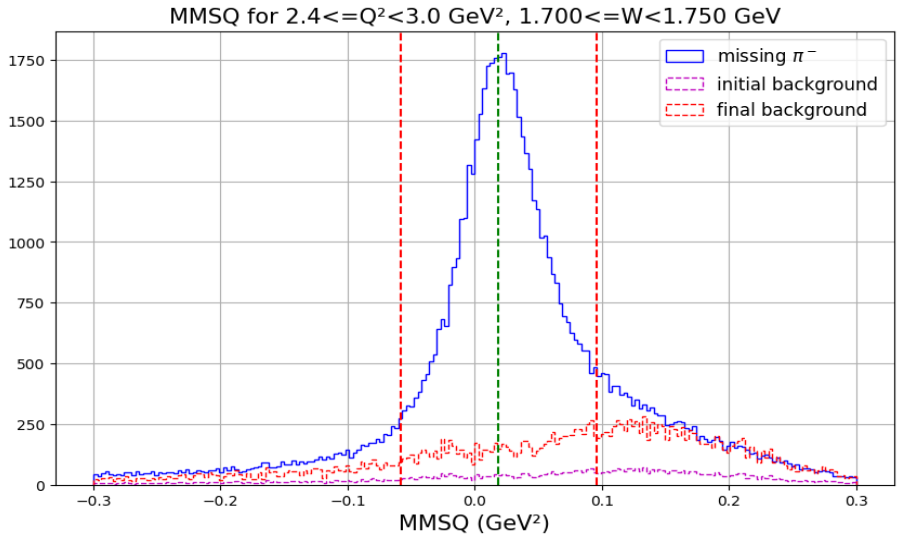

Figure 7.11 Background subtraction for experimental data in the W[1.7, 1.75] GeV and Q^2[2.4, 3.0] GeV^2 bin.

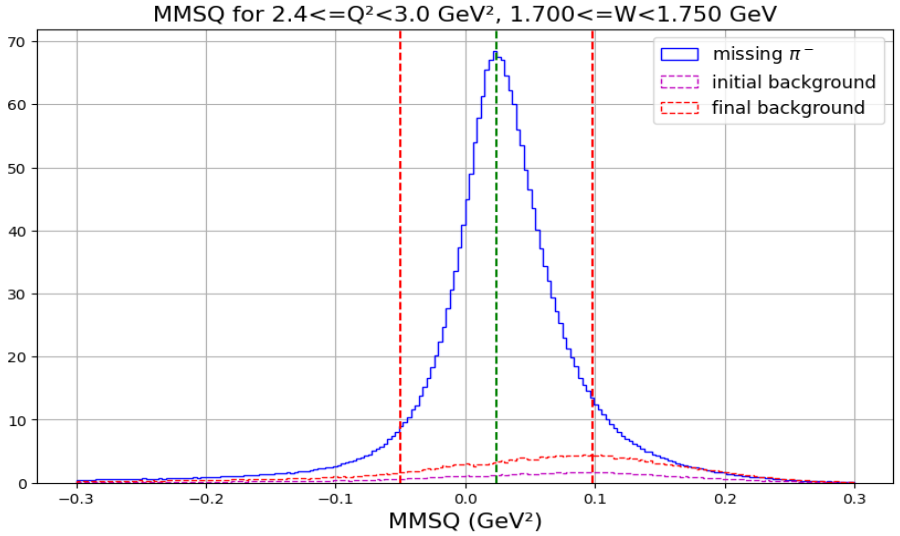

Figure 7.12 Background subtraction for simulation data for W[1.7, 1.75] GeV and Q^2[2.4, 3.0] GeV^2 bin.

W-Q^2 bin, a five-dimensional THnSparse histogram is constructed using the scaled background data within the MMSQ cuts, indicated by red dashed vertical lines in Figs. 7.11 and 7.12. The five dimensions correspond to the analysis variables described in Sec. 5.1. Three separate five-dimensional THnSparse histograms are created, each corresponding to one of the three sets of variables used for cross section extraction. These background THnSparse histograms represent the portion of the

background contributing to the total yield. Thus, they are subtracted from the original THnSparse histograms to obtain background-subtracted yields. This is done separately for both the measured and the MC reconstructed data with their corresponding background THnSparse histograms. These subtracted yields are used for further calculations of cross section extraction.

7.3 Bin centering corrections

The extracted single-differential or integrated cross sections are reported at the central value of each bin, which has a finite size. However, these reported values represent the average cross section across the entire bin. Therefore, bin-centering corrections are required to ensure improved accuracy of the reported cross sections. These corrections are particularly important for non-linear behaviors of cross sections within kinematic bins. In this analysis, single-differential cross sections are reported in three-dimensional W, Q^2, and one of the hadronic variable bins. As a result, bin-centering corrections must be calculated and applied to each W-Q^2, and specific hadronic variable bins in which the cross section is reported [46]. The remaining four hadronic variables, being integrated over during the single-differential cross section extraction process, do not require bin-centering corrections.

The bin-centering correction factor is determined using event yields generated by the TWOPEG event generator. For each bin where single-differential cross sections are reported, the correction factor is calculated individually for W, Q^2, and the hadronic variable. The procedure for computing the correction factor for a specific W bin is given as (7.2),

$$BC_{\mathrm{Corr}}(W) = \frac{\text{Yield of central sub-bin}(W, Q^2, \text{Hadronic Variable})}{\text{Average yield of all sub-bins}(W, Q^2, \text{Hadronic Variable})}. \tag{7.2}$$

To compute the bin-centering correction factor $BC_{\mathrm{Corr}}(W)$, the W distribution

within a given three-dimensional bin is divided into smaller sub-bins. The correction factor is the ratio of the yield in the central sub-bin to the average yield across all sub-bins. This process is repeated systematically for all W, Q^2, and the selected hadronic variable bins. The individual correction factors for W, (Q^2), and the hadronic variable are then combined to compute the final bin-centering correction factor,

$$BC_{\text{Corr\_final}} = BC_{\text{Corr}}(W) \times BC_{\text{Corr}}(Q^2) \times BC_{\text{Corr}}(\text{Hadronic Variable}). \tag{7.3}$$

The final bin-centering correction factor is applied to the uncorrected three-differential cross sections to obtain the corrected three-differential cross sections. This relationship is given by (7.4),

$$\sigma_{\text{corr}} = \sigma_{\text{uncorr}} \times BC_{\text{Corr\_final}}, \tag{7.4}$$

where,

- σ_{corr} is the bin-centering corrected cross section,
- σ_{uncorr} the uncorrected cross section, and
- $BC_{\text{Corr\_final}}$ the final bin-centering correction factor that accounts for W, (Q^2) and the hadronic variable.

Figure 7.13 shows the effect of bin-centering corrections on the nine single-differential cross sections for W[1.80, 1.85] GeV, Q^2[4.2, 5.0] GeV^2. Figure 7.14 shows the effect of bin-centering corrections on the integrated cross sections for Q^2[4.2, 5.0] GeV^2.

Each of the bin-centering corrections in a given variable (i.e. W, Q^2 or hadronic variable) has associated statistical error values, which are determined using,

$$BC_{\text{Err}} = N \times \sqrt{\left(\frac{\text{Err}_{mid}}{\text{Sum}}\right)^2 + \left(\text{Err}_{\text{Sum}} \times \frac{\text{Val}_{mid}}{(\text{Sum})^2}\right)^2}, \tag{7.5}$$

where,

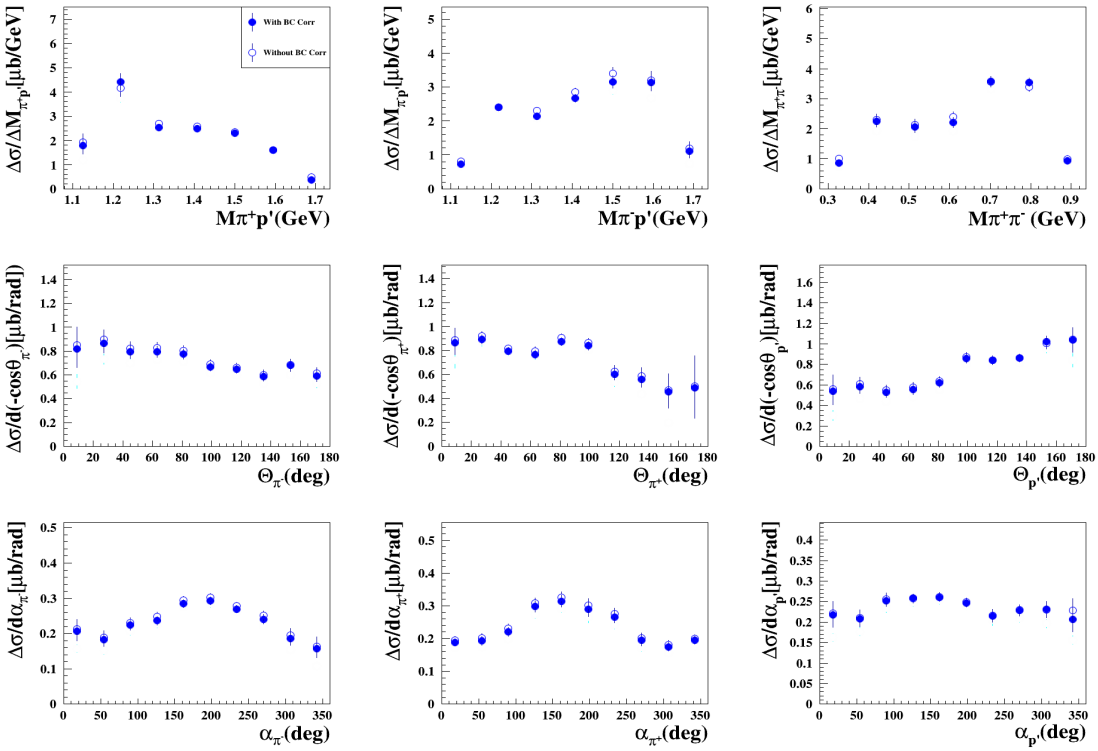

Figure 7.13 Effect of bin-centering corrections for nine single-differential cross sections on W[1.80, 1.85] GeV, Q^2[4.2, 5.0] GeV^2. The filled markers represent after bin-centering corrections and empty markers before. Error bars include both statistical and hole filling errors.

- BC_{Err} is the statistical error associated with the bin-centering correction,
- N is the number of sub-bins,
- Err_{mid} is the statistical error in the yield of the central sub-bin,
- Sum is the total yield summed over all sub-bins,
- Err_{Sum} is the sum of statistical error over all sub-bins (Sum),
- Val_{mid} is the yield of the central sub-bin.

This formula accounts for uncertainties in both the central sub-bin yield and the total yield.

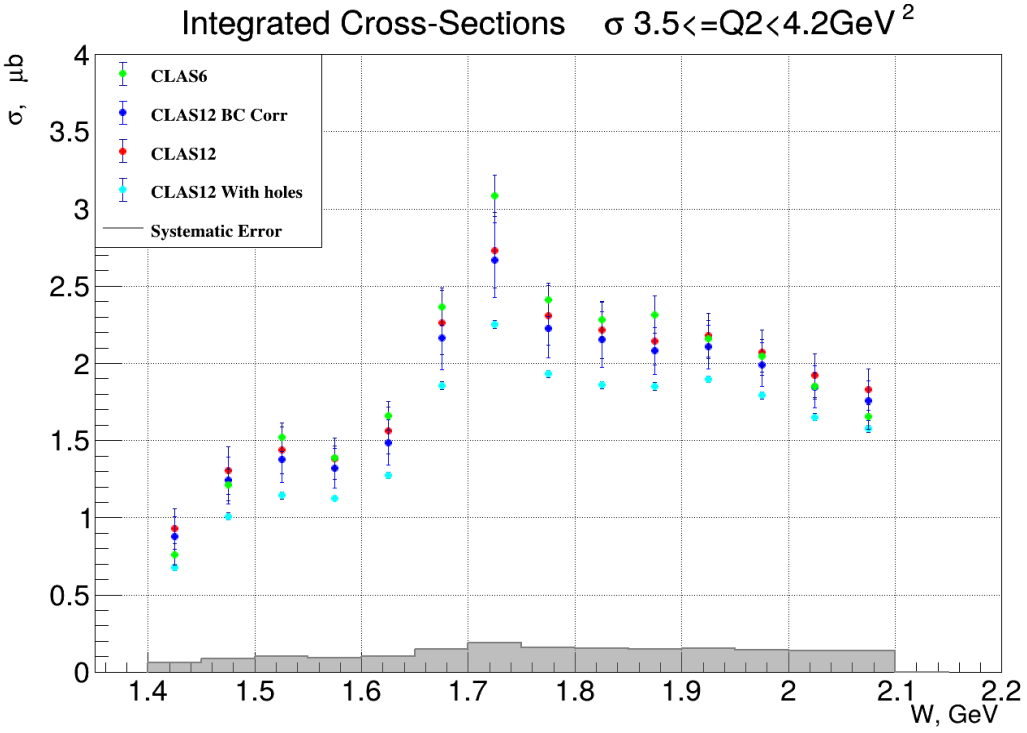

Figure 7.14 Effect of bin-centering corrections for integrated cross sections in $Q^2[3.5, 4.2]$ GeV^2. The blue points with error bars represent the bin centering corrected cross sections and the red points represent uncorrected.

Chapter 8

Statistical and Systematic Uncertainties

8.1 Statistical uncertainties

The large number of bins combined with the constrained amount of data in both experimental and MC data-sets give rise to statistical uncertainties and hole filling issues. The statistical uncertainties in each bin of the experimental five-dimensional THnSparse histogram are assigned using the square root of the bin content. This is implemented using the ROOT function SetBinError, where the bin error is set as the square root of the number of entries in that bin. The error is then properly propagated by ROOT. In case of simulations, the acceptance error cut discussed in the section 6.6 handles most of the five-dimensional bins with low statistics. As the simulation has many more events in each bin which are weighted with their individual cross sections, the significant part of the statistical uncertainty comes from the experimental data.

8.2 Systematic uncertainties

Each cut and correction applied in this analysis introduces systematic uncertainties that affect the measured cross sections. These uncertainties are evaluated by varying each selection criterion using loose, mid, and tight cuts to estimate their impact.

The sources of systematic uncertainties include PID selection cuts, fiducial volume cuts, and inefficient region cuts for all final-state particles, which account for uncertainties in reconstruction and detector acceptance. For hadron selection Δt cuts contribute to systematic errors related to particle identification. The removal of

CD-FD tracks introduces uncertainties in track reconstruction, while MMSQ cuts affect the final yield of double-pion events. In all these cases, loose, mid, and tight cuts are used to estimate the systematic uncertainties that they introduce in the results.

For both momentum corrections (from the task force) and hadron-specific corrections, a variation of 10% in the correction value is used to estimate systematic uncertainties. For particle efficiency corrections, the sigma values in Fig. 7.2 are varied to define the cut lines for the loose, mid and tight cases. Background subtraction uncertainties are determined by varying the cut position in the tail region (see Fig. 7.11) while matching the integral of the background data and the MMSQ distribution for π^- in the tail region.

For smearing factor systematics, the smearing term (3.7) is adjusted by 10% up and down to obtain the tight and loose cases. The background merging uncertainty is taken from [40]. The uncertainty of the radiative effects correction is taken from [3]. The uncertainties of the variable set are estimated using the integral cross sections of three invariant masses, three theta angles, and three alpha angles (these are the nine single-differential variables). This is a known issue from previous analyses in this channel [15][46]. However, extending the limits of invariant mass histograms with four additional bins of equal size at both ends mitigates the impact.

Due to statistical limitation, acceptance error cuts, see Figs. 6.7 and 6.8 play a significant role in systematics. In the low Q^2 region, there are a significant number of bins without enough data in the simulation. For that reason, a relatively loose cut of 0.7 is chosen in the relative acceptance error. However, the experimental data decrease rapidly for high Q^2 region and the cut at 0.7 allows a lot of bins without enough statistics, which leads to fluctuations in single-differential cross sections as well as systematic uncertainties. As suggested in Chapter 4 of [15], the relative acceptance error cut 0.3 is used for the last five Q^2 bins. After having enough simulations, a cut of 0.3 will be applied to all Q^2 bins.

Since kinematic holes with zero acceptance are filled using TWOPEG-generated cross section values, this process is model dependent. Therefore, the uncertainty due to hole filling is conservatively set to 50% of the contribution of the filled holes. However, this systematic is not included in the total uncertainty calculation but added to the statistical uncertainties, as the lack of sufficient simulation statistics creates the majority of the holes currently present. The total systematic uncertainty in hole filling for the integrated cross section is 5.76%. Once more simulations are available, this uncertainty is expected to decrease significantly.

The overall systematic uncertainty (excluding hole filling) is estimated to be 7.11%, as summarized in Table 8.1. Each component was carefully analyzed by adjusting the relevant selection criteria to determine its effect on the results.

Table 8.1 List of estimated systematic uncertainties.

Item	Source	Error (%)
1	Sampling fraction cut	0.02 [40]
2	PCAL inefficient region cuts	0.074[40]
3	Fiducial volume cuts (all particles)	0.75
4	Δt cuts (both proton and π^+)	1.10
5	Removal of CD-FD tracks	0.42
6	Event selection MMSQ cuts	2.03
7	Momentum corrections (Task Force)	0.59
8	Hadron momentum corrections	0.71
9	Particle efficiency corrections	2.11
10	Background merging	3.0 [40]
11	Smearing MC data	0.86
12	Background subtraction	0.75
13	Acceptance error cut	1.55
14	Radiative effects	5.0 [3]
15	Variable set dependence	1.05
16	Total uncertainty	7.11

Chapter 9

Results and Conclusions

Using the CLAS12 RGA Fall 2018 dataset, nine single-differential and integrated cross sections for double-pion electroproduction are extracted, focusing on photon virtualities Q^2 in the range [2.0, 8.0] GeV^2. Figures 9.1 and 9.2 present the integrated cross sections for various Q^2 bins. As these results and previous CLAS results overlap in the range Q^2[2.0, 5.0] GeV^2 [3], the first five plots include the comparison. It is important to note that the previous CLAS results were obtained with finer W bin sizes of 25 MeV, while this analysis uses 50 MeV bins. To do the comparison, two consecutive bins are summed, and their uncertainties are combined using standard error propagation. The comparison shows overall agreement within the margins of the error bars. However, a slight systematic discrepancy is observed in the first three Q^2 bins, which could be due to the limited simulation statistics in this analysis. As shown in Fig. 6.9, contributions from holes are significant in this region. Additional simulations are needed to improve the results and compare them in these bins Q^2. For higher Q^2 bins, the number of experimental events decreases rapidly, leading to larger statistical uncertainties.

The nine single-differential cross sections extracted in this analysis are presented in Appendix A1. In those nine single-differential histograms, the blue markers are for final hole-filled cross sections, and error bars include both statistical and hole-filling errors. The cyan color represents the acceptance-corrected cross sections before hole filling. All other systematic errors are presented in filled gray color histograms at the bottom of each single-differential cross section.

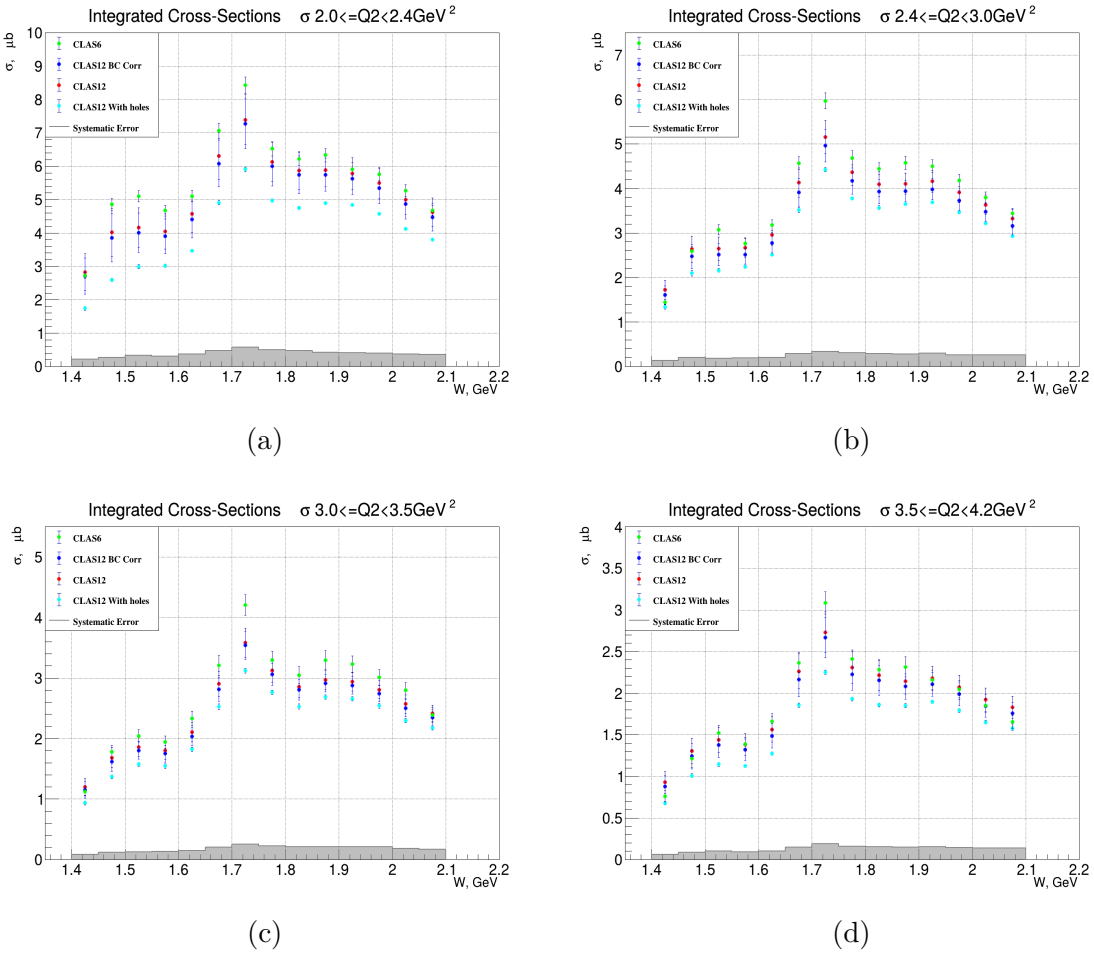

Figure 9.1 Measured integrated cross-section for all W ranges in $Q^2(\text{GeV}^2)$ bins of (a) $[2.0, 2.4]$, (b)$[2.4, 3.0]$, (c)$[3.0, 3.5]$, and (d)$[3.5, 4.2]$. The red dots with error bars are for the hole-filled cross sections, blue after bin centering corrections, cyan before hole filling and green previous CLAS results [3]. The filled gray histograms are for the total systematic error.

In conclusion, this dissertation presents, for the first time, the integrated and nine single-differential cross sections for two-pion electroproduction using the CLAS12 RGA Fall 2018 inbending dataset. These measurements span a broader kinematic range, covering Q^2 values from [2.0, 8.0] GeV^2 than previous CLAS results. The obtained cross sections mostly agree with previous CLAS results for Q^2 up to 5.0 GeV^2. The cross sections presented for Q^2 in the range of [5.0, 8.0] GeV^2 extend into a previously unexplored kinematic region where no prior CLAS measurements exist. By providing additional data points at higher Q^2, they enable improved cross-checks and

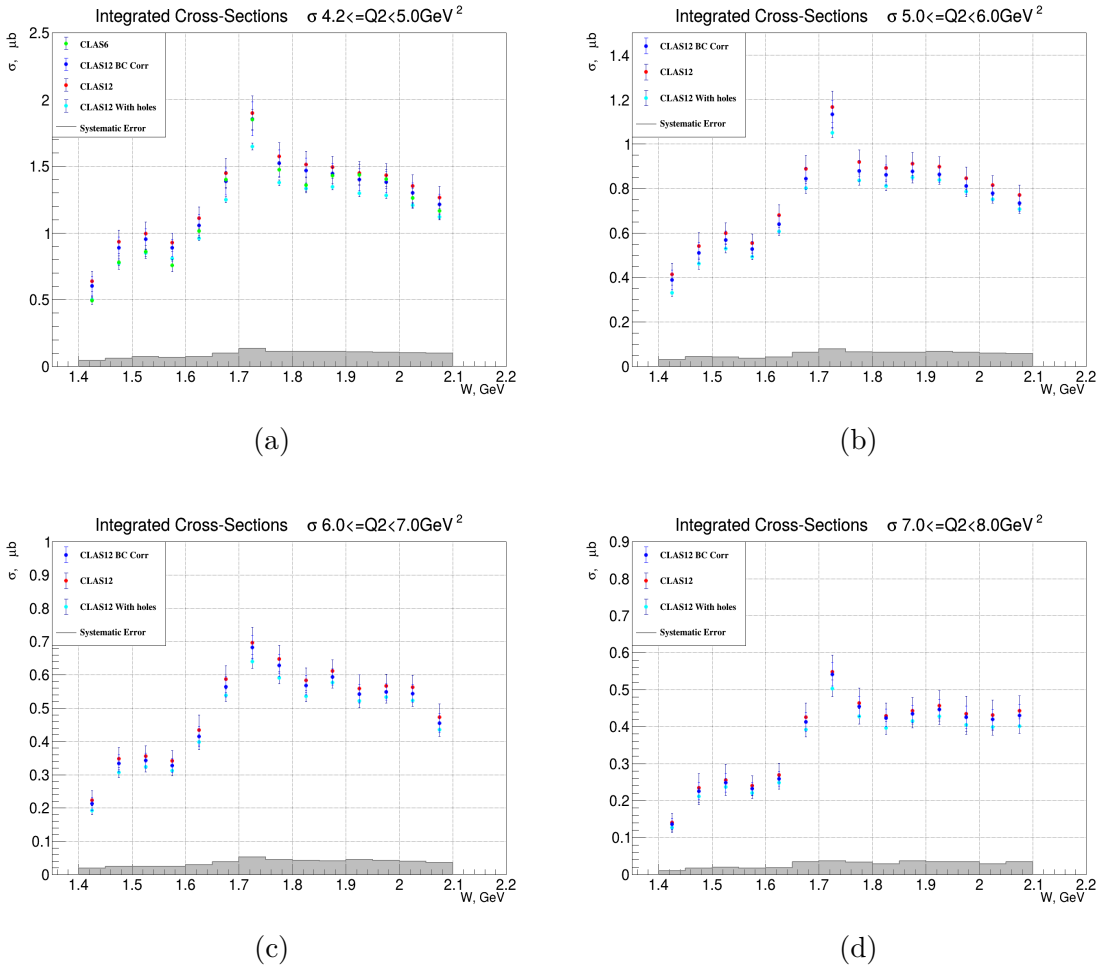

Figure 9.2 Measured integrated cross-section for all W ranges in $Q^2(\text{GeV}^2)$ of (a) $[4.2, 5.0]$, (b)$[5.0, 6.0]$, (c)$[6.0, 7.0]$, and (d)$[7.0, 8.0]$. The red dots with error bars are for the hole-filled cross sections, blue after bin centering corrections, cyan before hole filling and green (where available) previous CLAS results [3]. The filled gray histograms are for the total systematic error.

enhance the extraction of resonance electroexcitation amplitudes using the JM model framework. This extended dataset will contribute to the ongoing efforts in studying the structure of excited nucleon states and deepening the understanding of the strong interaction in the non-perturbative regime of QCD.

Bibliography

[1] V. I. Mokeev, P. Achenbach, V. D. Burkert, D. S. Carman, R. W. Gothe, A. N. Hiller Blin, E. L. Isupov, K. Joo, K. Neupane, and A. Trivedi. First results on nucleon resonance electroexcitation amplitudes from $ep \to e'\pi^+\pi^-p'$ cross sections at $W = 1.4$–1.7 GeV and $Q^2 = 2.0$–$5.0\,GeV^2$. *Phys. Rev. C*, 108:025204, Aug 2023.

[2] E. L. Isupov et al. Measurements of $ep \to e'\pi^+\pi^-p'$ cross sections with clas at $1.40\,\text{GeV} < W < 2.0\,\text{GeV}$ and $2.0\,\text{GeV}^2 < Q^2 < 5.0\,\text{GeV}^2$. *Phys. Rev. C*, 96:025209, Aug 2017.

[3] Arjun Trivedi. *Measurement of New Observables from the $\pi^+\pi^-$ Electroproduction off the Proton*. PhD thesis, Department of Physics and Astronomy, USC, Columbia, SC, 2016.

[4] V.D. Burkert et al. The CLAS12 spectrometer at Jefferson laboratory. *Nucl. Instrum. Methods A*, 959:163419, 2020.

[5] Christopher Dilks. CLAS12 Quality Assurance Database. `https://github.com/JeffersonLab/clas12-qadb/tree/main`. Accessed on: [02/27/2025].

[6] Jefferson Lab. Experimental Hall B, CLAS12. `https://www.jlab.org/Hall-B/clas12-web/`, note = Accessed on: [02/27/2025].

[7] R. Fair et al. The clas12 superconducting magnets. *Nucl. Instrum. Methods A*, 962:163419, 2020.

[8] M.D. Mestayer et al. The clas12 drift chamber system. *Nucl. Instrum. Methods A*, 959:163518, 2020.

[9] Y.G. Sharabian et al. The clas12 high threshold Cherenkov counter. *Nucl. Instrum. Methods A*, 968:163824, 2020.

[10] D.S. Carman et al. The clas12 forward time-of-flight system. *Nucl. Instrum. Methods A*, 960:163629, 2020.

[11] G. Asryan et al. The clas12 forward electromagnetic calorimeter. *Nucl. Instrum. Methods A*, 959:163425, 2020.

[12] M.A. Antonioli et al. The clas12 silicon vertex tracker. *Nucl. Instrum. Methods A*, 962:163701, 2020.

[13] A. Acker et al. The clas12 micromegas vertex tracker. *Nucl. Instrum. Methods A*, 957:163423, 2020.

[14] D.S. Carman et al. The clas12 central time-of-flight system. *Nucl. Instrum. Methods A*, 960:163626, 2020.

[15] Iuliia Skorodumina. *$\pi^+\pi^-$ electroproduction off protons in deuterium: measurements of quasi-free cross sections and kinematic probing of final state interactions*. PhD thesis, Department of Physics and Astronomy, USC, Columbia, SC, 2021.

[16] RGA JLab CLAS12. Pass-2 review for rga fall 2018 (inbending and outbending). `https://clasweb.jlab.org/wiki/index.php/Run_Group_A#tab=Pass\protect\discretionary{\char\hyphenchar\font}{}{}2_Review`. Accessed on: [04/03/2025].

[17] I. G. Aznauryan et al. Studies of Nucleon Resonance Structure in Exclusive Meson Electroproduction. *International Journal of Modern Physics E*, 22(06):1330015, 2013.

[18] Volker Burkert et al. Studies of Excited Nucleons in Exclusive Electroproduction. `https://indico.bnl.gov/event/857/contributions/18971/attachments/16722/20436/Write-up-for-the-White-Paper.pdf`. Accessed on: [01/26/2025].

[19] C. D. Roberts. Opportunities and challenges for theory in the N* program. *AIP Conference Proceedings*, 1432(1):19–25, 04 2012.

[20] A. V. Sarantsev et al. Photoproduction of two charged pions off protons in the resonance region. *Phys. Rev. C*, 111:035203, Mar 2025.

[21] G. V. Fedotov and other. Analysis report on the $ep \to e'p'\pi^+\pi^-$ reaction in the clas detector with a 2.039 GeV beam for 0.4 GeV^2 < Q < 1.0 GeV^2 and 1.3 GeV < W < 1.825 GeV, 2016.

[22] V. I. Mokeev et al. Model analysis of the $ep \to e'p'\pi^+\pi^-$ electroproduction reaction on the proton. *Phys. Rev.*, C 80, 2009.

[23] V. I. Mokeev et al. Experimental study of the $P_{11}(1440)$ and $D_{13}(1520)$ resonances from the CLAS data on $ep \to e'p'\pi^+\pi^-$. *Phys. Rev.*, C 86, 2012.

[24] V. I. Mokeev et al. New Results from the Studies of the $N(1440)1/2^+$, $N(1520)3/2^-$, and $\Delta(1620)1/2^-$ Resonances in Exclusive $ep \to e'p'\pi^+\pi^-$ Electroproduction with the CLAS Detector. *Phys. Rev.*, C 93(2):025206, 2016.

[25] I. G. Aznauryan et al. Electroexcitation of nucleon resonances from clas data on single pion electroproduction. *Physical Review C*, 80(5), November 2009.

[26] RGA. Common Analysis Note. https://www.jlab.org/Hall-B/shifts/admin/paper_reviews/2020/RGA_Analysis_Overview_and_Procedures_Nov_4_2020-6245173-2020-12-09-v3.pdf. Accessed on: [01/26/2025].

[27] M. Ungaro et al. The clas12 low threshold Cherenkov detector. *Nucl. Instrum. Methods A*, 957:163420, 2020.

[28] B. Raydo et. al. The clas12 trigger system. *Nuclear Instruments and Methods in Physics Research Section A: Accelerators, Spectrometers, Detectors and Associated Equipment*, 960:163529, 2020.

[29] S. Boyarinov et al. The clas12 data acquisition system. *Nuclear Instruments and Methods in Physics Research Section A: Accelerators, Spectrometers, Detectors and Associated Equipment*, 966:163698, 2020.

[30] V. Ziegler et al. The CLAS12 software framework and event reconstruction. *Nuclear Inst. and Methods in Physics Research, A*, 959:163472, 2020.

[31] N. Tyler Jefferson Lab. CLAS12 Hipo_tools. https://github.com/JeffersonLab/hipo_tools, note = Accessed on: [02/15/2025].

[32] Jefferson Lab CLAS12. CLAS12 Data Summary Tapes. https://clasweb.jlab.org/wiki/index.php/CLAS12_DSTs. Accessed on: [02/27/2025].

[33] Jefferson Lab CLAS12. CLAS12_Momentum_Correction. https://clasweb.jlab.org/wiki/index.php/CLAS12_Momentum_Corrections. Accessed on: [02/27/2025].

[34] CLAS12 Open Science Grid, Jlab. Clas12 monte-carlo job submission portal. https://gemc.jlab.org/web_interface/index.php. Accessed on: [03/10/2025].

[35] M. Ungaro et al. The clas12 geant4 simulation. *Nuclear Instruments and Methods in Physics Research Section A: Accelerators, Spectrometers, Detectors and Associated Equipment*, 959:163422, 2020.

[36] Iu. Skorodumina, G. V. Fedotov, V. D. Burkert, E. Golovach, R. W. Gothe, and V. Mokeev. Twopeg: An event generator for charged double pion electroproduction off proton, 2017.

[37] Stefan Diehl et al. A Multidimensional Study of Hard Exclusive π^+ BSA in the GPD Regime. `https://www.jlab.org/Hall-B/shifts/admin/paper_reviews/2022/pip_gpd_analysis_note_v3-7074513-2022-03-10-v7.pdf`. Accessed on: [01/26/2025].

[38] L.C. Andrews. *Special Functions of Mathematics for Engineers*. Online access with subscription: SPIE Digital Library. SPIE Optical Engineering Press, 1998.

[39] The lmfit development team. lmfit builtin models. `https://lmfit.github.io/lmfit-py/builtin_models.html#builtin-models-chapter`. Accessed on: [01/26/2025].

[40] V. Klimenko et. al. Inclusive electron scattering in the resonance region off a hydrogen target with clas12, 2025.

[41] C. Smith et al. EC Calibration Status Table. `https://clasweb.jlab.org/cgi-bin/ccdb/objects`. Accessed on: [02/27/2025].

[42] G. V. Fedotov et al. Electroproduction of $p\pi^+\pi^-$ off protons at 0.2 GeV^2 < Q < 0.6 GeV^2 and 1.3 GeV < W < 1.57 GeV with the clas detector. *Physical Review C*, 79(1), January 2009.

[43] G. V. Fedotov et al. Electroproduction of $p\pi^+\pi^-$ off protons at $0.2 < Q^2 < 0.6\ GeV^2$ and $1.3 < W < 1.57\ GeV$ with CLAS. *Phys. Rev.*, C79:015204, 2009.

[44] S. Stepanyan et al. Clas12 fd charged particle reconstruction efficiency and the beam background merging. https://misportal.jlab.org/mis/physics/clas12/viewFile.cfm/2020-005.pdf?documentId=70. Accessed on: [2025-02-27].

[45] L. W. MO and Y. S. TSAI. Radiative Corrections to Elastic and Inelastic ep and μp Scattering. *Rev.Mod.Phys.*, 41:205–235, 1969.

[46] Christopher Andrew McLauchlin. *Measurement of Single Differential Cross Sections, Polarization Observables, and Beam-Spin Asymmetry for Charged Two-Pion Electroproduction off the Proton with CLAS*. PhD thesis, Department of Physics and Astronomy, USC, Columbia, SC, 2024.

Appendix A

Measured single-differential cross sections

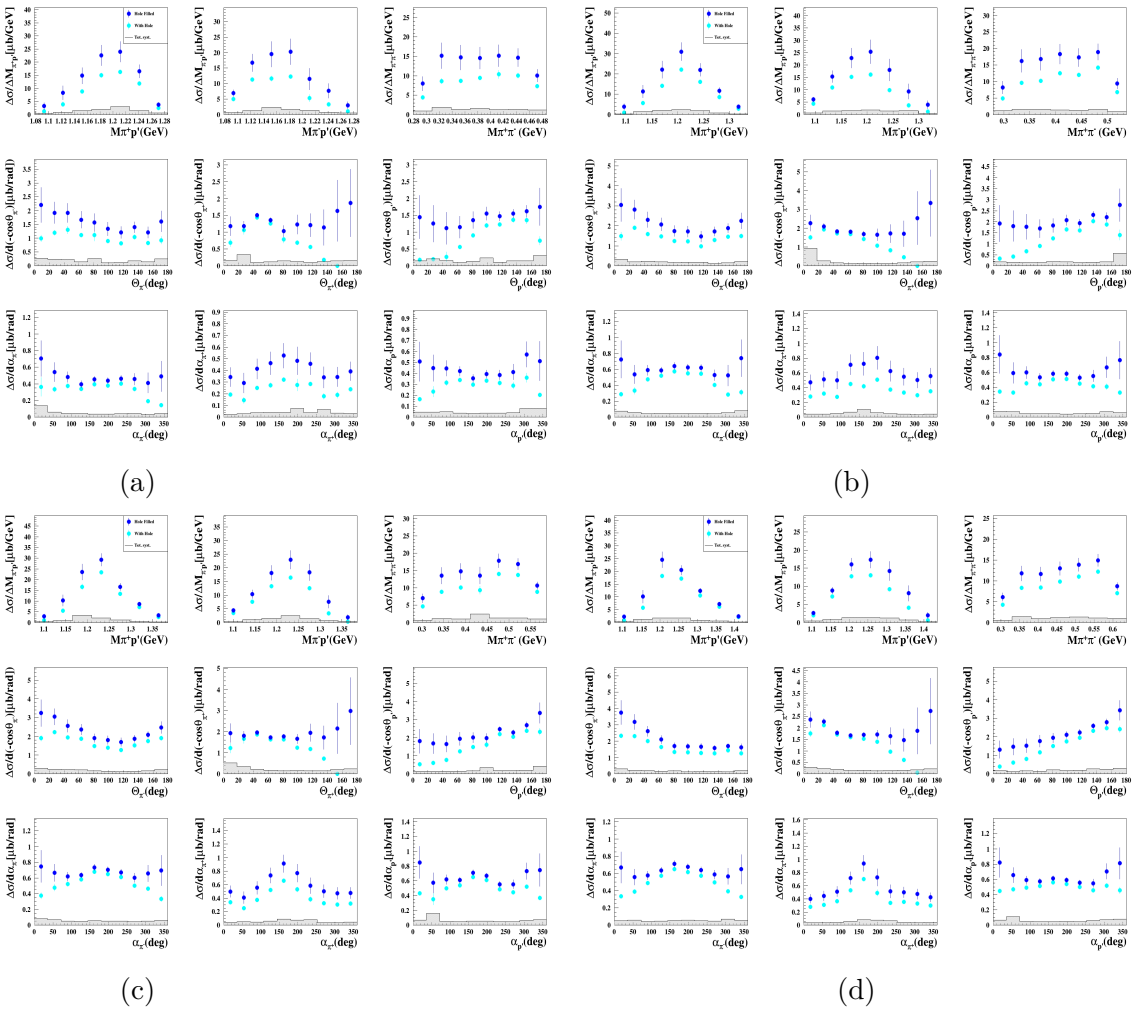

Figure A.1 Measured nine single-differential cross sections for $W(\mathrm{GeV})$–$Q^2(\mathrm{GeV}^2)$ bins: (a)$[1.40, 1.45] - [2.0, 2.4]$, (b)$[1.45, 1.50] - [2.0, 2.4]$, (c)$[1.50, 1.55] - [2.0, 2.4]$, and (d)$[1.55, 1.60] - [2.0, 2.4]$.

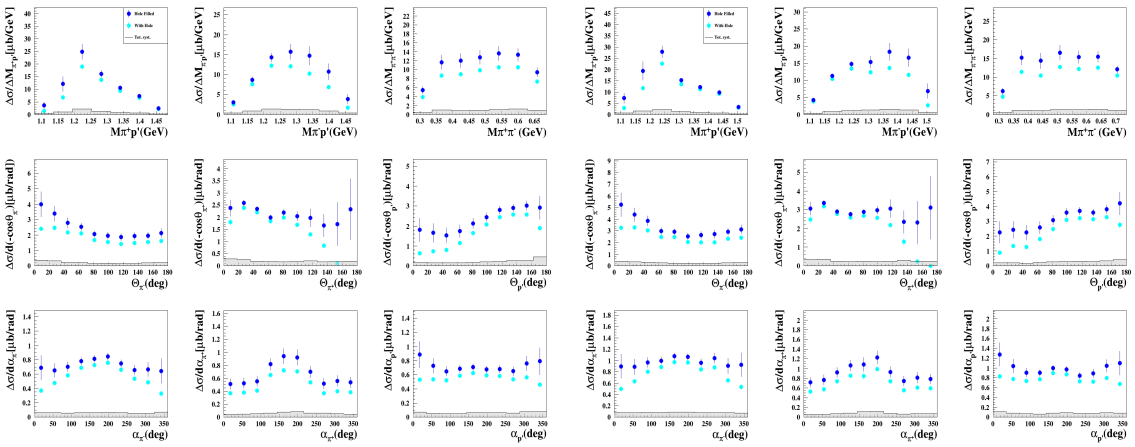

(a) (b)

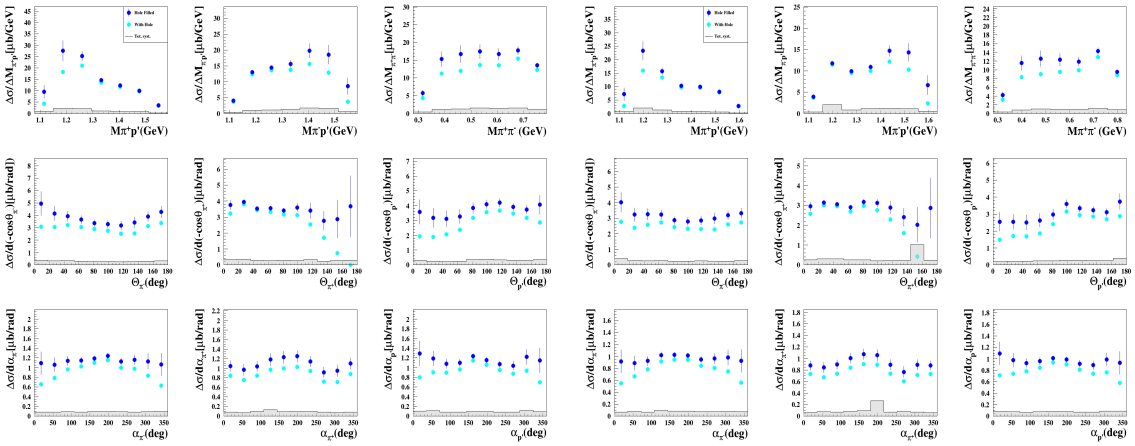

(c) (d)

Figure A.2 Measured nine single-differential cross sections for $W(\mathrm{GeV})$−$Q^2(\mathrm{GeV}^2)$ bins: (a)$[1.60, 1.65] - [2.0, 2.4]$, (b)$[1.65, 1.70] - [2.0, 2.4]$, (c)$[1.70, 1.75] - [2.0, 2.4]$, and (d)$[1.75, 1.80] - [2.0, 2.4]$.

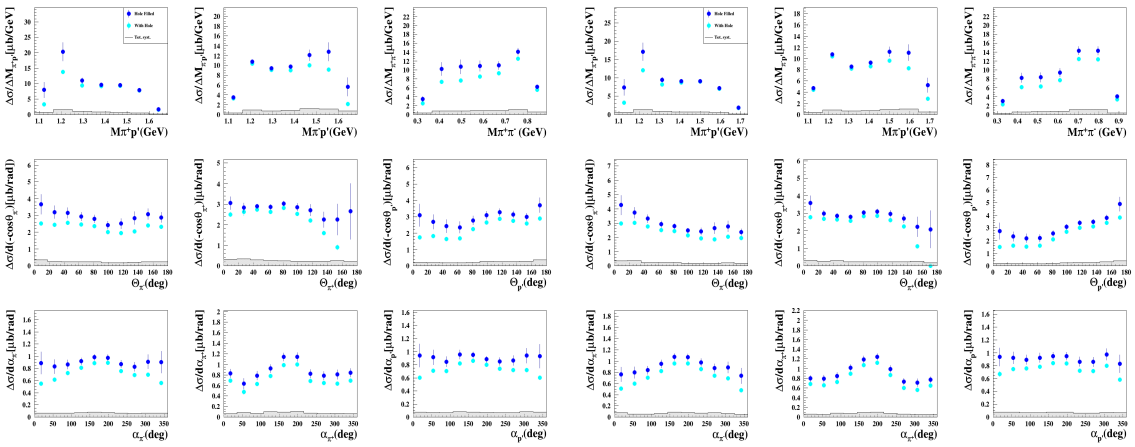

(a) (b)

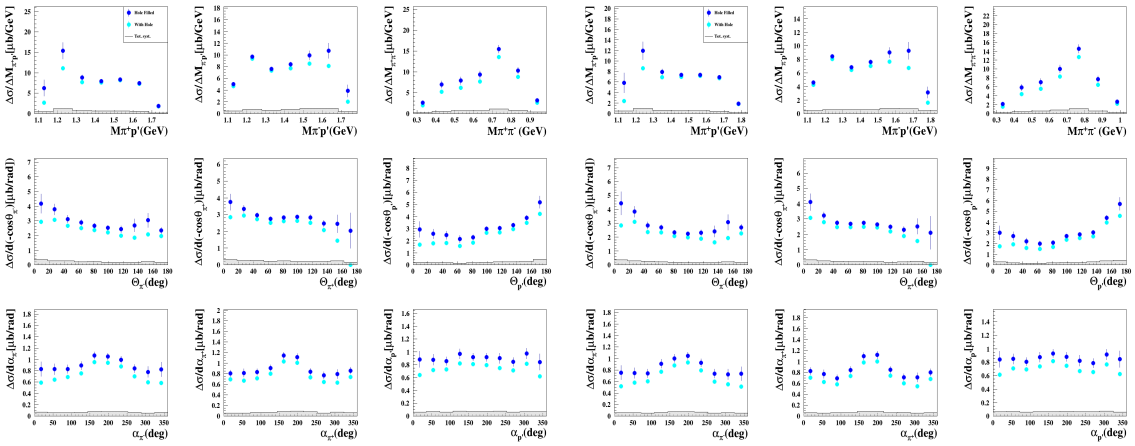

(c) (d)

Figure A.3 Measured nine single-differential cross sections for $W(\mathrm{GeV})-Q^2(\mathrm{GeV}^2)$ bins: (a)$[1.80, 1.85] - [2.0, 2.4]$, (b)$[1.85, 1.90] - [2.0, 2.4]$, (c)$[1.90, 1.95] - [2.0, 2.4]$, and (d)$[1.95, 2.00] - [2.0, 2.4]$.

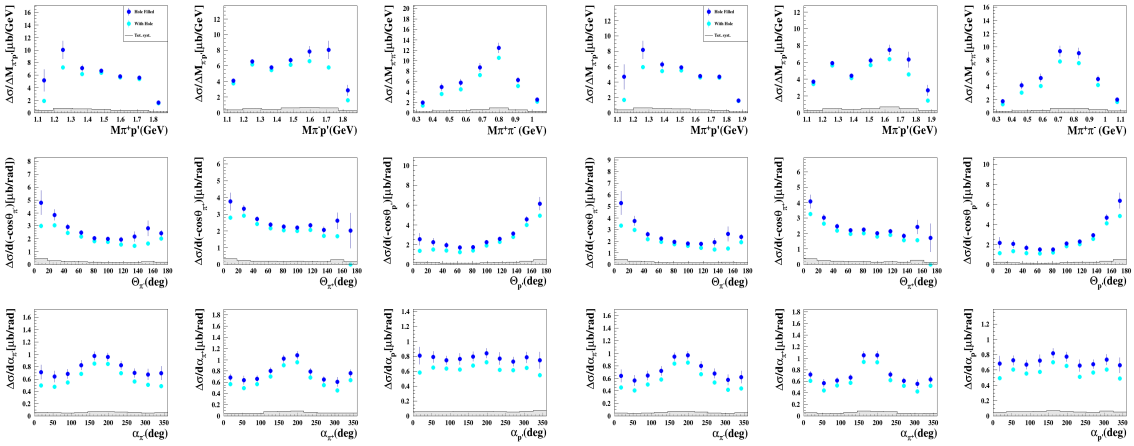

(a) (b)

Figure A.4 Measured nine single-differential cross sections for $W(\mathrm{GeV})-Q^2(\mathrm{GeV}^2)$ bins: (a)$[2.00, 2.05] - [2.0, 2.4]$, and (b)$[2.05, 2.10] - [2.0, 2.4]$.

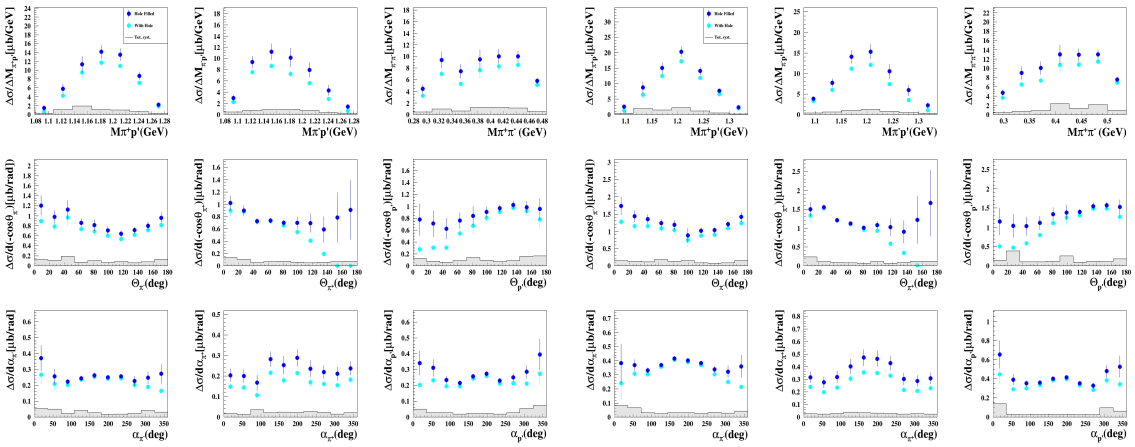

(a) (b)

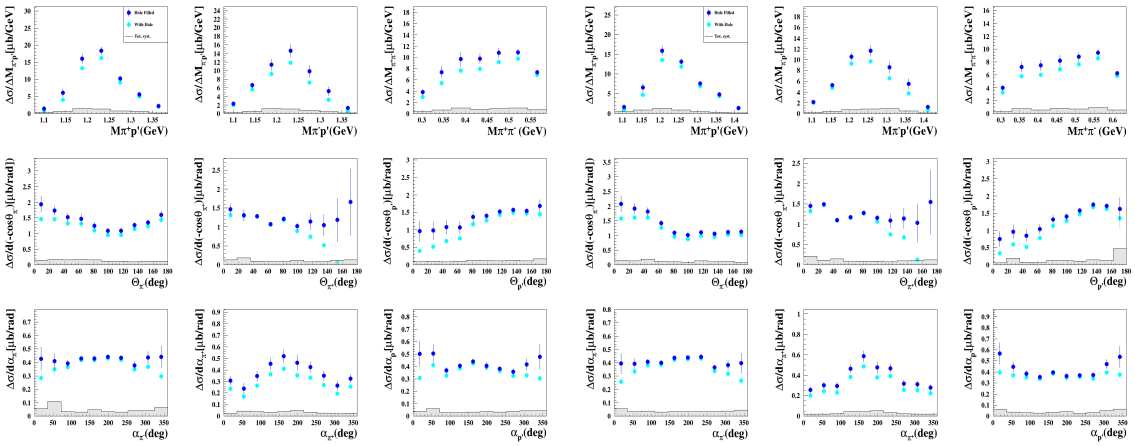

(c) (d)

Figure A.5 Measured nine single-differential cross sections for $W(\mathrm{GeV})-Q^2(\mathrm{GeV}^2)$ bins: (a)$[1.40, 1.45] - [2.0, 2.4]$, (b)$[1.45, 1.50] - [2.0, 2.4]$, (c)$[1.50, 1.55] - [2.4, 3.0]$, and (d)$[1.55, 1.60] - [2.4, 3.0]$.

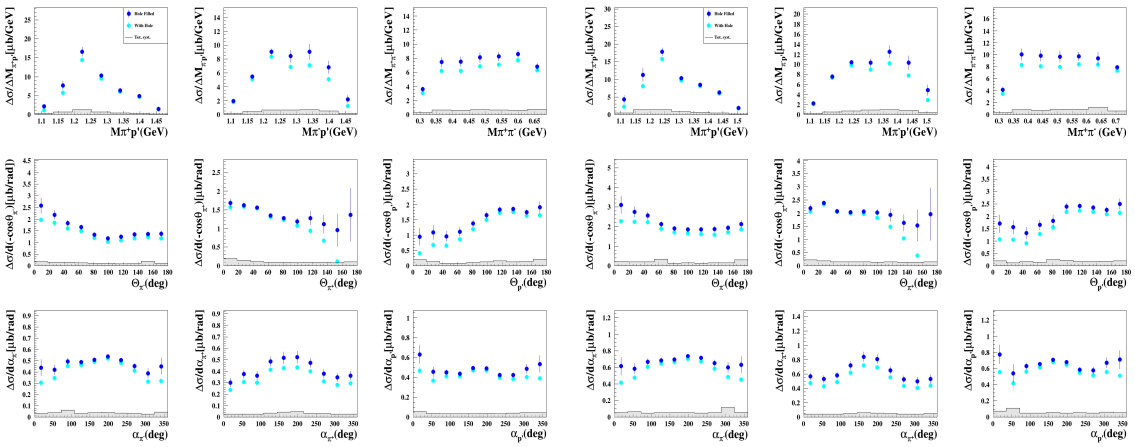

(a) (b)

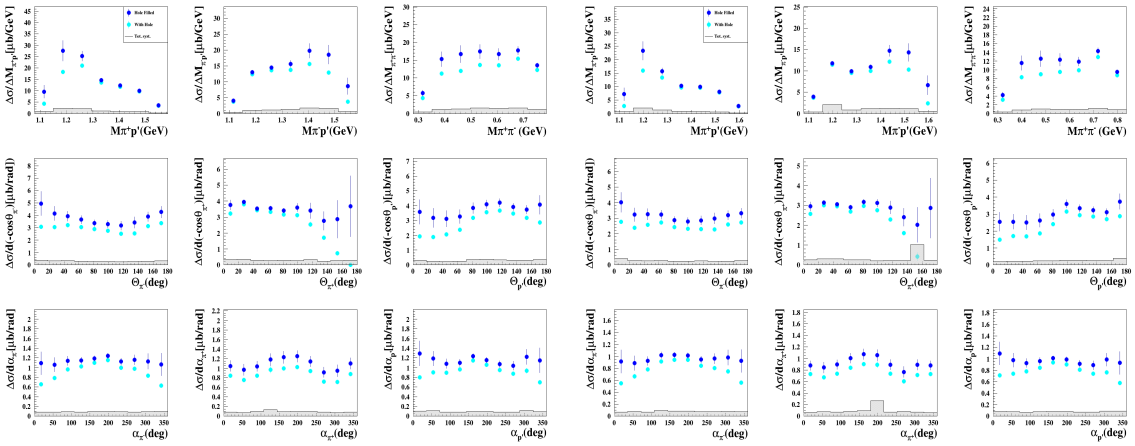

(c) (d)

Figure A.6 Measured nine single-differential cross sections for $W(\mathrm{GeV})$−$Q^2(\mathrm{GeV}^2)$ bins: (a)$[1.60, 1.65] - [2.0, 2.4]$, (b)$[1.65, 1.70] - [2.0, 2.4]$, (c)$[1.70, 1.75] - [2.4, 3.0]$, and (d)$[1.75, 1.80] - [2.4, 3.0]$.

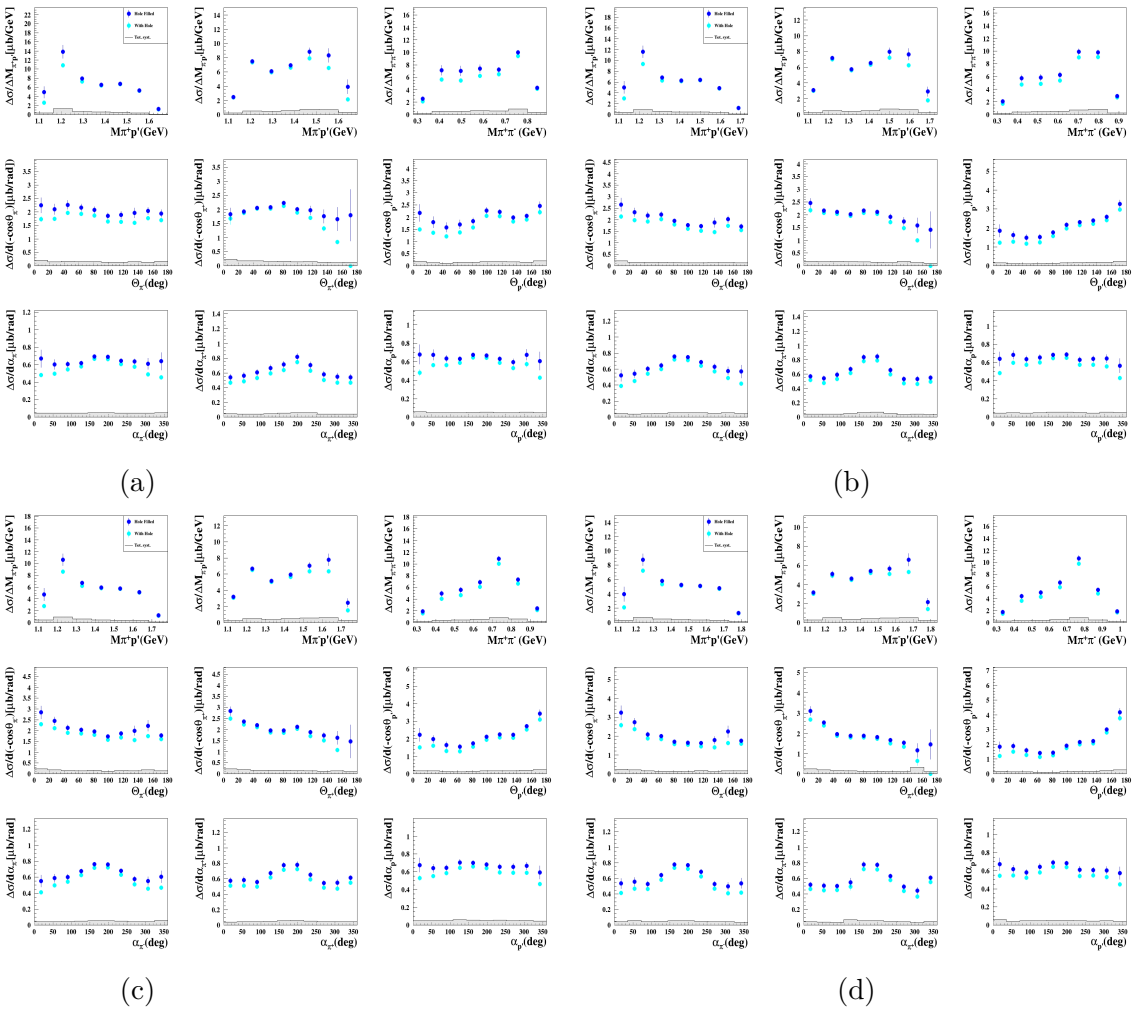

Figure A.7 Measured nine single-differential cross sections for $W(\mathrm{GeV})-Q^2(\mathrm{GeV}^2)$ bins: (a)$[1.80, 1.85] - [2.0, 2.4]$, (b)$[1.85, 1.90] - [2.0, 2.4]$, (c)$[1.90, 1.95] - [2.4, 3.0]$, and (d)$[1.95, 2.00] - [2.4, 3.0]$.

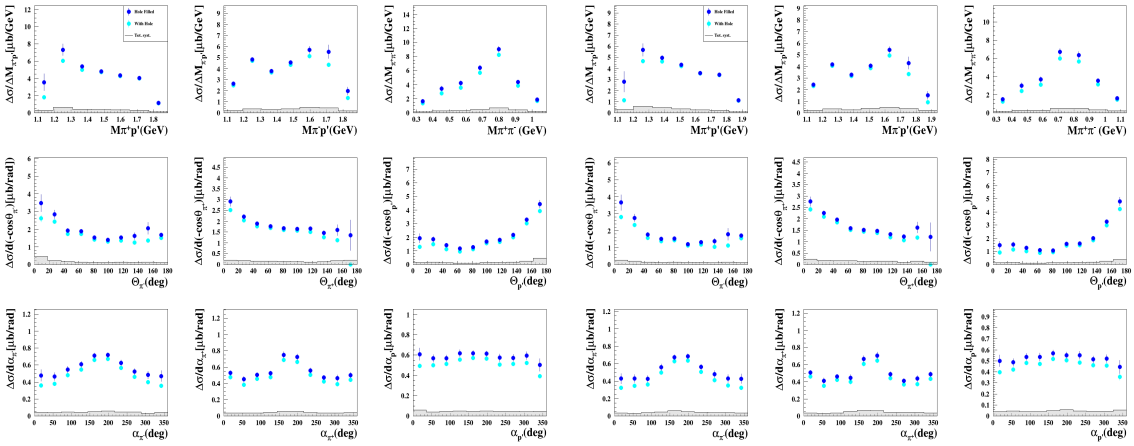

(a) (b)

Figure A.8 Measured nine single-differential cross sections for $W(\mathrm{GeV})-Q^2(\mathrm{GeV}^2)$ bins: (a)$[2.00, 2.05] - [2.4, 3.0]$, and (b)$[2.05, 2.10] - [2.4, 3.0]$.

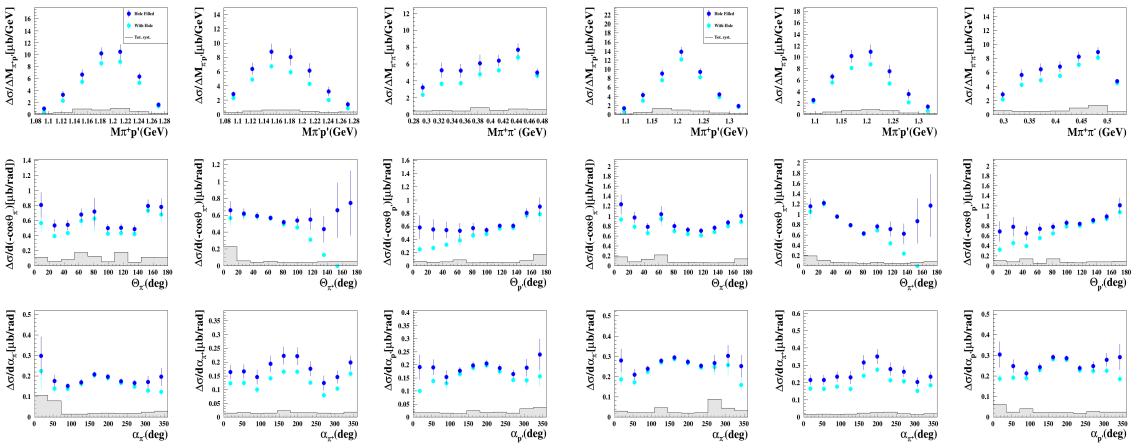

(a) (b)

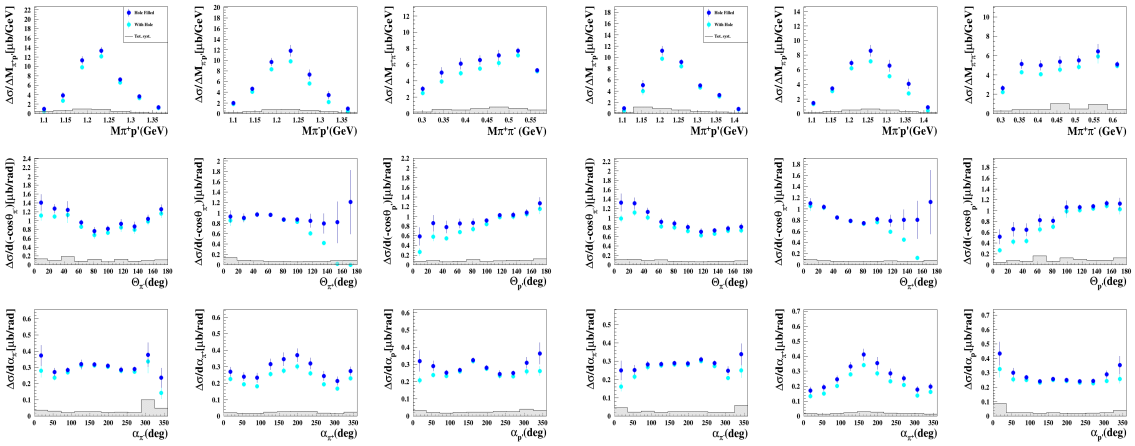

(c) (d)

Figure A.9 Measured nine single-differential cross sections for $W(\mathrm{GeV})-Q^2(\mathrm{GeV}^2)$ bins: (a)$[1.40, 1.45] - [3.0, 3.5]$, (b)$[1.45, 1.50] - [3.0, 3.5]$, (c)$[1.50, 1.55] - [3.0, 3.5]$, and (d)$[1.55, 1.60] - [3.0, 3.5]$.

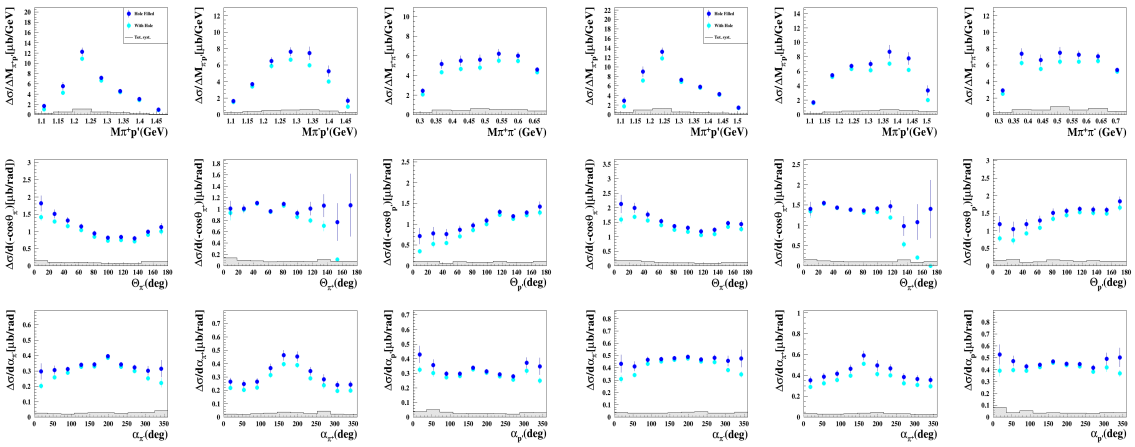

(a) (b)

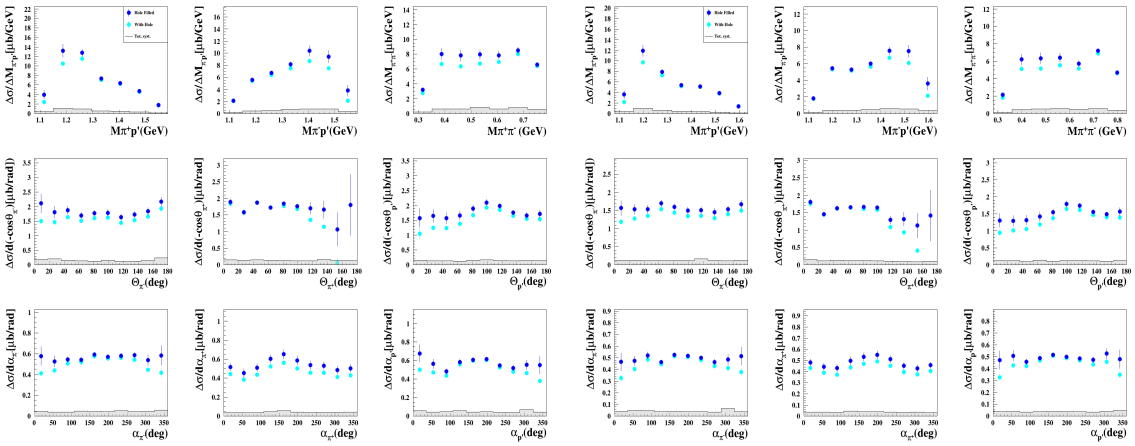

(c) (d)

Figure A.10 Measured nine single-differential cross sections for $W(\mathrm{GeV})$−$Q^2(\mathrm{GeV}^2)$ bins: (a)$[1.60, 1.65] - [3.0, 3.5]$, (b)$[1.65, 1.70] - [3.0, 3.5]$, (c)$[1.70, 1.75] - [3.0, 3.5]$, and (d)$[1.75, 1.80] - [3.0, 3.5]$.

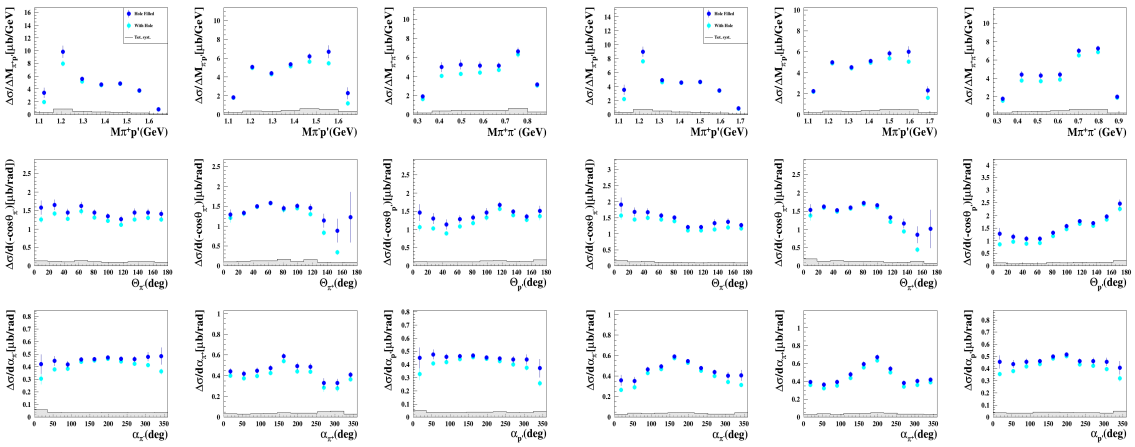

(a) (b)

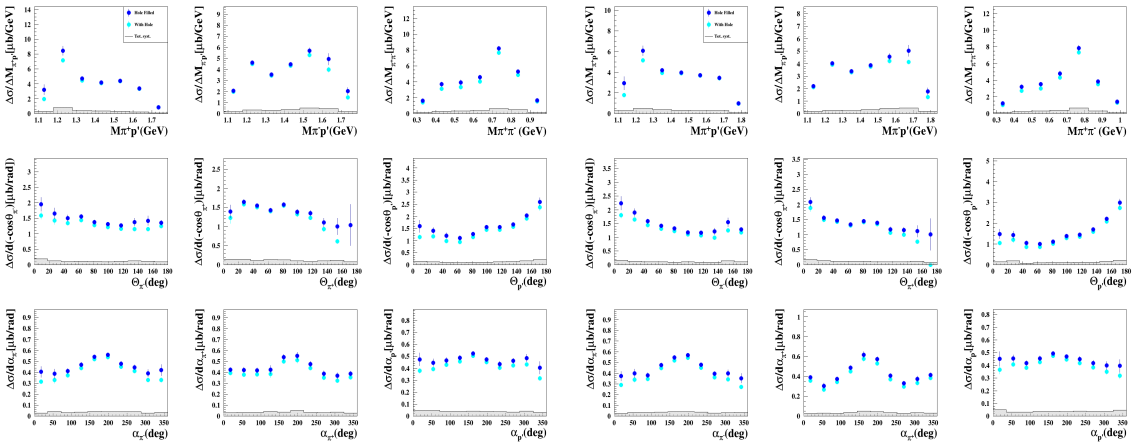

(c) (d)

Figure A.11 Measured nine single-differential cross sections for $W(\mathrm{GeV})-Q^2(\mathrm{GeV}^2)$ bins: (a)$[1.80, 1.85] - [3.0, 3.5]$, (b)$[1.85, 1.90] - [3.0, 3.5]$, (c)$[1.90, 1.95] - [3.0, 3.5]$, and (d)$[1.95, 2.00] - [3.0, 3.5]$.

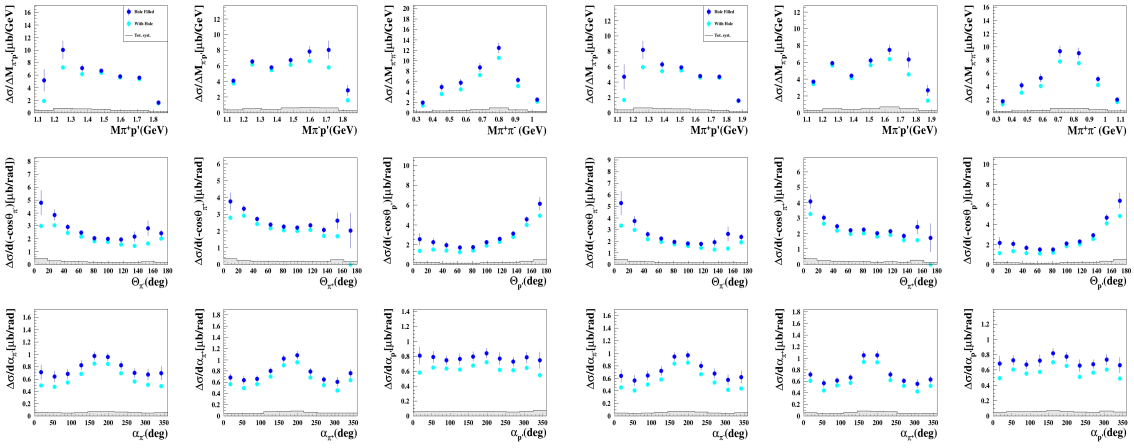

(a) (b)

Figure A.12 Measured nine single-differential cross sections for $W(\mathrm{GeV})-Q^2(\mathrm{GeV}^2)$ bins: (a)$[2.00, 2.05] - [3.0, 3.5]$, and (b)$[2.05, 2.10] - [3.0, 3.5]$.

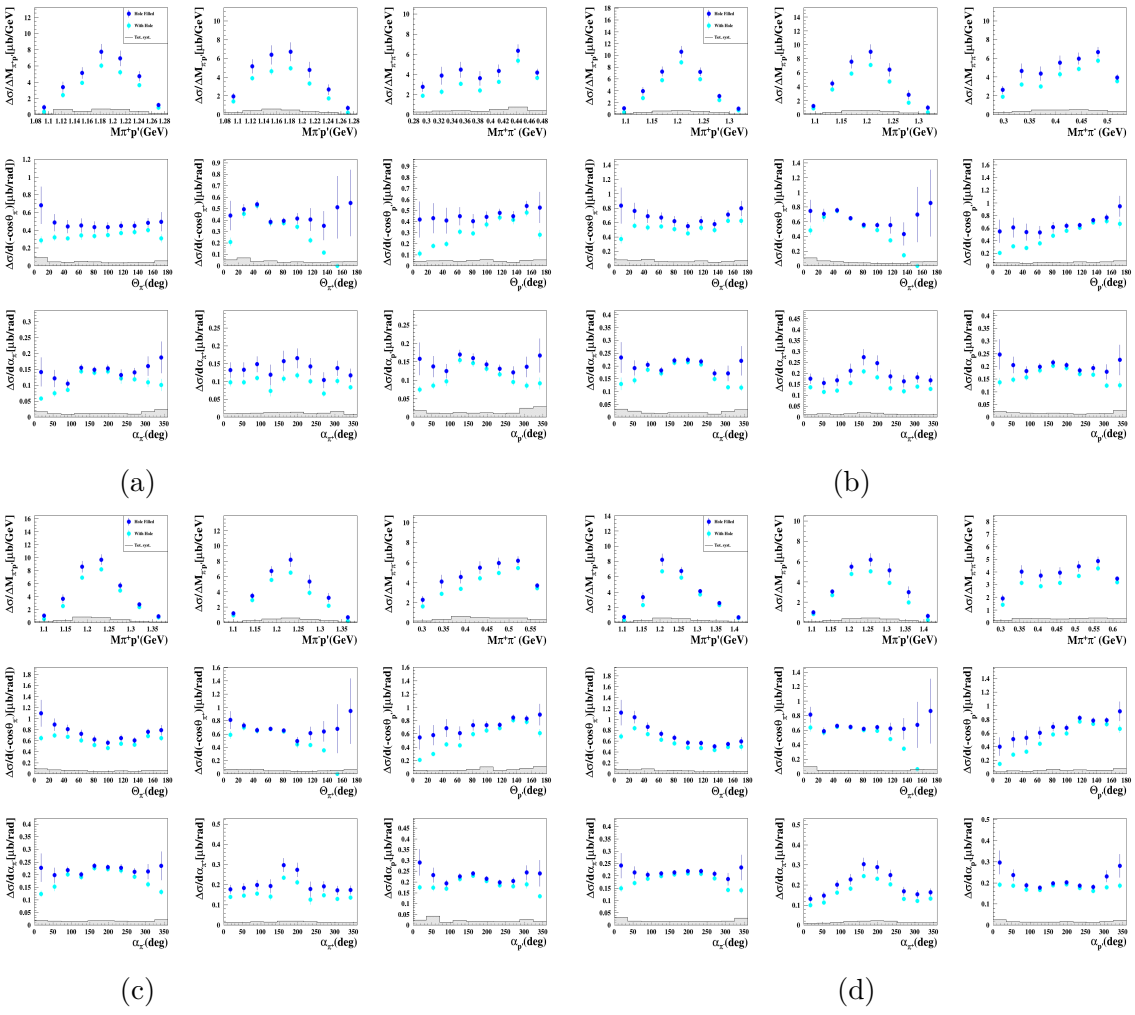

Figure A.13 Measured nine single-differential cross sections for $W(\mathrm{GeV})-Q^2(\mathrm{GeV}^2)$ bins: (a)$[1.40, 1.45] - [3.5, 4.2]$, (b)$[1.45, 1.50] - [3.5, 4.2]$, (c)$[1.50, 1.55] - [3.5, 4.2]$, and (d)$[1.55, 1.60] - [3.5, 4.2]$.

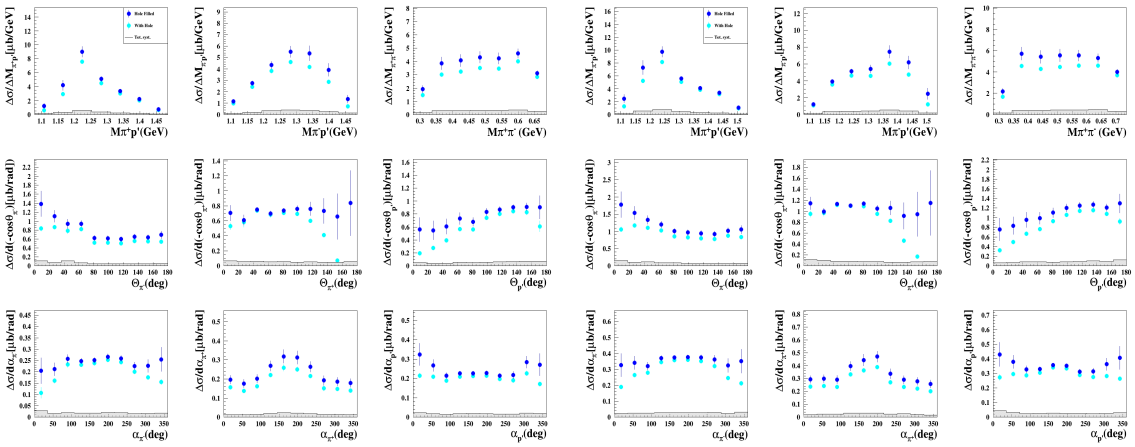

(a) (b)

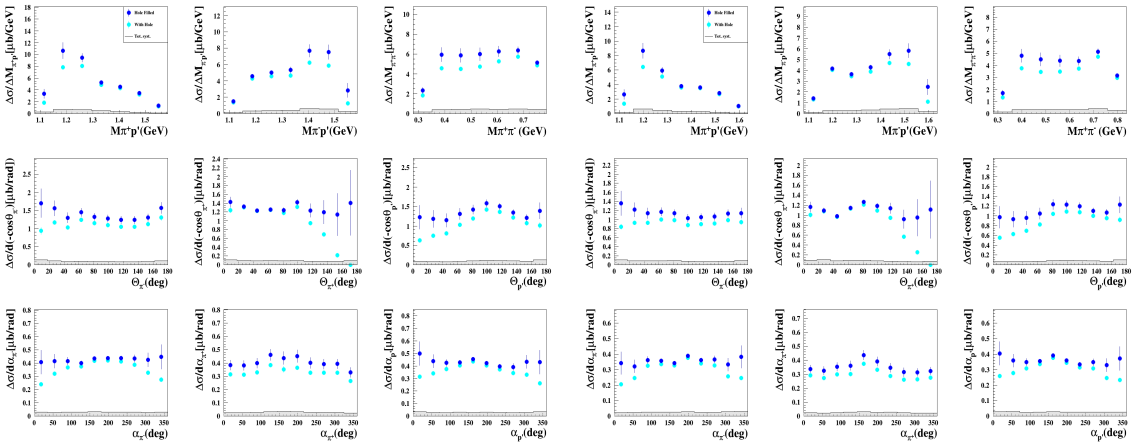

(c) (d)

Figure A.14 Measured nine single-differential cross sections for $W(\mathrm{GeV})$−$Q^2(\mathrm{GeV}^2)$ bins: (a)$[1.60, 1.65] - [3.5, 4.2]$, (b)$[1.65, 1.70] - [3.5, 4.2]$, (c)$[1.70, 1.75] - [3.5, 4.2]$, and (d)$[1.75, 1.80] - [3.5, 4.2]$.

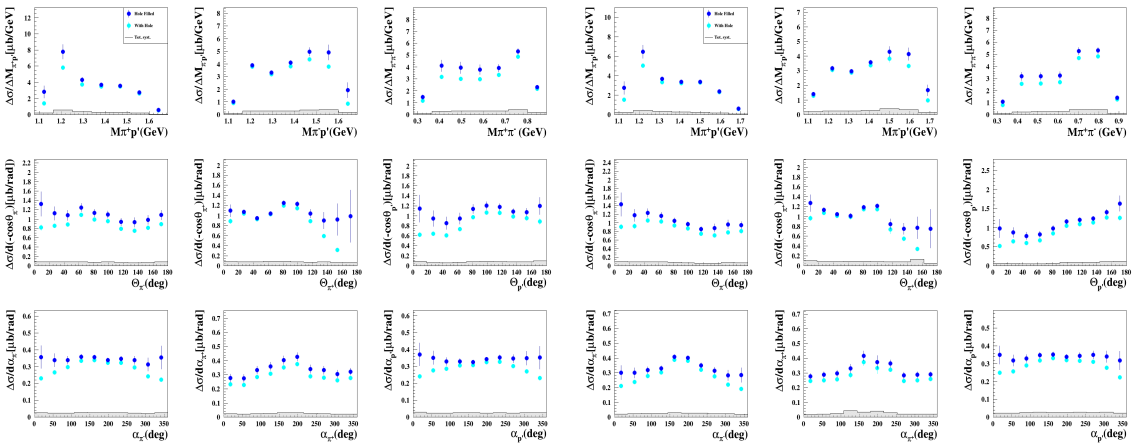

(a) (b)

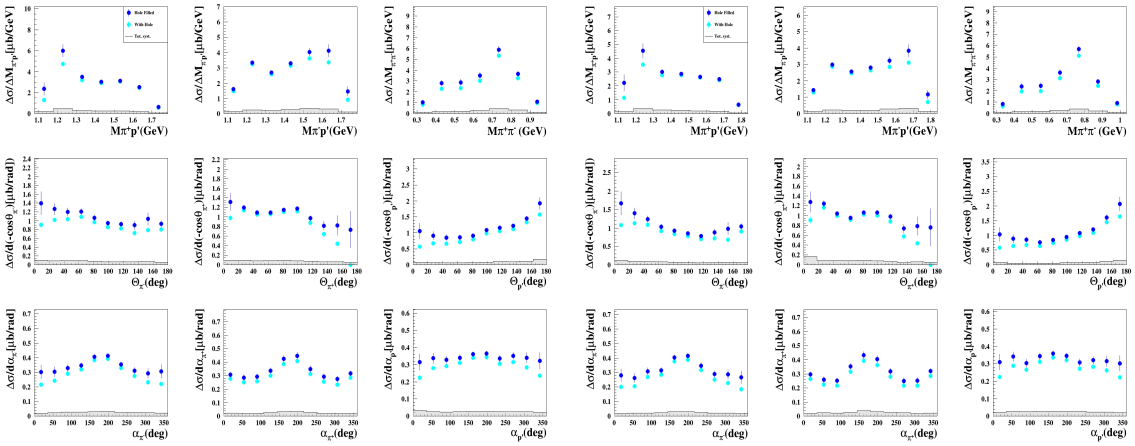

(c) (d)

Figure A.15 Measured nine single-differential cross sections for $W(\mathrm{GeV})-Q^2(\mathrm{GeV}^2)$ bins: (a)$[1.80, 1.85] - [3.5, 4.2]$, (b)$[1.85, 1.90] - [3.5, 4.2]$, (c)$[1.90, 1.95] - [3.5, 4.2]$, and (d)$[1.95, 2.00] - [3.5, 4.2]$.

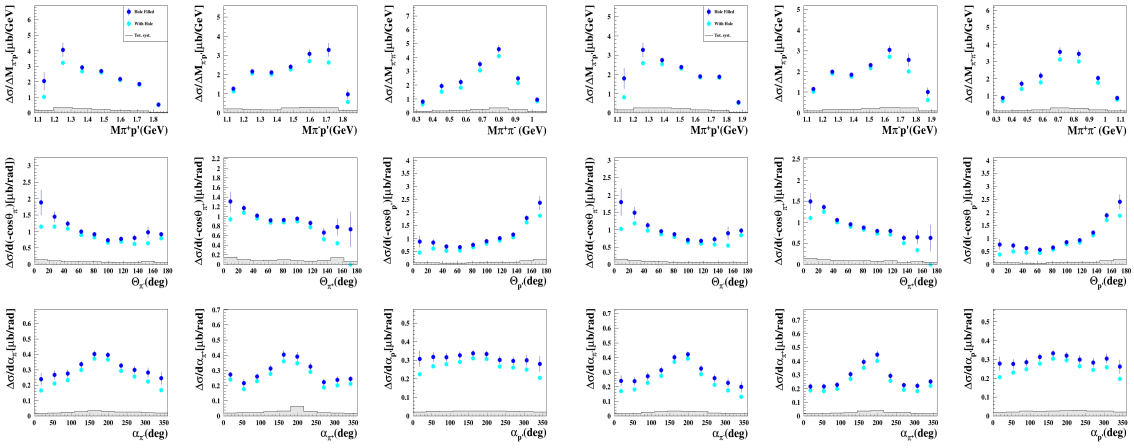

(a) (b)

Figure A.16 Measured nine single-differential cross sections for $W(\mathrm{GeV})-Q^2(\mathrm{GeV}^2)$ bins: (a)$[2.00, 2.05] - [3.5, 4.2]$, and (b)$[2.05, 2.10] - [3.5, 4.2]$.

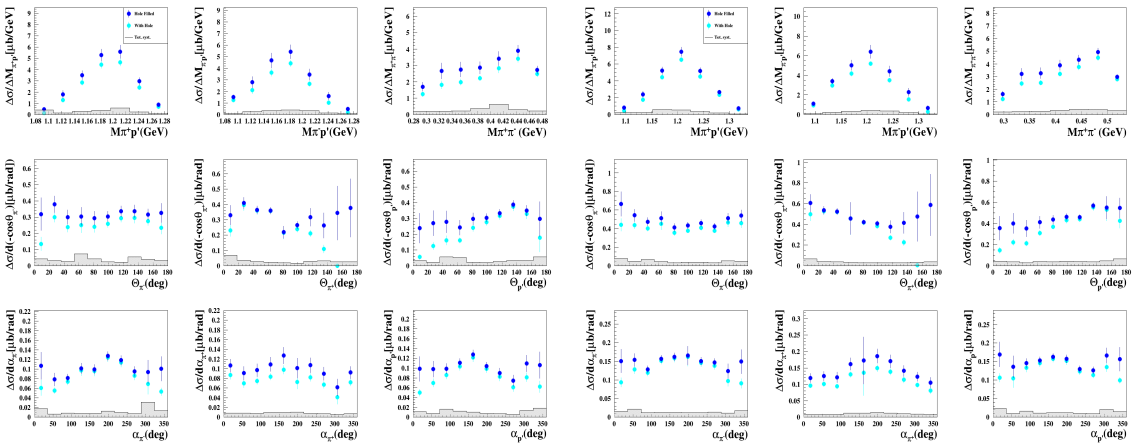

(a) (b)

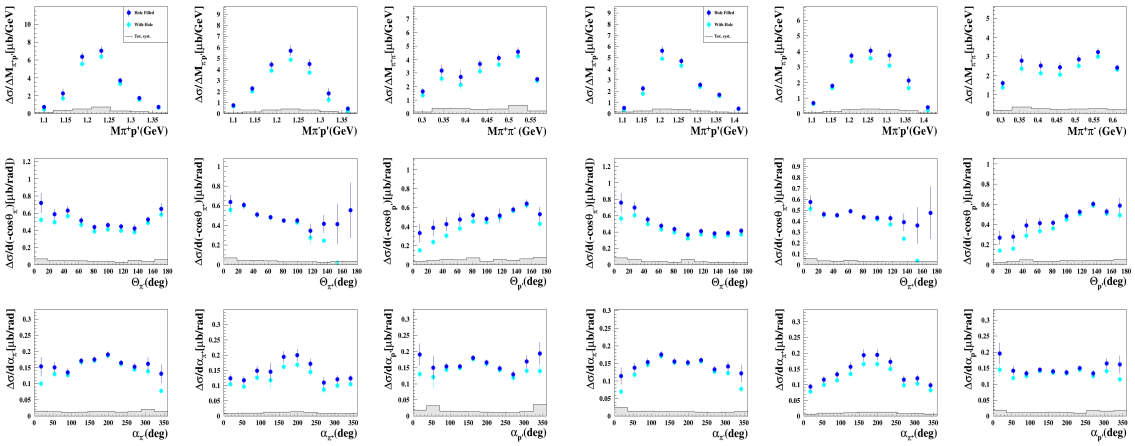

(c) (d)

Figure A.17 Measured nine single-differential cross sections for $W(\mathrm{GeV})$−$Q^2(\mathrm{GeV}^2)$ bins: (a)$[1.40, 1.45] - [4.2, 5.0]$, (b)$[1.45, 1.50] - [4.2, 5.0]$, (c)$[1.50, 1.55] - [4.2, 5.0]$, and (d)$[1.55, 1.60] - [4.2, 5.0]$.

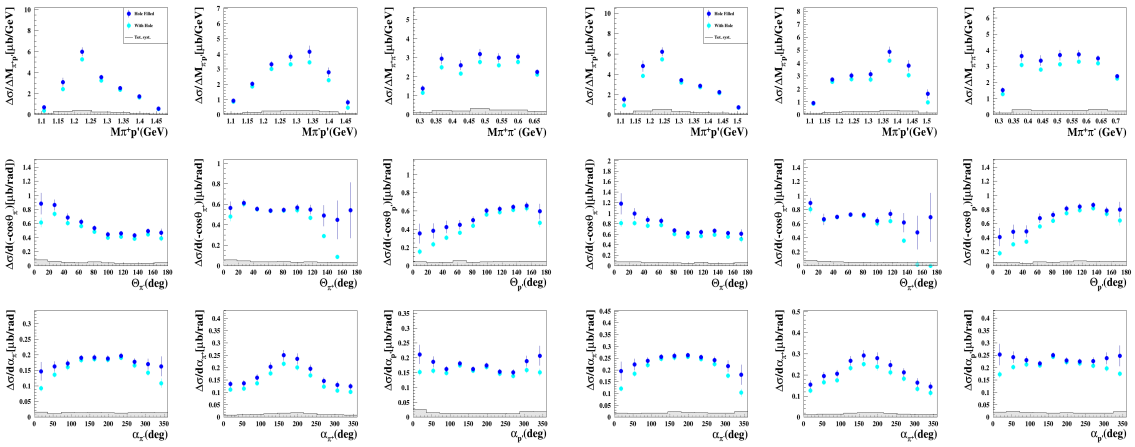

(a) (b)

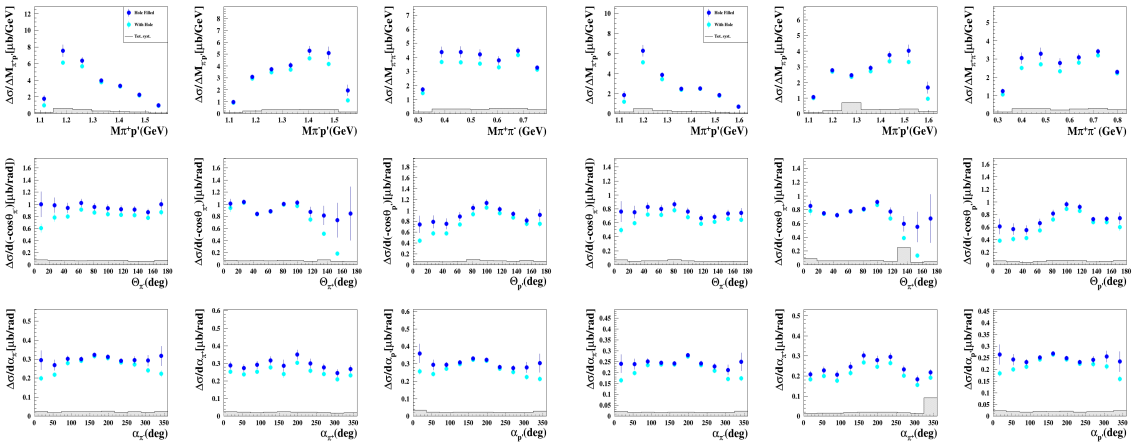

(c) (d)

Figure A.18 Measured nine single-differential cross sections for $W(\mathrm{GeV})$−$Q^2(\mathrm{GeV}^2)$ bins: (a)$[1.60, 1.65] - [4.2, 5.0]$, (b)$[1.65, 1.70] - [4.2, 5.0]$, (c)$[1.70, 1.75] - [4.2, 5.0]$, and (d)$[1.75, 1.80] - [4.2, 5.0]$.

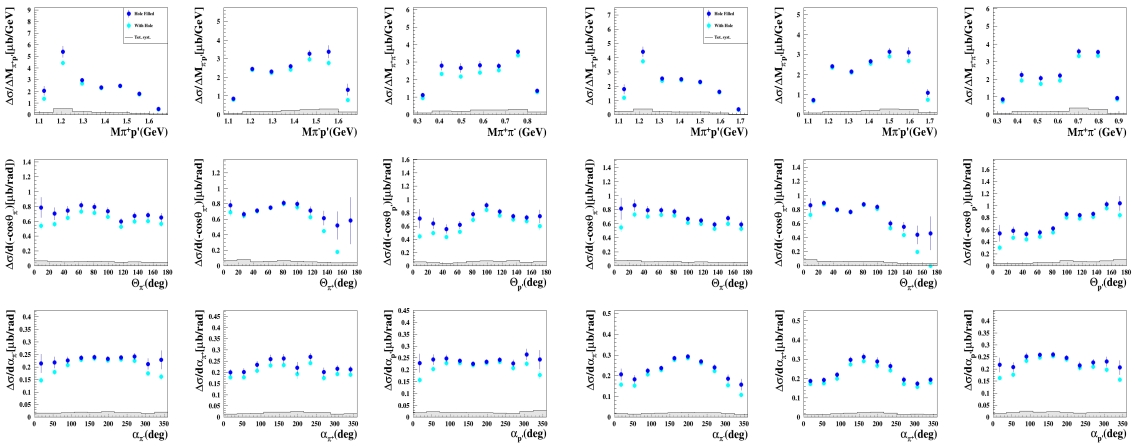

(a) (b)

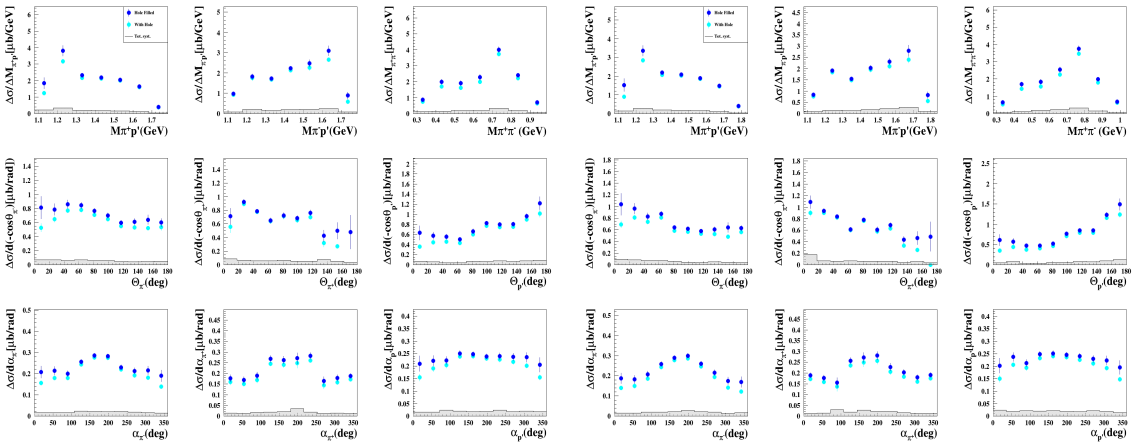

(c) (d)

Figure A.19 Measured nine single-differential cross sections for $W(\mathrm{GeV})$−$Q^2(\mathrm{GeV}^2)$ bins: (a)$[1.80, 1.85] - [4.2, 5.0]$, (b)$[1.85, 1.90] - [4.2, 5.0]$, (c)$[1.90, 1.95] - [4.2, 5.0]$, and (d)$[1.95, 2.00] - [4.2, 5.0]$.

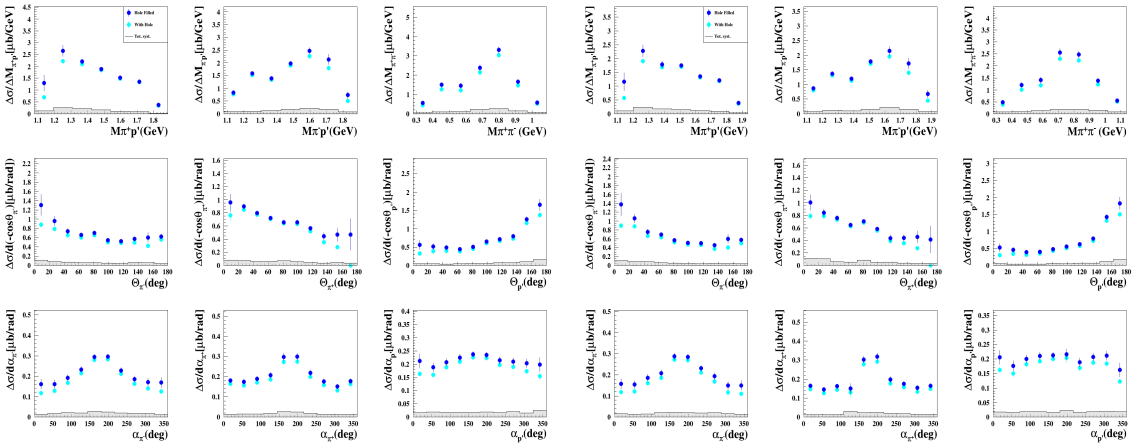

(a) (b)

Figure A.20 Measured nine single-differential cross sections for $W(\mathrm{GeV})-Q^2(\mathrm{GeV}^2)$ bins: (a)$[2.00, 2.05] - [4.2, 5.0]$, and (b)$[2.05, 2.10] - [4.2, 5.0]$.

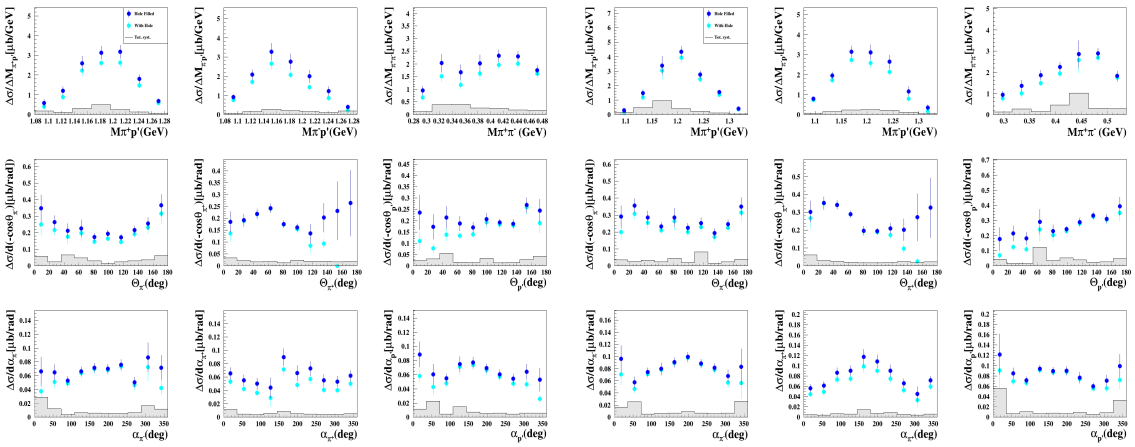

(a) (b)

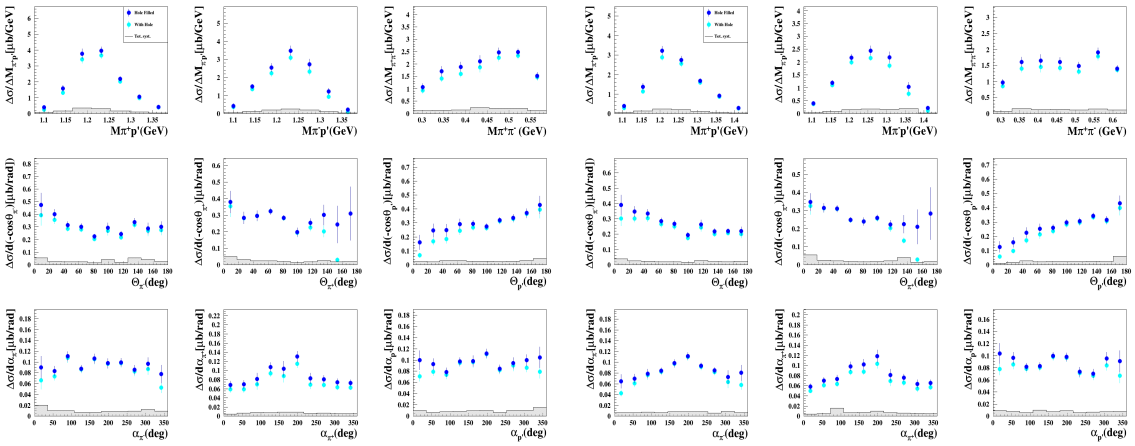

(c) (d)

Figure A.21 Measured nine single-differential cross sections for $W(\mathrm{GeV})-Q^2(\mathrm{GeV}^2)$ bins: (a)$[1.40, 1.45] - [5.0, 6.0]$, (b)$[1.45, 1.50] - [5.0, 6.0]$, (c)$[1.50, 1.55] - [5.0, 6.0]$, and (d)$[1.55, 1.60] - [5.0, 6.0]$.

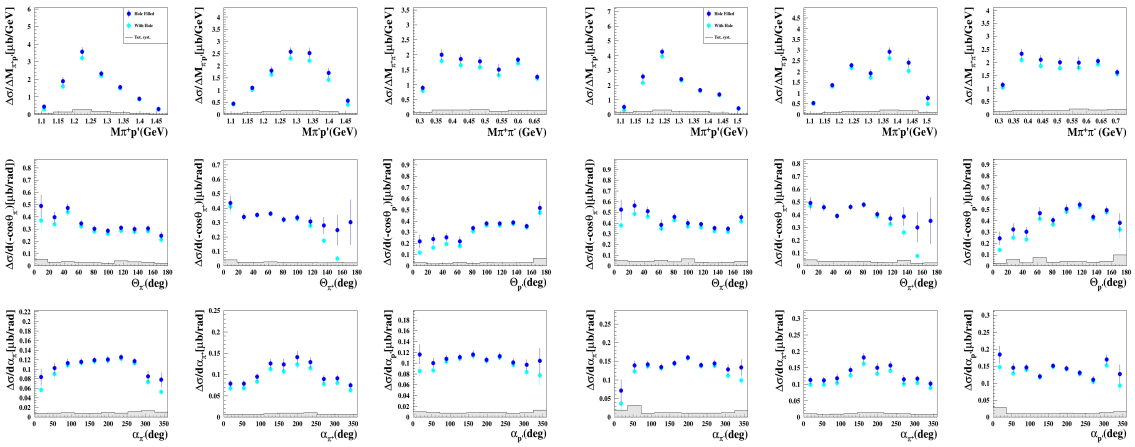

(a) (b)

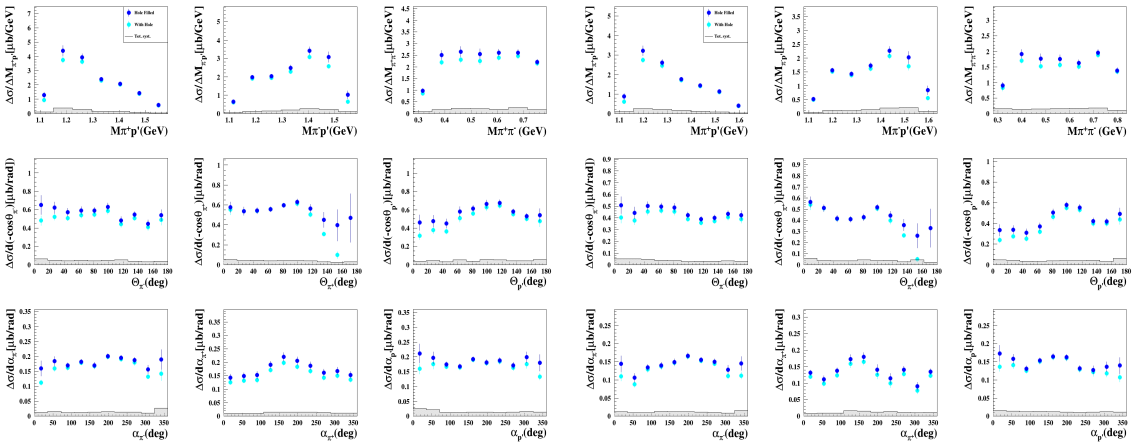

(c) (d)

Figure A.22 Measured nine single-differential cross sections for $W(\mathrm{GeV})$−$Q^2(\mathrm{GeV}^2)$ bins: (a)$[1.60, 1.65] - [5.0, 6.0]$, (b)$[1.65, 1.70] - [5.0, 6.0]$, (c)$[1.70, 1.75] - [5.0, 6.0]$, and (d)$[1.75, 1.80] - [5.0, 6.0]$.

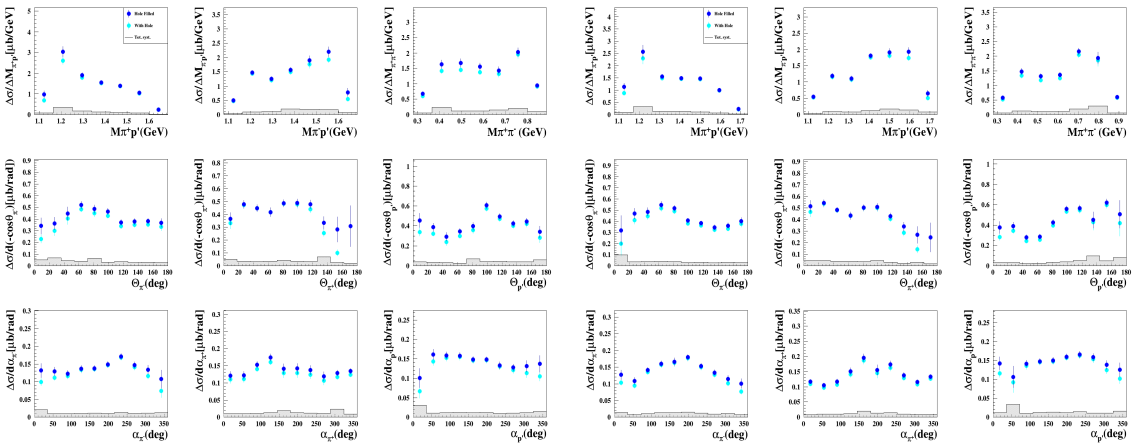

(a) (b)

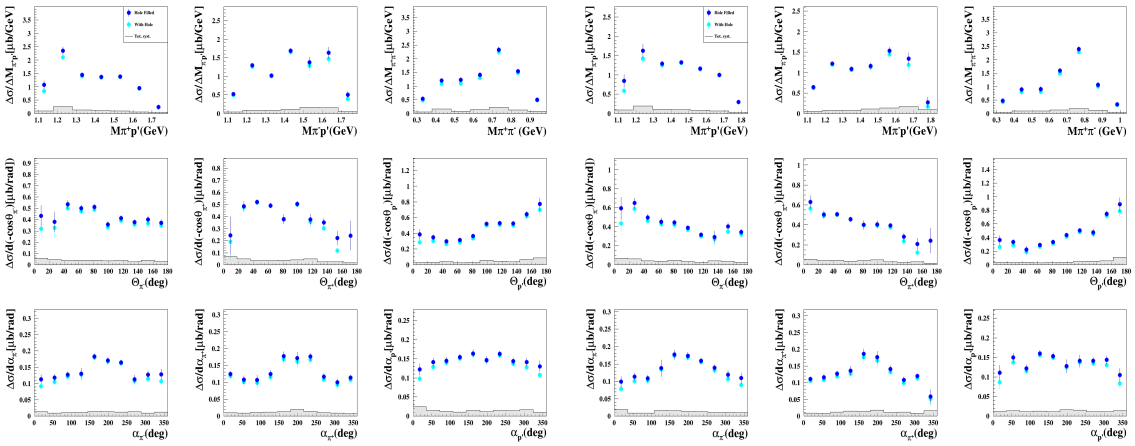

(c) (d)

Figure A.23 Measured nine single-differential cross sections for $W(\mathrm{GeV})-Q^2(\mathrm{GeV}^2)$ bins: (a)$[1.80, 1.85] - [5.0, 6.0]$, (b)$[1.85, 1.90] - [5.0, 6.0]$, (c)$[1.90, 1.95] - [5.0, 6.0]$, and (d)$[1.95, 2.00] - [5.0, 6.0]$.

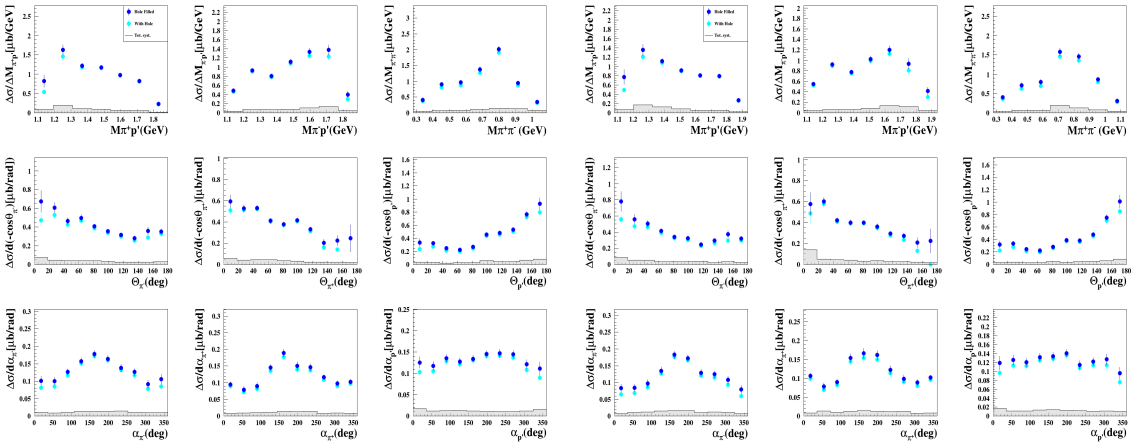

(a) (b)

Figure A.24 Measured nine single-differential cross sections for $W(\mathrm{GeV})-Q^2(\mathrm{GeV}^2)$ bins: (a)$[2.00, 2.05] - [5.0, 6.0]$, and (b)$[2.05, 2.10] - [5.0, 6.0]$.

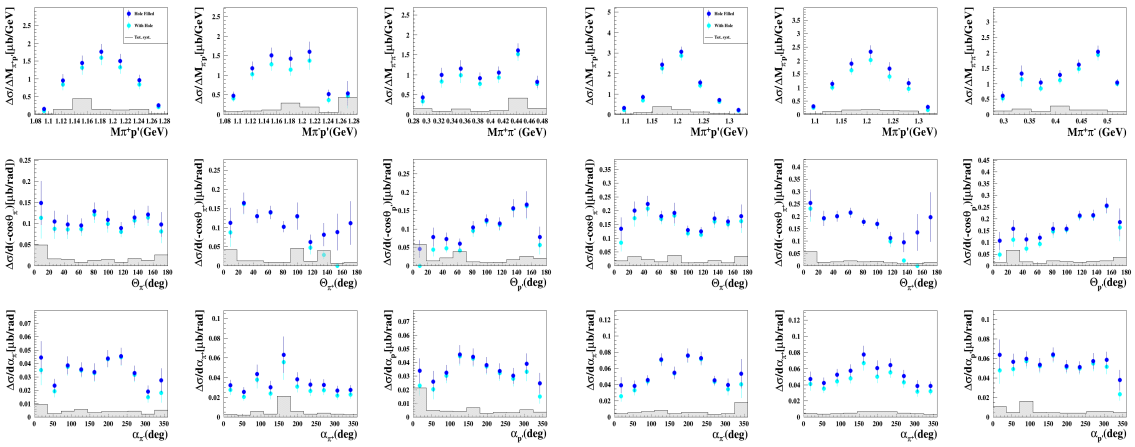

(a) (b)

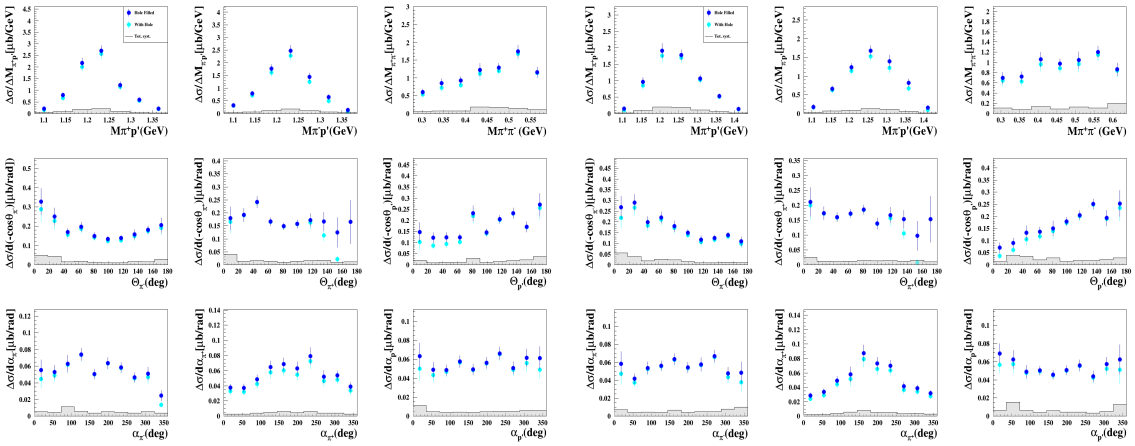

(c) (d)

Figure A.25 Measured nine single-differential cross sections for $W(\mathrm{GeV})-Q^2(\mathrm{GeV}^2)$ bins: (a)$[1.40, 1.45] - [6.0, 7.0]$, (b)$[1.45, 1.50] - [6.0, 7.0]$, (c)$[1.50, 1.55] - [6.0, 7.0]$, and (d)$[1.55, 1.60] - [6.0, 7.0]$.

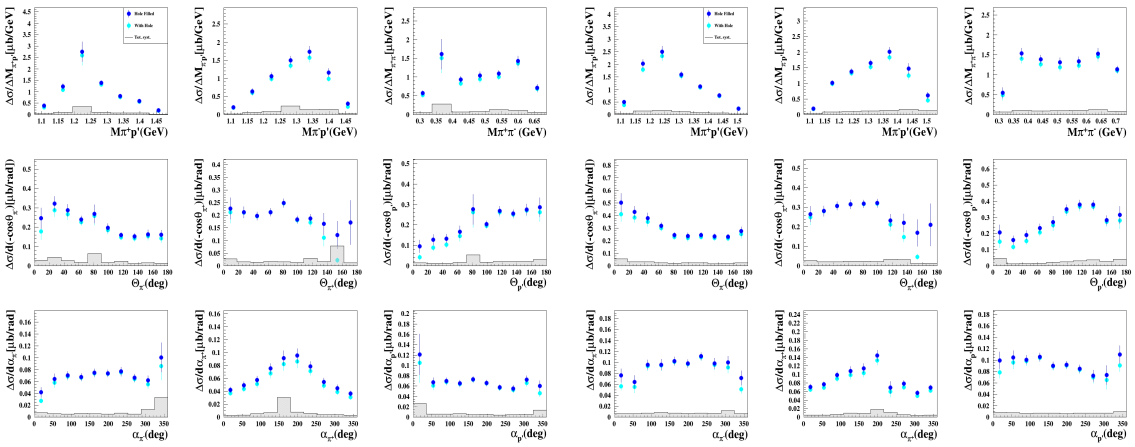

(a) (b)

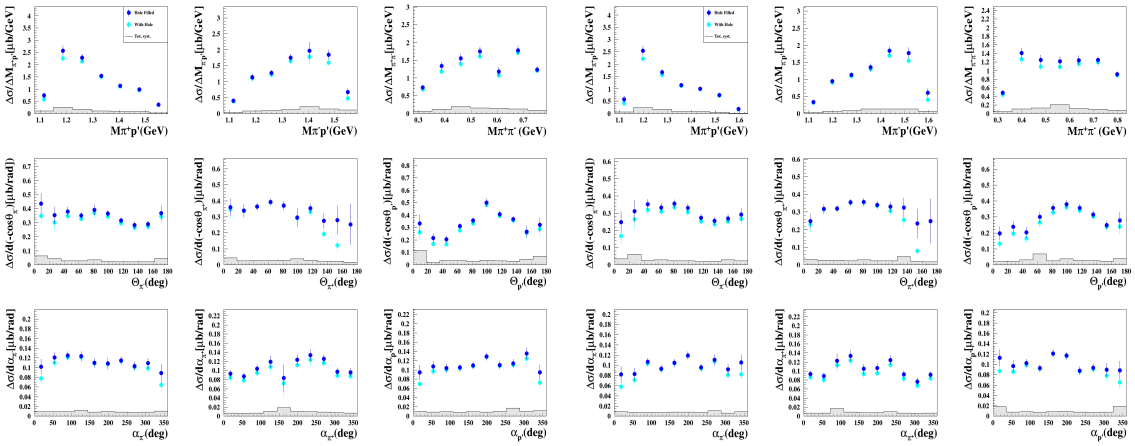

(c) (d)

Figure A.26 Measured nine single-differential cross sections for $W(\mathrm{GeV})-Q^2(\mathrm{GeV}^2)$ bins: (a)$[1.60, 1.65] - [6.0, 7.0]$, (b)$[1.65, 1.70] - [6.0, 7.0]$, (c)$[1.70, 1.75] - [6.0, 7.0]$, and (d)$[1.75, 1.80] - [6.0, 7.0]$.

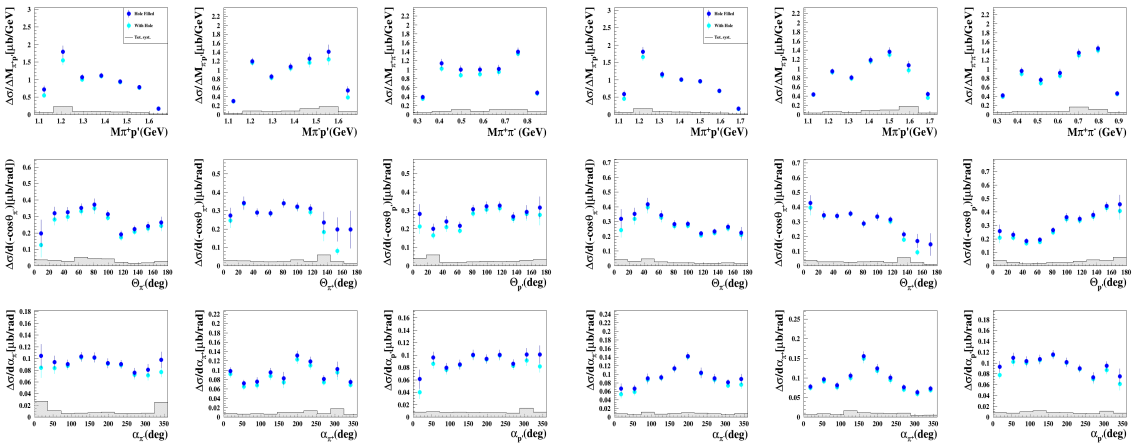

(a) (b)

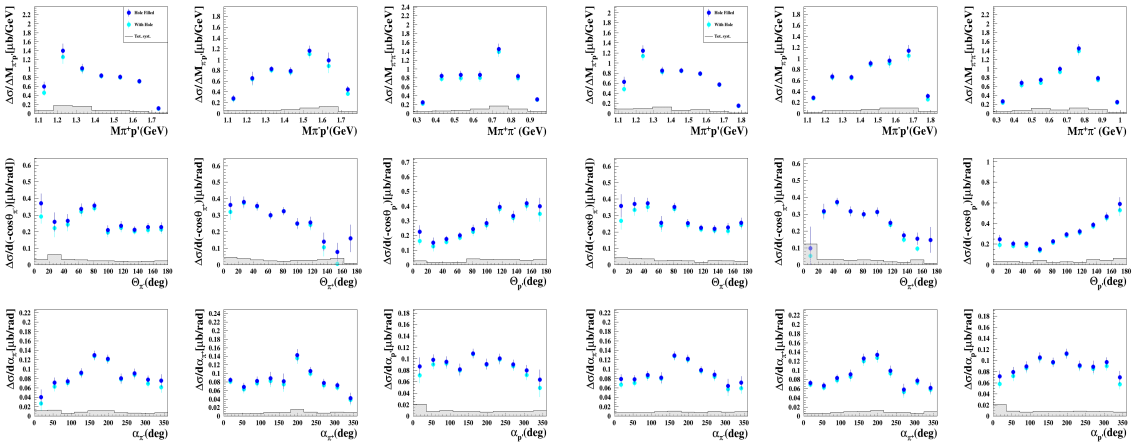

(c) (d)

Figure A.27 Measured nine single-differential cross sections for $W(\mathrm{GeV})-Q^2(\mathrm{GeV}^2)$ bins: (a)$[1.80, 1.85] - [6.0, 7.0]$, (b)$[1.85, 1.90] - [6.0, 7.0]$, (c)$[1.90, 1.95] - [6.0, 7.0]$, and (d)$[1.95, 2.00] - [6.0, 7.0]$.

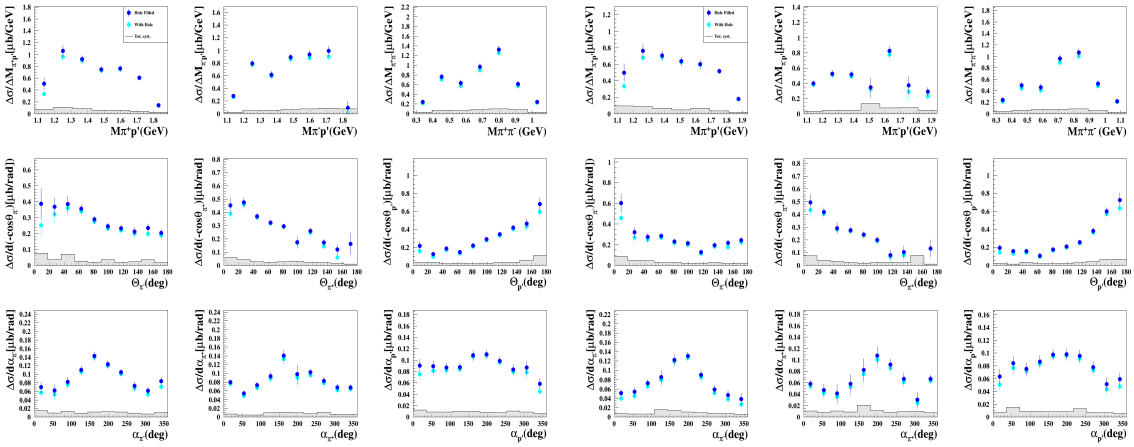

(a) (b)

Figure A.28 Measured nine single-differential cross sections for $W(\mathrm{GeV})-Q^2(\mathrm{GeV}^2)$ bins: (a)$[2.00, 2.05] - [6.0, 7.0]$, and (b)$[2.05, 2.10] - [6.0, 7.0]$.

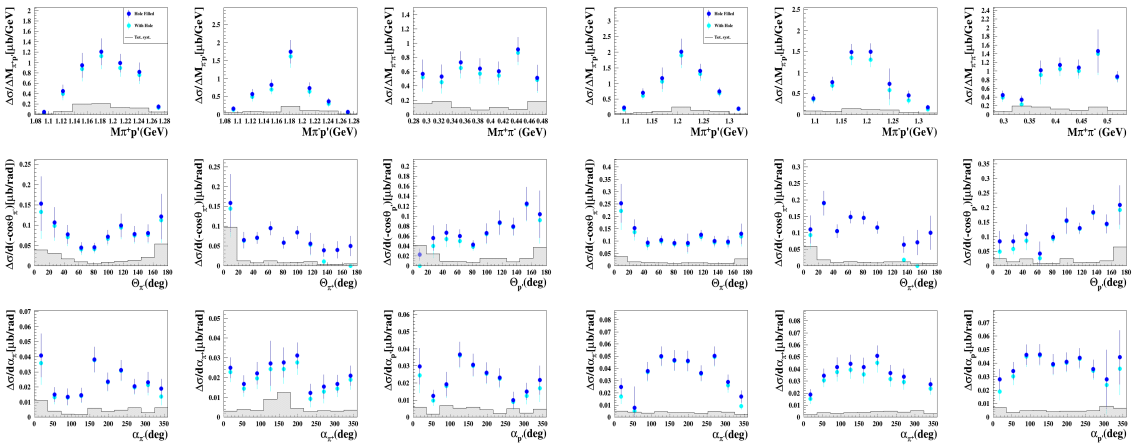

(a) (b)

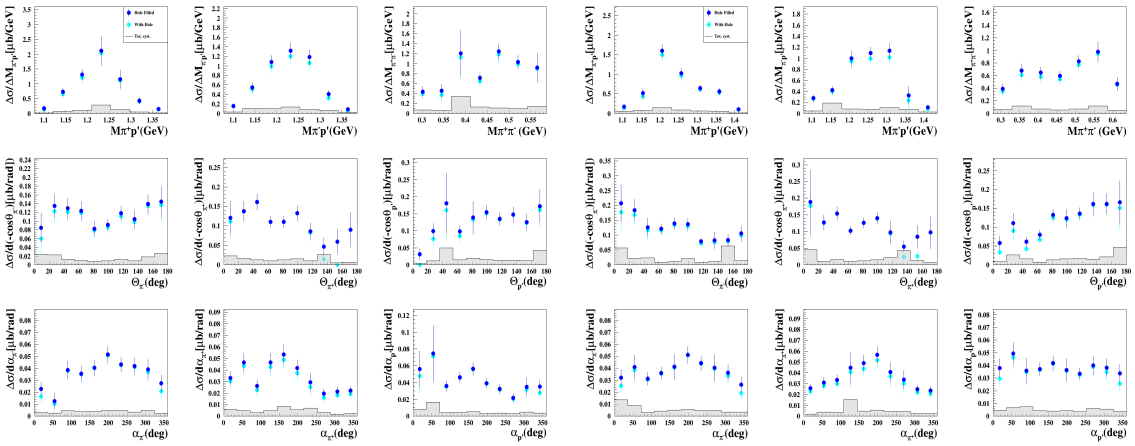

(c) (d)

Figure A.29 Measured nine single-differential cross sections for $W(\mathrm{GeV})-Q^2(\mathrm{GeV}^2)$ bins: (a)$[1.40, 1.45] - [7.0, 8.0]$, (b)$[1.45, 1.50] - [7.0, 8.0]$, (c)$[1.50, 1.55] - [7.0, 8.0]$, and (d)$[1.55, 1.60] - [7.0, 8.0]$.

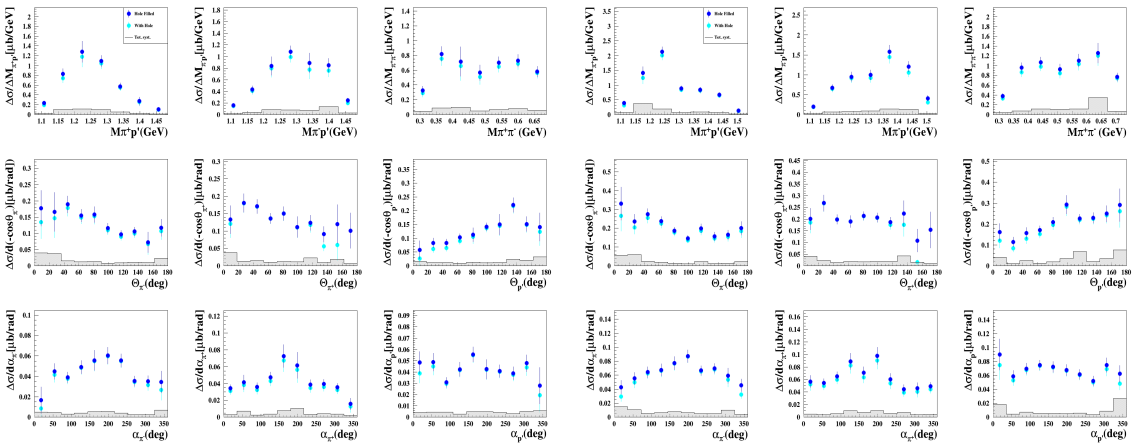

(a) (b)

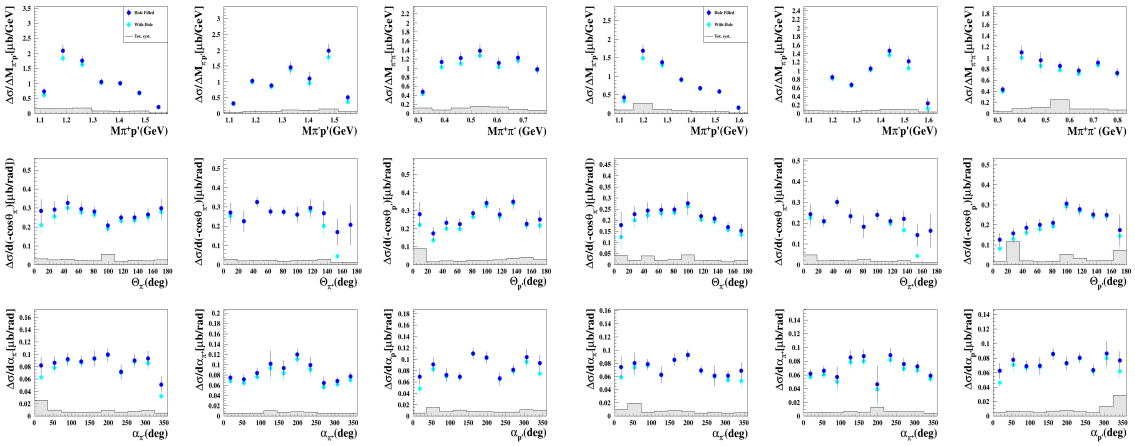

(c) (d)

Figure A.30 Measured nine single-differential cross sections for $W(\mathrm{GeV})$−$Q^2(\mathrm{GeV}^2)$ bins: (a)$[1.60, 1.65] - [7.0, 8.0]$, (b)$[1.65, 1.70] - [7.0, 8.0]$, (c)$[1.70, 1.75] - [7.0, 8.0]$, and (d)$[1.75, 1.80] - [7.0, 8.0]$.

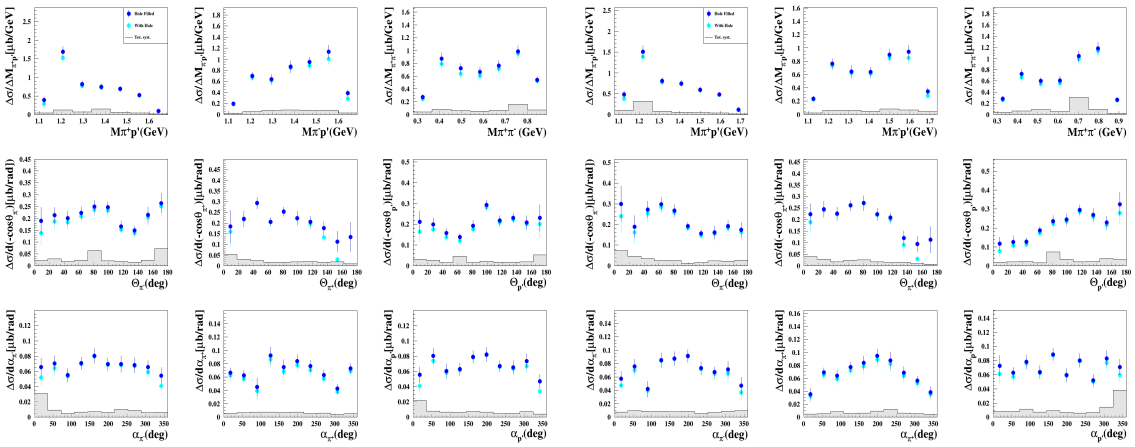

(a) (b)

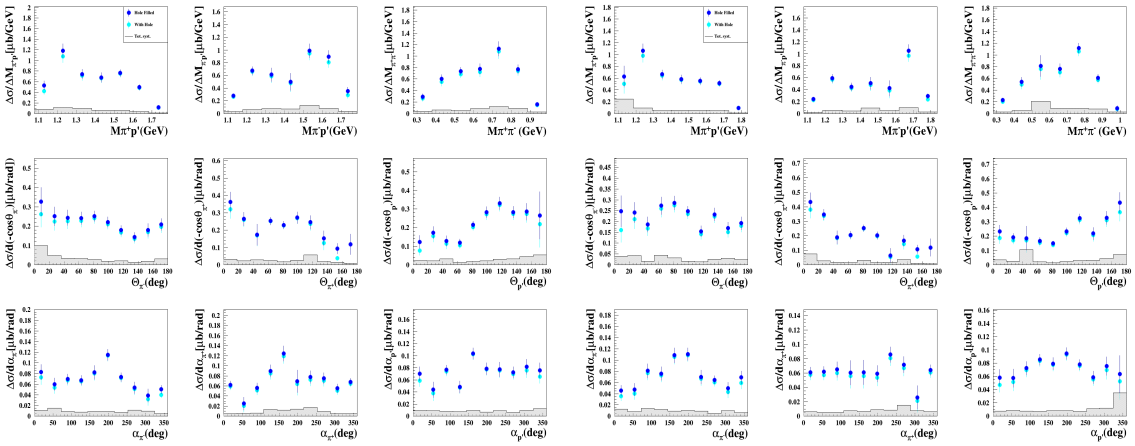

(c) (d)

Figure A.31 Measured nine single-differential cross sections for $W(\mathrm{GeV})-Q^2(\mathrm{GeV}^2)$ bins: (a)$[1.80, 1.85] - [7.0, 8.0]$, (b)$[1.85, 1.90] - [7.0, 8.0]$, (c)$[1.90, 1.95] - [7.0, 8.0]$, and (d)$[1.95, 2.00] - [7.0, 8.0]$.

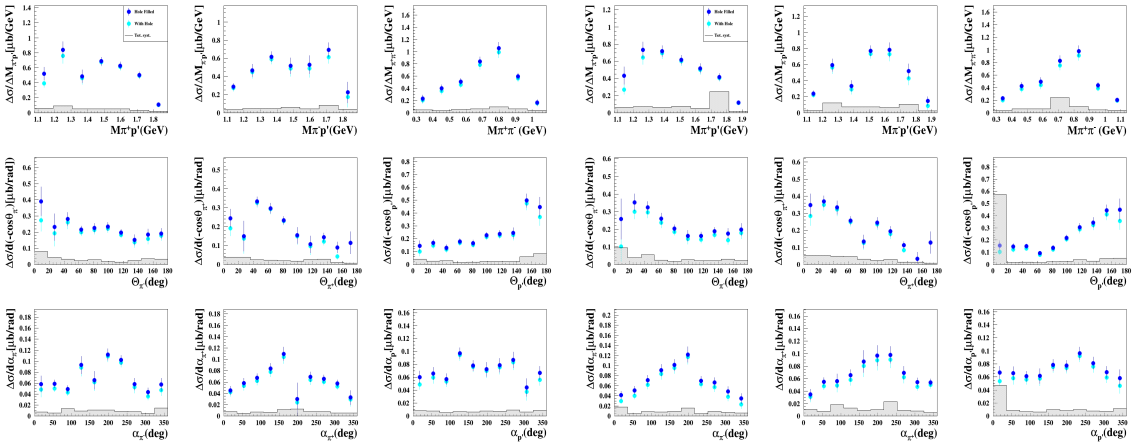

(a) (b)

Figure A.32 Measured nine single-differential cross sections for $W(\mathrm{GeV})-Q^2(\mathrm{GeV}^2)$ bins: (a)$[2.00, 2.05] - [7.0, 8.0]$, and (b)$[2.05, 2.10] - [7.0, 8.0]$.